DESIGN AND MODELING OF A NOVEL DIRECT CARBON MOLTEN CARBONATE FUEL CELL WITH POROUS BED ELECTRODES

Ritesh Agarwal

Dissertation submitted to the Faculty of the
Virginia Polytechnic Institute and State University
in partial fulfillment of the requirements for the degree of

DOCTOR OF PHILOSOPHY
in
MECHANICAL ENGINEERING

Alan A. Kornhauser(Chair)
Michael W. Ellis
Michael von Spakovsky
Douglas J. Nelson
Brian Vick
Amanda J. Morris

December 02, 2014
Blacksburg, Virginia

DESIGN AND MODELING OF A NOVEL DIRECT CARBON MOLTEN CARBONATE FUEL CELL WITH POROUS BED ELECTRODES

Ritesh Agarwal

(ABSTRACT)

A novel concept has been developed for the direct carbon fuel cell (DCFC) based on molten carbonate recirculating electrolyte. In the cathode, co-current flow of electrolyte with entrained CO_2 and O_2 is sent in the upward direction through a porous bed grid. In the anode, co-current flow of a slurry of electrolyte entrained with carbon particles is sent in the downward direction through a porous bed grid. The CO_2 and O_2 in the cathode react on the grid surface to form carbonate ions. The carbonate ions are then transported via conduction to the anode for reaction with carbon to produce CO_2 for temperatures under 750°C.

A mathematical model based on this novel DCFC concept has been developed. The model includes governing equations that describe the transport and electrochemical processes taking place in both the anode and cathode and a methodology for solving these equations. Literature correlations from multi-phase packed-bed chemical reactors were used to estimate phase hold-up and mass transfer coefficients. CO production and axial diffusion were neglected.

The results demonstrated that activation and ohmic polarization were important to the cell output. The impact of concentration polarization to the cell output was comparatively small. The bed depths realized were of the order of 10cm which is not large enough to accommodate the economies of scale for a large scale plant, however thousands of smaller cells (10 m^2 area) in series could be built to scale up to a 10 MW industrial plant. Limiting current densities of the order of 1000-1500 A/m^2 were achieved for various operating conditions. Maximum power densities of 200-350 W/m^2 with current densities of 500-750 A/m^2, and cell voltages of 0.4-0.5 V have been achieved at a temperature of 700 $^\circ$C. Over temperatures ranging from 700 to 800 $^\circ$C, results from the modeled cell are comparable with results seen in the literature for direct carbon fuel cells that are similar in design and construction.

VIRGINIA POLYTECHNIC INSTITUTE AND STATE UNIVERSITY

Date: **December 02, 2014**

ACKNOWLEDGEMENTS

This work was partially supported by the U.S. Department of Energy and the V.T. Department of Mechanical Engineering at Virginia Tech for which I am very thankful. Also, the research work was supported in part by the funding from the work on Fuel Doctor investigated by Dr. Kornhauser to whom my utmost thanks are due. Thanks are also due to Dr. Kornhauser, my supervisor, for his guidance through the early years of chaos and confusion and constant support during this research.

I am thankful to some of the faculty members in the Department of Mechanical Engineering, especially Dr. Dancey, Dr. Diller, and Dr. Tafti for providing me part support through teaching activities during my stay at Virginia Tech. I am thankful to all the administrative staff in the Department of Mechanical Engineering at Virginia Tech, especially Cathy Hill, Ben Poe, and Jamie Archual for their constant help in various administrative and technology matters.

Last but the most important, I am very grateful to my parents, my wife and my young son for their patience, love and constant support throughout the duration of my thesis.

Blacksburg, Virginia — Ritesh Agarwal
December 2, 2014

VIRGINIA POLYTECHNIC INSTITUTE AND STATE UNIVERSITY

Date: **December 02, 2014**

Author: **Ritesh Agarwal**

Title: **DESIGN AND MODELING OF A NOVEL DIRECT CARBON MOLTEN CARBONATE FUEL CELL WITH POROUS BED ELECTRODES**

Department: **Mechanical Engineering**

Degree: **Ph.D.** Convocation: **May** Year: **2015**

To My Parents.

Contents

1 Direct Carbon Fuel Cells **1**

1.1 Introduction 1

1.2 Objectives 5

1.3 Literature Review 7

1.4 Direct Carbon Fuel 16

2 Entrained Fuel Oxidizer - Design Concept **18**

2.1 Introduction 18

2.2 Co-current Flow Concept 20

2.3 Gravity Flow Concept 23

2.4 The Porous Bed Cell 26

2.4.1 Advantages of Porous Bed Cell 26

2.4.2 Disadvantages of Porous Bed Cells 29

2.5 Carbon Monoxide/Carbon Dioxide Production 29

2.6 Advantages of a Liquid Electrolyte 31

2.7 Molten Carbonate Stability 32

2.8 Potential and Current Density in Porous Beds 33

2.9 Balance of Plant 40

2.9.1 Introduction 40

2.9.2 Overall Plant Design and Modeling 40

2.9.3 Discussion of Results 42

3 Process Modeling **46**
3.1 Thermo-Physical Properties 48
3.1.1 Density of molten carbonate salts 50
3.1.2 Surface tension of molten carbonate salts 50
3.1.3 Viscosity of molten carbonate salts 50
3.1.4 Electrical conductance of molten carbonate salts 51
3.1.5 Solubility of Gases CO_2 and O_2 in Electrolyte 52
3.1.6 Diffusivity of Gases CO_2 and O_2 in Electrolyte 54
3.2 Electrode Kinetics 56
3.2.1 Cathode Kinetics 59
3.2.2 Anode Kinetics 66
3.3 Transport Equations in Porous Beds 74
3.3.1 Gas-Phase Equations 74
3.3.2 Liquid and Solid Phase Equations 77
3.4 Upflow in Packed Bed Cathode 78
3.4.1 Model assumptions and limitations 81
3.4.2 Modeling Cathode Packed Bed through linear ODE's 82
3.4.3 Mass Transfer Equations for Packed Bed Cathode 88
3.4.4 Molar Density equations: 92
3.5 Downflow in Packed Bed Anode 94
3.5.1 Model assumptions and limitations 96
3.5.2 Modeling Anode Packed Bed through linear ODE's 97
3.5.3 Slurry Properties 102
3.5.4 Mass Transfer in Anode Packed Bed 105
3.5.5 Molar Density Equations in Anode Bed 119
3.5.6 Bed Resistance in Anode 119
3.6 Solution Technique 126

4 Results and Discussion **131**
4.1 Base Case Results 132

4.1.1 Cell Performance Results 135
4.1.2 Voltage Gradient with Bed Thickness 141
4.1.3 Anode Kinetics and Mass Transfer 143
4.1.4 Cathode Kinetics and Mass Transfer 149
4.2 Parametric Analysis with Respect to Design Parameters 154
4.2.1 Feed Gas Flow Rate in the Cathode: 155
4.2.2 Variation in Cathode Bed Depth 156
4.2.3 Variation in Anode Bed Depth 158
4.2.4 Charge-Transfer Current Density in Cathode 158
4.2.5 Cell Temperature 164
4.2.6 Charge-Transfer Current Density in Anode 169
4.2.7 Liquid Electrolyte Superficial Velocity 169
4.2.8 Effect of intermediate electrolyte layer 173
4.2.9 Grid Packing Variations 173
4.2.10 Carbon Particle Diameter 180
4.3 Parametric Analysis with Respect to Uncertainties in Correlations Used 183
4.3.1 Charge-Transfer Current Density in Cathode 185
4.3.2 Charge-Transfer Current Density in Anode 191
4.3.3 Contact Resistance Variation in Anode 193
4.3.4 Mass Transfer 195
4.3.5 Solubility in Molten Carbonate Salts 202
4.3.6 Molecular Diffusivity of Gaseous species 208
4.3.7 Electrolyte Composition Variation 210
4.4 Discussion Of Results 213
4.4.1 Experimental data comparison with model at 700 $^{\circ}C$ 214
4.4.2 Experimental data comparison with model at 750 $^{\circ}C$ 219
4.4.3 Experimental data comparison with model at 800 $^{\circ}C$ 221
4.5 Results Summary 226

5 Conclusions **231**

6 Future Work **238**

Appendices **242**

A Contact Resistance Model **243**

B Open Circuit Potential **246**

C Estimation of Packed Bed Parameters **250**

D Thermo-Physical Properties **261**

E Transport Processes for Gravity Flow Concept **266**

Bibliography **289**

List of Figures

1.1 Conceptual designs by SRI for the direct carbon fuel cells. 9
1.2 Schematic representation of LLNL direct carbon molten carbonate fuel cell built inside an alumina tube and contained within an alumina crucible with porous nickel cathode and anode and a zirconia cloth separator. 12
1.3 Schematic representation of a direct carbon fuel cell using ternary eutectic molten carbonate electrolyte built by Kouchachvili and Ikura [2011]. 15

2.1 Schematic of the Packed Bed Direct Carbon Molten Carbonate Fuel Cell 21
2.2 Schematic of the gravity flow alternate concept for a direct carbon fuel cell. 24
2.3 Carbon monoxide production based on chemical equilibrium and from Stanford Research Institute experimental data [Weaver et al., 1979]. 30
2.4 One-dimensional Packed Bed Cathode showing path of current, solution and potential. 35
2.5 Electrode polarity in electrolyzer and fuel cell 36
2.6 Potential distribution in fuel cell with no electrolyte resistance. 37
2.7 Potential distribution in fuel cell with lumped electrolyte resistance. . 38
2.8 Potential distribution in fuel cell with distributed electrolyte resistance. 39

2.9 Balance of Plant for the Direct Carbon Molten Carbonate Fuel Cell. . 41
2.10 Work and Waste Heat vs. Mole Fraction Carbon Dioxide Leaving Anode, Cell Temperature as Parameter. 43
2.11 Non-Dimensional Work and Waste Heat vs. Mole Fraction Carbon Dioxide Leaving Anode, Cell Efficiency as Parameter, Cell T = 950 K. 44

3.1 Solubility data for O_2 in the ternary eutectic melt of Li_2CO_3 - Na_2CO_3 - K_2CO_3 (43.5 - 31.5 - 25.0 mol%). 55
3.2 Determination of Exchange Current Density and Charge-transfer coefficient in Anode. 68
3.3 Flow of gas-bubble entrained bulk liquid electrolyte through packed bed reactor. 75
3.4 Schematic of presence of bubbles in the liquid electrolyte and showing relationship between concentrations in gas-bubble phase, bulk liquid and concentration at the bulk liquid-bubble interface (equilibrium). 76
3.5 Fuel Cell schematic showing cathode/anode bed with electrolyte entrained with carbon (anode) and gas bubbles, and distributor channels in the intermediate layer. 79
3.6 Schematic of a possible cathode packed bed arrangement using wiremesh or perforated plates as the packing material 80
3.7 Cathode Model showing the Dependent and Independent Variables. 80
3.8 Carbon particle exchanging current with the bed. 94
3.9 Anode Model showing the Dependent and Independent Variables. . 95
3.10 Mechanism of charge transfer in the anode bed with carbon entrained in molten carbonate electrolyte as slurry. 121
3.11 Solution methodology to iterate for the current density and potential distribution factor for given design operating conditions. 127
3.12 Flowchart showing solution methodology for the overall fuel cell model.128

3.13 Mathematical solution technique used to solve 6 ordinary differential equations describing electrochemical processes in the cathode bed. 129
3.14 Mathematical solution technique used to solve 5 ordinary differential equations describing electrochemical processes in the anode bed. . 130

4.1 Current Density - Cell Voltage Plot showing various regions of polarization for the base case conditions. 136
4.2 Current Density - Voltage and Current Density - Power Density variations for base case conditions. 138
4.3 Current Density - Efficiency and Current Density - Power Density variations for base case conditions. 140
4.4 Potential Gradients in Cathode and Anode Beds varying with bed thickness for the base case conditions. 142
4.5 Potential Gradients in Cathode and Anode Beds varying with bed thickness showing voltage drop due to contact resistance. 144
4.6 Experimental results extracted from the work of Vutetakis [1985] indicating no influence of inert purge gas on the current density. 145
4.7 Molar Concentration of CO_2 at the carbon particle surface (reaction site) for base case conditions. 147
4.8 CO_2 Concentration Profiles in anode at the surface, bulk liquid, and at equilibrium for base case conditions. (a) High Current Density (=1179 A/m^2) region (b) Low Current density (=34 A/m^2) region. . . 148
4.9 CO_2 Concentration Profiles in cathode at the surface, bulk liquid, and at equilibrium for base case conditions. (a) High Current Density (=1179 A/m^2) region (b) Low Current density (=34 A/m^2) region. . . 151
4.10 O_2 Concentration Profiles in cathode at the surface, bulk liquid, and at equilibrium for base case conditions. (a) High Current Density (=1179 A/m^2) region (b) Low Current density (=34 A/m^2) region. . . 152
4.11 Current Density - Cell Voltage Variation with cathode feed gas flow rate. 157

4.12 Variation in current-density and cell potential characteristics with respect to variation in cathode bed depth shown for two cases of cathode feed gas flow rates, F_v. (a) 0.01 m3/hr (b) 0.1 m3/hr. 159
4.13 Current Density - Cell Voltage Variation with varying anode bed depth.160
4.14 Current Density - Cell Voltage Variation with varying O_2 inlet partial pressure. 163
4.15 Current Density - Cell Voltage Variation with varying CO_2 inlet partial pressure. 165
4.16 Current Density - Cell Voltage Variation with varying fuel cell temperature, $T = 923, 973 and 1023\,K$. 166
4.17 Current Density - Power Density Variation with varying cell temperature: 923, 973, and 1023 K. 168
4.18 Current Density - Cell Voltage Variation with varying liquid electrolyte superficial velocities at the cathode inlet. 170
4.19 Current Density - Cell Voltage Variation with varying liquid electrolyte superficial velocities at the anode inlet. 172
4.20 Current Density - Cell Voltage Variation with varying intermediate layer (between cathode and anode). 174
4.21 Current Density - Cell Voltage Variation with varying Cathode grid packing (Wire-Mesh #24, #30, and #40). 177
4.22 Current Density - Cell Voltage Variation with varying Anode grid packing (Wire-Mesh #20, #24, and #30). 178
4.23 Current Density - Cell Voltage Variation with varying Anode grid packing (Wire-Mesh #20, #24, and #30). 179
4.24 Current Density - Cell Voltage Variation with varying carbon particle diameter at the anode inlet (Carbon particle initial diameter, $D_{c,ini} = 50, 100, 175,$ and $250\,\mu m$). 181
4.25 Current Density - Cell Voltage Variation with varying exponents in the kinetic rate expression for cathode. 188

4.26 Current Density - Cell Voltage Variation with varying exchange current density in the kinetic rate expression for cathode. 190
4.27 Current Density - Cell Voltage Variation with varying exchange current density in anode bed. 192
4.28 Current Density - Cell Voltage Variation with varying carbon solid holdup at the anode inlet. 194
4.29 Current Density - Cell Voltage Variation with varying particle resistivity at settled conditions ($\rho_{ct,0}$). 196
4.30 Current Density - Cell Voltage Variation with varying liquid-solid mass transfer coefficients for both CO_2 and CO_2 in the cathode bed. . . . 198
4.31 Current Density - Cell Voltage Variation with varying liquid-solid mass transfer coefficients for CO_2 in the anode bed. 200
4.32 Current Density - Cell Voltage Variation with varying gas-liquid mass transfer coefficients for CO_2 and O_2 in the cathode bed. 201
4.33 Current Density - Cell Voltage Variation with varying solubility of CO_2 in the molten carbonate salt. 205
4.34 Current Density - Cell Voltage Variation with varying solubility of O_2 in the molten carbonate salt. 207
4.35 Current Density - Cell Voltage Variation with varying diffusion coefficient of O_2 in the molten carbonate salt. 209
4.36 Current Density - Cell Voltage Variation with varying specific conductance of molten carbonate electrolyte. 212
4.37 Current Density - Cell Voltage process simulation results comparison with experimental data from LLNL and others. 216
4.38 Current Density - Power Density process simulation results comparison with experimental data from LLNL and others. 217
4.39 Current Density - Cell Voltage process simulation results comparison with experimental data from LLNL [Cherepy et al., 2005][Figure 8, top 220

4.40 Current Density - Cell Voltage process simulation results comparison with experimental data from LLNL [Cherepy et al., 2005][Figure 8, top 222
4.41 Current Density - Power Density process simulation results comparison with experimental data from LLNL [Cherepy et al., 2005]. 223

A.1 Model development for contact resistance voltage loss using analogical concepts from heat transfer. 244

C.1 Schematic with a unit size of two wire-meshes. 252
C.2 Possible configurations of electrolyte flow over wire-mesh packed bed.258

E.1 Differential Element of a Cathode Model showing the Dependent and Independent Variables. 269
E.2 Mass Transfer in Porous Bed Anode in a gas-bubble free electrolyte. 270
E.3 Differential Element of Anode Model showing the Dependent and Independent Variables. 271
E.4 Mass Transport in Porous Bed Cathode in a gas-bubble free electrolyte. 282
E.5 Transverse dispersion in packed bed falling films. 285

List of Tables

3.1 CO_2 Solubility for various electrolyte melts at varying temperatures. 53
3.2 Kinetic parameters for oxygen reduction mechanism in MCFC cathode. 61
3.3 Correlations Used for the Cathode Packed Bed 90
3.4 Various Correlations Used for the Anode Packed Bed 118

4.1 Input Anode and Cathode Parameters for Base Case Conditions . . 133
4.2 Thermo-Physical Properties for Electrolyte and Gas Species for the Base Conditions. 134
4.3 Wire-mesh packing characteristics chart 175
4.4 Cathode Mechanism for oxygen reduction in Ternary Eutectic mixture of $(Li-Na-K)_2CO_3$ from the work of Wilemski et al. [1979], Wilemski [1983] 187
4.5 Solubility data for CO_2 in Ternary Eutectic mixture of $(Li-Na-K)_2CO_3$ from different sources in literature at 973 K. 204
4.6 Data-set information from LLNL [Cherepy et al., 2005], Kouchachvili and Ikura [2011], and Predtechenskii et al. [2009a] with experimental details, used for comparison with the model 215
4.7 Process simulation results comparison with experimental data from LLNL [Cherepy et al., 2005] and Kouchachvili and Ikura [2011] including current density, cell voltage, and power density at 700 $^{\circ}C$ temperature. 218

4.8 Process simulation results comparison with experimental data from LLNL [Cherepy et al., 2005] including current density, cell voltage, and power density at 800 $^{\circ}C$ temperature. 224

5.1 Fuel cell modeling parameters investigated in the current work. . . . 235

C.1 Wire-mesh selection and calculated parameters 259
C.2 Wire-mesh packing parameters calculation required for governing equations 259

D.1 Characteristics required to estimate diffusion coefficients of binary gas mixtures 264

E.1 Gas Chamber Specifications for Square Cross-section. 268
E.2 Gas Chamber Specifications for Annular Cross-section. 268
E.3 Boundary Conditions for the Partial Differential Equations 276
E.4 Gas-side mass transfer at cathode gas-liquid interface for square bed cross-section. 280
E.5 Liquid-solid mass transfer in the cathode bed. 283
E.6 Correlations Used for the Cathode Packed Bed Falling Film 286
E.7 Correlations Used for the Anode Packed Bed Falling Film 288

Nomenclature

Acronyms

Symbol	Description
$DCFC$	Direct Carbon Fuel Cell
$DCMC$	Direct Carbon Molten Carbonate
$DCMCFC$	Direct Carbon Molten Carbonate Fuel Cell
$HDCFC$	Hybrid Direct Carbon Fuel Cell
IGT	Institute of Gas Technology
$LLNL$	Lawrence Livermore National Laboratory
$SARA$	Scientific Applications and Research Associates
$SOFC$	Solid Oxide Fuel Cell
SRI	Stanford Research Institute

Dimensionless Numbers

Symbol	Description	Definition
$\overline{Re}$	Reynolds number based on dissipation	$\frac{\rho U d}{\mu}$

Ar	Archimedes number	$\frac{d^3 g \rho_c \lvert\Delta\rho\rvert}{\mu_c^2}$
Fr	Froude number	$\frac{U_{oL}^2}{g D_p}$
Pe	Peclet number	$\frac{\rho U d}{D}$
Re	Reynolds number	$\frac{\rho U d}{\mu}$
Sc	Schmidt number	$\frac{\mu}{\rho D}$
Sh	Sherwood number	$\frac{kd}{D}$

Greek Symbols

Symbol	Description	Units
α	charge transfer coefficient	–
β	voltage distribution factor	–
$\alpha(x)$	void fraction	
α_{s}	volume fraction carbon	
$\bar{\rho}$	concentration or molar density	$\mathrm{kmol-m^{-3}}$
$\bar{\rho}^*$	equilibrium molar concentration	$\mathrm{kmol-m^{-3}}$
δ	thickness of the liquid layer on the packing	m
η	chemical over-potential	V
γ_L	surface tension of molten carbonate salts	$\mathrm{dynes-cm^{-1}}$
κ	molten salt electrical conductivity	$\Omega\,\mathrm{m}$

μ	dynamic viscosity	$\mathrm{Pa-s}$
ν	kinematic viscosity	$m^2\ s^{-1}$
ϕ_c	Carman surface factor	
ρ	density	$\mathrm{kg-m^{-3}}$
σ	metal phase electrical conductivity	$\Omega\,\mathrm{m}$
τ	tortuosity	
ζ	volume fraction of electrode	

Molecules

Symbol	**Description**
Al_2O_3	Aluminum Oxide
CaO	Calcium Oxide
CO_2	Carbon-dioxide
CO_3^{2-}	Carbonate ion
Cs_2CO_3	Cesium Carbonate
Fe_2O_3	Ferric Oxide
K_2CO_3	Potassium Carbonate
Li_2CO_3	Lithium Carbonate
MgO	Magnesium Oxide
Na_2CO_3	Sodium Carbonate
Ni	Nickel

NiO	Nickel Oxide
O^-	Transient Oxygen ion
O^{2-}	Oxide ion
O_2	Oxygen
O_2^-	Superoxide ion
O_2^{2-}	Peroxide ion
SiO_2	Silica or Silicon Oxide

Roman Symbols

Symbol	Description	Units
A'''	area per unit volume	m^{-1}
A_{cell}	Cell area	cm^2
x	Bed thickness	m
C	Concentration	$\mathrm{kmol-m}^{-3}$
D, D_m	molecular diffusivity of solute	$\mathrm{m}^2\,\mathrm{s}^{-1}$
d_c	diameter of the carbon particle	m
d_e	Equivalent diameter of the packing	m
D_h	Diameter of the hole within packing	m
d_p	packing diameter of the bed	m
$\Delta P/\Delta Z$	pressure gradient within the reactor bed	$\mathrm{N\,m}^{-3}$
$\left(\frac{\Delta P}{\Delta Z}\right)$	Pressure Gradient within the reactor bed	$\mathrm{N-m}^{-3}$

$d_{\mathrm{p}}^{'}$	specific surface diameter	m
d	Mean solid diameter	m
D_t	tube diameter	m
E	rate of energy dissipation per unit mass of fluid	$\mathrm{m}^2\,\mathrm{s}^{-3}$
F	Faraday's constant	$\mathrm{Coulomb}-\mathrm{mol}^{-1}$
f	Friction factor	–
F_v	Cathode feed gas flow rate	$\mathrm{m}^3-\mathrm{hr}^{-1}$
G	Gibb's Energy	$\mathrm{J}-\mathrm{mol}^{-1}$
H, k_H	Henry's Law constant	$\mathrm{kmol\,m^{-3}\,kPa^{-1}}$
H_{b}	Height of the bed	m
h_{b}	Interspacing between the packing	m
h	hold-up	–
i''	Current density	$\mathrm{A\,m^{-2}}$
i''_m	Current density in metal phase	$\mathrm{A\,m^{-2}}$
i''_o	Exchange current density	$\mathrm{A\,m^{-2}}$
i''_s	Current density in solution phase	$\mathrm{A\,m^{-2}}$
k, K	mass transfer coefficient	$\mathrm{m\,s^{-1}}$
ℓ	Length characterizing contact surface area	m
L, L_{b}	Bed Thickness	m
M	Molecular weight	$\mathrm{kg\,kmol^{-1}}$

n_{part}	carbon moles per particle	–
$\dot{N}''$	particle flux	–
N_{hole}	Number of holes in the packing	–
$\dot{n}''_{\text{i,p,r}}$	mole flux of solute i in phase p of the packed bed reactor, r	$\text{kmol}\,\text{m}^{-2}\,\text{sec}^{-1}$
N'''	Particles per unit volume	–
OA	Open area of the packing	–
P	pressure, partial pressure	kPa
$P_{BM,G}$	log mean partial pressure	kPa
R	Ohmic Resistance	$\Omega - \text{m}$
$\bar{R}$	Universal gas constant	$\text{J} - \text{mol}^{-1} - \text{K}^{-1}$
S_h	horizontal pitch	m
S	Surface area of the packing bed	m^2
S_v	vertical pitch	m
T	Fuel cell temperature	K
t	Thickness of the packing	m
U_0	Superficial velocity	$\text{m}\,\text{s}^{-1}$
U	true velocity	$\text{m}\,\text{s}^{-1}$
V	Voltage	V
V_{a}	Anode cell potential	V
V_{c}	Cathode cell potential	V

V_{cell}	Cell potential	V
$V_{\text{m}}, \Phi_{\text{m}}$	Potential in metal phase	V
V_{oc}	Open-circuit potential	V
V_{oca}	Open-circuit potential for anode half-cell	V
V_{occ}	Open-circuit potential for cathode half-cell	V
V_p	volume of the packing bed	m^3
$V_{\text{s}}, \Phi_{\text{s}}$	Potential in solution phase	V
W_{b}	Width of the bed	m
y	Mole fraction	$\text{mol} - \text{mol}^{-1}$
$z, m1, m2$	Stoichiometric reaction orders	

Subscripts

Symbol	**Description**
c, cat	Cathode
g, G	Gas-Phase
l, L, f, ℓ	Liquid-Phase
a	anode
b	bubble
blk	liquid bulk phase
C	carbon
c	cathode

$g-l$	gas-to-liquid
i	solute
$init, ic$	initial conditions
$l-s$	liquid-to-solid
LG	liquid and gas phases flowing simultaneously and concurrently
LS	liquid and solid phases together
m	molecular
O	oxidized species
R	reduced species
rev	reversible
S	solid phase
s	surface
T	transverse

Chapter 1

Direct Carbon Fuel Cells

1.1 Introduction

Carbon (available as coal and biomass) is an abundantly available energy source. There are three main ways of utilizing energy available from oxidizing carbon:

- Burn coal or biomass to create thermal energy that converts water into steam (using Rankine cycle) which runs the steam turbines
- Gasify coal directly to be used in gas turbines or in gas fed fuel cells
- Use in direct carbon fuel cells that can achieve higher theoretical energy efficiency compared with conventional Rankine-cycle coal-fired power plants [Cooper et al., 2000, Steinberg et al., 2002]

Around 100 years ago, there was considerable effort to convert coal directly into electricity. In 1896, William Jacques, a pioneer in the field, built remarkably large carbon-air fuel cells [Jacques, 1896]. His chief problem was breakdown of the molten alkali electrolyte. Later, Baur and co-workers [1912, 1916, 1921],

after abandoning molten alkali electrolytes in favor of less reactive molten carbonate electrolytes, made many advances in fuel cell research, notably in high-temperature electrodes and in molten carbonate electrolytes. In conclusion, they advocated the conversion of coal to electricity indirectly via oxidation of coal-derived gaseous fuels instead of by direct electrochemical reaction of carbon. Interest in direct carbon fuel cells died out in the early years of the 20th century as the efficiency of Rankine cycle power plants increased dramatically. More recently, interest in coal-fed fuel cells has revived following pioneering research efforts by Weaver and co-workers at SRI [1975, 1976a, 1976b, 1979, 1982].

Development of direct carbon fuel cell based on molten hydroxide electrolyte has been pursued by SARA Inc. and others [Zecevic et al., 2003, 2004, 2005], who have designed and built prototypes using this electrolyte.

In the late 20th century, efforts were also put into gas-fueled cells using synthesis gas (hydrogen and carbon monoxide) produced by coal gasification plants [EG & G Inc, [2004]]. Studies, however, show that fuel cell plants that use carbon directly have the potential for higher efficiency than gasification-based plants at similar capital cost [Steinberg et al., 2002].

In the same period, several researchers [Nakagawa and Ishida, 1988, Gür and Huggins, 1992, Horita et al., 1995] have also demonstrated the concept of solid oxide fuel cells in which carbon is oxidized to form CO, which then electrochemically reacts with $\frac{1}{2}\,O^{2-}$ at the anode to form CO_2. More recently, a solid oxide concept for direct electrochemical oxidation is being used in the form of hybrid direct carbon fuel cells [Deleebeeck and Hansen, 2014]. In these cells carbon reacts with a molten salt electrolyte which receives oxygen ions from a solid oxide electrolyte.

The solid oxide electrolyte contains the molten salt and receives oxygen from the air.

Another concept for a solid oxide fuel cell, pioneered by CellTech Power, used proprietary technology to create a unique device that demonstrated capabilities with liquid, solid and gasesous fuels [Tao et al., 2007]. The company has also demonstrated a technology that uses a liquid metal-SOFC system in which liquid tin anode participates as an 'intermediary' for the oxidation of fuel delivered to the fuel cell [Abernathy et al., 2011].

Despite the difficulties inherent in building a solid-fed fuel cell, a direct carbon fuel cell offers distinct thermodynamic advantages over other options for utility-scale power generation. Steinberg et al. [2002] projected overall first-law efficiencies (based on higher heating value) of 68% for power plants using direct carbon fuel cells, as compared with 50% for combined cycle gasification plants and 38% for conventional Rankine-cycle plants. The efficiencies were based on equivalent projected capital costs.

Direct carbon fuel cells using molten carbonate electrolyte were investigated by SRI in the 1970s [Weaver, 1976b, Weaver et al., 1979, 1982] and later on by [Vutetakis, 1985, Peelen et al., 2000, Cherepy et al., 2005]. SRI cells used large pieces of solid carbons, while the others used various carbon-salt slurries or pastes.

In a direct carbon molten carbonate fuel cell (DCMCFC), the electrolyte is lithium carbonate, potassium carbonate, sodium carbonate, or a binary or ternary eutectic of these three alkali molten carbonate salts. Reactions occur at high temperatures (700 $^{\circ}$C and above) so rapid reaction rates can be obtained without the

use of expensive catalysts. Oxygen and carbon dioxide are supplied to the cathode, and the reaction that takes place at the cathode is:

$$\text{Cathode: } \mathrm{O_2 + 2CO_2 + 4e^- \longrightarrow 2CO_3^{2-}} \tag{1.1}$$

Carbonate ions generated at the cathode migrate to the anode via ionic conduction, where they react with carbon:

$$\text{Anode with } CO_2 \text{ formation: } \quad \mathrm{C + 2CO_3^{2-} \longrightarrow 3CO_2 + 4e^-} \quad \text{at low T} \tag{1.2}$$

$$\text{Anode with CO formation: } \quad \mathrm{2C + CO_3^{2-} \longrightarrow 3CO + 2e^-} \quad \text{at high T} \tag{1.3}$$

CO_2 is the dominant product at low temperatures ($< 700°C$) whereas at higher temperatures ($> 700°C$) yields of the formation of CO gradually becomes dominant [Hauser Jr., 1964, Weaver et al., 1979, Vutetakis, 1985]. Carbon dioxide from the anode is supplied to the cathode either by diffusion through the electrolyte or through external piping.

The overall cell reaction that takes place in a direct carbon fuel cell at T$< 700°C$ is:

$$\mathrm{C + O_2 \longrightarrow CO_2} \tag{1.4}$$

The DCMC fuel cell offers the following advantages over other fuel cell types that utilize carbon directly in a fuel cell:

- Molten carbonate cells produce high levels of carbon-dioxide (as opposed to carbon monoxide) even at fairly high temperatures.
- The liquid electrolyte simplifies the addition of solid fuel, allows the carbon fuel itself to be the anode material, and simplifies removal of contaminants through a side-stream plant.

- The electrolyte is not consumed in the reaction.

Molten hydroxide cells share the first two of these advantages with molten carbonate cells, but no other cells offer all three.

1.2 Objectives

The present work has three main objectives:

1. Concept Development

Refine, model, and evaluate a concept for a novel direct carbon fuel cell with recirculating electrolyte and porous bed electrodes. Develop fuel cell concept by finding suitable values for electrolyte blend, operating temperature, electrolyte flows, gas flows, anode dimensions, and cathode dimensions.

2. Process Model Development

Develop governing equations that describe the transport and electrochemical processes taking place in both the anode and cathode and a methodology for solving these equations

- Use literature correlations to develop models for gas and liquid superficial velocities, three-phase hold-ups, and gas-liquid and liquid-solid mass transfer coefficients.

- Examine the literature for work on electrochemical kinetics in the anode and cathode and develop the kinetic models to be used along with the transport equations.

- Use literature data to evaluate thermodynamic and physical properties (e.g. solubility and diffusivity) of participating gases in molten carbonate salts and carbon-molten carbonate salt slurry. Evaluate thermo-physical properties (e.g. viscosity and electrical conductivity) of the molten carbonate salt.

- Develop models for evaluating contact resistance in the anode and for electrolyte ionic current resistance in the presence of bubbles, solid carbon particles, and metal grid in the bulk electrolyte.

- Develop base case design and operating parameters from preliminary evaluation of the model, e.g. bed thickness, liquid superficial velocities, carbon loading, and operating temperature.

3. Evaluation of Model and of Cell Design

Once the model is developed, use it to:

- Evaluate base case fuel cell performance and compare with the experimental results from other researchers using similar cells. This will predict the feasibility of the proposed design relative to similar direct carbon fuel cell designs, while also giving a rough test of model accuracy.

- Perform parametric studies based on variations in design operating conditions.

- Perform parametric studies based on estimated uncertainties in literature correlations used in the model.

1.3 Literature Review

Fuel cells are electrochemical systems that are utilized in the generation of power while using continuous feed of fuel and oxidants. A fuel cell that uses carbon as fuel without prior gasification is called a direct carbon fuel cell (DCFC).

Direct carbon fuel cells are divided into three different categories based on the type of electrolyte that is used, i.e. molten hydroxide, solid oxide and molten carbonate. The molten carbonate fuel cell appears more attractive of the three because of:

- Advantage over both fuel cell types in terms of production of CO_2 relative to CO [Hauser Jr., 1964, Weaver et al., 1979, Vutetakis, 1985]
- Ease of solid fuel addition and removal of contaminants through side-stream plant when liquid electrolyte is used compared to SOFC
- Stability of electrolyte compared with molten-hydroxide based DCFC

Also, direct carbon molten carbonate fuel cells can be integrated into an overall plan for both stationary and transportation energy uses. When high-volatile coals are coked to provide carbon fuel for fuel cells, the volatiles can be converted to compressed hydrogen and liquid hydrocarbons for transportation energy use. Direct carbon fuel cells could also be used with biomass-derived carbon or with refinery waste coke. The molten carbonate electrolyte also demonstrates greater

stability to coal-ash which can be removed in a side-stream plant [Weaver et al., 1982]. It appears that direct carbon molten carbonate fuel cells may have a significant impact on energy supplies and on the environmental impact of energy production.

Most of the research work focus has been on utilizing various molten carbonate salts as the electrolyte for the DCFCs[1]. Other systems utilize molten hydroxide as the electrolyte (Zecevic et al. [2003, 2004, 2005]) and also quite recently hybrid direct carbon fuel cells (HDCFC) Deleebeeck and Hansen [2014]. The HDCFCs, as the name suggests, utilizes the SOFC technology for cathode in conjunction with direct carbon oxidation approach for the anode. The review work of Deleebeeck and Hansen [2014] covers most of the work done to date on the hybrid direct carbon fuel cells.

Early efforts directed towards the construction of a direct carbon fuel cell using molten carbonate salts were at Stanford Research Institute [Weaver et al., 1975, Weaver, 1976a,b, Weaver et al., 1979, 1982]. Researchers at SRI built laboratory-scale cells using anodes fabricated from graphite and from coked samples of various coals. A preliminary design for a 150 MW plant was developed with solid coked coal electrodes continuously fed into electrolyte baths. A ternary eutectic mixture of alkali carbonates ($Li_2CO_3/Na_2CO_3/K_2CO_3$ in mol% 43.5/31.5/25.0) was the electrolyte for the laboratory work, but a binary carbonate mixture of Na/K electrolyte was considered for larger plants because the water solubility of sodium and potassium carbonates would make it easier to remove ash from the electrolyte. Three different configurations investigated at SRI are shown in figure 1.1. Researchers

[1] [Weaver et al., 1975, Weaver, 1976a,b, Weaver et al., 1979, 1982, Vutetakis, 1985, Vutetakis et al., 1987, Cooper et al., 2002, 2003, Cooper, 2004a, Cherepy et al., 2005]

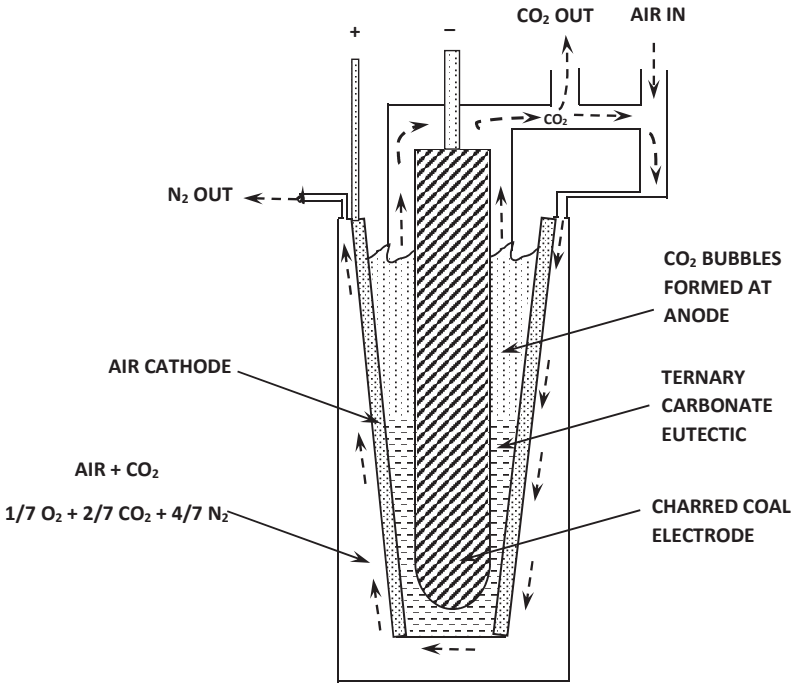

(a) Cross-section of conceptual coal/air fuel cell; solid anode

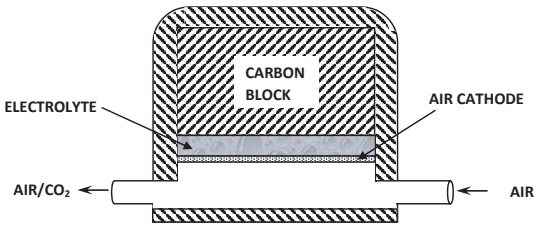

(b) Matrix coal/air "Battery type" fuel cell

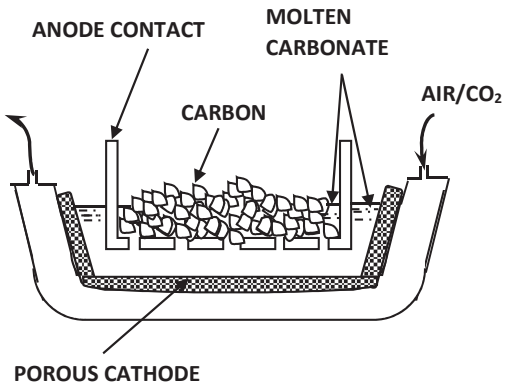

(c) Basket cell

Figure 1.1: Conceptual designs by SRI for the direct carbon fuel cells. Figures redrawn based on the reference [R.D. Weaver, S. Leach, and L. Nanis. Electrolyte management for the coal air fuel cell. In *Proceedings of the* 16^{th} *Intersociety Energy Conversion Engineering Conference*, volume 1, pages 717–721. ASME, 1982] used under fair use, 2014.

at SRI performed electrochemical studies to estimate kinetic data, including anode exchange current density and charge transfer coefficient for graphite anodes, and compared porosities of coal-derived anodes with that of graphite anodes. Their most surprising and significant experimental result, was that the production of CO_2 was much larger than that predicted by the Boudouard equilibrium, while the production of CO was lower. From some of their findings, the parameter P_{CO}^2/P_{CO_2} was up to 5 orders of magnitude lower than predicted by thermodynamic equilibrium for the Boudouard reaction, $CO_2 + C \rightleftharpoons 2\,CO$. It appeared that the increase in CO_2 production was significant mainly at medium and high overpotentials, while at low overpotentials the reaction $C + CO_2 \rightleftharpoons 2\,CO$ approached equilibrium. While these results were detected, not enough data was collected to quantify the CO-CO_2 balance.

Researchers at Ohio State University [Vutetakis, 1985, Vutetakis et al., 1987] built a molten carbonate fuel cell with particulate anode in which graphite, activated carbon, and coal particles were suspended in an agitated bath of $(Li/Na/K)_2CO_3$ ternary eutectic slurry. The particles acted as the anode, exchanging current with a gold rod that was nominally the anode but was very likely only a current collector. The slurry cell was operated over a range of conditions. It was found that current density increased as expected with increased overpotential, with increased particle loading, with increased cell temperature, with increased agitation, and with decreased particle size. The electrochemical reaction appeared to produce 100% CO_2, but this CO_2 production was superposed on a large CO production from the reaction $C + CO_2 \rightleftharpoons 2\,CO$ occurring in the coal/carbonate slurry away from the electrode.

Researchers at Lawrence Livermore National Laboratory [Cooper et al., 2002, 2003, Cooper, 2004a, Cherepy et al., 2005] developed a cell in which a paste of carbon particles suspended in $(Li/K)_2CO_3$ binary eutectic electrolyte was fed to a porous membrane current collector. Rather than using the common molten carbonate practice of feeding CO_2 to the cathode, CO_2 was allowed to diffuse through the electrolyte from the anode to the cathode. A net flux of carbonate was maintained from the cathode to the anode, preventing ash-fouling of the current collector. The LLNL workers attained 1.0 kW/m^2 membrane at 80% efficiency and 4.5 kW/m^2 membrane at maximum power, using a variety of coal and biomass derived fuels. They observed the same high CO_2 concentrations seen in the SRI work, and proposed a mechanism (discussed in later sections on electrode kinetics) to explain the phenomenon. A schematic representation of the carbon/air molten carbonate fuel cell by the LLNL researchers is shown in figure 1.2.

Chen et al. [2010] utilized various ternary mixtures of Li_2CO_3, K_2CO_3 and Al_2O_3 in a direct electrochemical oxidation of different feedstocks for the anode, viz. flake graphite, vapor-grown carbon fiber, carbon black, and green needle coke. CO_2 and air in a mole ratio of 3:5 was fed into the cathode. Maximum power density of $\approx 1.4\,kW/m^2$ at significantly high current densities of 3500 A/m^2 was achieved at a temperature of 650 $^\circ C$ and $Li_2CO_3/K_2CO_3/Al_2O_3$ in a ratio of mole% 43.4/26.6/30. The work however does not report clearly on the cell construction, cathode configuration, or the reference potential conditions.

Li et al. [2010] evaluated different kinds of ground 1-2 mm size raw coal particles feedstock suspended in molten carbonate as a slurry and under stirred conditions. 5:2 mole ratio air/CO_2 mixture was fed to the counter-electrode (cathode)

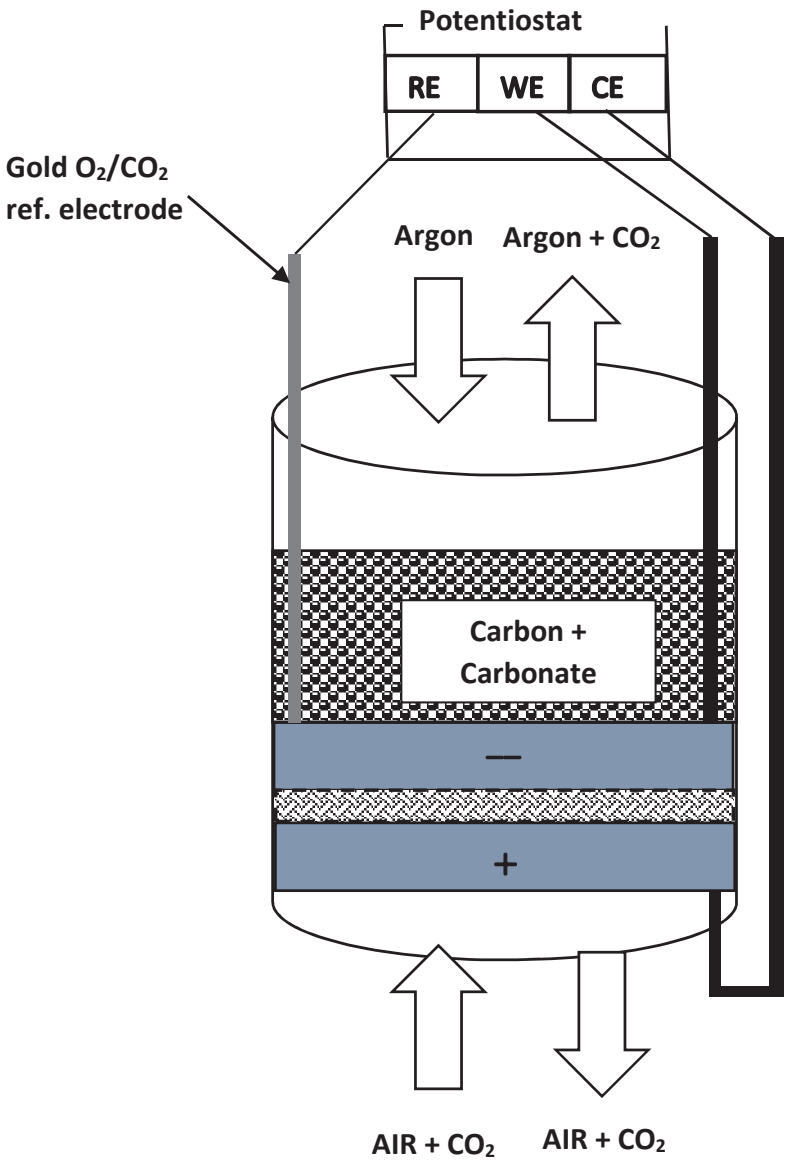

Figure 1.2: Schematic representation of LLNL direct carbon molten carbonate fuel cell built inside an alumina tube and contained within an alumina crucible with porous nickel cathode and anode and a zirconia cloth separator. Figure redrawn based on reference [N.J. Cherepy, R. Krueger, K.J. Fiet, A.F. Jankowski, and J.F. Cooper. Direct conversion of carbon fuels in a molten carbonate electrolyte. *Journal of Electrochemical Society*, 152(1):A80–A87, 2005] and used under fair use, 2014

and to the reference electrode. The focus of this work was to measure anode reactivity and thus authors didn't measure cathode potential and no cell voltages were reported. Polarization curves at 700 $^{\circ}C$ temperature indicated current densities of 820-1280 A/m^2 for anodic over-potentials of 0.8-0.9 V and maximum power densities of 300-530 W/m^2. The main outcome of this study was to show the importance of intrinsic properties of coal, e.g. chemical composition, surface area, concentrations of oxygen-containing surface functional groups and the nature of the mineral matter in coal ash. The authors went on to suggest that impurities such as Al_2O_3 and SiO_2 inhibit the anode performance whereas CaO, MgO, and Fe_2O_3 have a catalytic effect on the electrochemical oxidation of carbon. The suggestion that Al_2O_3 inhibits the anode performance is in stark contrast with the work done by Chen et al. [2010] however, due to non-availability of essential experimental configuration from Chen et al., the work of Li et al. [2010] seems to be more reliable with regard to Al_2O_3 as an additive.

Zhang et al. [2011] investigated performance of a fluidized bed configuration for a direct carbon fuel cell anode which employed bamboo, oak-wood based activated carbon and also graphite (one cell run) as the feedstock. The authors employed pretreatment with K_2CO_3 and HNO_3 to enhance surface activity of carbon and facilitate ash removal. The fluidizing gas was N_2 and the configuration was basically like a half-cell with a reference electrode (67%/33% CO_2/O_2) in ionic contact with the anode through the molten carbonate mixture of lithium and potassium salts. The anodic reactions takes place on the surface of the carbon particles and charge was transferred to nickel based current collector. Experiments for different operating conditions were conducted and limiting current densities of 700-950 A/m^2

for anodic over-potentials of 0.2-0.3 V were observed. The experimental run with graphite produced limiting current density of 800 A/m^2 for anodic over-potentials of 0.3 V. Since this work studied only an anode half-cell, it is difficult to compare results with those for a fuel cell.

Kouchachvili and Ikura [2011] explored DCFC performance at $700°C$ using different sources of carbon, different electrolytes, and additives for cathode. Nickel foam was used as the anode current collector but the actual anodic reaction takes place on the surface of the carbon particle, releasing CO_2 which is recycled back to the cathode. Molten carbonate electrolyte in the anode keeps the nickel foam wetted and is supported by the zirconia felt (filled with molten carbonate) which serves as the intermediate layer between cathode and anode. In the cathode, oxidized nickel foam is kept wetted with molten carbonate salt while at its surface CO_2 is oxidized into carbonate ions that transport to the anode. The authors found that petroleum coke with ternary eutectic blended with 20 wt% Cs_2CO_3 gave better performance than similar designs using only Li-Na-K carbonate eutectics. Maximum power density of 490 W/m^2 at cell temperatures of 700 °C and current densities of 780 A/m^2 were achieved in this work. A schematic representation of the cell is shown in figure 1.3

Predtechensky and co-workers [2009a, 2009b, 2010, 2012] investigated a new architecture of direct carbon molten carbonate fuel cell where a cylindrical container of cathode and graphite annular anode were separated by a thin layer of electrolyte with eutectic composition of 38%Li_2CO_3/62%K_2CO_3. The working surface of the cathode turned towards the anode was made from stainless steel with a nickel coating. This also served as a current collector. The cathode chamber

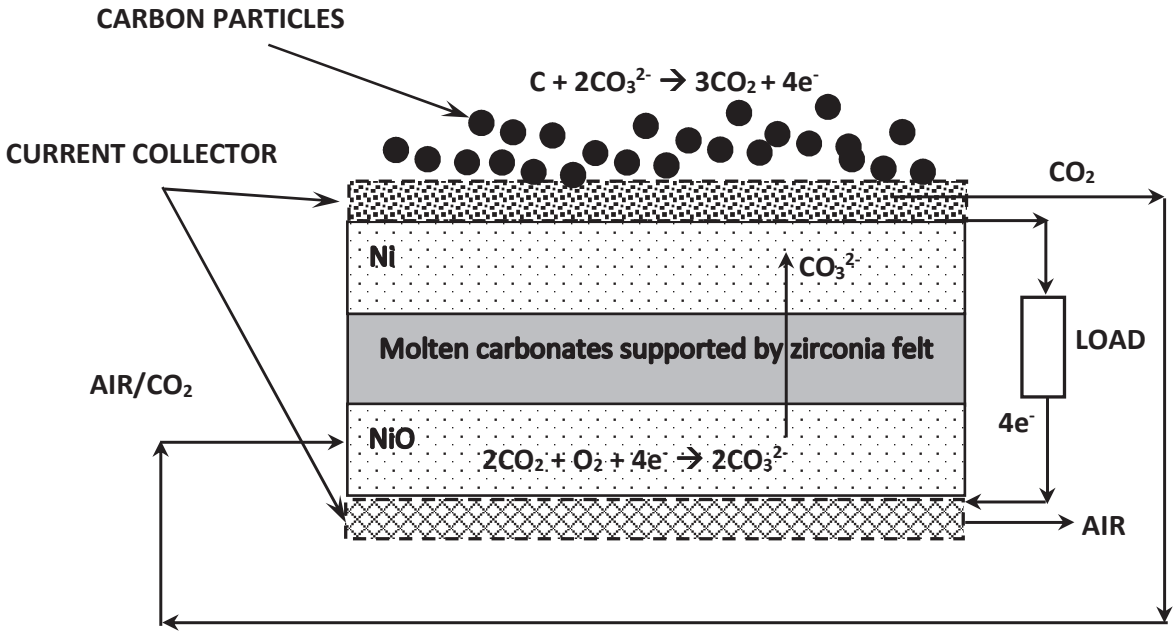

Figure 1.3: Schematic representation of a direct carbon fuel cell using ternary eutectic molten carbonate electrolyte.

Figure redrawn based on reference [L. Kouchachvili and M. Ikura. Performance of direct carbon fuel cell. *International J. of Hydrogen Energy*, 36:10263–10268, 2011] and used under fair use, 2014

was kept pressurized (in excess by 200-700 mm water column for various experiments) with various ratios of the mixture of CO_2/O_2 gases transporting onto the reaction sites (nickel coated SS grid). Gold reference electrodes were supplied with standard mixture of $33\%O_2/67\%CO_2$. One important results was that cathode polarization reached a minimum value with a 0.1 molar CO_2/O_2 gas fed to the cathode. These results were consistent with Lu [1985], Yuh and Selman [1991], Lu and Selman [1992] where higher O_2 partial pressures enhanced the cathode kinetics. Predtechenskii et al. found that fuel cell operation using dispersed graphite produced current densities in the range of 1000-1500 A/m^2 at maximum power densities of 600 W/m^2.

Various researchers have explored the use of additives, e.g. Cs_2CO_3, to improve DCFC performance [Smith and Winnick, 1999, Kouchachvili and Ikura, 2011, Chen et al., 2010] while Zhang et al. [2011] has employed fluidized bed electrodes to build DCFC prototypes.

1.4 Direct Carbon Fuel

The main advantages of using direct carbon (coal or biomass) over the more conventional fuel cell fuels like hydrogen and methane are:

- Abundant availability of coal, while biomass is both abundant and renewable.
- DCFCs can achieve theoretical efficiencies of 100% at a wide range of operating temperatures due to almost identical free energy (ΔG_T°) and standard enthalpy (ΔH_{298}°) changes of the CO_2 reaction.

- Near-zero entropy change is possible. This minimizes heat rejection requirements and eliminates large and non-uniform thermal loads on the cell [Cooper et al., 2000].

The limitations in using direct carbon fuel approach are:

- While solid carbon can be fed to a cell in a liquid electrolyte, cell construction is more complicated than when using gaseous fuels.
- Electrolyte can be contaminated by ash and sulfur present in the coal or similar substances in biomass. It is believed that through a side-stream ash-treatment plant as described by Weaver et al. [1982] this limitation can be resolved.
- Treating coal or biomass to produce a carbon that has a large concentration of reacting sites.

Chapter 2

Entrained Fuel Oxidizer - Design Concept

2.1 Introduction

The design concepts presented in this section are based in part on porous bed electrochemical cells employed in industrial processes as described by Le Goff et al. [1969]. From an engineering standpoint, the anticipated design and construction of the fuel cell is very attractive owing to

- Design simplicity,
- Better adaptability to economies of scale leading to commercial feasibility,
- Large surface areas for reaction rates per unit volume of the bed,
- Significant mass transfer rates,
- High stability and electrical conductivity, low volatility and toxicity and relatively low melting points of molten carbonates

- Better suited for a trade-off between economics of material selection and overall cell performance.

The porous-bed grid in the cathode (nickel or stainless steel wire mesh or perforated plates) acts as electrode and current collector. Complete wettability of the grid with the molten carbonate salt electrolyte allows the chemical reaction to take place on the entire surface of the grid. In addition, making the whole grid the current collector (versus maintaining only a sheet of current collector as demonstrated by most researchers) eliminates packed-bed electron conduction loss. The CO_2 and O_2 molecules react on the surface of the grid ($O_2 + 2\,CO_2 + 4\,e^- \longrightarrow 2\,{CO_3}^{2-}$) releasing carbonate ion, ${CO_3}^{2-}$ which then transports from the grid surface into the bulk electrolyte. The total charge that can be transferred follows the Faraday's Law and would be zF where $z = 4$ considering 4 electrons are consumed during the reaction to produce carbonate ions that can transport towards the anode. The 4 electrons required for the reaction come from anode via the external circuit.

The half-cell anode is similar in construction to the cathode, but the anode particles work as floating electrodes while transferring charge to the porous-bed grid (similar in construction to the cathode bed) that works as the current collector. The actual anode cell reaction takes place on the surface of the carbon particle [Weaver et al., 1979, Vutetakis, 1985]. The carbonate ions migrating from cathode react with the carbon to produce CO_2 and 4 electrons per mole of carbon reacted (or CO with 1 electron per mole of carbon). The carbon particles then collide with the anode packed bed current collector grid and transfer the charge, which flows back to the cathode via the external circuit. The following reactions takes place on the surface of the carbon anode (depending upon equilibrium). The equation for the CO_2

production (temperature less than 750 $^{\circ}C$) is:

$$\mathrm{C} + 2\,\mathrm{CO_3}^{2-} \longrightarrow 3\,\mathrm{CO_2} + 4\,\mathrm{e}^{-} \tag{2.1}$$

and the equation for the CO production (temperature higher than 750 $^{\circ}C$) is:

$$2\,\mathrm{C} + \mathrm{CO_3}^{2-} \longrightarrow 3\,\mathrm{CO} + 2\,\mathrm{e}^{-} \tag{2.2}$$

If the temperature of fuel cell is kept below 750 $^{\circ}C$, production of CO can be neglected [Hauser Jr., 1964, Weaver et al., 1979, Vutetakis, 1985]. Two different conceptual designs were considered: the cco-current flow cell and the gravity flow cell.

2.2 Co-current Flow Concept

The primary concept studied is the one in which the liquid electrolyte flow is parallel to the direction of electrolyte current as shown in figure 2.1. Liquid electrolyte, with fuel and oxidizer entrained, is circulated through the electrodes. The cell concept described here is based partly on those industrial electrolysis technologies which use porous bed electrodes [Le Goff et al., 1969] and partly on the work of Vutetakis [1985], Vutetakis et al. [1987].

As shown schematically in figure 2.1, both the anode and the cathode are electrically connected porous beds. In the cathode, the molten carbonate salt entrained with gases CO_2 and O_2 is pumped upward. Using the electrons from the current collector, the gases react at the surface of the porous-bed grid producing carbonate ions. Salt and unreacted gases are removed from the outlet before being recirculated back into the fuel cell system after addition of feed gases, i.e. CO_2 from the anode and O_2 from the external air supply.

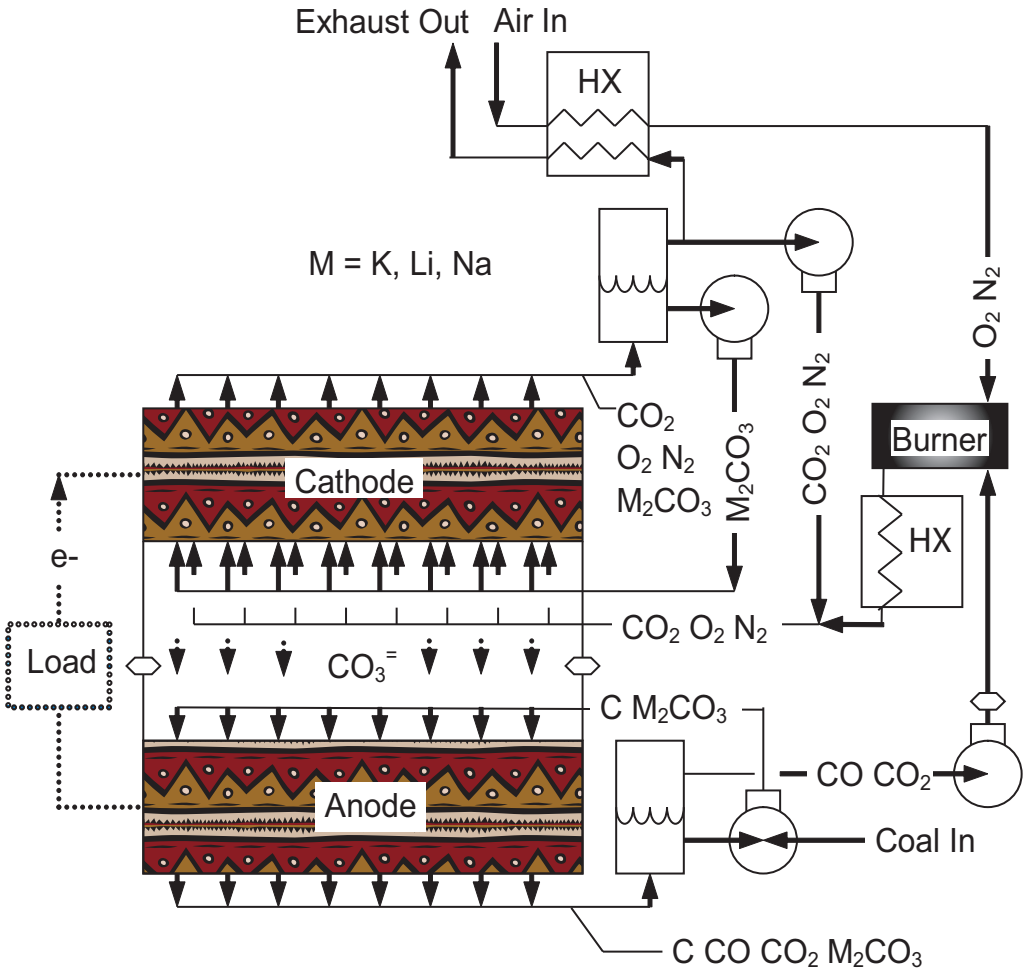

Figure 2.1: Schematic of the Packed Bed Direct Carbon Molten Carbonate Fuel Cell

Molten carbonate salt, with particles of carbon entrained, is pumped downward through the anode bed. It reacts with CO_3^{2-} ions diffusing from the cathode to form CO_2 (and perhaps some CO) while sending electrons to the load. Downward velocity of the salt is adequate to ensure that both carbon and evolved gases move downwards. Salt, evolved gases, and overfed carbon exit the bottom of the anode and gases are separated from the liquid/solid slurry with the use of gravity separators. The slurry is enriched with more carbon and recirculated through the anode, while the evolved gases are used to supply CO_2 to the cathode.

Because this cell has a continuous flow of salt through the anode, fuel contaminants will be carried off with the flow. They can then be removed by a side-stream treatment plant such as that described by Weaver et al. [1981].

Axial diffusion has not been considered, but is assumed to be negligible. The reactions taking place within the cell are:

At the cathode:

$$\mathrm{O_2 + 2CO_2 + 4e^- \longrightarrow 2{CO_3}^{2-}} \tag{2.3}$$

At the anode:

$$\mathrm{C + 2{CO_3}^{2-} \longrightarrow 3CO_2 + 4e^-} \tag{2.4}$$

$$\mathrm{2C + {CO_3}^{2-} \longrightarrow 3CO + 2e^-} \tag{2.5}$$

The type of fuel cell described in this work utilizes a metallic (stainless steel, nickel or some other appropriate alloy) packed bed that serves as the electrode and the current collector in cathode and simply as the current collector in the anode.

2.3 Gravity Flow Concept

The alternate concept described here also uses the entrainment of carbon directly in the molten carbonate electrolyte in the anode. The development of this concept was begun but not completed; it may be the subject of future work. The concept schematic portraying gravity fed flow in the cathode and anode packed beds is shown in figure 2.2.

The cell concept shows cathode and anode porous beds placed in parallel arrangement to each other but kept separated by a non-conducting membrane. The molten salt electrolyte is sent downward through the cathode porous bed made of nickel or stainless steel grid (wiremesh or perforated plates). The gases CO_2-O_2-N_2 are flown upwards through the space between the falling liquid flow and the container vessel. The gases CO_2 and O_2 are transported into the falling molten salt through diffusion. The unused CO_2-O_2-N_2 leave the container vessel and after being replenished with additional CO_2 and O_2 is recycled back into the system. The cathode reaction takes place on the surface of the grid electrode that also functions as a current collector. The CO_2 and O_2 diffuse into the molten salt to react on the surface of the grid, that receives electrons from the external circuit, to form carbonate ions. The carbonate ions migrate via conduction through the non-conducting membrane that separates the anode and the cathode beds into the anode to react with carbon.

The following reaction can take place on the surface of the electrodes in the cathode packed bed:

$$\mathrm{O_2 + 2CO_2 + 4e^- \longrightarrow 2CO_3^{2-}} \tag{2.6}$$

In the anode, molten salt electrolyte with entrained carbon is sent downward

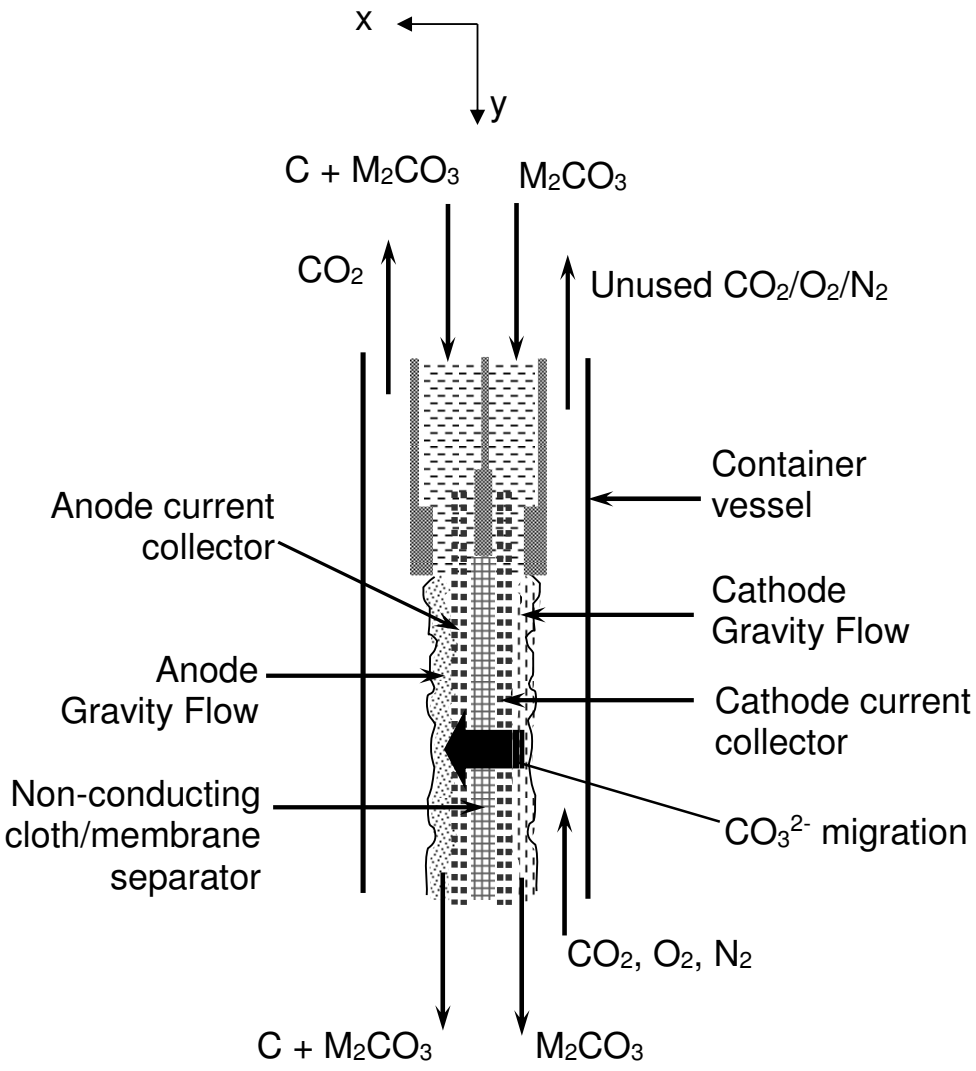

Figure 2.2: Schematic of the gravity flow alternate concept for a direct carbon fuel cell.

through the anode porous bed made of nickel or stainless steel grid. The carbonate ions transported from the cathode into the anode react at the surface of the carbon particles (electrode) producing 4 electrons per mole of carbon considering only CO_2 production. The carbon particles transfer the charge to the grid current collector via collision which is then further transferred back to the cathode through the external circuit. The carbon + molten salt slurry is removed from the bottom and recirculated back into the anode system after being replenished with additional carbon. The reaction of carbonate ions with the carbon produces carbon-dioxide which is released through the space between the falling liquid flow and the container vessel and later removed. The CO_2 may be used with an inert type purge gas but this aspect has not been developed yet in the current work.

The following reactions take place at the anode:

$$\mathrm{C} + 2\,\mathrm{CO_3}^{2-} \longrightarrow 3\,\mathrm{CO_2} + 4\,\mathrm{e}^- \tag{2.7}$$

$$2\,\mathrm{C} + \mathrm{CO_3}^{2-} \longrightarrow 3\,\mathrm{CO} + 2\,\mathrm{e}^- \tag{2.8}$$

As explained before, the production of CO is dominant at temperatures exceeding 750°C.

The path traversed by the ionic current may be smaller when compared with that in the co-current concept explained above. Smaller bed thickness may be possible leading to lower ohmic losses. However, diffusion might be a limiting factor in the fuel cell performance. Mass transport via convection in the direction of flow will provide concentration gradient in the axial direction but would be insignificant compared to concentrations across the bed controlled by diffusion.

The CO_3^{2-} ion migrates from the bulk electrolyte into the anode packed bed via the intermediate space between cathode and anode. This intermediate space

could be filled with stagnant or flowing electrolyte allowing for the passage of ions and adding only minimally to the overall bed resistance. There is a possibility of a portion of CO_2 and O_2 that is fed into the cathode bed to diffuse through the intermediate electrolyte layer and into the anode packed bed. This however, will be much dependent upon the individual partial pressures used in the gas chamber for both anode and cathode half cells and can be optimized. This is considered a possibility owing to lower solubility of O_2 in the molten carbonate salts when compared with CO_2 and it would be possible to control O_2 crossover into the anode which is not a desirable aspect of cell operation.

2.4 The Porous Bed Cell

2.4.1 Advantages of Porous Bed Cell

1. *Effective delivery of solid fuel.* With any membrane electrode cell, the delivery of solid fuel to the anode can be problematic. In the porous bed cell the carbon particles themselves act as the anode, exchanging current by collision with the fixed bed, which is not itself the anode but simply a current-collecting grid. The feasibility of this type of operation was demonstrated by Vutetakis et al. [1987], but in their apparatus the anodic current collector was a single rod in a crucible of stirred carbon-molten salt slurry.

   The original concept for the cell was that the carbon particles (probably coked coal) would be mixed with the recirculating molten salt stream with an eductor or some sort of mechanical feeder.

2. *Economies of Scale.* Membrane electrode cells are by nature compact devices, excellent for portable and transportation energy needs. They do not, however, scale up well. Utility-scale generating plants are envisioned as having tens of thousands of individual cells. Although there are some economies in assembling cells into stacks, the cost per kilowatt decreases only slightly as plant size increases.

   The porous bed cell promises to be cost-effective in very large sizes. The beds (sintered from packed shapes or assembled from screens or perforated plates) can be fabricated in large sizes, in contrast to the size limitations on membrane electrodes. Pumps, piping, and vessels all decrease in cost per kilowatt as size increases. It can be envisioned that the practical limits on cell size will be set by the need to transport cells by railcar or truck. A utility-size plant will consist of perhaps a few thousand such large cells. Extra cells could be included to allow the plant to remain on-line while one or more cells are down for maintenance.

3. *Potential for electrolyte cleaning or replacement.* In fuel cells with immobile electrolytes, any contaminants build up in the electrolyte can eventually cause cell failure. With mobile electrolyte, a side-stream treatment plant to continuously remove ash from the circulating molten salt could be possible.

   Fuel ash is not the only source of contamination in molten carbonate fuel cells. Electrode materials gradually dissolve in the salt. In cells with immobile electrolytes, these dissolved materials eventually precipitate in the electrolyte and short-circuit the cell. In the porous bed cell, dissolved electrode materials could likely be removed by a side-stream treatment plant. If some dissolved

materials or fuel contaminants are not removed by side-stream treatment, the porous bed cell can be designed so that the electrolyte charge can be drained off and replaced with fresh electrolyte as a part of scheduled maintenance.

4. *Flexibility in Electrode Materials.* Membrane electrodes for fuel cells must be fabricated of materials which can be sintered into a microscopically-fine porous membrane. Furthermore, the materials must have good creep resistance so that the pores do not close up with time during high-temperature operation.

   The porous bed cathode and anode current collector are porous on a macroscopic rather than microscopic scale. Length scales for porous bed electrodes used in chemical processing are on the order of millimeters. Pores of this size can be produced mechanically as well as by sintering, and will not be closed by creep. Electrode materials may thus be selected for catalytic properties, corrosion resistance, and cost, without many of the limitations imposed on materials for porous membrane electrodes.

5. *Decreased Diffusion Losses.* The porous membrane cell depends on diffusion to carry reactants and products in and out of the membrane pores. In the porous bed cell electrolyte is pumped through the bed pores so that the mass transfer is enhanced by bulk convection. The improved mass transfer should reduce diffusion voltage loss. In practical cell designs there will be a tradeoff between decreased diffusion losses and increased pumping costs, leading to some optimum electrolyte flow rate.

2.4.2 Disadvantages of Porous Bed Cells

1. *Increased Resistance Losses.* In the porous membrane cell, electrolyte thickness is of the order of one millimeter, keeping losses from the ionic resistance of the electrolyte low. In the porous bed cell the total thickness (space between electrodes as well as distance within electrodes) will probably be larger by one or two orders of magnitude. This will greatly increase resistance losses.

2. *Pumping Costs.* A part of electric power generated by the cell will be used to pump electrolyte. This energy cost is expected to be small relative to energy production.

2.5 Carbon Monoxide/Carbon Dioxide Production

The efficiency of a DCMC fuel cell is much higher for 100% CO_2 production than it is for the case of a partial reaction producing some amount of CO as well [Agarwal and Kornhauser, 2004]. Early workers in direct carbon molten carbonate cells [Weaver et al., 1975] assumed that balance between reaction 1.2 and reaction 1.3 at the anode would be determined by the $C + CO_2 \longleftrightarrow 2\,CO$ (Boudouard) equilibrium (equation 2.9):

$$\log_{10}\left[\frac{P_{co}^{\,2}}{(P_{co_2})(1\ atm)}\right] = -\frac{8919K}{T} + 9.115 \tag{2.9}$$

which predicts that carbon monoxide production is significant in the temperature range of interest.

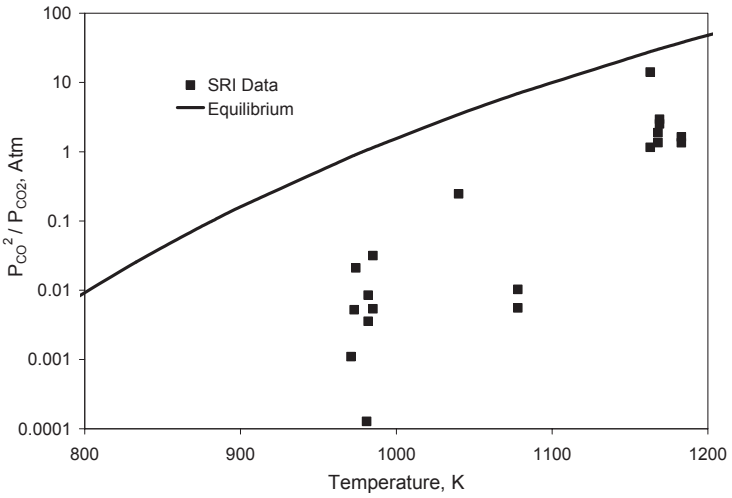

Figure 2.3: Carbon monoxide production based on chemical equilibrium and from Stanford Research Institute experimental data [Weaver et al., 1979].

However, their subsequent work, as well as the work of others [Vutetakis et al., 1987, Cooper, 2004b] indicated that CO_2 production is dominant at much higher temperatures than predicted by equilibrium. Figure 2.3 shows the equilibrium constant at one atmosphere for the reaction $C + CO_2 \longleftrightarrow 2\,CO$, together with concentration data from the Stanford Research Institute experiments [Weaver et al., 1975]. The values of the concentration ratio are in most cases an order of magnitude less than predicted by equilibrium and in some cases several orders of magnitude less. Some Stanford Research Institute experiments [Weaver, 1976a] showed that relative carbon monoxide levels were low when reaction rates were high, and that relative levels increased at low reaction rates. Cherepy et al. [2005] have concluded that carbon monoxide production is low whenever chemical overpotential

at the anode is significant, but that carbon and carbon dioxide react to form carbon monoxide ($C + CO_2 \longleftrightarrow 2\,CO$) when no overpotential is present. They have proposed a reaction scheme to explain this result.

Development of a model describing the relative production of CO and CO_2 is needed for further molten carbonate DCFC development.

2.6 Advantages of a Liquid Electrolyte

Any large-scale energy conversion or chemical production process is complicated by the need to handle solids. In industrial processes solids are, as much as possible, conveyed either as slurries or pneumatically. When coal is used for utility power generation it is burned either as pneumatically conveyed powder or in a pneumatically fluidized bed. A liquid electrolyte offers similar advantages when using solid carbon in a fuel cell:

- It allows conveying of carbon particles into and within the apparatus. The density of carbon is close to that of molten carbonate salts, so the particles can be easily entrained.

- It allows removal of ash/slag from the fuel with sidestream treatment. Both Weaver et al. [1975], Vutetakis et al. [1987] found that a certain level of coal ash dissolved in the electrolyte would not adversely affect cell output. Weaver et al. [1982] presented various techniques for slag removal. For easy slag removal, sodium carbonate - potassium carbonate blends have an advantage over salts containing lithium carbonate, since the sodium and potassium

carbonates are much more water soluble that lithium carbonate. The silica compounds which make up most of coal ash have low water solubility.

- It reduces diffusion resistance by providing turbulent transport of dissolves gases to the anode and cathode surfaces.

Molten hydroxide electrolytes would offer similar advantages to molten carbonate electrolytes if they were stable.

2.7 Molten Carbonate Stability

Carbonates are not consumed in reactions 1.1, 1.2, and 1.3. One of the problems, however, with typical membrane-electrode molten carbonate fuel cells is limited cell life [EG&G Services Inc.,2004]. The life is limited not by breakdown of the electrolyte but by dissolution of electrode materials (typically nickel oxide) in the electrolyte. When dissolved electrode materials reach a certain level they begin to precipitate. In the membrane-electrode molten carbonate fuel cell the electrolyte is contained in a thin layer between anode and cathode. Small amounts of precipitated electrode material can bridge this gap, short circuiting the cell. One of the advantages (with respect to cell life) of the cell design described in the present work is that liquid electrolyte is continuously pumped into the gap between the electrodes. If dissolved cathode material precipitates it will do so in the electrode beds, not in the gap between anode and cathode. While such precipitation could block flow passages and reduce cell output somewhat, its impact would probably not be major. Side-stream treatment to remove ash/slag could also remove dissolved electrode material.

2.8 Potential and Current Density in Porous Beds

The difference between the potential, V, that exists between the grid electrodes when a current (current density, i'') is generated and the equilibrium potential (V_{oc}) under the conditions of passing of no current is theoretically referred to as the "*over-potential*, $\eta = V - V_{oc}$. In fuel cells, the anodic (positive) and cathodic (negative) current generates a positive and negative over-potential [Vetter, 1967][pg 106] in a conventional sense. In the present work, both anode and cathode are treated as separate half-cells with respective forward and reverse reaction rates. A full Butler-Volmer equation with the forward and reverse current density components are used for each of the anode and cathode that lead to the generation of positive current. Absolute values for the chemical over-potential (η) have been consistently used for both anode and cathode to avoid any disparities.

The type of fuel cell described in this work uses a metallic (stainless steel, nickel or some other appropriate alloy) porous bed that serves as an electrode and a current collector in the cathode and as a current collector in the anode. It is known [Newman and Tobias, 1962, Newman, 1967] that in such type of porous bed electrochemical cells, the total current density through the cell is the sum of current densities through the metallic grid and the solution electrolyte phase. Application of Ohm's law to the metallic grid and the solution electrolyte phase yields:

$$i''_m = -\sigma \nabla V_m \tag{2.10}$$

$$i''_s = -\kappa \nabla V_s \tag{2.11}$$

Conservation of charge enables us to write the following equation (as given by

Newman and others) that connects the current density in the metal grid and electrolyte solution:

$$\nabla \cdot i_m'' + \nabla \cdot i_s'' = 0 \tag{2.12}$$

Now, in a methodology similar to that used by *Newman and others*, the flux of the ionic (area-dependent) current density is a function of charge-transfer current density equation which can be expressed in the form of a Butler Volmer equation. As per Newman and Tobias [1962], this is necessary to express the dependence of the local rate of reaction on the various concentrations and on the potential jump at the grid-electrolyte interface and in it's general form is written as:

$$\nabla \cdot i_m'' = a i_o'' \left[\frac{C_1}{C_1^o} \exp\left\{ -\frac{\alpha n F}{\bar{R}T} (\Phi_m - \Phi_s) \right\} - \frac{C_2}{C_2^o} \exp\left\{ -\frac{(1-\alpha) n F}{\bar{R}T} (\Phi_m - \Phi_s) \right\} \right] \tag{2.13}$$

The above Butler-Volmer equation describing rate kinetics is referred to as the "surface current density" or sometimes also as "charge-transfer current density". The development of "ionic current density" equation by integrating the "surface current density" using the total surface area of the porous bed is shown in the process modeling section.

The representation of concentrations and other kinetic constants is quite arbitrary in the above equation and the development of this particular equation is treated in a separate section. The reason for using this generalized equation in this section is to demonstrate qualitative nature of some variables in relation to each other. Now, it's known that the electrical conductivity of the metallic phase (σ) is roughly 5 orders of magnitude higher than that of the electrolyte phase (κ). This means that the derivative of the grid potential relative to the derivative of the electrolyte phase potential is negligible. In other words, the metallic phase potential can be treated as constant when the difference of the two potentials are taken for

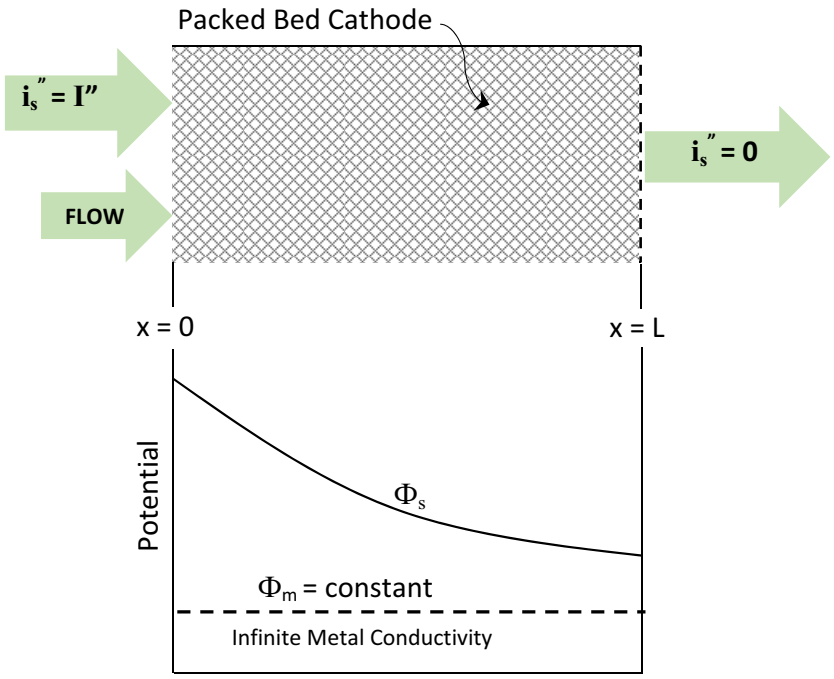

Figure 2.4: One-dimensional Packed Bed Cathode showing path of current, solution and potential.

the purpose of evaluating charge-transfer current density equation. This concept is schematically shown in figure 2.4.

Understanding potential variation relative to porous bed thickness is very helpful in understanding the concept of overpotential in porous beds used in the present work. For this, we first try to understand conceptually using system with no ohmic losses (electrolyte resistance mainly) to system with concentration polarization. This is done by first understanding the polarities in anode and cathode beds. Electrochemical reactor concepts from Pickett [1977] have been used to develop some of this work.

As can be seen from the figure 2.5a, in an electrolyzer, electrons flow through

power supply from positive to negative potential and there is an external energy provided at the power supply and therefore the anode potential is more positive than the cathode potential. Now, the situation is opposite in the fuel cell as is seen in figure 2.5b, where electrons flow through the external load from negative to positive, energy output goes out of the system from the load and anode potential is more negative than the cathode potential.

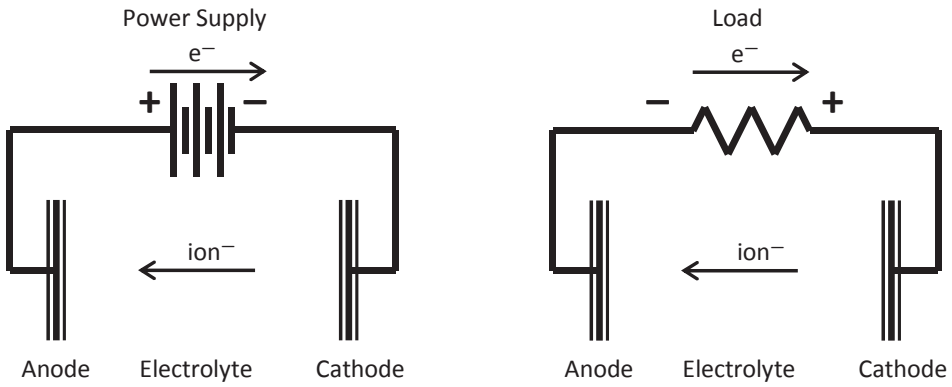

(a) Electrolyzer (b) Fuel Cell

Figure 2.5: Electrode polarity in electrolyzer and fuel cell

The potential distribution in anode and cathode half-cells with no electrolyte resistance is shown in figure 2.6. Strictly speaking, in terms of a practical cell design, the potential within the electrolyte can only be measured relative to a reference electrode. For the purpose of conceptual demonstration, this reference potential is assumed to be the same potential used to define the open circuit half-cell potential in anode and cathode.

The cell potential can be calculated by using the expressions:

$$V_{cell} = V_c - V_a = (V_{oca} + V_{occ}) - (\eta_a + \eta_c) \tag{2.14}$$

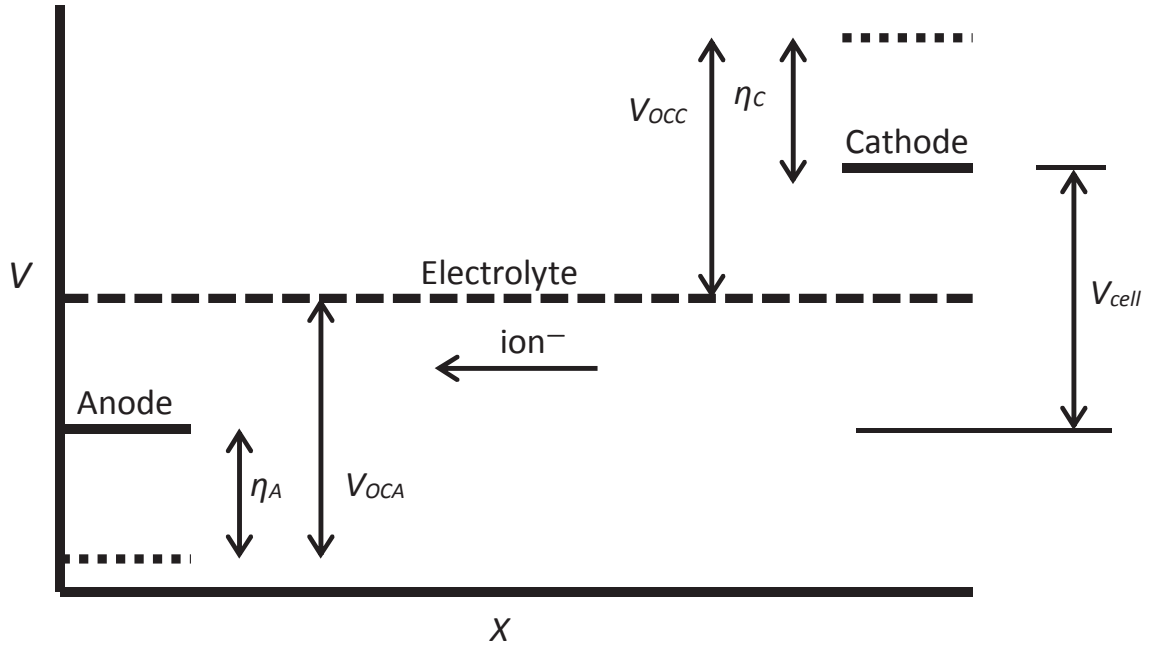

Figure 2.6: Potential distribution in fuel cell with no electrolyte resistance.

Here the sign of η_a and η_c are defined to be positive in normal cell operation.

The overpotential in anode can be re-written as:

$$\eta_a = V_{oca} - (V_{electrolyte,a} - V_a) \tag{2.15}$$

and overpotential in cathode can be re-written as:

$$\eta_c = V_{occ} - (V_c - V_{electrolyte,c}) \tag{2.16}$$

$V_{electrolyte,c}$ is the electrolyte potential in the cathode

$V_{electrolyte,a}$ is the electrolyte potential in the anode

V_c is the cell potential in the cathode

V_a is the cell potential in the anode

V_{occ} is the open-circuit potential in the cathode

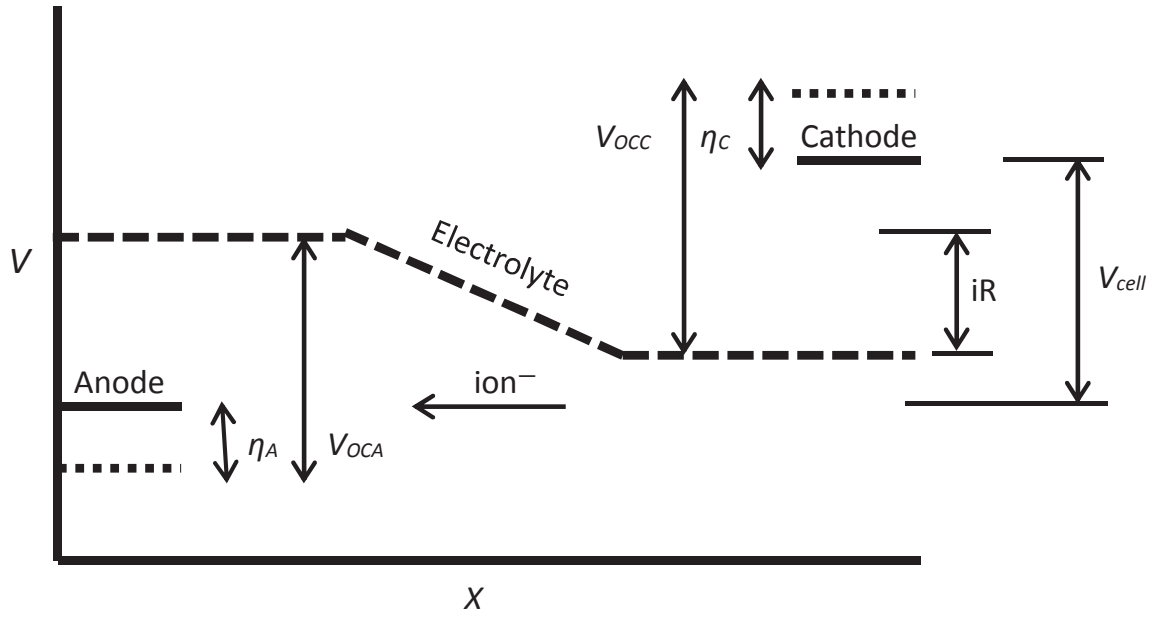

Figure 2.7: Potential distribution in fuel cell with lumped electrolyte resistance.

V_{oca} is the open-circuit potential in the anode

η_c is the chemical overpotential in the cathode

η_a is the chemical overpotential in the anode

Considering ohmic losses in the electrolyte as a lumped resistance model (assuming resistance R and current density i), revised voltage gradients for anode and cathode half-cells are shown in figure 2.7. And the revised equations for cell voltage in anode and cathode and how to calculate the electrode overpotential for half-cells are given as:

$$V_{cell} = V_c - V_a = (V_{oca} + V_{occ}) - (\eta_a + \eta_c) - iR \tag{2.17}$$

and the overpotential equations in anode and cathode remains unchanged as shown above in equations 2.15 and 2.16. It's clearly seen that in the presence

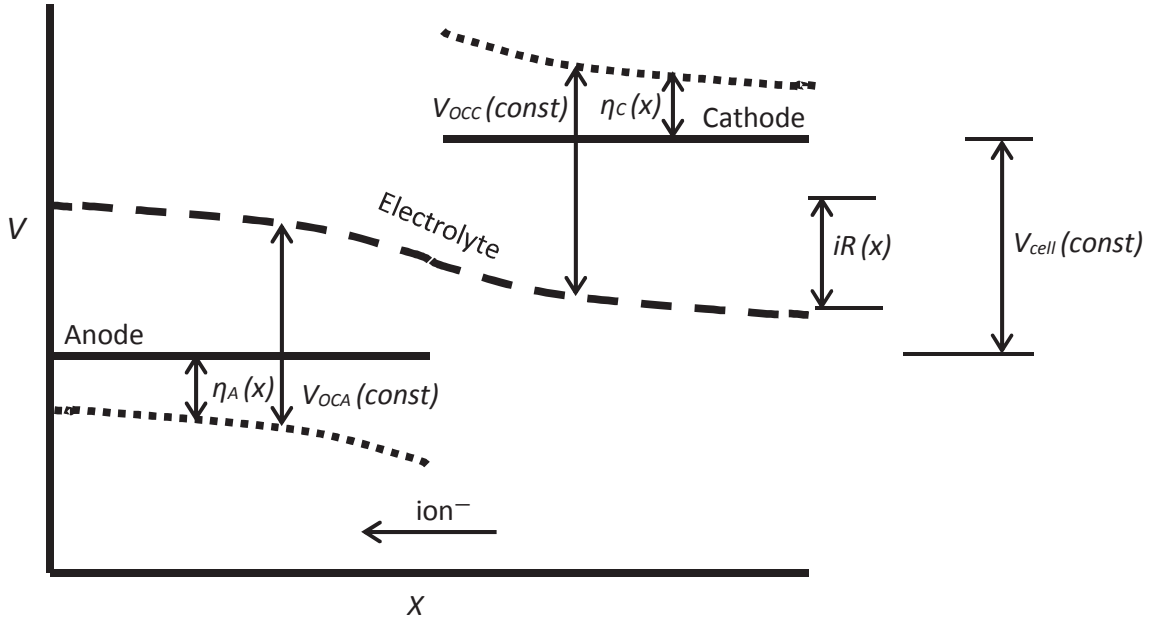

Figure 2.8: Potential distribution in fuel cell with distributed electrolyte resistance.

of ohmic resistance from the electrolyte, the net chemical over-potential available for each half-cell (cathode and anode) is greatly reduced.

We complicate the situation further by assuming distributed electrolyte resistance that makes the overall ohmic loss vary with bed position due to variation in volumetric current density which itself is a function of over-potential and therefore a function of bed position. This situation is shown in figure 2.8. And the revised equations for cell voltage in anode and cathode and how to calculate the electrode over-potential for half-cells are given as:

$$V_{cell} = V_c - V_a = (V_{oca} + V_{occ}) - [\eta_a(x_a) + \eta_c(x_c)] - \int_{x_a}^{x_c} i(x)Rdx \tag{2.18}$$

and therefore, the revised equations for over-potential in anode are written as:

$$\eta_a(x) = V_{oca} - (V_{electrolyte,a}(x) - V_a) \tag{2.19}$$

and overpotential in cathode can be re-written as:

$$\eta_c(x) = V_{occ} - (V_c - V_{electrolyte,c}(x)) \tag{2.20}$$

The last concept with the distributed electrolyte resistance is applicable to the kind of direct carbon fuel cell using porous bed electrodes that has been designed and analytically simulated in the current work.

2.9 Balance of Plant

2.9.1 Introduction

The energy balance presented here is more concerned with the ”balance of plant” components than with the details of the cell itself. It is, in fact, applicable to other types of direct carbon molten carbonate fuel cells and is therefore generic in nature. The energy balance work done here in this section is totally independent of the modeling of processes within the cell as far as this work is concerned. Unlike the assumption of no carbon monoxide in the modeling of processes within the cell, the mole fraction of CO/CO_2 is not limited in this section. The actual design calls for the CO-CO_2 mixture leaving the anode to be burned to supply an O_2-N_2-CO_2 mixture to the cathode. Two heat exchangers are employed: an air preheater cooling the exhaust and a waste heat exchanger cooling the gases entering the cathode.

2.9.2 Overall Plant Design and Modeling

The plant design used for the energy balance is shown schematically in Figure 2.9. CO and CO_2 generated in the anode are supplied to a burner, where they are

combusted with excess air. The resulting O_2-N_2-CO_2 mixture is supplied to the cathode. The air supplied to the burner is preheated by the N_2, CO_2, and excess O_2 leaving the cathode, and waste heat is recovered from the gases leaving the burner.

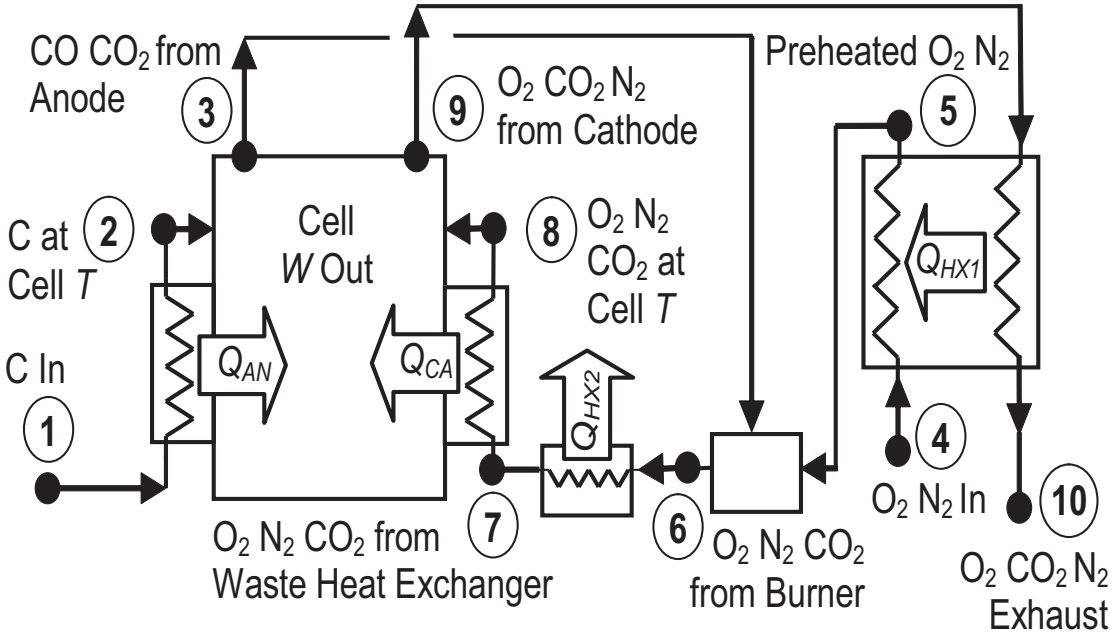

Figure 2.9: Balance of Plant for the Direct Carbon Molten Carbonate Fuel Cell.

Two imaginary ”heat exchangers” are included in the cell, one to bring the incoming carbon to cell temperature in the anode and the other to bring incoming O_2-N_2-CO_2 mixture to cell temperature in the cathode.

The preliminary design calls for atmospheric pressure operation. Higher pressure operation would drive equilibrium toward carbon dioxide production and might also increase power density, but would increase first cost due to the need for compressors and expanders.

2.9.3 Discussion of Results

An overall plant energy balance was performed based on this design [Agarwal and Kornhauser, 2004] for which the fuel cell itself was assumed to be at uniform temperature. The irreversibilities inherent in thermally equilibrating the incoming streams with the fuel cell were accounted for with two imaginary heat exchangers, while those within the fuel cell itself were expressed in terms of a fuel cell internal efficiency. Overall plant efficiency was presented in terms of electric work out of the fuel cell and fuel heating value in, without regard to the value of any waste heat recovered. The modeling showed that relative carbon monoxide / carbon dioxide production was of primary importance in determining efficiency.

Figure 2.10 shows work and waste heat as a fraction of fuel energy plotted against carbon dioxide fraction leaving the anode. Cell temperature is a parameter, with curves shown for fixed values and also for the equilibrium temperature corresponding to the carbon dioxide fraction. Cell internal efficiency is 100% and air heater pinch point temperature difference is zero. The plot shows that plant performance is a strong function of carbon dioxide fraction and a weaker function of cell temperature. The plot is for stoichiometric air, but the addition of excess air has negligible effect other than increasing required air heater size.

The effect of cell efficiency versus the carbon dioxide fraction leaving the anode on the work and waste heat was also considered as shown in figure 2.11. Cell internal efficiency variation over the range shown has a greater effect on performance than cell temperature but its effect is less important than that of carbon dioxide fraction leaving anode.

In any case, for the range of cell internal efficiencies (70%-100%) studied here,

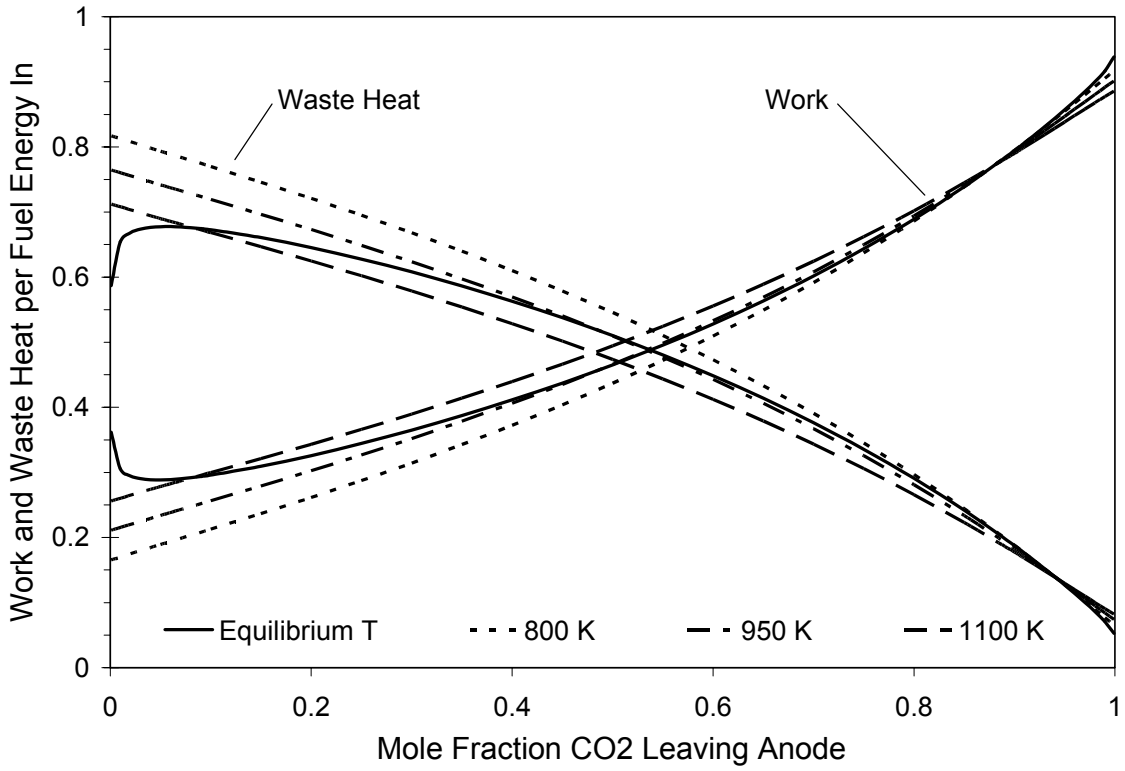

Figure 2.10: Work and Waste Heat vs. Mole Fraction Carbon Dioxide Leaving Anode, Cell Temperature as Parameter.

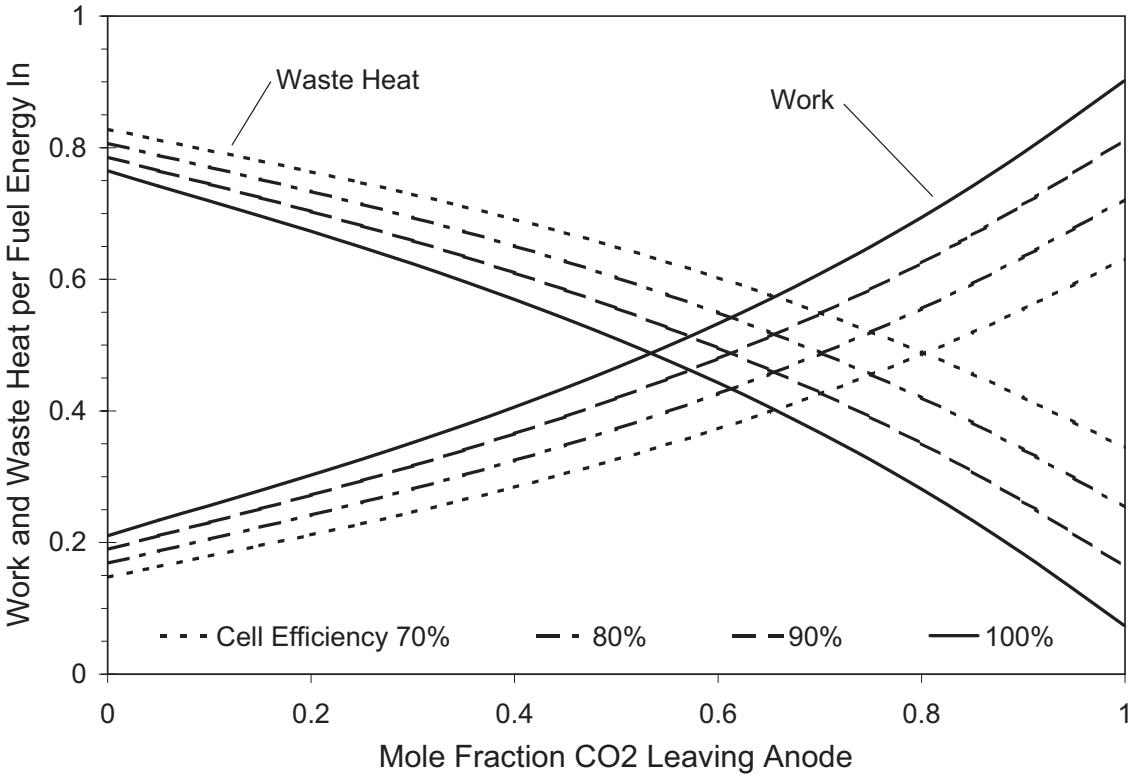

Figure 2.11: Non-Dimensional Work and Waste Heat vs. Mole Fraction Carbon Dioxide Leaving Anode, Cell Efficiency as Parameter, Cell T = 950 K.

cell internal losses (ohmic, overpotential, and diffusion losses) doesn't seem to be as crucial as the CO/CO_2 balance. Therefore, for the direct carbon molten carbonate cells, it is evident that the design will largely be a three-way tradeoff between cell losses and CO/CO_2 balance. But given a model that correctly describes the CO/CO_2 balance, cell design will naturally depend upon the cell internal losses.

Based on the modeling, the cell and plant described here appear to have good potential for utility-scale power production. The chief limitations of the modeling are in the assumption that the cell is isothermal and in the uncertainty of evaluating two parameters - CO_2 fraction and cell internal efficiency - that lump together many complicated non-idealities.

Chapter 3

Process Modeling

Introduction

Porous bed electrodes have been historically used in primary and secondary batteries and in continuous feed galvanic cells [Newman and Tobias, 1962, Le Goff et al., 1969]. The concept is reasonable for use in direct carbon fuel cells that are based off of high temperature cells that use molten carbonates as the electrolyte. Compared to the conventional solid electrodes, the concept of porous bed electrodes provides larger contact areas per unit volume between electrolyte, solid (or gaseous) reactant, and electronic conductor [Newman and Tobias, 1962]. Therefore, a wire-mesh or perforated plate arrangement is used to represent the grid in both anode and cathode beds. This kind of packed bed grid enables a larger contact area per unit volume resulting in relatively lower mass transfer resistance and higher reaction rates due to availability of more activation sites for the reactions to proceed. The ohmic resistance (iR losses) might be relatively larger when compared to the conventional solid electrodes but it's also possible to determine

a trade-off between the benefits from mass transfer and negative effects from increased bed depths.

The basic idea elaborated in the thesis is to utilize carbon directly within the molten carbonate salt to produce electricity through chemical reactions taking place within anode and cathode. The ionic current direction is parallel to the direction of the flow and bulk convection is mainly responsible for the transport of gas species from gas phase (bubbles) to the reaction sites (solid grid surface, cathode) or from reaction sites (carbon particle surface, anode) to the gas phase (bubbles). Mass transport via diffusion in the direction perpendicular to the direction of flow provides concentration gradient in the transverse direction which is insignificant compared to gas species concentration along the bed depth controlled by convection.

In this chapter, the following topics are discussed.

The literature data utilized to estimate the thermo-physical properties for electrolyte salts, and the participating gases is first discussed. The thermodynamic properties include density, viscosity, electrical conductivity, and surface tension of the molten carbonate salts. For the gases, diffusivity and solubility of CO_2 and O_2 in molten carbonate salts is presented and discussed.

Next, electrode kinetic models for anode and cathode are discussed. Both models are based off of best available experimental data from literature. The kinetic model comprises of full Butler Volmer type charge-transfer current density equation that depend upon overpotential, surface concentrations and kinetic data.

Next section covers basic concepts that were used to develop transport equations for the porous beds discussed in this work. The further development of governing equations for the cathode and the anode is based off these concepts.

After that, complete process modeling for the cathode and the anode beds is presented. Process modeling includes development of governing equations for various gas/liquid mole fluxes of components, electrolyte voltage, electrolyte current density, initial conditions, estimation of gas, liquid and solid hold-ups, and determination of gas-liquid and liquid-solid mass transfer coefficients.

The last section then demonstrates solution methodology used for solving the fuel cell model comprising of 11 ordinary differential equations and many intermediate variables through simulations using shooting method and iterative algorithms.

3.1 Thermo-Physical Properties

The properties of eutectic mixture of the carbonate of alkali metals, Li-Na-K has been studied in much detail by Janz et al. [1979]. For the present work, various thermo-physical properties like density, viscosity, conductivity, etc have been used to solve and analyze the fuel cell model. The diffusion coefficients for transport of solute gases like CO_2, and O_2 through the molten salt electrolyte have been used to solve differential equations through the packed bed of electrolyte for different solute gases, i.e. CO_2, and O_2. In the anode bed, the molten salt electrolyte is entrained with coal/biomass particles. The correlations and differential equations in anode have been developed in a manner similar to that for cathode, by replacing the liquid properties with the slurry properties of entrained mixture of molten electrolyte and coal.

In the current work, the binary molten carbonate mixture of Li-K (eutectic) and the ternary molten carbonate mixture of Li-Na-K (eutectic) have been considered

in the development of the fuel cell model. The cathode kinetic model is based off from the work of Wilemski [1983] and Lu and Selman [1992] utilizing different oxygen reduction mechanisms. The work of Wilemski [1983] that uses the ternary eutectic mixture of Li-Na-K carbonates is used to evaluate:

1. Solubility of CO_2 and O_2 in the molten carbonate salt.
2. Molecular Diffusivity of CO_2 and O_2 in the molten carbonate salt.
3. Cathodic exchange current density as a function of temperature
4. Cathodic reaction orders for CO_2 and O_2

The work of Lu and Selman [1992] utilizes the binary mixture of Li-K (62% - 38% eutectic) molten carbonate salt and provides the following parameters:

1. Cathodic exchange current density at 650$^\circ C$ temperature.
2. Cathodic reaction orders for CO_2 and O_2

Further details on kinetics is covered in later sections.

The melting points for pure lithium carbonate, sodium carbonate and potassium carbonate are 723, 858, and 898 $^\circ C$ respectively. However, when the eutectic composition of 43.5 mol % Li_2CO_3, 31.5 mol % Na_2CO_3 and 25.0 mol % K_2CO_3 is used, melting point comes down significantly to 397$^\circ C$ [Janz et al., 1979]. This makes it possible to use the molten carbonate salts for fuel cell temperature in the mid-range of 500-800 $^\circ C$ and keeping the carbon-monoxide generation to a minimum . Properties like density, viscosity, electrical conductivity, surface tension are used from the compiled properties data by Janz et al. [1979] and is covered here in some detail.

3.1.1 Density of molten carbonate salts

Density of ternary eutectic mixture of alkali carbonates $(Li/Na/K)_2CO_3$ in mol% 43.5/31.5/25.0 is measured using Archimedean technique [Janz et al., 1979] and valid for a temperature range of 680-1060 K.

$$\rho = 2512.8 - 0.54405T \qquad [kg/m^3] \tag{3.1}$$

Precision of $\pm 0.8\%$ and uncertainty of $\approx \pm 1\%$ has been predicted by Janz et al. [1979]. Use of the correlation for temperatures $> 1060K$ can produce errors that may be higher then predicted by the uncertainty in the correlation.

3.1.2 Surface tension of molten carbonate salts

Surface Tension of ternary eutectic mixture of alkali carbonates $(Li/Na/K)_2CO_3$ in mol% 43.5/31.5/25.0 is measured using pin detachment method [Janz et al., 1979] and valid for a temperature range of 740-1050 K.

$$\gamma = 287.07 - 6.944 \times 10^{-2}T \qquad [dynes - cm^{-1}] \tag{3.2}$$

Precision of $\approx \pm 0.4\%$ and uncertainty of $\approx \pm 0.5\%$ has been predicted by Janz et al. [1979]. Use of the correlation for temperatures $> 1050K$ can produce errors that may be higher then predicted by the uncertainty in the correlation.

3.1.3 Viscosity of molten carbonate salts

Viscosity of ternary eutectic mixture of alkali carbonates $(Li/Na/K)_2CO_3$ in mol% 43.5/31.5/25.0 is measured using oscillating (liquid filled) cylinder method [Janz

et al., 1979] and valid for a temperature range of 760-870 K.

$$\mu = 4.64 \times 10^{-3} \exp(10661/RT) \qquad [centipoise] \tag{3.3}$$

Precision of $\approx \pm 0.05\%$ and uncertainty of $\approx \pm 25\%$ has been predicted by Janz et al. [1979]. Use of the correlation for temperatures $> 870K$ can produce errors that may be higher then predicted by the uncertainty in the correlation.

Considering that the operating temperatures of direct carbon fuel cells as investigated in this thesis are well higher than 870K, it's possible that much higher errors can be introduced into the simulations due to these errors.

3.1.4 Electrical conductance of molten carbonate salts

Conductivity of ternary eutectic mixture of alkali carbonates $(Li/Na/K)_2CO_3$ in mol% 43.5/31.5/25.0 is measured using a.c. bridge techniques [Janz et al., 1979] and valid for a temperature range of 670-1000 K.

$$\kappa = A \exp(-E/RT) \qquad [Ohm^{-1} - cm^{-1}] \tag{3.4}$$

where A = 83.8192 $Ohm^{-1} - cm^{-1}$ and E = 7385 cal/mol for the ternary eutectic mixture. Also, for the ternary eutectic mixtures, precision of $\approx \pm 0.5\%$ and uncertainty of $\approx \pm 2\%$ has been detected by Janz et al. [1979]. Use of the correlation for temperatures outside the predicted range can produce errors that may be higher then predicted by the uncertainty in the correlation.

Considering significant variation in specific conductance with variation in salt mixtures, sensitivity in the fuel cell performance has been investigated.

3.1.5 Solubility of Gases CO_2 and O_2 in Electrolyte

Solubility of CO_2 in binary and ternary molten carbonate salts

Appleby and Van Drunen [1980] has reported solubility data of O_2 and CO, however for CO_2 only one data-point has been reported. As per this reference, the solubility determination of CO_2 in the ternary eutectic melt of Li-Na-K was done using dynamic weighing and supplemental data using quenching method was used to confirm the findings from dynamic weighing. A mean solubility (six separate readings) of $3.60 \times 10^{-3}\ mole - dm^{-3} - atm^{-1}$ was obtained by the quenching method in good agreement with the value obtained by weighing [$2.84 \times 10^{-3}\ mole - dm^{-3} - atm^{-1}$]. This solubility data was reported at 700$^{\circ}C$ or $973K$.

Some experimental data from Institute of Gas Technology (IGT) reports and work by Broers has been put in an empirical form by Wilemski [1983] and made available in the form of Arrhenius type equations as a function of temperature. The solubility of CO_2 (in $kmol/(m^3 - kPa)$) as referenced from this work is given by:

$$k_{H,\mathrm{CO_2}} = 1.71 \times 10^{-4} \exp\left(\frac{-364.6}{T}\right) \quad [kmol - m^{-3} - kPa^{-1}] \tag{3.5}$$

The above empirical equation, however, does not match closely with limited data presented by Tomkins and Bansal [1991] and sourced from Dubois (1965) and Appleby and Drunen (1980). The differences in the data is seen from the Table 3.1. The reason for difference maybe explained by the fact that different estimation methods were used and also that solubility of CO_2 varies vastly in different mixtures of binary and ternary molten carbonate salts.

Some work on estimating the solubility of CO_2 in the ternary eutectic mixture of Li-Na-K (43.5:31.5:25 mol%) using titration method was done by Claes et al.

Table 3.1: CO_2 Solubility for various electrolyte melts at varying temperatures.

Electrolyte Melt	T [K]	k_H $[kmol \cdot m^{-3} \cdot kPa^{-1}]$	Reference
Li-Na-K [43.5:31.5:25] Eutectic	833	8.88×10^{-4}	Dubois [1965]
Li-Na-K [43.5:31.5:25] Eutectic	973	3.55×10^{-5}	Appleby and Van Drunen [1980]
Li-Na-K [43.5:31.5:25] Eutectic	973	1.17×10^{-4}	Broers (1977)
Li-Na-K (composition N/A)	923	1.15×10^{-4}	Wilemski [1983]
Li-Na-K (composition N/A)	973	1.17×10^{-4}	Wilemski [1983]
Li-Na-K (composition N/A)	1023	1.20×10^{-4}	Wilemski [1983]
Na-K	1073	1.8×10^{-3}	Claes et al (1996)
Li-Na-K [43.5:31.5:25] Eutectic	973	9.38×10^{-4}	Claes et al. [1999]
Li-Na-K [43.5:31.5:25] Eutectic	684-973	$1.46 - 2.00 \times 10^{-3}$	Kanai et al. [2013]

[1999]. The work was performed at a single temperature of 973 K and under atmospheric pressure conditions. More recently, Kanai et al. [2013] determined solubilities of CO_2 with a simplified elution method described by Sada et al. [1980]. The molten salts used for the experiments were: 1) Binary mixture of Li-K (38:62 mol%), and 2) Ternary eutectic mixture of Li-Na-K (43.5:31.5:25 mol%). The experiments were conducted at 101 kPa and temperatures ranging from 673 - 1173 K.

It's very clear that the majority of reliable data is only available for the ternary eutectic mixture of Li-Na-K. The data for binary eutectic mixture of Li-K (62:38 mole %) is not available at all. The data from Broers seems to be more reliable and has been the source for a regressed equation presented by Wilemski [1983].

The solubility of CO_2 given by Wilemski [1983] has been used in the present work.

Solubility of O_2 in binary and ternary molten carbonate salts

For the solubility of O_2, the original measurements were performed by Schenke et al. [1966] and Appleby and Van Drunen [1980]. Both set of measurements were done in a ternary eutectic melt of Li_2CO_3 - Na_2CO_3 - K_2CO_3 (43.5 - 31.5 - 25.0 mol%). It is interesting to note the close match of the experimental data from amperometric titration method used by Schenke et al. [1966] to the melt chilling technique used by Appleby and Van Drunen [1980]. Tomkins and Bansal [1991] having consolidated these experimental results also provided two different empirical equations. For the purpose of the mathematical modeling in the current work, the two sets of experimental data have been regressed into one single equation for use in the fuel cell model. Wilemski [1983] has also looked at other experimental data and produced an empirical equation that does not match closely with the two sets of experimental data provided earlier. The equation for solubility of O_2 , probably using experimental data from Broers, is produced by Wilemski [1983] here:

$$k_{H,\mathrm{o}_2} = 0.014456 \exp\left(\frac{-7589}{T}\right) \quad [kmol - m^{-3} - kPa^{-1}] \tag{3.6}$$

All this work is represented in the attached graph in figure 3.1.

3.1.6 Diffusivity of Gases CO_2 and O_2 in Electrolyte

The axial diffusion of gases (CO_2 and O_2) in the co-current packed bed electrodes is neglected, and molecular diffusion has been used to quantify mass transport of gas species (CO_2 and O_2) from bulk liquid to the grid surface in the cathode and mass transport of of CO_2 from carbon particle surface to the bulk liquid in the

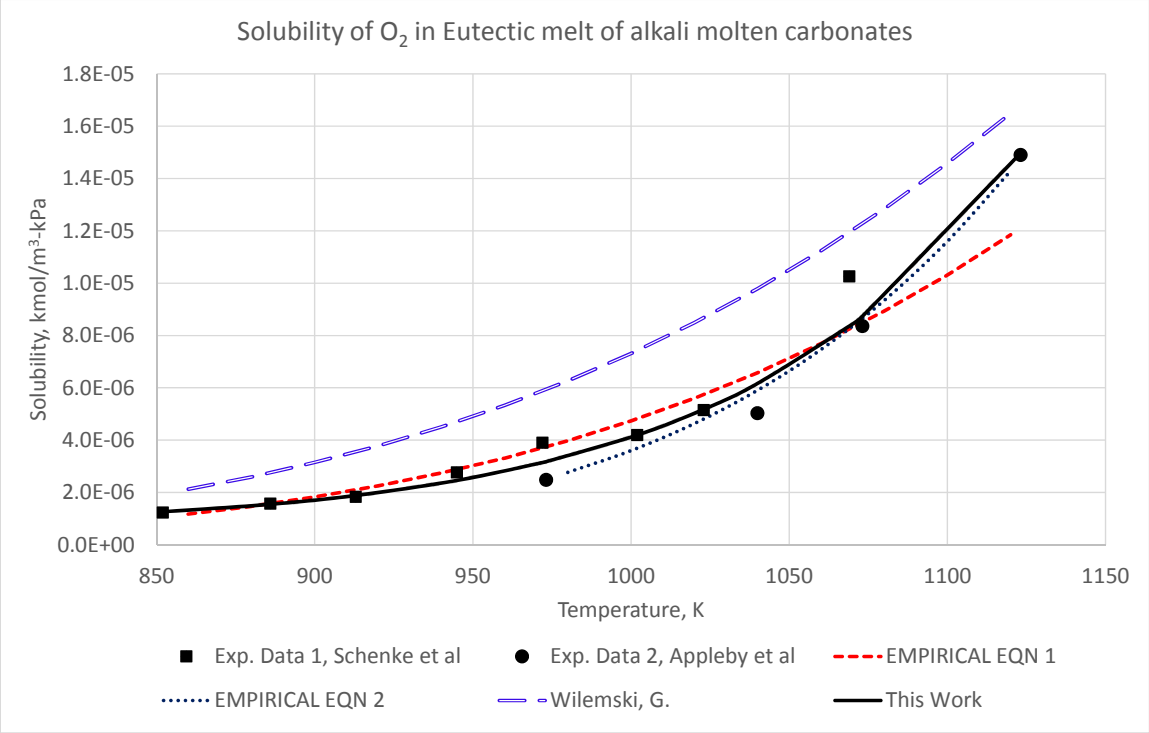

Figure 3.1: Solubility data for O_2 in the ternary eutectic melt of Li_2CO_3 - Na_2CO_3 - K_2CO_3 (43.5 - 31.5 - 25.0 mol%).

anode. Wilemski [1983] has used data from several IGT reports to produce an empirical equation for the diffusivity of CO_2 and O_2 in molten carbonate salts. The equations are produced below:

$$D_{\mathrm{co_2}} = 3.38 \times 10^{-7} \exp\left(\frac{-5432}{T}\right) \ [m^2 - s^{-1}] \tag{3.7}$$

$$D_{\mathrm{o_2}} = 4.32 \times 10^{-7} \exp\left(\frac{-5503}{T}\right) \ [m^2 - s^{-1}] \tag{3.8}$$

3.2 Electrode Kinetics

The kinetic models needed to describe charge-transfer current densities in direct carbon molten carbonate fuel cells is not readily available in the literature. For the cathode, some models are available for the charge-transfer current density equations describing reaction rate kinetics in a conventional molten carbonate fuel cell. These models have been modified and used in the present work. For the anode, no kinetic model is available in the literature and therefore a charge-transfer current density equation has been developed using kinetic data from the work of Ateya[1].

The following reaction takes place at the cathode,

$$\mathrm{O_2 + 2CO_2 + 4e^- \longrightarrow 2{CO_3}^{2-}} \tag{3.9}$$

and if the Boudouard equilibrium points towards only CO_2 formation (by keeping cell temperature $< 750^\circ C$) then the following reaction takes place at anode,

$$\mathrm{C + 2{CO_3}^{2-} \longrightarrow 3CO_2 + 4e^-} \tag{3.10}$$

[1] SRI project reports [Weaver et al., 1979][Appendix B]

If O represents a molecule of an oxidized species and R a molecule of reduced species, then at equilibrium, a general electrode reaction will proceed like this:

$$O + ze \rightleftharpoons R \tag{3.11}$$

If the equilibrium of the above reaction is disturbed by applying an external potential, the above reaction proceeds from left to right for a cathodic polarization. The current which flows when the electrode is polarised cathodically represents the difference between forward and reverse reaction rates. The equation for net current density, as given by Pickett [1977, page 53], then can be written as a function of the surface overpotential (η_s) and species concentration:

$$i'' = i_o'' \left[\frac{C_{O_s}}{C_{O_{blk}}} \exp\left(\frac{-\alpha z \mathbf{F} \eta_s}{\bar{R} T} \right) - \frac{C_{R_s}}{C_{R_{blk}}} \exp\left(\frac{(1-\alpha) z \mathbf{F} \eta_s}{\bar{R} T} \right) \right] \tag{3.12}$$

Equation 3.12 serves as a general expression for the rate of an electrode reaction that combines the exchange current density i_0'', and the transfer coefficient α both of which can be experimentally determined. C_{O_s}, C_{R_s}, and $C_{O_{blk}}$, $C_{R_{blk}}$ are respectively the concentration of the oxidized/reduced species at the surface of the electrode and in the bulk liquid. The overpotential (η_s) has a negative value in the equation 3.12 for the net forward or cathodic reaction.

Now, it's clear that a simplified equation as eqn 3.11 cannot possibly indicate as to the actual reaction mechanism that takes place and what (or how many steps) really constitutes a rate determining step (r.d.s.). Normally, the slowest reaction step having electron transfer provides the r.d.s. But it could be more than one reaction that can constitute the determination of reaction rate. For this reason, a revised form of Butler Volmer equation for characterizing charge-transfer current

density shown in equation 3.12 is produced by Pickett [1977, page 55] using the theory propounded originally by Vetter [1967, page 432]:

$$i'' = i_o'' \left[\left(\frac{C_{O_s}}{C_{O_{blk}}} \right)^{m_1} \exp\left(\frac{-\alpha z \mathbf{F} \eta_s}{\bar{R} T} \right) - \left(\frac{C_{R_s}}{C_{R_{blk}}} \right)^{m_2} \exp\left(\frac{(1-\alpha) z \mathbf{F} \eta_s}{\bar{R} T} \right) \right] \qquad (3.13)$$

where m_1 and m_2 are the electrochemical reaction orders for the forward and reverse reactions respectively. The reaction orders should not be confused with stoichiometric molecularity of participating species in any r.d.s portion of the complex reaction mechanism.

Although, the reaction orders do not necessarily improve our understanding of the fundamental processes inherent in a electrochemical reaction, they are useful in calculating changes of rate with concentration and potential in kinetic investigations. This may be better understood in later section while illustrating the development of a standard charge-transfer current density equation for a MCFC cathode utilizing the work of Wilemski [1983]. It is important to note that the exchange current density, i_o'', in equations 3.12 and 3.13 is not same, nor it is a constant. Essentially, the exchange current density, i_o'' is a function of both concentration and potential. Also, i_o'' is not an absolute value but is based on a reference equilibrium potential. This will be covered in some detail in later sections where cathode and anode for a direct carbon fuel cell are separately discussed. Pickett [1977, page 58] also provides certain clues into understanding the significance of exchange current density with respect to mass transfer processes influencing the electrochemical activity. According to the author, a perfectly reversible electrode can have high value of exchange current density, i.e. $i_o \to \infty$ whereas, $i_o \to 0$ is an

ideally polarisable electrode. A reaction having a high i_o'' is generally termed as a "fast electrochemical reaction" and correspondingly a low values of i_o'' characterizes "slow electrochemical reaction". This also means that if the value of i_o'' is low for a certain electrochemical cell, then the electrode processes might not be sufficiently limited by mass transfer but by kinetics only and in that special case concentration at the surface of the electrode and in the bulk liquid might be approximately equal in value, i.e. $C_{O_s} = C_{O_{blk}}$ and $C_{R_s} = C_{R_{blk}}$. This will transform equations 3.12 and 3.13 into:

$$i'' = i_o'' \left[\exp\left(\frac{-\alpha z \mathbf{F} \eta_s}{\bar{R} T} \right) - \exp\left(\frac{(1-\alpha) z \mathbf{F} \eta_s}{\bar{R} T} \right) \right] \tag{3.14}$$

The development of models for the reaction rate kinetics in cathode and anode is described next.

3.2.1 Cathode Kinetics

The cathode kinetics in the direct carbon molten carbonate fuel cells is dictated by reduction of oxygen species and it's clear from Appleby and Nicholson [1977] that molecular oxygen does not participate in the chemical reactions. During the 1970s, Appleby and Nicholson [1972, 1974, 1977, 1980] provided evidence that the oxygen dissolves as a mixture of peroxide (O_2^{2-}) and superoxide (O_2^{-}) ions and that the relative amounts of these ions strongly depend upon the composition of the alkali carbonate melt. The authors proposed that the peroxide mechanism is the dominant (or rate-determining) step in the pure Li or Li rich molten carbonates salts and that both peroxide and superoxide ions are the electroactive species present in

the Na/K electrolyte melt, but the superoxide only predominates at higher temperatures and higher O_2/CO_2 partial pressures. Some [Vogel et al., 1983, Smith et al., 1982, Lu, 1985, Yuh and Selman, 1991, Lu and Selman, 1992] have suggested that the superoxide is the dominant species present even in the Li/K melts. McHardy [1979] suggested that since melt composition might be a major factor influencing the kinetics of O_2 reduction and that a systematic study of reaction kinetics as a function of melt composition was clearly required to establish better quantitative understanding. Thermodynamic evidence for the complex reaction mechanism involving peroxide and superoxide mechanisms has been provided by Andersen [1975] during his doctoral work on chemical-equilibria in alkali carbonate melts.

Another mechanism has been proposed by Dunks and Stelman [1983] that involves a hypothetical species called percarbonate ion, CO_4^{2-} and set of reactions proposed as below. However, this mechanism has been studied sparingly in the literature and is not the focus of the current work.

$$\tfrac{1}{2}\mathrm{O_2} + {\mathrm{CO_3}}^{2-} \longleftrightarrow {\mathrm{CO_4}}^{2-} \tag{3.15}$$

$${\mathrm{CO_4}}^{2-} + \mathrm{e}^- \longleftrightarrow {\mathrm{CO_3}}^{2-} + (\mathrm{O}^-)\ (rds) \tag{3.16}$$

$$(\mathrm{O}^-) + \mathrm{CO_2} + \mathrm{e}^- \longleftrightarrow {\mathrm{CO_3}}^{2-} \tag{3.17}$$

For various partial pressure of CO_2 and O_2 at the cathode, the equilibrium between different oxygen ion species in various mixtures of alkali carbonate melts at different temperatures is not clearly understood. Table 3.2 explains a bit of history regarding the oxygen reduction mechanism in MCFC cathode:

[2] i_o for O_2 90%, CO_2 10%

[3] at $650^\circ C$, eutectic

[4] pure Li at $750^\circ C$

Table 3.2: Kinetic parameters for oxygen reduction mechanism in MCFC cathode.

$$i_o = i_o^o (O_2)^a (CO_2)^b$$

i_o = Bulk exchange current density, mA/cm^2

i_o^o = Standard exchange current density, mA/cm^2

$i_o\ mA/cm^2$	a	b	Method	Electrode	Dominant Mechanism	Electrolyte	Reference
	0.85	-0.45	Potential-step, AC Imped.	Au(ref), Ni(cathode)	Superoxide	62/38 Li-K	Yuh and Selman [1991]
10,27,39	0.1	-0.15[2]	Potential-step, Coul. relax., and AC Imped.	Au smooth	Superoxide	43/57 Li-K eutectic	Uchida et al. [1986]
11[3],26.3[4]	0.1	-0.15[5]	SS potentiostatic, potential step	Au smooth	Superoxide	Li, Li-K eutectic	Lu and Selman [1992]
$0.023 - 0.065$[6]	-	-	SS potentiostatic	Au smooth		Li-Na-K eutectic	Borucka and Sugiyama [1969]
10	0.15	-0.15	Potential-step	Au, smooth	Superoxide		Lu [1985]
-	0.3	0	SS, kinetic control assumed	NiO, porous			Tang et al (1980)
-	0.6	0.6		NiO, porous			Tang et al (1980)
1	0.5	0	C	NiO, porous		Li-K eutectic	Winnick and Ross Jr. [1981]
4-7	-	-	Transient potentiostatic	Au			IGT report Proj 9105
0.78	0.2	0.2	Modeling of SS data	NiO, porous	Peroxide	Na-K	Wilemski [1983]
0.16-0.5	0.875	-0.25	Modeling of SS data	NiO, porous			Kunz et al. [1984]
0.45[7], 1.12[8], 2.5[9]	-	-	Potential-sweep	Au	Peroxide	53/47 Li-K eutectic	Appleby and Nicholson [1980]
	0.375	-1.25	Modeling of SS data	NiO, porous			Prins-Jansen (1997)
	0.4	0	Modeling of SS data	SS porous	Superoxide	Li-Na-K, Li-K	This work

It's clear that the mechanism for reaction kinetics in cathode for molten carbonate fuel cells is very complex[10] and difficult to understand and quantify in terms of equations that can be used for modeling purposes. Therefore, efforts have been made in the current work and two different models have been presented for predicting cathode reaction kinetics. One that utilizes model developed by Wilemski [1983] and is based on the peroxide being the dominant mechanism and another model that has been developed in the current work and kinetic data in the literature and is based on the superoxide being the dominant mechanism.

Model based on peroxide mechanism

The peroxide (or the first wave) mechanism for oxygen reduction has originally been proposed by Appleby and Nicholson [1974] and is:

$$\tfrac{1}{2}\mathrm{O_2} + {\mathrm{CO_3}}^{2-} \quad \rightleftharpoons \quad {\mathrm{O_2}}^{2-} + \mathrm{CO_2} \tag{3.18}$$

$${\mathrm{O_2}}^{2-} + \mathrm{e}^- \quad \rightleftharpoons \quad \mathrm{O}^{2-} + \mathrm{O}^- \ (rds) \tag{3.19}$$

$$\mathrm{O}^- + \mathrm{e}^- \quad \rightleftharpoons \quad \mathrm{O}^{2-} \tag{3.20}$$

$$\mathrm{O}^{2-} + \mathrm{CO_2} \quad \rightleftharpoons \quad {\mathrm{CO_3}}^{2-} \tag{3.21}$$

[5] i_o for O_2 90%, CO_2 10%

[6] at $650 - 750^\circ$C, and $P_{O_2}/P_{CO_2} = 0.33/0.67$

[7] at 700 C, Peroxide wave - 0.37, Superoxide wave - 0.08

[8] at 750 C, Peroxide wave - 0.82, Superoxide wave - 0.3

[9] at 800 C, Peroxide wave - 1.2, Superoxide wave - 1.3

[10] Appleby and Nicholson [1972, 1974, 1977], McHardy [1979], Winnick and Ross Jr. [1981], Smith et al. [1982], Vogel et al. [1983], Kunz et al. [1984], Uchida et al. [1986], Lu [1985], Yuh and Selman [1991], Nishina et al. [1994], Moyaux et al. [1993], Lu and Selman [1992], Selman [1992]

Wilemski et al. [1979] has used the quasi-equilibrium assumption to develop the cathode reaction mechanism for O_2 reduction on smooth gold electrodes in alkali carbonate melts. The charge-transfer current density equation is reproduced below:

$$i''_{s,c} = i''^{0}_{s,c}\left[\left(\frac{\bar{\rho}_{O_2,s,c}}{\bar{\rho}_{O_2,ref}}\right)^{1/2}\left(\frac{\bar{\rho}_{CO_2,s,c}}{\bar{\rho}_{CO_2,ref}}\right)^{-1}\exp\left(\frac{\alpha_c \mathbf{F}}{\bar{R}T}\eta_c\right) - \left(\frac{\bar{\rho}_{CO_2,s,c}}{\bar{\rho}_{CO_2,ref}}\right)^{-2}\exp\left(\frac{(\alpha_c - 2)\mathbf{F}}{\bar{R}T}\eta_c\right)\right] \tag{3.22}$$

and exchange current density is:

$$i''^{0}_{s,c} = i''^{0}_{c}\,(p_{O_2}/P)^{(2-\alpha_c)/4}\,(p_{CO_2}/P)^{-(2+\alpha_c)/2} \tag{3.23}$$

Cathode kinetic model based on superoxide mechanism

The superoxide (or the second wave) mechanism for oxygen reduction originally proposed by Appleby and Nicholson [1974] is:

$$\tfrac{3}{4}O_2 + \tfrac{1}{2}{CO_3}^{2-} \quad \rightleftharpoons \quad {O_2}^{-} + \tfrac{1}{2}CO_2 \tag{3.24}$$

$${O_2}^{-} + e^{-} \quad \rightleftharpoons \quad {O_2}^{2-}\,(rds) \tag{3.25}$$

$${O_2}^{2-} + e^{-} \quad \rightleftharpoons \quad O^{2-} + O^{-} \tag{3.26}$$

$$O^{-} + e^{-} \quad \rightleftharpoons \quad O^{2-} \tag{3.27}$$

$$O^{2-} + CO_2 \quad \rightleftharpoons \quad {CO_3}^{2-} \tag{3.28}$$

Wilemski et al. [1979] has used the quasi-equilibrium assumption to develop the cathode reaction mechanism for O_2 reduction on smooth gold electrodes in alkali carbonate melts. The charge-transfer current density equation is reproduced below:

$$i''_{s,c} = i''^{0}_{s,c}\left[\left(\frac{\bar{\rho}_{O_2,s,c}}{\bar{\rho}_{O_2,ref}}\right)^{3/4}\left(\frac{\bar{\rho}_{CO_2,s,c}}{\bar{\rho}_{CO_2,ref}}\right)^{-1/2}\exp\left(\frac{\alpha_c \mathbf{F}}{\bar{R}T}\eta_c\right) - \left(\frac{\bar{\rho}_{CO_2,s,c}}{\bar{\rho}_{CO_2,ref}}\right)^{-2}\exp\left(\frac{(\alpha_c - 3)\mathbf{F}}{\bar{R}T}\eta_c\right)\right] \tag{3.29}$$

and exchange current density is:

$$i''^{0}_{\mathrm{s,c}} = i''^{0}_{c}\ (p_{\mathrm{o_2}}/P)^{(3-\alpha_\mathrm{c})/4}\ (p_{\mathrm{co_2}}/P)^{-(1+\alpha_\mathrm{c})/2} \tag{3.30}$$

Cathode Kinetic Model used in the Current Work

As per Wilemski et al. [1979], the models for first-wave (peroxide) and second-wave (superoxide) mechanisms, presented above, suffer from inaccurate predictions of electrode performance with increasing partial pressure of oxygen plus carbon-dioxide when compared with experimental data. Therefore, a general form of charge-transfer current density (equations 3.31 and 3.32) has been used.

$$i''_{\mathrm{s,c}} = i''^{0}_{\mathrm{s,c}} \left[f_{\mathrm{o_2}}^{\ s}\ f_{\mathrm{co_2}}^{\ t} \exp\left(\frac{\alpha_\mathrm{c}\mathbf{F}}{\bar{R}T}\eta_\mathrm{c}\right) - f_{\mathrm{o_2}}^{\ u}\ f_{\mathrm{co_2}}^{\ v} \exp\left(\frac{(\alpha_\mathrm{c}-n)\mathbf{F}}{\bar{R}T}\eta_\mathrm{c}\right)\right] \tag{3.31}$$

$$i''^{0}_{\mathrm{s,c}} = i''^{0}_{c}\ (p_{\mathrm{o_2}}/P)^{\sigma}\ (p_{\mathrm{co_2}}/P)^{\tau} \tag{3.32}$$

where $p_{\mathrm{co_2}}$ and $p_{\mathrm{o_2}}$ are respectively the partial pressures of O_2 and CO_2 in the molten salt and P is the cell pressure which is typically 1 atm. The quantity f_k denotes the ratio $\rho_{k,s,c}/\rho^e_k$ where $\rho_{k,s,c}$ is the concentration of the species k "at" the electrode surface under load conditions and ρ^e_k is the equilibrium (open circuit) value.

Given that the equilibrium potential is governed by the Nernst equation, $E = E^o + (RT/2\mathbf{F})\ln(p_{\mathrm{o_2}}^{1/2}\, p_{\mathrm{co_2}})$ and that the solubilities of molecular CO_2 and O_2 obey Henry's law relationships, Wilemski [1983] proposed that the exponents s, t, u, and v can be determined by evaluating values of α, σ, and τ through the use of following

relationships:

$$\sigma = s - \alpha/4 = u + (n-\alpha)/4 \tag{3.33}$$

$$\tau = t - \alpha/2 = v + (n-\alpha)/2 \tag{3.34}$$

As per Henry's law, $\rho^e = Hp$, therefore equilibrium molar concentrations for CO_2 and O_2 are given by:

$$\bar{\rho}^e_{\mathrm{co}_2} = H_{\mathrm{co}_2}\, p_{\mathrm{co}_2} \tag{3.35}$$

$$\bar{\rho}^e_{\mathrm{o}_2} = H_{\mathrm{o}_2}\, p_{\mathrm{o}_2} \tag{3.36}$$

where the Henry's law constants are described in the thermodynamic properties section.

In the equations above, the overpotential $\eta_{\mathrm{c}} = V_{\mathrm{c}}$, $f_{\mathrm{o}_2} = \bar{\rho}_{\mathrm{o}_2,\mathrm{s,c}}/\bar{\rho}_{\mathrm{o}_2,\mathrm{ref}}$ and $f_{\mathrm{co}_2} = \bar{\rho}_{\mathrm{co}_2,\mathrm{s,c}}/\bar{\rho}_{\mathrm{co}_2,\mathrm{ref}}$. The standard exchange current density (in A/m^2) according to the model [Wilemski, 1983] is given by,

$$i''^0_{\mathrm{c}} = k^0_{\mathrm{c}} \exp\left[\frac{E_{\mathrm{c}}(T - T_{923})}{T_{923}\, T}\right] (P_{\mathrm{o}_2}/P)^{\,\sigma}\, (P_{\mathrm{co}_2}/P)^{\,\tau} \tag{3.37}$$

where E_{c} was estimated to be 5800 K, and k^0_{c} to be 7.8 A/m^2. The values of the partial pressures, P_{o_2} and P_{co_2} are 0.33 and 0.67 atm respectively. Overall electron transfer (n) is assumed to be 2 and according to Wilemski [1983] the model is best described by values of $\sigma \approx 0.4$, $\tau \approx 0.0$, $\alpha_{\mathrm{c}} = 0.75$, $s = 0.5875$, $t = 0.375$, $u = 0.0875$, and $v = -0.625$.

Relationship between concentrations at surface and in bulk liquid

The concentration of the species k "at" the electrode surface under load conditions in the cathode is given by:

$$\bar{\rho}_{k,s} = \bar{\rho}_{k,\ell,\mathrm{c}} - \frac{i''_{\mathrm{s,c}}}{z_k \mathbf{F} k_{\ell\text{-s},k}} \tag{3.38}$$

The term $i''_{\mathrm{s,c}}/z_k\mathbf{F}$ represents the molar flux of species (in $kmol/m^2 - sec$) that is used up in the reaction to produce z_k number of electrons. The concentration gradient between the bulk liquid ($\bar{\rho}_{k,\ell,\mathrm{c}}$) and the electrode surface ($\bar{\rho}_{k,s}$) is limited by the mass transfer coefficient, $k_{\ell\text{-s},k}$ which is evaluated empirically from literature and documented in section 3.4.3. Parameter z_k is equal to 4 and 2 respectively for the species CO_2 and O_2. The bulk liquid concentration ($\bar{\rho}_{k,\ell,\mathrm{c}}$) can be estimated from the solution of differential equations in the fuel cell model.

3.2.2 Anode Kinetics

The purpose of the present work is to determine various processes that dictate the modeling of direct carbon fuel cell. Of these various processes, determining the exact mechanism is very important to predict anode kinetics that utilize Butler-Volmer equation as a function of exchange current density, charge-transfer coefficient and the rate determining (slowest) step in case of multi-step reactions which is needed to formulate dependence on species concentration.

The reaction kinetics for anode in a direct carbon fuel cell has been studied to some degree by Weaver et al. [1979], Vutetakis [1985], Cherepy et al. [2005]. The work in Weaver et al. [1979] as a part of bigger work involving complete analysis of direct electrochemical conversion of carbon was presented in the Appendix A, and Appendix B of the report and performed by Masaki Yasuda and Badr Ateya respectively.

Work by Yasuda involved looking at anode polarization of various carbon electrodes in ternary eutectic electrolyte mixture of molten carbonates of alkali. Current-potential experimental data was studied to evaluate the effect on polarization made by surface area and the nature of the surface of various porous carbon electrodes. Electrodes with large surface area, high purity, and reproducible structure were obtained by using spectroscopic carbon and a fuel-cell-grade commercial carbon (PC-60 from Union Carbide). Also used was a locally prepared SRI coal with very high surface area. JPL coal from extrusion process was another carbon electrode that was studied in this work. The experiments were conducted with 67/33 CO_2/O_2 reference electrodes (gold) and in the temperature range of 600-800 $^{\circ}C$. Open Circuit Potentials for both pyrolitic graphite and spectroscopic carbon were found to be slightly lower than the theoretical open circuit potential.

The work involved experiments done on pyrolitic graphite and the resulting kinetic data includes determination of exchange current density and charge transfer coefficient from the Tafel slopes of Potential-Current curves generated at various temperatures. The exchange current densities and charge-transfer coefficient estimated from this work have been put in an empirical form through least squares regression analysis. The data and the empirical fit is shown in the figure 3.2. The data for exchange current density from this work was empirically fitted to produce the following equation. The units for the current density are in Amp/m^2 and temperature is in Kelvin.

$$i''_{\mathrm{s,a,0}} = 5.7987 \times 10^{9} \exp\left(\frac{-22174.6}{T}\right) \tag{3.39}$$

Charge transfer coefficient (α_z) from the SRI work is observed to be decreasing with temperature and above a certain temperature of 700 $^{\circ}C$, it's clear that the

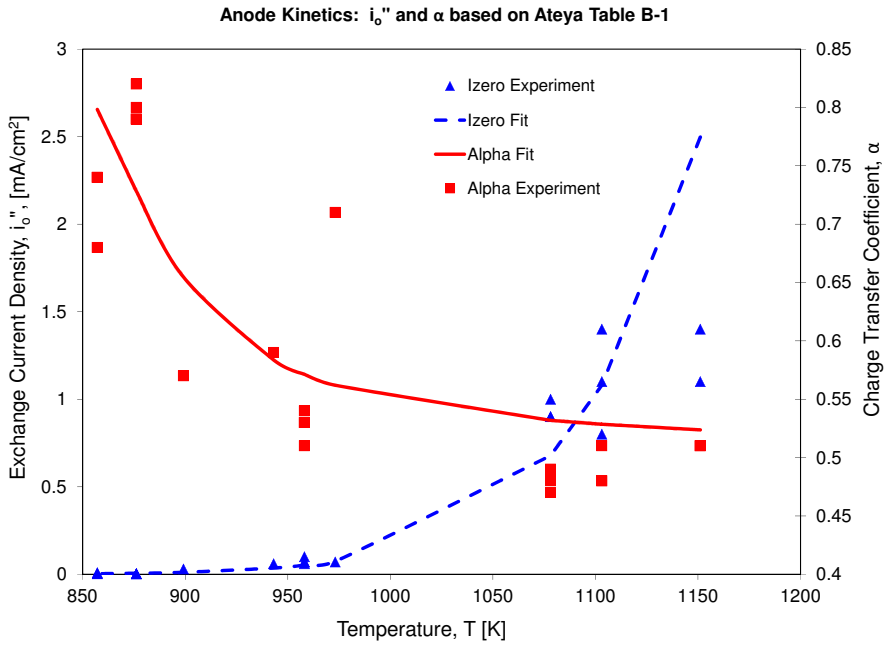

Figure 3.2: Determination of Exchange Current Density and Charge-transfer coefficient in Anode.

value becomes constant at 0.5 which indicates the presence of activation over-potential. The empirically fitted equation is produced below:

$$\alpha_a z(T) = \frac{1}{2\pi}\arctan\left(-\frac{T}{42.19}+20.63\right)+0.75 \tag{3.40}$$

Vutetakis [1985] has done experiments on darco-activated coal and also proposed various possible reaction mechanisms though none of the mechanisms have been tested to be able to know the dominant mechanism. In addition, some kinetic data has also been provided but very low confidence on it's usage has been indicated. Due to difference in porosity and therefore presence of more activation sites in the darco-activated coal, the indicated exchange current densities are roughly one order of magnitude higher than that estimated from Weaver et al. [1979]. The values of charge transfer coefficient from the work in both research demonstrate magnitude of 0.5 for temperatures exceeding 700 deg C indicating the confirmation of the presence of activation over-potential in that region.

According to Cherepy et al. [2005], the suggested mechanism for anodic reaction of carbon for basic melts (carbonates) is posited to be similar to that in acidic melts (cryolite). The equation steps proposed by the authors are given as below:

$$2\mathrm{CO_3}^{=} \longrightarrow 2\mathrm{CO_2}+2\mathrm{O}^{=} \quad \text{dissociation} \tag{3.41}$$

$$\mathrm{C_{RS}}+\mathrm{O}^{=} \longrightarrow \mathrm{C_{RS}O}^{=} \quad 1^{st}\text{adsorption} \tag{3.42}$$

$$\mathrm{C_{RS}O}^{=} \longrightarrow \mathrm{C_{RS}O}^{-}+\mathrm{e}^{-} \quad \text{Fast discharge} \tag{3.43}$$

$$\mathrm{C_{RS}O}^{-} \longrightarrow \mathrm{C_{RS}O}+\mathrm{e}^{-} \quad \text{Fast discharge} \tag{3.44}$$

The rate-determining slow reaction step is given by the following equation 3.45:

$$\mathrm{C_{RS}O}+\mathrm{O}^{=} \longrightarrow \mathrm{C_{RS}O_2}^{=} \quad \text{Slow adsorption: RDS} \tag{3.45}$$

The CO_2 in the end evolves into the gas phase as given by the last reaction step.

$$C_{RS}O_2^{=} \longrightarrow C_{RS}O_2^{-} + e^{-} \quad \text{Fast discharge} \tag{3.46}$$

$$C_{RS}O_2^{-} \longrightarrow CO_2(g) + e^{-} \quad \text{Fast discharge and evolution} \tag{3.47}$$

The above mechanism is a postulated theory and no data has been correlated against a theoretical equation to prove or disprove it. Determination and validation of an exact multi-step mechanism to realize an appropriate charge-transfer current density equation is not the focus of this work but in the absence of any such equation in the literature, an equation has been proposed assuming reaction step of 1. Although, this equation has not been validated with any experimental data, however, preliminary comparison of this equation with experimental data from Weaver et al. [1979] doesn't generate large errors and therefore will be used to study the fuel cell model presented in the current work. The formulation of this equation is presented in the next section. Sensitivity analysis on various different formulations can be investigated if required.

In addition, it's also suggested by Cherepy et al. [2005] that the evolution of CO_2 remains dominant as long as the cell temperature remains below 650 $^{\circ}C$. According to Vutetakis [1985], at temperatures around 700 $^{\circ}C$ although production of CO_2 is still dominating, there is presence of some CO in purge gases. As per the work of Li et al. [2009] also, CO_2 seems to be predominant at 700 $^{\circ}C$ but mole fraction of CO goes up significantly at 800 $^{\circ}C$. The present work does not try to investigate the applicability of Boudouard Equilibrium to slurry based alkali molten carbonate salts to determine the $CO-CO_2$ equilibrium. Therefore for the purpose of modeling the various processes in the fuel cell, the production of carbon monoxide is neglected and cell operation limited to 700 $^{\circ}C$.

Butler-Volmer Equation for Anode

The Butler-Volmer equation describing charge-transfer current density as a function of surface over-potential for the anode is given by:

$$i_a'' = i_{o,a}'' \left[\exp\left(\frac{\alpha_a z_a \mathbf{F} \eta_{s,a}}{\bar{R} T} \right) - \exp\left(-\frac{(1-\alpha_a) z_a \mathbf{F} \eta_{s,a}}{\bar{R} T} \right) \right] \tag{3.48}$$

where, i_a'' is the charge-transfer current density in anode, $[A/m^2]$

α_a - charge-transfer coefficient in anode

z_a - electron exchange of the rate-determining step (RDS) (=4 with a single-step assumption)

F - Faraday's constant, [=96487 Coulomb/mol]

$\bar{R}$ - Universal gas constant, [=8.3144 J/mol-K]

T - Cell Temperature, [K]

$\eta_a = E_{oc} - E$ - Over-potential, [V]

E is the absolute value for Electrolyte-cathode voltage difference, and

E_{oc} is the absolute value at open circuit for existing concentrations

The exchange current density has been defined by a method similar to that used in cathode and made a function of the ratio of concentration of CO_2 on the carbon-particle surface (reaction site) to the reference concentration of CO_2 raised to an exponent a. In theory, the determination of a should be carried out using experimental data or from a similar work available in literature. It's also possible to assume a value of -3 with a single-step assumption.

$$i_{o,a}'' = i_{o,a}^{0\,\prime\prime} \left(\frac{\rho_{CO_2}}{\rho_{CO_2}^0} \right)^a \tag{3.49}$$

Subsituting equation 3.49 into equation 3.48 for $i''_{o,a}$ and for the over-potential, η_a:

$$i''_a = i^{0''}_{o,a}\left(\frac{\rho_{CO_2}}{\rho^0_{CO_2}}\right)^a\left[\exp\left(\frac{\alpha_a z_a \mathbf{F}(E_{oc}-E)}{\bar{R}T}\right)-\exp\left(-\frac{(1-\alpha_a) z_a \mathbf{F}(E_{oc}-E)}{\bar{R}T}\right)\right] \tag{3.50}$$

The Nernst equation for Open Circuit Voltage (E_{oc}) for the anode reaction:

$2CO_3^{=} + C \longrightarrow 3CO_2 + 4\,e^-$ is given by:

$$E_{oc} = E^0_{oc} + \frac{RT}{nF}\ln\left[\left(\frac{\rho_{CO_2}}{\rho^0_{CO_2}}\right)^{-3}\right] = E^0_{oc} - \frac{3RT}{nF}\ln\left[\frac{\rho_{CO_2}}{\rho^0_{CO_2}}\right] \tag{3.51}$$

where, E^0_{oc} is the Open Circuit Voltage at reference conditions (0.67 atm CO_2/0.33 atm O_2), and

n is the electron exchange of full anode process (=4)

Substituting the expression for Nernst equation into the Butler Volmer equation for i''_a and further simplifying, one gets:

$$i''_a = i^{0''}_{o,a}\left[\left(\frac{\rho_{CO_2}}{\rho^0_{CO_2}}\right)^{a-0.75\alpha_a z_a}\exp\left(\frac{\alpha_a z_a \mathbf{F}\eta^0_a}{\bar{R}T}\right)-\left(\frac{\rho_{CO_2}}{\rho^0_{CO_2}}\right)^{a+0.75\alpha_a z_a}\exp\left(-\frac{(1-\alpha_a) z_a \mathbf{F}\eta^0_a}{\bar{R}T}\right)\right] \tag{3.52}$$

where, η^0_a is the over-potential given by $\eta^0_a = E^0_{oc} - E$.

According to limited current density-potential available from Vutetakis [1985] for cases involving 3% or 100% CO_2 in the purge gas, it's found that the results do not differ very much, indicating the possibility of exponent on the CO_2 concentration of forward reaction $a - 0.75\alpha_a z_a = 0$. The reverse reaction order then is equal to $a + 0.75\alpha_a z_a = 1.5\alpha_a z_a$. Also, the existing concentration indicated in the above equations refer to the concentration of CO_2 on the surface of the carbon-particle. And after adding the subscript s to the current density (indicating dependence upon

surface over-potential, and also to differentiate with the ionic current density in anode), the resulting Butler Volmer equation for constant potential is thus:

$$i''_{s,a} = i^{0''}_{o,a}\left[\exp\left(\frac{\alpha_a z_a \mathbf{F}\,\eta^0_a}{\bar{R}T}\right) - \left(\frac{\rho_{\mathrm{CO}_2,s,a}}{\rho^0_{\mathrm{CO}_2,a}}\right)^{1.5\alpha_a z_a}\exp\left(-\frac{(1-\alpha_a)\,z_a \mathbf{F}\,\eta^0_a}{\bar{R}T}\right)\right] \tag{3.53}$$

The molar density (concentration) of CO_2 [Units: $kmol/m^3$] at reference conditions inside the molten salt depend upon the Henry's law at the reference conditions and is given by:

$$\bar{\rho}^0_{\mathrm{co}_2,\mathrm{a}} = P^0_{\mathrm{CO}_2} H_{\mathrm{CO}_2} \tag{3.54}$$

where $P^0_{\mathrm{CO}_2}$ is the partial pressure of CO_2 at reference conditions, [kPa] and H_{CO_2} is the Henry's Law coefficient, [$kmol/m^3 - kPa$]

The molar density (concentration) of CO_2 [Units: $kmol/m^3$] at the surface of carbon particle (reaction site), $\bar{\rho}_{\mathrm{co}_2,\mathrm{s,a}}$ is given by,

$$\bar{\rho}_{\mathrm{co}_2,\mathrm{s,a}} = \bar{\rho}_{\mathrm{co}_2,\ell,\mathrm{a}} + \frac{3}{4F}\frac{i''_{\mathrm{s,a}}}{k_{\ell\text{-s},\mathrm{co}_2}} \tag{3.55}$$

where, $\bar{\rho}_{\mathrm{co}_2,\ell,\mathrm{a}}$ - molar concentration of CO_2 [Units: $kmol/m^3$] in bulk-liquid phase - is determined from the solution of the differential equations for molar species flux as detailed in further sections on the development of ordinary differential equations, and

$k_{\ell\text{-s},\mathrm{co}_2}$ - Solid-to-liquid mass transfer coefficient [Units: m/s] is determined in further sections on Mass Transfer.

3.3 Transport Equations in Porous Beds

In this section, we develop the necessary equations that govern mass transport in porous bed involving convective flow of liquid entrained with gas phase bubbles. The transport processes in the type of packed bubble bed column described for both cathode and anode are described using a one-dimensional steady state approach in the direction of the flow. The equations for gas phase can be applied to both CO_2 and O_2 in the cathode bed and for CO_2 in the anode bed. The equations have been developed partially from the work done by Herrmann and Emig [1998] on liquid phase hydrogenation in packed bed column reactors and some work on transport processes for electrochemical cells by Tobias et al. [1952], Newman [1967], Le Goff et al. [1969].

3.3.1 Gas-Phase Equations

If we assume the flow of gas-bubble entrained liquid through a packed bed of cross-sectional area A of thickness dx (as shown in figure 3.3), then the following equations will hold.

$$\frac{d\dot{n}''_{i,g}}{dx} = -K_{g\rightarrow l,i} A'''_{\mathrm{b}} \left(\bar{\rho}^{*}_{i,g} - \bar{\rho}_{i,l}\right) \tag{3.56}$$

where, $\dot{n}''_{i,g}$ is the mole flux of the component i in gas phase with units of $kmol - m^{-2} - sec^{-1}$.

$K_{g\rightarrow l,i}$ is the gas-liquid mass transfer coefficient and has units of $m - sec^{-1}$.

A'''_{b} is the bubble surface are per unit bed volume (total volume) and has units of $m^{-2} - m^{-3}$.

$\bar{\rho}^{*}_{i,g}$ is the concentration (or molar density) of the component i in the liquid phase

that is in equilibrium with the gas phase (bubble) and has units of $kmol - m^{-3}$.

$\bar{\rho}_{i,l}$ is the concentration (or molar density) of the component i in the bulk liquid phase and has units of $kmol - m^{-3}$.

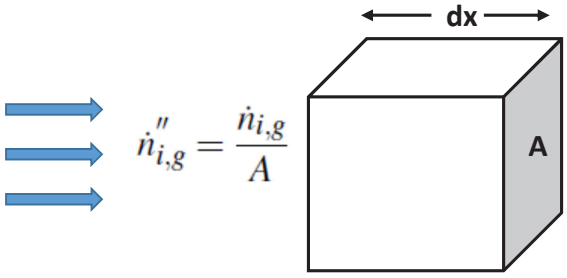

Figure 3.3: Flow of gas-bubble entrained bulk liquid electrolyte through packed bed reactor.

The concentration of the component i in the liquid phase that is in equilibrium with the gas phase (bubble) can be related to the partial pressure of the component which can then be related to molar density of the component in the gas phase. The equilibrium relationship between concentrations of species in gas and liquid phase is given from the Henry's Law $\bar{\rho}^*_{i,l} = H_i P_{i,g}$ where H_i is the Henry's Law constant of the species i, $P_{i,g}$ is the partial pressure of species i, and $\bar{\rho}^*_{i,l}$ is the concentration of the species i in the liquid phase that is in equilibrium with the gas phase. The situation is shown in figure 3.4. Here the Henry's Law constant can have units of $kmol - m^{-3} - kPa^{-1}$ if the partial pressure of the components species is in kPa and the equilibrium concentration carries units of $kmol - m^{-3}$.

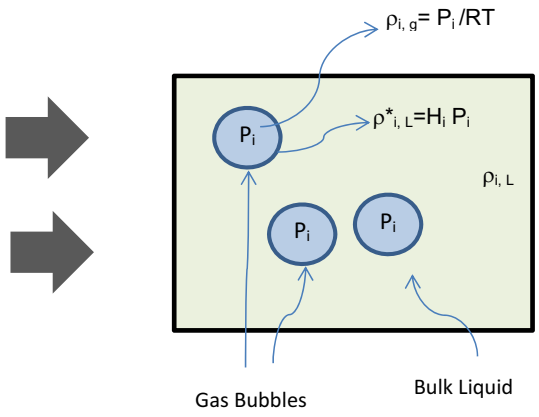

Figure 3.4: Schematic of presence of bubbles in the liquid electrolyte and showing relationship between concentrations in gas-bubble phase, bulk liquid and concentration at the bulk liquid-bubble interface (equilibrium).

This relationship essentially holds true at the surface of the entrained gas bubble within the flowing liquid and represents equilibrium between the bulk liquid phase and the gaseous phase inside the bubble. Since, $P_{ig} = \bar{\rho}_{i,g}\bar{R}T$ the above relationship can also be written as:

$$\bar{\rho}^{*}_{i,l} = H_i \bar{\rho}_{i,g} \bar{R} T \tag{3.57}$$

The molar flux ($\dot{n}''_{i,g}$) includes both convected by main flow and that which is axially diffused by turbulence or molecular diffusion. This can be written as:

$$\dot{n}''_{i,g} = \underbrace{u_g \bar{\rho}_{i,g}}_{Convection\,Term} - \underbrace{D_{Axg} \frac{d\bar{\rho}_{i,g}}{dx}}_{Axial\,diffusion\,term} \tag{3.58}$$

where u_g is the gas superficial velocity in m/s and D_{Axg} is the axial diffusion term.

However, it's seen that gas superficial velocities (u_g) are of the order of $10^{-3} - 10^{-2}$ m/s, and gas molar densities ($\bar{\rho}_{i,g}$) of the order of 10^{-3} $kmol/m^3$. So the

convective first term is of the order of $10^{-6} - 10^{-5}$. Axial (Molecular) diffusion (D_{Axg}) is of the order of $10^{-9}\ m^2/s$ and the derivative term is much smaller which makes the whole axial diffusive term (due to molecular diffusion) small and therefore can be neglected.

The superficial velocity of the gases, therefore, can be easily calculated by considering the sum of the molar fluxes of all gas species. For the case of cathode, this would mean sum of the molar fluxes of CO_2, O_2 and N_2. This is further discussed in the later section on model development for the cathode bed.

3.3.2 Liquid and Solid Phase Equations

The governing equations in the liquid-phase are similarly written using the approach by Herrmann and Emig [1998] by including the liquid-solid mass transport term in addition to the flux transport from/to the gas-bubble phase.

$$\frac{d\dot{n}''_{i,l}}{dx} = +K_{g\to l,i}A'''_{\mathrm{b}}\left(\bar{\rho}^{*}_{i,g} - \bar{\rho}_{i,l}\right) - K_{l\to s,i}A'''_{s}\left(\bar{\rho}_{i,l} - \bar{\rho}_{i,s}\right) \tag{3.59}$$

The axial diffusion term is neglected as explained before. For the electrochemical reaction, the second term can also be written as:

$$\bar{\rho}_{i,s} = \bar{\rho}_{i,l} - \frac{i''_s}{zFK_{l\to s,i}} \tag{3.60}$$

using which the mole flux of component in liquid phase can be written as:

$$\frac{d\dot{n}''_{i,l}}{dx} = +K_{g\to l,i}A'''_{\mathrm{b}}\left(\bar{\rho}^{*}_{i,g} - \bar{\rho}_{i,l}\right) - \left(\frac{A'''_s i''_s}{zF}\right) \tag{3.61}$$

where A'''_s is the grid surface area per unit volume of the bed where the reaction takes place and can be calculated geometrically if grid configuration is known. i''_s is

the charge transfer current per unit area of reactive surface, development of which is given in section on electrode kinetics. zF shows the amount of charge passed in the proceeding reaction, where z is the number of electrons transferred and F is the Faraday constant.

3.4 Upflow in Packed Bed Cathode

The reaction taking place at the cathode is:

$$\mathrm{O_2} + 2\mathrm{CO_2} + 4\mathrm{e^-} \longrightarrow 2\mathrm{CO_3}^{2-} \tag{3.62}$$

The packed bed cathode has a structure that allows flow of gases and electrolyte while the cathode structure remains electrically connected. The concept for cathode design is a stack of screens or perforated plates, spaced and supported by vertical rods that double as electron conductors as illustrated in figure 3.5 and 3.6. The outer electrode vessel is in contact with the electrode plates and thus forms part of the electrode, but its contribution to the reaction will be small and has been neglected.

The anode and cathode vessels are separated by an electrically insulated joint. The molten salt electrolyte along with the CO_2 and the air is pumped upward through the cathode packed bed. The reaction of CO_2 and O_2 produces carbonate ion CO_3^{2-} which travels down by ionic conduction towards the anode. The gases CO_2 and O_2 diffuse through the molten salt to reach the electrode reaction sites where the reaction takes place. There is mass transfer of CO_2 and O_2 occurring from the gas bubble to the bulk electrolyte and mass transfer of CO_2 and O_2 from the bulk electrolyte to the electrode surface.

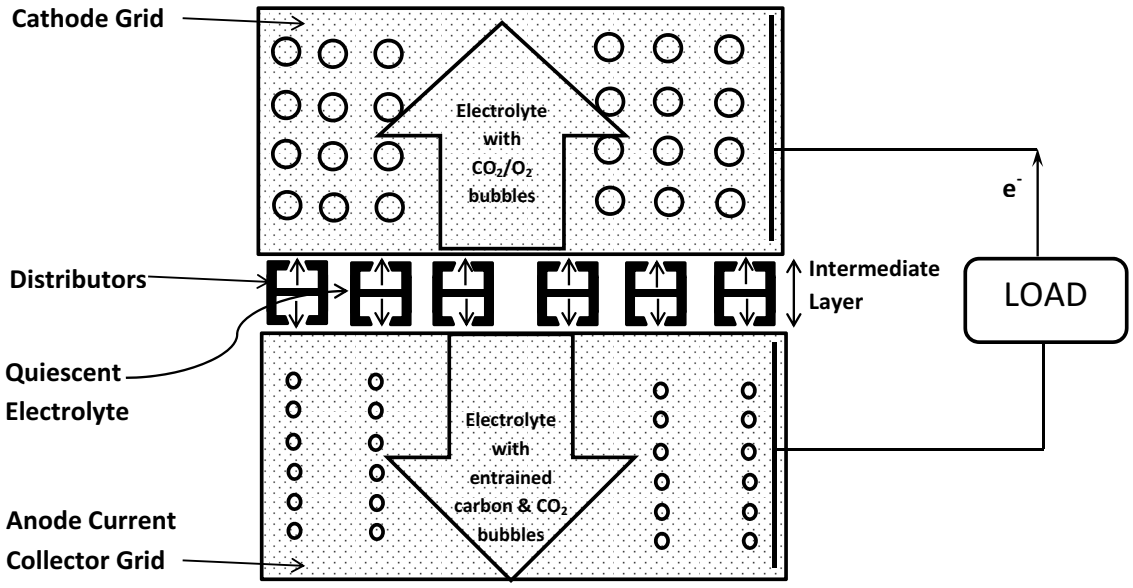

Figure 3.5: Fuel Cell schematic showing cathode/anode bed with electrolyte entrained with carbon (anode) and gas bubbles, and distributor channels in the intermediate layer.

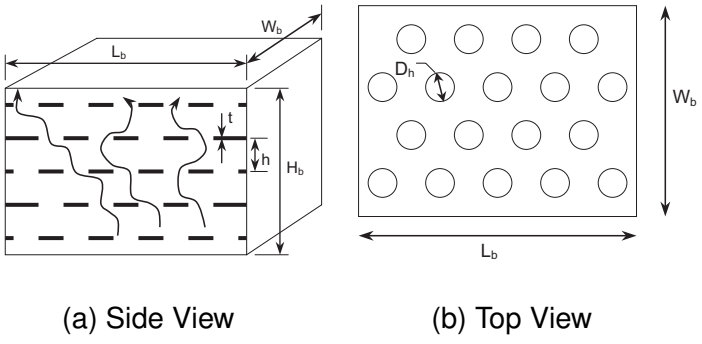

Figure 3.6: Schematic of a possible cathode packed bed arrangement using wiremesh or perforated plates as the packing material

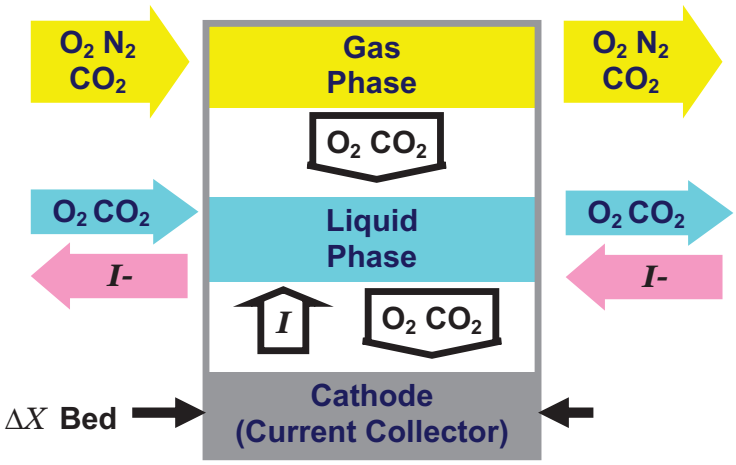

Figure 3.7: Cathode Model showing the Dependent and Independent Variables.

The model for the cathode, schematically shown in Figure 3.7, is written with distance into the cathode as independent variable and with six dependent variables that are:

- molar CO_2 flux in the gas phase, $\dot{n}''_{\mathrm{co_2,g,c}}$
- molar CO_2 flux in the liquid phase, $\dot{n}''_{\mathrm{co_2},\ell,\mathrm{c}}$
- molar O_2 flux in the gas phase, $\dot{n}''_{\mathrm{o_2,g,c}}$
- molar O_2 flux in the liquid phase, $\dot{n}''_{\mathrm{o_2},\ell,\mathrm{c}}$
- ionic current density in the liquid phase, i''_{c}
- electrolyte voltage, V_{c}

3.4.1 Model assumptions and limitations

The following assumptions have been made while modeling the electrochemical processes within the cathode bed:

1. It is assumed that the electrochemical reaction for cathode takes place on the grid packing surface that also act as the current collector. The grid packing would be completely submerged and flooded with the entrained flow of gas bubbles in the molten salt electrolyte.
2. There is a net CO_2 mass transport from the gas bubble phase into the bulk liquid and further onto the grid surface to form carbonate ions after reaction with O_2.

3. The packed bed grid serve as the current collector and also as a mechanism to enhance mass transfer within the bed.

4. Mole fractions of gas do not change dramatically within the thickness of the bed owing to large capacity of molten carbonate to hold gases like CO_2 and O_2. Therefore, liquid at the cathode inlet can be assumed to be saturated with the entering gas.

5. Relatively small amount of liquid O_2 diffuses from the cathode inlet into the anode reacting with carbon at anode inlet to form bubble nucleation.

6. N_2 remains invariant due to low solubility and inert nature as the gases pass through the bed thickness.

3.4.2 Modeling Cathode Packed Bed through linear ODE's

A gas volumetric flow rate is arbitrarily assumed per cm^2 cross-sectional area in the cathode bed. The base case operating value is assumed to be $F_v = 0.1\, m^3/hr$. This gives a gas superficial velocity of $\approx 0.28 m/s$ which is a reasonable value for co-current flow of gas-liquid in packed beds. The base case gas composition at the cathode inlet is assumed to be $y_{co_2,ic} = 0.2$ mole % for CO_2 and the rest to be air that evaluates to O_2 mole fraction of $y_{o_2,ic} = 0.168$ and remaining $y_{N_2,ic} = 0.632$ for N_2. Parametric effects on the cell performance with variation in gas volumetric flow rate, CO_2 mole fraction and O_2 mole fraction are observed in results section. The molecular weight of the gas mixture can be estimated from stoichiometric relation, $MW_{gasmix} = y_{co_2,ic} \times 44.01 + y_{o_2,ic} \times 32 + y_{N_2,ic} \times 28$. Gas mixture density can

be estimated from:

$$\rho_{gasmix} = \frac{0.001\, P_{atm} MW_{gasmix}}{RT} \qquad [\frac{kg}{m^3}] \tag{3.63}$$

The total mole flow of gases is:

$$\dot{n}''_{total,\mathrm{g,c}} = \frac{\rho_{gasmix} F_v}{MW_{gasmix} A_{cell} 3600} \qquad [\frac{kmol}{m^2 - sec}] \tag{3.64}$$

The simultaneous first-order ordinary differential equations (ODE's) in the cathode bed are presented below. These equations are solved with bed thickness as the independent variable. The dependent variables are described below.

Mole Flux of CO_2 in the Gas (Bubble) Phase ($\dot{n}''_{\mathrm{co_2,g,c}}$):

This dependent variable indicates the mole rate of transport of gaseous CO_2 per unit cross-sectional area of the packed bed. The derivative of flux is proportional to the driving force between the concentration in the bulk liquid phase and concentration of CO_2 in the liquid phase which is in equilibrium with the gas phase (defined by Henry's law). The ODE for CO_2 mole flux in the gas phase is:

$$\frac{d\dot{n}''_{\mathrm{co_2,g,c}}}{dx_{\mathrm{c}}} = -K_{\mathrm{co_2,g-\ell,c}} A'''_{\mathrm{b,c}} \left(\frac{\bar{R}T}{H_{\mathrm{co_2}}} \bar{\rho}_{\mathrm{co_2,g,c}} - \bar{\rho}_{\mathrm{co_2},\ell,\mathrm{c}} \right) \tag{3.65}$$

The initial condition (at $x_c = 0$) is:

$$\left. \dot{n}''_{\mathrm{co_2,g,c}}(x_c) \right|_{x_c=0} = y_{\mathrm{co_2},ic}\, \dot{n}''_{total,\mathrm{g,c}} \tag{3.66}$$

The mole fraction for CO_2 within the bed can be estimated from:

$$y_{\mathrm{co_2}}(x) = \left(\frac{\dot{n}''_{\mathrm{co_2,g,c}}(x)}{\dot{n}''_{\mathrm{co_2,g,c}}(x) + \dot{n}''_{\mathrm{o_2,g,c}}(x) + \dot{n}''_{\mathrm{N_2,g,c}}(x)} \right) \tag{3.67}$$

Mole Flux of O_2 in the Gas (Bubble) Phase ($\dot{n}''_{\mathrm{o}_2,\mathrm{g,c}}$):

This dependent variable indicates the mole rate of transport of gaseous O_2 per unit cross-sectional area of the packed bed. The derivative of flux is proportional to the driving force between the concentration in the bulk liquid phase and concentration of O_2 in the liquid phase which is in equilibrium with the gas phase (defined by Henry's law). The ODE for O_2 mole flux in the gas phase is:

$$\frac{d\dot{n}''_{\mathrm{o}_2,\mathrm{g,c}}}{dx_\mathrm{c}} = -K_{\mathrm{o}_2,\mathrm{g}-\ell,\mathrm{c}} A'''_{\mathrm{b,c}} \left(\frac{\bar{R}T}{H_{\mathrm{o}_2}} \bar{\rho}_{\mathrm{o}_2,\mathrm{g,c}} - \bar{\rho}_{\mathrm{o}_2,\ell,\mathrm{c}} \right) \tag{3.68}$$

The initial condition (at $x_c = 0$) is:

$$\left. \dot{n}''_{\mathrm{o}_2,\mathrm{g,c}}(x_c) \right|_{x_c=0} = y_{\mathrm{o}_2,ic}\, \dot{n}''_{total,\mathrm{g,c}} \tag{3.69}$$

The mole fraction for O_2 within the bed can be estimated from:

$$y_{\mathrm{o}_2}(x) = \left(\frac{\dot{n}''_{\mathrm{o}_2,\mathrm{g,c}}(x)}{\dot{n}''_{\mathrm{co}_2,\mathrm{g,c}}(x) + \dot{n}''_{\mathrm{o}_2,\mathrm{g,c}}(x) + \dot{n}''_{\mathrm{N}_2,\mathrm{g,c}}(x)} \right) \tag{3.70}$$

Mole Flux of CO_2 in the Bulk Liquid Phase ($\dot{n}''_{\mathrm{co}_2,\ell,\mathrm{c}}$):

This dependent variable indicates the mole rate of transport of liquid CO_2 per unit cross-sectional area of the packed bed. Liquid Mole flux is decreased by the reaction rate due to transport from the bulk liquid phase to the grid surface in proportion to the ionic current produced at cathode. The ODE is:

$$\frac{d\dot{n}''_{\mathrm{co}_2,\ell,\mathrm{c}}}{dx_\mathrm{c}} = K_{\mathrm{co}_2,\mathrm{g}-\ell,\mathrm{c}} A'''_{\mathrm{b,c}} \left(\frac{\bar{R}T}{H_{\mathrm{co}_2}} \bar{\rho}_{\mathrm{co}_2,\mathrm{g,c}} - \bar{\rho}_{\mathrm{co}_2,\ell,\mathrm{c}} \right) - \left(\frac{A'''_{\mathrm{s,c}} i''_{\mathrm{s,c}}}{2F} \right) \tag{3.71}$$

For the initial conditions, saturated conditions at the cathode inlet is assumed. Due to high holding capacity of molten salt for CO_2, no significant variation in the gas

phase mole fraction is observed and therefore conditions at the cathode outlet are also very close to saturation. The initial condition is:

$$\left[\dot{n}''_{\mathrm{co}_2,\ell,\mathrm{c}}\right]_{x_c=0} = \frac{[y_{\mathrm{co}_2}]_{x_c=0}\, P_{atm}}{H_{\mathrm{co}_2}} U_{0L,c} \tag{3.72}$$

where gaseous mole fraction of CO_2, y_{co_2} at $x_c = 0$ is used from above.

Mole Flux of O_2 in the Bulk Liquid Phase ($\dot{n}''_{\mathrm{o}_2,\ell,\mathrm{c}}$):

This dependent variable indicates the mole rate of transport of O_2 per unit cross-sectional area of the packed bed. Liquid Mole flux is decreased by the reaction rate due to transport from the bulk liquid phase to the grid surface in proportion to the ionic current produced at cathode. The ODE is:

$$\frac{d\dot{n}''_{\mathrm{o}_2,\ell,\mathrm{c}}}{dx_{\mathrm{c}}} = K_{\mathrm{o}_2,\mathrm{g}-\ell,\mathrm{c}} A'''_{\mathrm{b,c}} \left(\frac{\bar{R}T}{H_{\mathrm{o}_2}} \bar{\rho}_{\mathrm{o}_2,\mathrm{g,c}} - \bar{\rho}_{\mathrm{o}_2,\ell,\mathrm{c}}\right) - \left(\frac{A'''_{\mathrm{s,c}} i''_{\mathrm{s,c}}}{4F}\right) \tag{3.73}$$

For the initial conditions, saturated conditions at the cathode inlet is assumed. Due to high holding capacity of molten salt for O_2, no significant variation in the gas phase mole fraction is observed and therefore conditions at the cathode outlet are also very close to saturation. The initial condition is:

$$\left[\dot{n}''_{\mathrm{o}_2,\ell,\mathrm{c}}\right]_{x_c=0} = \frac{[y_{\mathrm{o}_2}]_{x_c=0}\, P_{atm}}{H_{\mathrm{o}_2}} U_{0L,c} \tag{3.74}$$

where gaseous mole fraction of O_2, y_{o_2} at $x_c = 0$ is used from above.

Electrolyte Voltage, V_c:

The fifth equation represents the Ohm's law in the ionic solution and the dependent variable is a function of ionic current (reaction rate) and the resistivity of the bed.

It is posited that, the ionic current is maximum at x=0, and goes to zero at the end of the bed. And therefore electrolyte voltage at x=0 is '0' which is also the initial condition. The ODE is:

$$\frac{dV_{\mathrm{c}}}{dx_{\mathrm{c}}} = -i_c'' R_c \tag{3.75}$$

The effective resistivity of the cathode bed, R_c, that includes the effect of grid and gas bubbles on the electrolyte resistance is calculated through the use of Bruggemann's equation from De La Rue and Tobias [1959] and shown in table 3.3. According to the Bruggeman equation in [De La Rue and Tobias, 1959], the resistivity of a bed of mixed materials depends on the resistivity of both materials. In the case of the cathode bed, however, the conductivity of the gas phase is negligible relative to that of the molten salt. While the solid cathode bed material is electronically conductive, it has no ionic conductivity. This gives us the simplified version of the Bruggeman's equation in Table 3.3. In the correlation, ε_g is a combination of solid volume fraction and gas volume fraction, and so is determined from the gas holdup and the known bed properties. Correlations for K_{salt} as a function of temperature and composition are covered in the thermodynamic properties section.

And the initial condition is:

$$|V_c|_{x_c=0} = (1-\beta)\cdot(V_{oc} - V_{\mathrm{cell}}) \tag{3.76}$$

where β is arbitrarily chosen factor which is sequentially iterated to force zero ionic current at the end of anode and cathode beds while also exhausting the chemical over-potential (η_a and η_c) at the end of each bed. The open circuit potential, V_{oc} is estimated from Gibbs Energy change and V_{cell} is specified as the program input.

Ionic Current, i_c'':

The sixth equation represents the relationship between the ionic current and the reaction rate in cathode. At $x_c = 0$, ionic current (current in the electrolyte) is maximum as determined by the current density in the cell for a given cell voltage. At the end of the bed, the ionic current diminishes to '0', which also signifies electrochemical reduction of the CO_2 and O_2available for reaction while also evolving equivalent moles of carbonate ions ($CO_3^=$) that migrates toward the anode bed. The ODE is:

$$\frac{di_{\mathrm{c}}''}{dx_{\mathrm{c}}} = -i_{\mathrm{s,c}}'' \, A_{\mathrm{s,c}}''' \tag{3.77}$$

The initial condition is provided by:

$$\left| i_{\mathrm{c}}'' \right|_{x_c=0} = i_0'' \tag{3.78}$$

where i_0'' is the iteratively computed ionic current density (also cell current density) that diminishes through the bed and goes to zero at $x = L_c$ due to ohmic, chemical (mass transfer) and activation polarization.

The 6 differential equations are summarized below:

CO_2 and O_2 in gas phase:

$$\frac{d\dot{n}''_{\mathrm{co_2,g,c}}}{dx_{\mathrm{c}}} = -K_{\mathrm{co_2,g-\ell,c}} A_{\mathrm{b,c}}''' \left(\frac{\bar{R}T}{H_{\mathrm{co_2}}} \bar{\rho}_{\mathrm{co_2,g,c}} - \bar{\rho}_{\mathrm{co_2,\ell,c}} \right) \tag{3.79}$$

$$\frac{d\dot{n}''_{\mathrm{o_2,g,c}}}{dx_{\mathrm{c}}} = -K_{\mathrm{o_2,g-\ell,c}} A_{\mathrm{b,c}}''' \left(\frac{\bar{R}T}{H_{\mathrm{o_2}}} \bar{\rho}_{\mathrm{o_2,g,c}} - \bar{\rho}_{\mathrm{o_2,\ell,c}} \right) \tag{3.80}$$

CO_2 and O_2 in liquid phase:

$$\frac{d\dot{n}''_{\mathrm{co_2,\ell,c}}}{dx_{\mathrm{c}}} = K_{\mathrm{co_2,g-\ell,c}} A_{\mathrm{b,c}}''' \left(\frac{\bar{R}T}{H_{\mathrm{co_2}}} \bar{\rho}_{\mathrm{co_2,g,c}} - \bar{\rho}_{\mathrm{co_2,\ell,c}} \right) - \left(\frac{A_{\mathrm{s,c}}''' i_{\mathrm{s,c}}''}{2F} \right) \tag{3.81}$$

$$\frac{d\dot{n}''_{\mathrm{o_2,\ell,c}}}{dx_{\mathrm{c}}} = K_{\mathrm{o_2,g-\ell,c}} A_{\mathrm{b,c}}''' \left(\frac{\bar{R}T}{H_{\mathrm{o_2}}} \bar{\rho}_{\mathrm{o_2,g,c}} - \bar{\rho}_{\mathrm{o_2,\ell,c}} \right) - \left(\frac{A_{\mathrm{s,c}}''' i_{\mathrm{s,c}}''}{4F} \right) \tag{3.82}$$

ΔV in molten salt:

$$\frac{dV_{\mathrm{c}}}{dx_{\mathrm{c}}} = -i_{\mathrm{c}}^{''} R_{\mathrm{c}} \tag{3.83}$$

Ionic current flux perpendicular to face of bed:

$$\frac{di_{\mathrm{c}}^{''}}{dx_{\mathrm{c}}} = i_{\mathrm{s,c}}^{''} A_{\mathrm{s,c}}^{'''} \tag{3.84}$$

3.4.3 Mass Transfer Equations for Packed Bed Cathode

Gas-Liquid Mass Transfer

The gas-liquid mass transfer coefficient is used from the work of Reiss [1967]. It's clear that the scope of their investigation is limited to air-water system with packings made of polyethylene or ceramic. The mass transfer measurements were made with the ammonia absorption and oxygen desorption systems. And if the results from this work are used for the design of systems involving other fluids, effects of fluid physical properties must be known. The pressure gradient needed for the determination of mass transfer coefficient is estimated from the work of Turpin and Huntington [1967]. It's been asserted by Reiss [1967] that scatter of data around the mass transfer equations could be as great as $\pm 50\%$. This could justify the usage of sensitivity analysis to measure the impact of mass transfer coefficients on the cell performance. The liquid side and the gas side mass transfer coefficients as given by Reiss [1967] are produced below:

$$k_L A_b^{'''} = 0.12 \left[\frac{U_{0L}}{47.88} \left(\frac{\Delta P}{\Delta Z} \right)_{LG} \right]^{0.5} \tag{3.85}$$

$$k_G A_b^{'''} = 2 + 0.91 \left[\frac{U_{0L}}{47.88} \left(\frac{\Delta P}{\Delta Z} \right)_{LG} \right]^{2/3} \tag{3.86}$$

The pressure drop term by Turpin and Huntington [1967] is:

$$\left(\frac{\Delta P}{\Delta Z}\right)_{LG} = \frac{2\rho_G f_{LG} U_{0G}^2}{d_e} \tag{3.87}$$

where U_{0L} and U_{0G} are respectively the superficial velocities of liquid and gas phase and ρ_G is the density of the gas.

Friction factor f_{LG} is estimated from Turpin and Huntington [1967] using the following equation:

$$f_{LG} = \exp\left[8.0 - 1.12\log\bar{Z} - 0.0769(\log\bar{Z})^2 + 0.0152(\log\bar{Z})^3\right] \tag{3.88}$$

The equivalent diameter of the packing from Turpin and Huntington [1967] is:

$$d_e = \frac{2}{3} d_p \frac{\varepsilon}{1-\varepsilon} \tag{3.89}$$

These correlations are also summarized in table 3.3. The superficial velocities used in the correlations are all in m/sec. The molten salt superficial velocity, U_{0L}, is an input parameter and is set within the range of 0.05-0.15 m/s. The gas superficial velocity, U_{0G}, is determined from gas flux and ideal gas density,

$$U_{0G} = \left(\dot{n}''_{\mathrm{co_2,g,c}} + \dot{n}''_{\mathrm{o_2,g,c}} + \dot{n}''_{\mathrm{n_2,g,c}}\right) \frac{\bar{R}T}{P_{\mathrm{atm}}} \tag{3.90}$$

where the molar fluxes of CO_2 ($\dot{n}''_{\mathrm{co_2,g,c}}$) and O_2 ($\dot{n}''_{\mathrm{o_2,g,c}}$) in the gas phase, are determined from the solution of the differential equations and the molar flux of N_2 ($\dot{n}''_{\mathrm{n_2,g,c}}$) is same as that used for the inlet conditions. The net gas-liquid mass transfer coefficient is obtained by combining gas-side and liquid-side coefficients:

$$K_{\mathrm{g}-\ell,\mathrm{c}} A'''_{\mathrm{b,c}} = \frac{1}{\left(1/k_L A'''_b + 1/k_G A'''_b\right)} \tag{3.91}$$

The Gas-Liquid Mass Transfer Coefficients for each gas, $(K_{\mathrm{co_2,g}-\ell,\mathrm{c}}\, A'''_{\mathrm{b,co_2,c}})$ and $(K_{\mathrm{o_2,g}-\ell,\mathrm{c}} A'''_{\mathrm{b,o_2,c}})$ for CO_2 and O_2 respectively, can then be found from the individual gas properties.

Table 3.3: Correlations Used for the Cathode Packed Bed

Parameter	Description	Correlation	Remarks	References
h_G	Gas Holdup	$h_G = \dfrac{1}{1+4.33\,(100\times U_{0L})^{-0.433}\left(\dfrac{U_{0L}}{U_{0G}}\right)^{0.563}}$		Achwal and Stepanek [1976]
h_L	Liquid Holdup	$h_L = 1 - h_G$		
f_{LG}	Two-phase friction factor	$f_{LG} = \exp\left[8.0 - 1.12\log\bar{Z} - 0.0769(\log\bar{Z})^2 + 0.0152(\log\bar{Z})^3\right]$	$\bar{Z} = \dfrac{Re_G^{1.167}}{Re_L^{0.767}}$	Turpin and Huntington [1967]
		where $Re_G = \dfrac{U_{0G}d_p}{\nu_G}$ and $Re_L = \dfrac{U_{0L}d_p}{\nu_L}$		
$\left(\dfrac{\Delta P}{\Delta Z}\right)_{LG}$	Pressure Gradient	$\left(\dfrac{\Delta P}{\Delta Z}\right)_{LG} = \dfrac{2\rho_G f_{LG} U_{0G}^2}{d_e}$	$d_e = \dfrac{2}{3}d_p\dfrac{\varepsilon}{1-\varepsilon}$	Turpin and Huntington [1967]
$k_L A_b'''$	Liquid side mass transfer coefficient	$k_L A_b''' = 0.12\left[\dfrac{U_{0L}}{47.88}\left(\dfrac{\Delta P}{\Delta Z}\right)_{LG}\right]^{0.5}$		Reiss [1967]
$k_G A_b'''$	Gas side mass transfer coefficient	$k_G A_b''' = 2 + 0.91\left[\dfrac{U_{0L}}{47.88}\left(\dfrac{\Delta P}{\Delta Z}\right)_{LG}\right]^{2/3}$		Reiss [1967]
Sh	Sherwood number	$Sh = 3.02\left(0.7 + 0.12\left[\dfrac{U_G(1-h_G)}{U_L h_G}\right]^{0.62}\right)\left(\dfrac{Re_L^* S_c d_e}{\delta}\right)^{1/3}$	$U_L = U_{0L}/(1-\zeta_c)$	Kirillov and Nasamanyan [1976]
		where $Re_L^* = \dfrac{U_L d_e}{2\nu_L(1-h_G)}$ and $\delta = 0.15\,d_p\left(\dfrac{U_G^2}{g d_p}\right)^{-0.1}$	$U_G = U_{0G}/(1-\zeta_c)$	
R_c	Resistivity	$R_c = \dfrac{1}{K_{salt}}(1-\varepsilon_{g,c})^{-3/2}$	$\varepsilon_{g,c} = h_G(1-\zeta_c)+\zeta_c$	Tobias [1966]

Liquid-Solid Mass Transfer

As discussed earlier in the kinetics section, the concentration of gaseous species, CO_2 and O_2 on the grid surface (reaction site) is a function of bulk liquid concentration, charge-transfer current density, and the liquid-solid mass transfer coefficient as evident from equations reproduced from before:

$$\bar{\rho}_{\mathrm{co}_2,\mathrm{s,c}} = \bar{\rho}_{\mathrm{co}_2,\ell,\mathrm{c}} - \frac{i''_{\mathrm{s,c}}}{2Fk_{\ell\text{-s,co}_2}}$$

$$\bar{\rho}_{\mathrm{o}_2,\mathrm{s,c}} = \bar{\rho}_{\mathrm{o}_2,\ell,\mathrm{c}} - \frac{i''_{\mathrm{s,c}}}{4Fk_{\ell\text{-s,o}_2}}$$

The bulk liquid concentrations are determined from the solution of differential equations. The charge transfer current density equation is also a function of surface concentrations as shown by Butler-Volmer type kinetic equation 3.31. Due to this interdependence of variables, charge-transfer current density is estimated using iterative algorithm. The liquid-solid mass transfer links these set of equations to the solution of differential equations through bulk liquid concentrations.

The liquid-solid mass transfer coefficient is estimated from correlation in the literature provided by Kirillov and Nasamanyan [1976]. The correlation was developed looking at the mass transfer between liquid and the packing for a three-phase fixed bed configuration. Steady-state experiments were conducted to measure decrease in weight of soluble control solids placed in a bed of similar particles. Gas velocities ranged from 0-0.5 m/sec and the liquid velocities varied over 0.0001 - 0.02 m/sec. Even though the liquid superficial velocities in the present work are considered around 0.1 m/s, it's possible to address the arising uncertainties in the evaluation of mass transfer coefficient in the sensitivity analysis. Experimental data was empirically correlated to generate the following equation for the Sherwood

number:

$$Sh = 3.02\left(0.7+0.12\left[\frac{U_G(1-h_G)}{U_L h_G}\right]^{0.62}\right)\left(\frac{Re_L^* S_c d_e}{\delta}\right)^{1/3} \tag{3.92}$$

and from the knowledge of bed void fraction, gas/liquid hold-ups, and the superficial gas/liquid velocities, liquid-solid mass transfer coefficient in the cathode can be determined:

$$K_s = \frac{Sh\,D}{d_e/2} \tag{3.93}$$

where D is the molecular diffusivity of the solute (CO_2 and O_2) in the molten salt.

The gas hold-up (h_G) is based off of the work of Achwal and Stepanek [1976], where electrical conductivity measurement techniques were employed to investigate hold-up profiles in packed bubble columns with co-current gas-liquid flow. Gas superficial velocities in the range of 0-0.5 m/s and liquid superficial velocities of 0.004 - 0.07 m/s were used. The system tested was of air-water and sodium chloride was used to vary electrical conductivity of the solution.

$$h_G = \frac{1}{1+4.33\,(100\times U_{0L})^{-0.433}\left(\frac{U_{0L}}{U_{0G}}\right)^{0.563}} \tag{3.94}$$

The correlations are also summarized in the table 3.3.

3.4.4 Molar Density equations:

Molar density of CO_2 in gas phase is calculated from the ideal gas law and the mole fraction CO_2. The molar density of CO_2 in the liquid phase is calculated from

mole fraction CO_2 and salt density. Units are $kmol/m^3$:

$$\bar{\rho}_{\mathrm{co_2,g,c}} = \left(\frac{\dot{n}''_{\mathrm{co_2,g,c}}}{\dot{n}''_{\mathrm{co_2,g,c}} + \dot{n}''_{\mathrm{o_2,g,c}} + \dot{n}''_{\mathrm{N_2,g,c}}} \right) \left(\frac{101.325}{\bar{R}T} \right) \tag{3.95}$$

$$\bar{\rho}_{\mathrm{co_2},\ell,\mathrm{c}} = \left(\frac{\dot{n}''_{\mathrm{co_2},\ell,\mathrm{c}}}{\dot{n}''_{\mathrm{co_2},\ell,\mathrm{c}} + \dot{n}''_{\mathrm{o_2},\ell,\mathrm{c}} + \dot{n}''_{L}} \right) \bar{\rho}_{\mathrm{salt}} \tag{3.96}$$

Molar density of O_2 is calculated in the same way as that of CO_2:

$$\bar{\rho}_{\mathrm{o_2,g,c}} = \left(\frac{\dot{n}''_{\mathrm{o_2,g,c}}}{\dot{n}''_{\mathrm{co_2,g,c}} + \dot{n}''_{\mathrm{o_2,g,c}} + \dot{n}''_{\mathrm{N_2,g,c}}} \right) \left(\frac{101.325}{\bar{R}T} \right) \tag{3.97}$$

$$\bar{\rho}_{\mathrm{o_2},\ell,\mathrm{c}} = \left(\frac{\dot{n}''_{\mathrm{o_2},\ell,\mathrm{c}}}{\dot{n}''_{\mathrm{co_2},\ell,\mathrm{c}} + \dot{n}''_{\mathrm{o_2},\ell,\mathrm{c}} + \dot{n}''_{L}} \right) \bar{\rho}_{\mathrm{salt}} \tag{3.98}$$

3.5 Downflow in Packed Bed Anode

The equation for the CO_2 production is:

$$C + 2CO_3^{2-} \longrightarrow 3CO_2 + 4e^- \tag{3.99}$$

The equation for the CO production is:

$$2C + CO_3^{2-} \longrightarrow 3CO + 2e^- \tag{3.100}$$

As in the cathode, the packed bed anode consists of an electrically-connected porous bed. The openings in the bed allow passage of molten salt with carbon particles and generated gases entrained. Unlike the cathode bed, which acted as an electrode, the anode bed acts only as a current collector. The carbon particles themselves act as the anode, exchanging electronic current with each other and with the bed through collisions as shown in Figure 3.8. Carbon entrained in

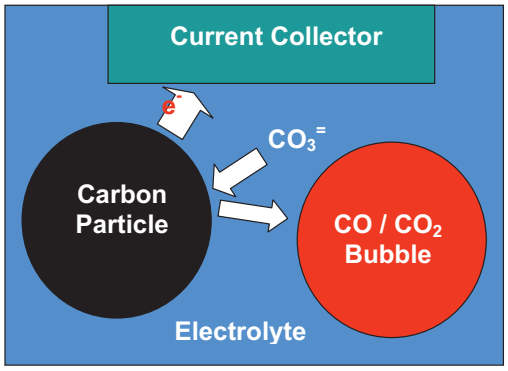

Figure 3.8: Carbon particle exchanging current with the bed.

the molten salt is pumped downward into the bed through the electrode plates. The carbonate ion, CO_3^{2-}, traveling from the cathode to anode through ionic conduction, diffuses through the molten salt electrolyte and reacts on the surface of

the anode carbon to form CO and CO_2, the ratio depending upon the chemical equilibrium and kinetics. The downward velocity of the electrolyte is such that the entrained carbon (lighter than molten salt) and the formed CO/CO_2 are kept flowing downwards. As explained previously, the analysis done so far neglects the production of CO and considers only the production of CO_2.

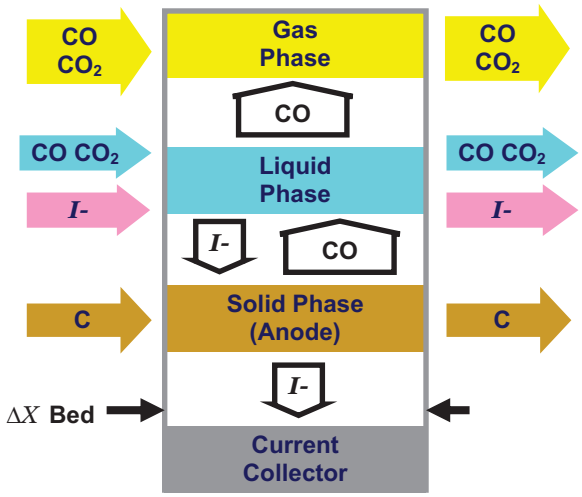

Figure 3.9: Anode Model showing the Dependent and Independent Variables.

The model for the anode, schematically shown in Figure 3.9, is written with distance into the anode as independent variable and with five dependent variables that are:

- molar CO_2 flux in the gas phase, $\dot{n}''_{\mathrm{co_2,g,a}}$
- molar CO_2 flux in the liquid phase, $\dot{n}''_{\mathrm{co_2},\ell,\mathrm{a}}$
- mole flux solid carbon, $\dot{n}''_{c,s,a}$
- electrolyte voltage, V_{a}

- ionic current density in the liquid phase, i''_{a}

3.5.1 Model assumptions and limitations

The following assumptions have been made while modeling the electrochemical processes within the anode bed:

1. It is assumed that the electrochemical reaction for a direct carbon type of fuel cell takes place on the surface of the carbon particle, possibly within the crevices and pores that are exposed and wetted by the molten carbonate electrolyte.

2. From assumption 1, it follows that the CO_2 mass transport takes place from the surface pores into the bulk liquid film that is in contact with the carbon particle and then some from the bulk liquid into the gas phase (bubbles).

3. It is assumed that the packed bed grid in the anode serve as the current collector and possibly as a mechanism to enhance mass transfer within the bed.

4. It is assumed that the carbon particle comes into contact with the packed bed grid (serving as the current collector). Figure 3.8 shows interaction of carbon particle with the bubble packed bed.

5. 100 % CO_2 evolution is assumed as indicated by Weaver et al. [1979], Vutetakis [1985]. Accordingly, cell temperature is maintained below 973 K.

3.5.2 Modeling Anode Packed Bed through linear ODE's

The simultaneous first-order ordinary differential equations (ODE's) in the anode bed are presented below. These equations are solved using MATLAB ODE45 solver and involve bed thickness as the independent variable whereas the dependent variables are described as below:

Mole Flux of CO_2 in the Gas (Bubble) Phase ($\dot{n}''_{\mathbf{co}_2,\mathrm{g,a}}$):

This dependent variable indicates the mole rate of production of gaseous CO_2 per unit cross-sectional area of the packed bed. The derivative of flux is dependent upon the driving force between the concentration in the bulk liquid phase and concentration of CO_2 in the liquid phase which is in equilibrium with the gas phase (defined by Henry's law). The ODE is given as:

$$\frac{d\dot{n}''_{\mathrm{co}_2,\mathrm{g,a}}}{dx_{\mathrm{a}}} = -K_{\mathrm{co}_2,\mathrm{g}-\ell,\mathrm{a}} A'''_{B,\mathrm{co}_2,\mathrm{a}} \left(\bar{\rho}^{*}_{\mathrm{co}_2,\mathrm{a}} - \bar{\rho}_{\mathrm{co}_2,\ell,\mathrm{a}}\right) \tag{3.101}$$

where the equilibrium concentration ($\bar{\rho}^{*}_{\mathrm{co}_2,\mathrm{a}}$) is evaluated at the interface of the bulk liquid and the gas bubble. By definition, the equilibrium concentration of CO_2 is estimated using Henry's Law, i.e.

$$\bar{\rho}^{*}_{\mathrm{co}_2,\mathrm{a}} = P_{\mathrm{co}_2} H_{\mathrm{co}_2} \tag{3.102}$$

where P_{co_2} is the partial pressure of CO_2 in the gas bubble and in the absence of carbon-monoxide (assuming cell operation stays below the temperature of 973 K) or any purge inert gas is equal to 1 atm or 101.325 kPa.

The Henry's law coefficient as given in previous sections using empirical equations from Wilemski [1983] and has units of $kmol/m^3 - kPa$.

The resulting equilibrium concentration for CO_2 has units of $kmol/m^3$.

The initial condition for this variable is defined by making few assumptions. Firstly, under steady-state conditions, it can be assumed that the molten salt electrolyte that is circulated within the anode bed is typically under CO_2 saturated conditions at the feed inlet which is the top part of the bed. Now, due to production of CO_2 through the chemical reaction within the anode bed, the molten salt electrolyte coming out from the bottom of the bed should be in a state of slight super-saturation. This assumption is also reinforced by hypothesis of Yasuda in Weaver et al. [1979][Appendix A] where the author does believe the state of super-saturation near the vicinity of electrodes where the anode reaction takes place. The electrolyte is super-saturated in the vicinity of the reaction surface sites and the concentration in the bulk liquid electrolyte liquid is dictated by the mass-transfer from the reaction surface to the bulk liquid. Similarly, the mass transfer from bulk liquid to the gas phase will be responsible for the growth of gas bubbles. The nucleation of bubbles is however, a separate matter for discussion.

The physics of bubble nucleation in the electrolytic cells can be considerably important if the gas evolution is quite significant and large size bubbles are formed in the bed during the cell operation. The gas bubbles have a tendency to block the ionic conduction path through the electrolyte and essentially adds to the ionic resistance in addition to the packing material. Therefore, gas bubble evolution and characterization through the use of gas-holdup estimation might be useful for predicting correct fuel cell performance.

For the carbon anode bed in the present investigation, the initial conditions for CO_2 in the gas phase should be evaluated from assuming diffusion of O_2 from the electrolyte in the cathode bed at the feed inlet through the intermediate electrolyte

layer and cross-over into the anode causes direct oxidation of carbon forming CO_2 which could be considered as one contributor for CO_2 bubble nucleation in the anode.

It is anticipated that the CO_2 gas evolution does not instantly start from zero at the start of bed but from nucleation arising from the diffusion of liquid O_2 from cathode inlet through the intermediate electrolyte (electrochemically separating cathode and anode beds) and into the anode bed where at x = 0, all the liquid O_2 chemically reacts with the carbon to produce the CO_2. The amount of CO_2 produced from this reaction determines the initial condition for mole flux of CO_2 in the gas phase for the anode bed. The initial condition (at x_a = 0) is given as:

$$\left|\dot{n}''_{\mathrm{co_2,g,a}}(x_a)\right|_{x_a=0^+} = \left|\dot{n}''_{\mathrm{O_2},l,c}(x_c)\right|_{x_c=0^-} \tag{3.103}$$

And from the equation presented for the initial conditions in cathode, we get,

$$\left|\dot{n}''_{\mathrm{co_2,g,a}}\right|_{x_a=0^+} = \frac{D_{\mathrm{o_2}}}{L_{int}} \left|\bar{\rho}^*_{\mathrm{o_2,c}}\right|_{x_c=0^-} \tag{3.104}$$

Mole Flux of CO_2 in the Bulk Liquid Phase ($\dot{n}''_{\mathbf{co_2},\ell,\mathrm{a}}$):

This dependent variable indicates the mole rate of transport of CO_2 per unit cross-sectional area of the packed bed. From the differential equations, it can clearly be seen that this mole flux is increased by the solid to liquid mass transport, and decreased by the liquid-to-gas mass transport, and is proportional to the driving force between the concentration in the bulk liquid phase and concentration of CO_2 in the liquid phase which is in equilibrium with the gas phase. The ODE is given as:

$$\frac{d\dot{n}''_{\mathrm{co_2},\ell,\mathrm{a}}}{dx_{\mathrm{a}}} = K_{\mathrm{co_2,g-}\ell,\mathrm{a}} A'''_{B,\mathrm{co_2,a}} \left(\bar{\rho}_{\mathrm{co_2,g,a}} H_{\mathrm{co_2}} \bar{R}T - \bar{\rho}_{\mathrm{co_2},\ell,\mathrm{a}}\right) + \left(\frac{3}{4F}\right) A'''_{C,\mathrm{a}}\, i''_{\mathrm{s,a}} \tag{3.105}$$

The initial condition for this variable at x = 0 is from the assumption that the concentration in the liquid phase is in equilibrium with the gas phase and therefore the bulk electrolyte at x=0 is assumed a saturated liquid (with CO_2). As more gas is evolved (at the surface of carbon particle) going into the bed, more CO_2 will be transported from the carbon surface to the bulk liquid causing over-saturation and CO_2 gas bubble growth. The initial condition (at $x_a = 0$) is given by assuming that the liquid electrolyte entering the anode bed is saturated with CO_2. If CO_2 is the only gas present in the anode (assuming Boudouard equilibrium towards 100% CO_2 production and no carbon-monoxide (CO)), then the partial pressure of CO_2 is 1 atm. The molar flux is then the product of CO_2 concentration in the bulk liquid phase (in equilibrium with gas) and the superficial liquid velocity (U_{ola}). The initial condition is therefore:

$$\left|\dot{n}''_{\mathrm{co_2},\ell,\mathrm{a}}\right|_{x_a=0} = P_{\mathrm{CO_2}} H_{\mathrm{co_2}} U_{ola} = P_{atm} H_{\mathrm{co_2}} U_{ola} \tag{3.106}$$

Mole Flux of C in the Solid Phase ($\dot{n}''_{c,s,a}$):

This dependent variable indicates the mole rate of consumption of fuel (carbon/coal) per unit cross-sectional area of the packed bed. This variable is decreased by the reaction rate. Theoretically, if there is no overfeed of carbon (γ_c = 1), then the mole flux at the end of anode bed will be zero. In the present work, there is significant overfeed of carbon maintained (to achieve higher reaction rates) and the un-reacted carbon at the end of bed is recycled back into the anode after CO_2 has been separated from the electrolyte. The surface area per unit bed volume

available for reaction, $A'''_{C,\mathrm{a}}$ is given from equation 3.148. The ODE is given as:

$$\frac{d\dot{n}''_{C,S,\mathrm{a}}}{dx_{\mathrm{a}}} = -\left(\frac{1}{4F}\right) A'''_{C,\mathrm{a}}\, i''_{\mathrm{s,a}} \tag{3.107}$$

And the initial condition is given as:

$$\left|\dot{n}''_{C,\mathrm{s,a}}\right|_{x_a=0} = \gamma_C \cdot \frac{i''_0}{4F} \tag{3.108}$$

Electrolyte Voltage, V_a:

The fourth equation represents the Ohm's law in the ionic solution and the dependent variable is a function of ionic current (reaction rate) and the resistivity of the bed. It is posited that, the ionic current is maximum at x=0, and goes to zero at the end of the bed. And therefore electrolyte voltage at x=0 is '0' which is also the initial condition. The chemical over-potential is maximum at x=0 due to availability of full reaction rate and diminishes to zero at the end of the bed. The resistivity, R_a, is given from table 3.4. The ODE is given as:

$$\frac{dV_{\mathrm{a}}}{dx_{\mathrm{a}}} = -i''_{\mathrm{a}} R_{\mathrm{a}} \tag{3.109}$$

And the initial condition is given as:

$$|V_{\mathrm{a}}|_{x_a=0} = \beta \cdot (V_{\mathrm{oc}} - V_{\mathrm{cell}}) \tag{3.110}$$

where β is arbitrarily chosen factor which is sequentially iterated to force zero ionic current at the end of anode and cathode beds while also exhausting the chemical over-potential (η_a and η_c) at the end of each bed. The open circuit potential, V_{oc} is estimated from Gibbs Energy change and V_{cell} is specified as the program input.

Ionic Current, i_a'':

The fifth equation represents the relationship between the ionic current and the reaction rate in anode. At x=0, ionic current (current in the electrolyte) is maximum as determined by the current density in the cell for a given cell voltage. At the end of the bed, the ionic current diminishes to '0', which also signifies complete electrochemical oxidation of carbon available for reaction while also evolving equivalent moles of gaseous CO_2 in the electrolyte which is separated in a separate external loop. The ODE is given as"'

$$\frac{di_{\mathrm{a}}''}{dx_{\mathrm{a}}} = -i_{\mathrm{s,a}}'' A_{C,\mathrm{a}}''' \tag{3.111}$$

The initial condition is provided by:

$$\left| i_{\mathrm{a}}'' \right|_{x_a=0} = i_0'' \tag{3.112}$$

where i_0'' is the iteratively computed ionic current density (also cell current density) that diminishes through the bed and goes to zero at $x = L_a$ due to various polarizations, i.e. ohmic, chemical (mass transfer), activation, and contact resistance.

3.5.3 Slurry Properties

The effective viscosity of a slurry mixture as a function of solid fraction has been studied in the past by many researchers [Einstein, 1906, Thomas, 1965, Frankel and Acrivos, 1967, Chong et al., 1971]. The correlation from [Chong et al., 1971] is used to determine the effective viscosity of coal entrained molten carbonate slurry. The effective density of the slurry has been evaluated using conservation of mass. The slurry can be considered to be moving at roughly the same true velocity since carbon particles have almost same densities as molten carbonate.

Typical velocities for flow of slurry through packed beds can be determined from the pressure drop considerations using the work of Leva [1949]. This has also been elaborated in detail in the appendix section C. Assumption of homogenous flow of slurry has been made so as to use the correlations described further in this section.

Slurry Viscosity

The absolute viscosity of the slurry mixture as investigated by many researchers is essentially in trying to correlate a relative viscosity, μ_r in terms of the solids volume fraction, ϕ is given as:

$$\mu_r = \frac{\mu_{sl}}{\mu_l} \tag{3.113}$$

where, μ_{sl} is the absolute viscosity of the slurry mixture and μ_l is the absolute viscosity of the liquid.

For very dilute concentrations (less than 1%), a linear relationship linking the relative viscosity to the solids volume fraction is given by Einstein [1906]:

$$\mu_r = 1 + 2.5\phi \tag{3.114}$$

In developing this equation, Einstein assumed that the particles are fairly rigid and that the mixture is fairly dilute and there is no interaction between the particles.

Thomas [1965] then used Einstein's equation to develop the relative viscosity of the slurry/Newtonian mixtures for higher solid volume fraction. For concentrations of solids less than 20% he gave:

$$\mu_r = 1 + K_1\phi + K_2\phi^2 \tag{3.115}$$

where K_1 is the Einstein constant equal to 2.5 and K_2 ranges from 10.05 to 14.1.

For concentrations of solids more than 20% Thomas [1965] added an exponential component to the previous equation and got:

$$\mu_r = 1 + K_1\phi + K_2\phi^2 + A\exp(B\phi) \tag{3.116}$$

where the constants are $A = 0.00273$ and $B = 16.6$.

Frankel and Acrivos [1967] later developed an equation of the form:

$$\mu_r = 1 + C\left[\frac{(\phi/\phi_m)^{1/3}}{1-(\phi/\phi_m)^{1/3}}\right] \tag{3.117}$$

which was based on the theoretical presumption that viscous dissipation of energy, in highly concentrated suspensions, arises primarily from the flow within the narrow gaps separating the various solid spheres from one another. Also, within each gap, this flow is imposed by the relative motion of the spherical particles. In the equation, ϕ_m is the maximum attainable solids volume fraction in the suspension and C is a constant depending on the assumed geometrical arrangement of spheres and was experimentally determined to be $9/8$. This particular equation is particularly good for coal-slurry fuels and might be a good model to use for coal-molten salt slurry mixture.

However, later on Chong et al. [1971] developed an empirical equation which was supported by experimental data from broad range of sources. The equation given was:

$$\mu_r = \left[1 + 0.75\left(\frac{(\phi/\phi_m)}{1-(\phi/\phi_m)}\right)\right]^2 \tag{3.118}$$

In both the above equations, the maximum solid volume fraction is computed from the solid packing considered. For cubic packing, $\phi_m = \pi/6$ and for hexagonal packing, $\phi_m = \pi/(3\sqrt{2})$.

The absolute/dynamic viscosity of the carbon-molten carbonate slurry within the packed bed anode can now be determined using the relationship given by Chong et al. [1971]. The solid fraction (ϕ or also termed solid-holdup h_s) is assumed for the model to be between 0.19 and 0.23 due to constraints of using particle resistivity model from Kusakabe et al. [1981].

Slurry Density

The effective density of the slurry mixture can be computed using simple equation developed using material balance:

$$\rho_{sl} = h_s \rho_c + (1 - h_s)\rho_L \tag{3.119}$$

The solid-holdup as used above doesn't include the fraction of the packing grid.

Here, ρ_c is the true density of the carbon particle and for the present work the density of the pyrolitic graphite is $\approx 2200\, kg/m^3$. ρ_L is the density of the binary/ternary mixtures of the molten carbonate electrolyte that is used in the work.

3.5.4 Mass Transfer in Anode Packed Bed

The ordinary differential equations (ODE's) described in earlier sections through equations 3.101 through 3.111 utilize mass transfer coefficients to exhibit mass transport of CO_2 from the:

1. *Carbon particle surface into the bulk liquid.* CO_2 is electrochemically produced on the surface of the carbon particle. The driving force required for the mass transport of CO_2 from carbon particle surface into the bulk liquid phase is directly proportional to the difference in concentration of CO_2 in the respective

phases. The proportionality constant is what constitutes the mass transfer coefficient. The coefficient defines the rate of mass transfer (in units of m/s) and is most generally a function of liquid (molten carbonate electrolyte) velocity, and hold-ups of solid and liquid phases.

2. *Bulk liquid phase to the gas phase.* Again the proportionality constant for driving force exhibits the rate of mass transfer and generally is a function of gas and liquid velocity, and gas and liquid hold-ups.

To evaluate the two important mass transfer effects, hold-up of various phases (solid, liquid, and gas) is important.

Assumptions and Limitations

1. The flow through the anode bed can be described as a flow of slurry (containing some gas bubbles generated in the anode) through a fixed bed of some sort of packing, either plane wire-meshes or perforated plates placed perpendicular to the flow with a particular inter-spacing. It can be assumed that placing these packing perpendicular to the flow will ensure homogenous flow devoid of any channeling effects.

2. Slurry properties like density, viscosity, etc can be characterized by various equations from literature (CITE) which are described as mixed effects from the properties of alkali molten carbonate salts and the coal (or graphite).

3. Liquid/Slurry entering the anode bed is assumed to be at saturation as far as solubility of CO_2 in the molten salt is considered. CO_2 gas bubbles are formed within the anode bed through electrochemical reactions. There is no suitable

correlation in the literature that can quite define the physics of gas bubbles evolution and their growth (owing to mass transport through diffusion from bulk liquid to gas phase) in electrochemical reactors. However, preliminary calculations show that the volume fraction of the generated gas transported from the liquid phase into the gas phase maybe quite small.

4. Since densities of carbon and the molten carbonate salt are very close, no relative slip has been assumed between the movement of carbon particle and the salt.

5. Due to assumption # 3, effect of gas-holdup is assumed minimal and negligible in considering the physics of slurry flow through fixed bed to evaluate liquid-solid mass transport. Correlation for liquids flow through fixed beds is available in the literature which is assumed to be valid for flowing slurry as well. The slurry movement through the fixed bed is assumed to cause agitation effects that provide a basis for an energy dissipation term and can be evaluated using hydrodynamic calculations.

Gas-Liquid Mass Transfer:

The anode bed for the present work comprises of a flowing slurry of a mixture of carbon (in the form of coal particles or graphite crystal flakes) and molten carbonate salt electrolyte. The incoming molten carbonate salt electrolyte is assumed to be in a saturated state in the matter of solubility of gaseous CO_2. The saturation assumption can be justified by having the electrolyte inflow to the anode coming from a gas-liquid separator where the excess CO_2 is released into the exhaust gases.

It is hypothesized that as the electrochemical reaction proceeds in the anode, CO_2 is evolved within the pores of carbon particles on the surface that is wetted by the molten carbonate electrolyte containing carbonate ions, CO_3^{2-} that have diffused from the cathode.

It's important to understand what happens at the entry of anode bed. The molten salt electrolyte is saturated with CO_2 and the formation of CO_2 should facilitate nucleation of bubbles from the surface of carbon particles. The physics of bubble evolution from electrochemical reactors is a big field of its own and it's not the purpose of the current work to explore on that. From the view of modeling the electrochemical processes within anode, it's assumed that there is some cross-over (diffusion) of oxygen from the liquid electrolyte in cathode. And this transported oxygen reacts directly with the carbon in the anode to form CO_2 that provides a basis for bubble nucleation at the anode bed entry. Now, the solubility of O_2 in molten salt is much lower when compared to CO_2. From simple calculations involving orders of magnitude, it's simple to show that since the concentration of O_2 in cathode is of the order of $10^{-4}\,kmol/m^3$ at cell temperatures of 700 $^{\circ}C$ or $973K$. Since the diffusivity of O_2 in the molten carbonate salt is around $10^{-4}\,m^2 - s^{-1}$, the molar flux of O_2 diffusing from cathode to the anode is of the order of $10^{-11}\,kmol/m^2 - sec$ assuming the diffusing intermediate layer of 0.5 cm thickness. However, these are very crude calculations to show the order of magnitude of how much CO_2 can possibly form in anode by assuming some cross-over diffusion of O_2.

Now, the molar flux of CO_2 that can be formed from the electrochemical reaction, assuming an average current density of $500A/m^2$ can be calculate from

$\dot{n}''_{co_2,a} = 3/4\, i''/F$ which comes out to be roughly $10^{-6}\, kmol/m^2 - sec$ orders of magnitude. This mole flux is significantly higher than $10^{-11}\, kmol/m^2 - sec$ that is assumed to be the mole flux of CO_2 in the gas bubble phase at the anode bed entry.

It is possible that most of the CO_2 that is generated electrochemically within the anode bed remains in the bulk liquid in a slightly super-saturated state whereas only small fraction is transported via diffusion into the gas bubbles contributing to their growth. The only way gas hold-up has any kind of effect on the fuel cell performance is by affecting the free available area for ionic conduction through the electrolyte. For the expected case of very low gas hold-up, the conductivity of the electrolyte solution is not affected negatively and has relatively better cell performance.

Various correlations describing mass transfer coefficients in two and three-phase co-current downward flow are referred from the literature. Most of these correlations use air, water, and solid particles in the form of glass beads or gravel. These correlations use correction factors to justify the use of other gases, liquids and solids. These correction factors are function of physical properties of phases used in generating the correlations and of the phases that are used in this work. Limits of non-dimensional numbers are used to check the results of correlations limited to dependent parameters variability. It is posited that the output from these correlations may at best represent the actual scenario with a uncertainty of at least one order of magnitude and therefore it might be necessary to look at sensitivity analysis and ascertain trustworthiness of using such correlations.

The gas-liquid mass transfer coefficient is used from the work of Reiss [1967].

However, it has been made very clear by Reiss [1967] that the scope of their investigation is limited to air-water system with packings made of polyethylene or ceramic. The mass transfer measurements were made with the ammonia absorption and oxygen desorption systems. And if the results from this work are used for the design of systems involving other fluids, effects of fluid physical properties must be known. However, the mass transfer correlations from Reiss [1967] needs determination of pressure gradient as well. And in the present work, the pressure gradient is estimated from the work of Specchia and Baldi [1977] where, the factor, Ψ, is estimated and used for a system other than air-water. The factor Ψ is estimated using physical properties of selected molten carbonate electrolyte at the cell temperature and the properties of water at room temperature of 25 °C. This is the only fluid system correction that has been considered in the present work. Also, it's been asserted in Reiss [1967] that scatter of data around the mass transfer equations could be as great as $\pm 50\%$. Therefore, it would be fair to assume that most of these concerns could be addressed by considering variance of one order of magnitude of $K_{GL}A^{'''}$ in the sensitivity analysis done on cell performance. The liquid side and the gas side mass transfer coefficients as given by Reiss [1967] are produced below:

$$k_L A_b^{'''} = 0.12 \left[\frac{U_{0L}}{47.88} \left(\frac{\Delta P}{\Delta Z} \right)_{LG} \right]^{0.5} \tag{3.120}$$

$$k_G A_b^{'''} = 2 + 0.91 \left[\frac{U_{0L}}{47.88} \left(\frac{\Delta P}{\Delta Z} \right)_{LG} \right]^{2/3} \tag{3.121}$$

The pressure drop term is given by Turpin and Huntington [1967]:

$$\left(\frac{\Delta P}{\Delta Z} \right)_{LG} = \frac{2 \rho_G f_{LG} U_{0G}^2}{d_e} \tag{3.122}$$

where U_{0L} and U_{0G} are respectively the superficial velocities of liquid and gas phase

and ρ_G is the density of the gas.

Friction factor f_{LG} is given from Specchia and Baldi [1977] by:

$$f_{LG} = \exp\left(7.82 - 1.30\ln\left(\frac{\bar{Z}}{\Psi^{1.1}}\right) - 0.0573\left[\ln\left(\frac{\bar{Z}}{\Psi^{1.1}}\right)\right]^2\right) \tag{3.123}$$

The equivalent diameter of the packing is given by Turpin and Huntington [1967] as:

$$d_e = \frac{2}{3} d_p \frac{\varepsilon}{1-\varepsilon} \tag{3.124}$$

The liquid+solid hold-up is given by the correlation from Specchia and Baldi [1977] that essentially describes the dynamic liquid saturation in trickle bed reactors for two-phase concurrent downward flow in packed beds within high gas-liquid interaction regime and for non-foaming systems. The relationship is given as:

$$h_{LS} = 0.125\left(\frac{\bar{Z}}{\Psi^{1.1}}\right)^{-0.312}\left(\frac{A'''_{g,a}\, d_p}{\varepsilon}\right)^{0.65} \tag{3.125}$$

where $\bar{Z}$ is given by:

$$\bar{Z} = \frac{Re_G^{1.167}}{Re_L^{0.767}} \tag{3.126}$$

$A'''_{g,a}$, d_p, and ε are respectively the surface area per unit bed volume of the anode grid, nominal packing diameter, and the bed void fraction and the evaluation methodology for a wire-mesh or perforated plate type of packing is provided in the appendix section C.

The Reynolds numbers for gas and liquid phases are given by:

$$Re_L = \frac{U_{0L} d_p}{\nu_L} \tag{3.127}$$

$$Re_G = \frac{U_{0G} d_p}{\nu_G} \tag{3.128}$$

where ν_L and ν_G respectively the kinematic viscosity of liquid and gas phase.

The liquid superficial velocity, U_{0L}, is set to values within the range specified by the

correlation. The superficial gas velocity, U_{0G}, is determined from the mole flux and the ideal gas law:

$$U_{0G} = \dot{n}''_{\mathrm{co_2,g,a}} \frac{\bar{R}T}{101.325} \tag{3.129}$$

where the molar flux of CO_2 ($\dot{n}''_{\mathrm{co_2,g,a}}$) in the gas phase is determined from the solution of the differential equations.

The correction factor, Ψ, for using fluid systems other than air-water is given by:

$$\Psi = \frac{\sigma_w}{\sigma_L} \left[\frac{\mu_{sl}}{\mu_w} \left(\frac{\rho_w}{\rho_{sl}} \right)^2 \right]^{0.3} \tag{3.130}$$

where the properties for the electrolyte slurry (molten carbonate + carbon) is considered except for the surface tension for which there is no methodology available. The gas-holdup can be determined using $h_G = 1 - h_{LS}$. However, to find the respective liquid and solid holdups, literature reference Kim et al. [1972] is used. This reference provides hold-up characteristics for liquid-solid systems with gas velocities being zero. The glass beads or gravel is considered held between perforated plates while water flows through the system. Superficial liquid velocities of 0.035 - 0.1 m/s have been considered in this reference and the liquid hold-up was shown to vary from 0.30 - 0.60. Superficial velocities in the same range have also been selected for the current work but lower values of liquid holdup is observed owing to difference in physical properties between water-gravel/glass-beads system in the reference versus molten carbonate - carbon system in the current work. It is posited that the amount of error resulting from these differences can be accounted for by observing one order magnitude uncertainty in the estimation of the mass transfer coefficients. The liquid hold-up equation as referenced from Kim

et al. [1972] is given by:

$$h_L = h_{LS} \cdot \left[0.409 \left(Fr_L \frac{\rho_S}{\rho_L} \right)^{0.178} Re_L^{0.074} \right] \tag{3.131}$$

where Re_L is based on the particle diameter and is given by:

$$Re_L = \frac{\rho_L U_{0L} d_c}{\mu_L} \tag{3.132}$$

where d_c is the average diameter of the carbon particles and also varies with bed length and

ρ_s and ρ_L are respectively the densities of carbon and molten carbonate salt and μ_L is the absolute viscosity of the molten carbonate salt. Fr_L is the Froude number based on the particle diameter and given by:

$$Fr_L = \frac{U_{0L}^2}{g\, d_c} \tag{3.133}$$

where g is the gravitational constant.

The solid holdup can then be determined using the relationship $h_S = h_{LS} - h_L$. Using the above correlations that have also been summarized in Table 3.4, gas-side and liquid-side mass transfer coefficients can be determined, and the overall gas-liquid mass transfer coefficient can then be determined by adding the two mass transfer resistances,

$$K_{GL} A_B''' \ (\text{/sec}) = \frac{1}{\left(1/k_L A_B''' + 1/k_G A_B'''\right)} \tag{3.134}$$

Solid-Liquid Mass Transfer

The liquid-solid mass transfer can be evaluated in the anode using simple film theory basis from the work of Shah [1979]. This work indicates that in the limiting case of mass transfer from a single sphere resting in an infinite stagnant liquid, the

expression for mass transfer coefficient, K_s is equal to $2D/d_p$ where D is the molecular diffusivity of the solute and d_p is the particle diameter. This simply implies that in dimensionless form, the Sherwood number $Sh = K_s d_p/D$ is 2. It is also clear that any form of convection would increase the value of K_s.

In the present work, there are large number of carbon particles that are assumed to flow along with the molten carbonate salt without any slip. The assumption can be justified since the densities of carbon and salt are very similar. There are many theories in the literature that take the form of equation as given by Ranz [1952] and first proposed by Frössling that utilize relative slip velocities to calculate Reynolds number portraying increased mass transfer effects:

$$Sh = 2 + K\,\overline{Re}^{1/2} Sc^{1/3} \tag{3.135}$$

Later on some researchers have utilized Kolmogoroff's theory to correlate the effective relative velocity with some macroscopic variables, such as stirrer speed and particle diameter Shah [1979]. Subsequently, Sano et al. [1974] derived a relation for the liquid-solid mass transfer coefficient based on the Kolmogoroff's theory for isotropic turbulence. The Reynolds number based on this theory is defined in terms of the rate of dissipation energy per unit mass of liquid, the specific surface diameter, and the kinematic viscosity of liquid. The Reynolds number is thus given as:

$$\overline{Re} = \xi\,\frac{d_p^4}{\nu_L^3} \tag{3.136}$$

where the calculation of dissipation energy per unit mass (ξ) in this work is estimated by the following equation because it is assumed that the convection that increases the mass transfer coefficient in the present work is the movement of

slurry through the fixed bed which causes agitation effects.

$$\xi = \frac{1}{\rho_{sl}} \frac{dP}{dx} U_{true,sl} \tag{3.137}$$

The pressure drop term dP/dx should be calculated for the flowing slurry through the fixed beds and is estimated using the following methodology.

The anode bed encounters a slurry flow through a bed of stainless steel (or nickel) perforated plates or wire-mesh placed perpendicular to the flow to ensure homogenous flow. The slurry consists of a mixture of coal/graphite particles and molten carbonate mixture of various alkali salt (Li_2CO_3, Na_2CO_3, K_2CO_3). Assuming negligible effect of gas-holdup, correlation for pressure drop in liquids flow through fixed beds is available in the literature as given by Leva [1949] and has been supported by extensive data. The correlation is assumed to be valid for flowing slurry for the present work and produced below:

$$\left[\frac{\Delta p}{L}\right] = \frac{2f\rho_{sl}U_{o,sl}^2(1-\varepsilon)^{3-n}}{D_p\,\phi_s^{3-n}\varepsilon^3} \tag{3.138}$$

In this equation, n is the state of flow factor and can be estimated from the plot provided by Leva [1949] once Re' is estimated.

f is the friction factor, and is equal to $100/Re'$ for laminar flow and also given as a plot of f vs Re' by Leva [1949], where Re' is given as:

$$Re' = \frac{\rho_{sl}\,U_{o,sl}\,D_p}{\mu_{sl}} \tag{3.139}$$

ρ_{sl}, and μ_{sl} are the density and viscosity of coal-molten salt slurry,

$U_{o,sl}$ is the superficial velocity of the slurry assuming no relative slip between the carbon particles and the molten carbonate salt,

ε is the packing void fraction,

D_p is given as:

$$D_p = \frac{6(1-\varepsilon)}{\phi_s A'''} \tag{3.140}$$

where A''' is the surface area per unit volume of the packing,

ϕ_s is the shape factor, and in the above equations is defined as the area of sphere of diameter D_p divided by the actual surface area of the packing and is evaluated as:

$$\phi_s = 4.87 \frac{V_p^{2/3}}{S_p} \tag{3.141}$$

where for a fixed bed using wire-mesh packing, Packing Volume (V_p) and Packing Surface Area (S_p) are given (see Appendix C for details) by:

$$V_p = \frac{\pi D_T^2 S_T}{2} \tag{3.142}$$

$$S_p = 2\pi S_T D_T \tag{3.143}$$

where D_T is the wire diameter and S_T is the wire-mesh size (wire to wire spacing).

The above correlation simplified for laminar flow ($Re' \leq 10$) presented in English units by the author and used in the SI units in the present work is given as:

$$\left[\frac{\Delta p}{L}\right]_{lam} = \frac{200\, U_{o,sl}\, \mu_{SL}(1-\varepsilon)^2}{D_p^2\, \phi_s^2\, \varepsilon^3} \tag{3.144}$$

The approximate correlation for turbulent flow is given by:

$$\left[\frac{\Delta p}{L}\right]_{turb} = \frac{3.50\, \rho_{sl}^{0.9}\, U_{o,sl}^{1.9}\, \mu_{sl}^{0.1}(1-\varepsilon)}{D_p^{1.1} \phi_s^{1.1} \varepsilon^3} \tag{3.145}$$

Estimation of pressure drop term enables calculation of energy dissipation term in the anode bed which subsequently can be used to estimate the modified Reynolds

number that represents increased liquid-solid mass transfer effects due to convective agitation of slurry moving through a wire-mesh packed bed. The non-dimensional Sherwood number representing liquid-solid side mass transfer coefficient in the anode is given by Sano et al. [1974] through the following equation:

$$Sh = \left[2 + 0.4\,\overline{Re}^{1/4} Sc^{1/3}\right] \phi_c \tag{3.146}$$

Schmidt number (Sc) is given by $Sc = \nu_L / D_{\mathrm{CO_2}}$

$D_{\mathrm{CO_2}}$ is the molecular diffusivity of CO_2 in the molten carbonate salt and

ν_L is the kinematic viscosity of the molten carbonate salt.

ϕ_c as shown by Sano et al. [1974] in his work for various kinds of packing is estimated to be roughly 0.5.

The mass transfer coefficient (units - m/s), that is used in the ordinary differential equations (ODE's) described before, can then be given by:

$$K_{s,\mathrm{CO_2}} = \frac{Sh\, D_{\mathrm{CO_2}}}{d_c} \tag{3.147}$$

where d_c is the carbon particle diameter within the bed.

The surface area of carbon per unit volume of the bed is given by equation 3.148 which is developed in the Appendix section C.

$$A'''_{C,\mathrm{a}} = \frac{6\, h_S}{d_C(x_{\mathrm{a}})}\,(1 - \zeta_{\mathrm{a}}) \tag{3.148}$$

where $d_C(x_{\mathrm{a}})$ is given by,

$$d_C(x_{\mathrm{a}}) = d_C(0) \left[\frac{\dot{n}''_{C,S,\mathrm{a}}(x_{\mathrm{a}})}{\dot{n}''_{C,S,\mathrm{a}}(0)}\right]^{1/3} \tag{3.149}$$

Table 3.4: Various Correlations Used for the Anode Packed Bed

Parameter	Description	Correlation	Remarks	References
h_{LS}	Liquid + Solid Holdup	$h_{LS} = 0.125\left(\frac{\bar{Z}}{\Psi^{1.1}}\right)^{-0.312}\left(\frac{A'''_{\mathrm{g,a}}\, d_{\mathrm{p}}}{\varepsilon}\right)^{0.65}$	$\bar{Z} = \frac{Re_G^{1.167}}{Re_L^{0.767}}$	Specchia and Baldi [1977]
		where $Re_L = \frac{U_{0L} d_p}{\nu_L}$, $Re_G = \frac{U_{0G} d_p}{\nu_G}$ and $A'''_{g,a}$ is given from Appendix C		
h_L	Liquid Holdup	$h_L = 0.409\left(Fr_L \frac{\rho_S}{\rho_L}\right)^{0.178} Re_L^{0.074}\, h_{LS}$	$Fr_L = U_{0L}^2/g d_{\mathrm{p}}$	Kim et al. [1972]
h_S,h_G	Solid,Gas holdups	$h_S = h_{LS} - h_L$,$h_G = 1 - h_{LS}$		
$k_L A'''_b$	Liquid side Mass Transfer coefficient	$k_L A'''_b = 0.12\left[\frac{U_{0L}}{47.88}\left(\frac{\Delta P}{\Delta Z}\right)_{LG}\right]^{0.5}$		Reiss [1967]
$k_G A'''_b$	Gas side Mass Transfer coefficient	$k_G A'''_b = 2 + 0.91\left[\frac{U_{0L}}{47.88}\left(\frac{\Delta P}{\Delta Z}\right)_{LG}\right]^{2/3}$		Reiss [1967]
f_{LG}	Two-phase friction factor	$f_{LG} = \exp\left[7.82 - 1.30\ln(\bar{Z}/\Psi^{1.1}) - 0.0573\{\ln(\bar{Z}/\Psi^{1.1})\}^2\right]$		Specchia and Baldi [1977]
$\left(\frac{\Delta P}{\Delta Z}\right)_{LG}$	Pressure Gradient	$\left(\frac{\Delta P}{\Delta Z}\right)_{LG} = \frac{2\rho_G f_{LG} U_{0G}^2}{d_{\mathrm{e}}}$	$d_{\mathrm{e}} = \frac{2}{3} d_{\mathrm{p}} \frac{\varepsilon}{1-\varepsilon}$	Turpin and Huntington [1967]
Sh	Sherwood number	$Sh = \left[2 + 0.4\,\overline{Re}^{1/4} Sc^{1/3}\right]\phi_{\mathrm{c}}$	$\overline{Re} = E d_{\mathrm{p}}^4/\nu_L^3$	Sano et al. [1974]
		where $E = U_{0G}\, g$, $Sc = \nu_L/D_{\mathrm{co_2}}$ and $\phi_{\mathrm{c}} = d_{\mathrm{p}}/d'_{\mathrm{p}}$		
R_{a}	Resistivity of anode bed	$R_{\mathrm{a}} = \frac{1}{K_{\mathrm{salt}}}(1-\varepsilon_{\mathrm{g,a}})^{-3/2}$	$\varepsilon_{\mathrm{g,a}} = \zeta_{\mathrm{a}} + \left(h_{\mathrm{g}} + h_{\mathrm{s}}\right)\left(1-\zeta_{\mathrm{a}}\right)$	Tobias [1966]

3.5.5 Molar Density Equations in Anode Bed

Previous sections have described differential equations for the evaluation of mole fluxes of the participating species, i.e. CO_2 and C. The driving forces required to enable electrochemical reactions in the anode arise from the concentration gradients for species in different phases, i.e. gas, liquid and solid. What happens in the anode is that there is a super-saturation of CO_2 on the surface of carbon particle (wetted by the molten salt electrolyte) where the anodic reaction takes place. There is a net mass transport of CO_2 from the carbon particle surface to the bulk liquid which is mainly the function of concentration gradient and the mass transfer coefficient. The evaluation of solid-liquid mass transfer coefficient can be done as shown in previous sections on mass transfer.

Molar densities of CO_2 in the gas phase comes from the ideal gas law. Densities in the liquid phase are from mole fraction and liquid salt density. Units are $kmol/m^3$:

$$\bar{\rho}_{\mathrm{co_2,g,a}} = \frac{101.325}{\bar{R}T} \tag{3.150}$$

$$\bar{\rho}_{\mathrm{co_2},\ell,\mathrm{a}} = \left(\frac{\dot{n}''_{\mathrm{co_2},\ell,\mathrm{a}}}{\dot{n}''_{\mathrm{co_2},\ell,\mathrm{a}} + \dot{n}''_{\ell} + \dot{n}''_{C}} \right) \bar{\rho}_{\mathrm{salt}} \tag{3.151}$$

where $\bar{\rho}_{\mathrm{salt}}$ is given by $\bar{\rho}_{\mathrm{salt}} = \rho_L / M_L$, ρ_L and M_L are respectively the density and molecular weight of the molten salt.

3.5.6 Bed Resistance in Anode

In the present work the gas velocities are mostly negligible (for the purpose of utilization of fluidization theories). The liquid superficial velocities are in the range of 0.1 m/s and perhaps may involve some degree of turbulence owing to movement

of slurry flow (carbon + molten salt electrolyte) through a current collector grid made out of stainless steel wire-mesh or perforated plates. The bed resistance to the flow of ionic current through the solution (molten salt electrolyte) phase is easily determined from the equation given by Bruggeman [1935]:

$$\rho_l = \frac{1}{\kappa_{salt}} \varepsilon^{-3/2} \tag{3.152}$$

where κ_{salt} is the conductivity of the molten carbonate salt and ε is the void fraction in the bed and excludes packing, gas bubbles, and carbon particles.

After the carbonate ions transport from cathode into the anode bed through the inter-connected electrolyte, the carbonate ions react on the surface of the carbon particles with carbon to form CO_2 bubbles. The charge transfer from the ionic solution to the carbon particle electrode would involve the bed resistance calculated as above. This charge transfer mechanism will be on a more macroscopic scale in the bed involving resistance to the movement of ionic current from solution phase to the electrode phase. On a microscopic scale, there will be contact resistance due to transfer of charge from the carbon particle to the current collector grid. The time between various collisions and charge transfers could be quite small but could take place through two different mechanism as shown in figure 3.10:

The methods of ascertaining particle phase resistivity or the charge transfer rate in gas-liquid-solid packed beds or in fluidized bed electrodes has been studied by many authors and research that has been most relevant to the present work is by Fleischmann and Oldfield [1971], Beenackers et al. [1977], Chen et al. [1977], Morooka et al. [1981], Kusakabe et al. [1981].

The work by Fleischmann and Oldfield [1971] involved studying particle size in

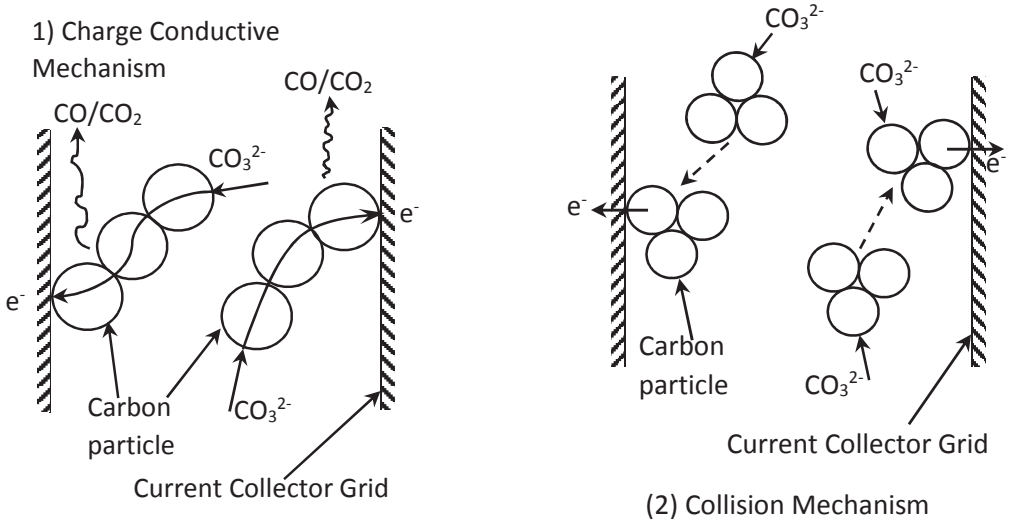

(a) Charge Conduction Mechanism (b) Collision Mechanism

Figure 3.10: Mechanism of charge transfer in the anode bed with carbon entrained in molten carbonate electrolyte as slurry.

the range of 50 $\mu m < r <$500 μm, bed expansion range <25% and density difference between the solution and the particle phase to be at least 2 g/cc. The author looked at the times and frequency of particle collision and also at yield strength of the material of the particle and surface tension of the solution phase in arriving at a theoretical equation to calculate effective conductivity of discontinuous metal phase in the solution phase.

Beenackers et al. [1977] also derived a theoretical model for estimating charge transfer resistance of particle phase, however the authors concluded that this model based on ideal particulate fluidization with single particle collisions cannot explain the metal phase conductivity observed experimentally. However, their work goes on to indicate that the ideal particulate state have a tendency to transition towards aggregative fluidization. They also indicated that density difference between particle phase and the solution phase is one of the main driving force towards this transition and that even a small density difference of 0.290 g/cc is sufficient to provide the tendency towards this transition. The authors eventually derive a revised theoretical model for the particle resistivity (ρ_m) in terms of aggregate parameters but due to lack of information on number of particles per aggregate and collision frequency for aggregate particles did not permit a experimentally validated model.

Chen et al. [1977] conducted measurements of bed and electrode-bed contact resistances in a fluidized bed using calcined coke and graphite particles in conjunction with electrode made of various materials like brass, stainless steel and silicon carbide. The bed resistance and the contact resistance both show a dependence upon the gas velocity which in the present work is quite small (and negligible). The authors also show that the ratio of contact resistance to the total bed resistance

(prior to fluidization, which represents the present work) for graphite particles (size: 0.171 - 0.21 mm) and stainless steel electrode to be roughly 50%.

Reed and Goldberger [1966] conducted small scale experiments with fluidized graphite beds and various fluidizing gases to evaluate factors affecting the electrical properties. The conclusion relevant for the present work is that increased particle size decreases resistivity. The reason for this outcome is attributed to the mechanism dominating the resistivity measurement. If the current flows via charge transfer mechanism (as per the authors - this seems similar to the collision mechanism as explained above), any factor which would increase the number of particle contact per unit time might be expected to increase the rate of transfer and thereby lower the bed resistivity. Alternately, if current flows by particle to particle linkages (conduction mechanism as explained above), then any factor causing linkages to break would be expected to increase the measured resistivity of the bed. The authors cite another work and propose that the latter mechanism (conduction) predominates and that the resistivity of a fluidized bed is orders of magnitude less than that calculated by a charge transfer mechanism (collision mechanism). The authors expected that resistivity would vary directly with those factors that increase the particle to particle contact resistance and the number of contacts needed to form a linkage. The factors causing increased breaking of linkages were then expected to increase resistivity. This theory was eventually shown to be validated with experimental data.

Kusakabe et al. [1981] investigated effective specific resistance of the particle

phase by studying copper deposition from acidic aqueous solutions containing copper ion. The authors added in parallel the resistivity from the two different mechanisms (see above) for charge transfer that have been proposed in earlier literature to indicate the effective specific resistivity. The experiment was conducted for fluidized beds (without gas) with bed expansion ranging from 10% to 35%. One of the conclusions of this work was that at lower values of bed expansion (10%) which also indicated relatively higher solid-holdup, conduction mechanism was dominating whereas for the higher values of bed expansion (35%) collision mechanism was dominating. The experimental data and model from this work also matched an earlier data point from Beenackers et al. [1977]. The proposed relationship for the resistivity of particle phase as a function of bed expansion as given by the authors is:

$$\rho_m = (0.0004 \pm 0.0002)\, E^2 \tag{3.153}$$

The bed expansion E defined by the authors as $\left\{\frac{(H_f - H_o)}{H_o}\right\} \times 100$ can be calculated as follows, where H_o and H_f are the bed thickness under settled and fluidized conditions respectively.

The solid holdup in terms of bed thickness is defined as:

$$h_s = \frac{H_o\, h_{so}}{H_f} \tag{3.154}$$

where h_{so} is the solid holdup under settled condition.

For graphite particles (or powder of 200 mesh size), the bulk density is given as 561 kg/m^3 and the true density is roughly 2200 kg/m^3. Therefore, the solid hold-up under settled condition (h_{so} - also the maximum solid hold-up) is roughly $561/2200 \cong 0.26$. And, according to the experimental conditions of Kusakabe et al. [1981], the resistivity correlation (above) is valid between expansion of 10% and

35%. For these limiting conditions of expansion (E), the solid hold-up can be calculated to be 0.23 and 0.19 respectively. Using the resistivity correlation of Kusakabe et al. [1981], Morooka et al. [1981] outside these limits might be questionable. The resistivity calculated for the limiting conditions yield values of 0.04 and 0.49 $\Omega - m$ respectively.

The correlation as proposed above by Morooka et al. [1981], Kusakabe et al. [1981] is valid for copper particles. Now, typical resistivity of graphite particles (transverse) can be roughly 2 orders of magnitude higher than that of copper in addition to copper being a softer material than graphite. The contribution of hardness factor to the contact resistance (also called constriction resistance) is a subject that is covered in great detail by Holm [1967]. This simply means that softer the material, lower will be the constriction resistance because of larger contact area and therefore larger available path for conduction. For reference, Shore Scleroscope Hardness (SSH) for graphite could be even higher than 70 whereas it's lower than 10 for copper. However, there is no other literature reference that can help establish a connection between the resistivity of copper particles to that of graphite particles.

In the present work, the above correlation for copper particles maybe applied for graphite particles (in slurry form with molten carbonate salt) in a stainless steel bed after an introduction of 2 orders of magnitude factor (higher for graphite) to account for resistivity difference between copper and graphite.

The resulting resistivity can be given as:

$$\rho_{ct} = (0.04 \pm 0.02) \left\{ \left(\frac{h_{so}}{h_s} - 1 \right) \times 100 \right\}^2 \tag{3.155}$$

where $h_{so} = 0.26$ and h_s can vary from 0.19 - 0.23.

Voltage drop due to contact resistance of the carbon particles can then be given by:

$$\Delta V_{\text{ct}} = \frac{1}{3} \frac{i''_{\text{s,a}} A'''_{c,\text{a}} \rho_{ct}}{\left(A'''_{\text{g,a}}\right)^2} \tag{3.156}$$

where $A'''_{\text{g,a}}$ is given from Table 3.4. And putting in the expression for $A'''_{c,\text{a}}$, we get:

$$\Delta V_{\text{ct}} = \frac{2\, i''_{\text{s,a}} \rho_{ct}}{\left(A'''_{\text{g,a}}\right)^2} \frac{h_s}{d_{\text{c}}} (1 - \zeta_{\text{a}}) \tag{3.157}$$

3.6 Solution Technique

In this section, the solution technique for solving the governing equations for electrochemical processes in anode and cathode bed is discussed.

The five ordinary differential equations (ODE's) in the anode bed and six ODE's in the cathode bed are solved numerically using the MATLAB ODE45 implementation of the explicit Runge-Kutta (4,5) pair of Dormand and Prince called variously RK5(4)7FM, DOPRI5, DP(4,5) and DP54.

For both anode and cathode, the MATLAB solver is used so that the boundary value problem is converted to an initial value problem by using "shooting method". For a given total cell voltage, two guesses were needed to form the initial value problem: the total cell current density (same for cathode and anode) and the division of the total overpotential between the anode and the cathode (equations 3.76 and 3.110). The cell current and the voltage division were both iterated until current density was zero at the end of both beds. The iteration technique is shown in figure 3.12, while current density - position plots for various guesses are shown in figure 3.11. The iteration was done at various total output voltages to get a V-I curve.

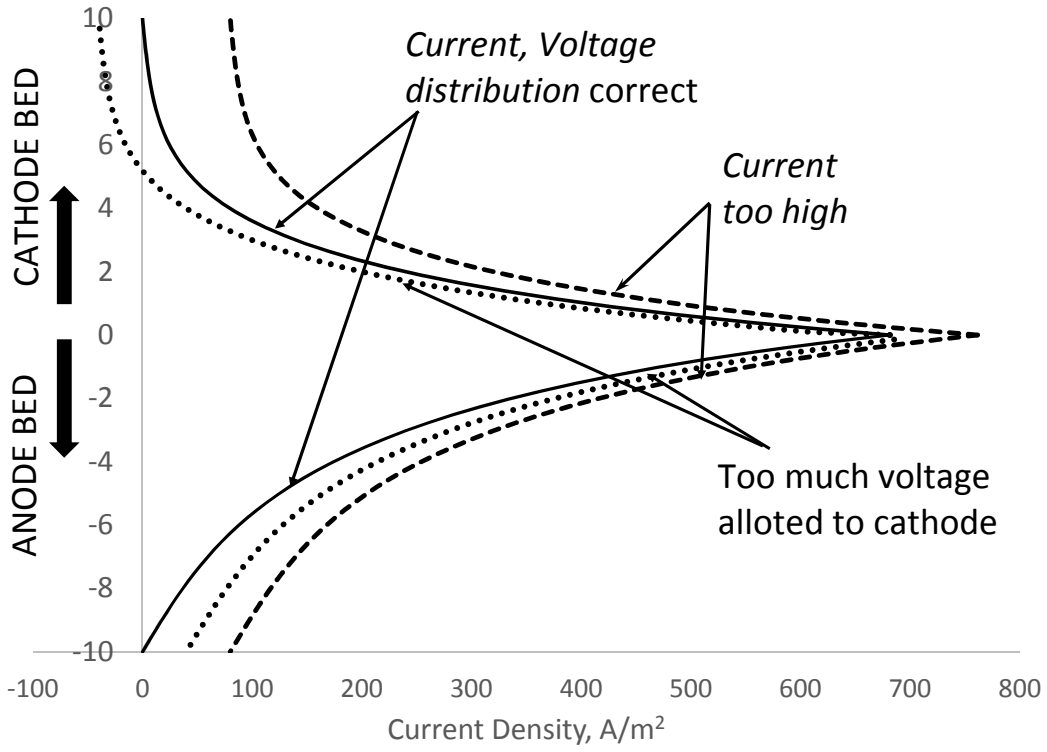

Figure 3.11: Solution methodology to iterate for the current density and potential distribution factor for given design operating conditions.

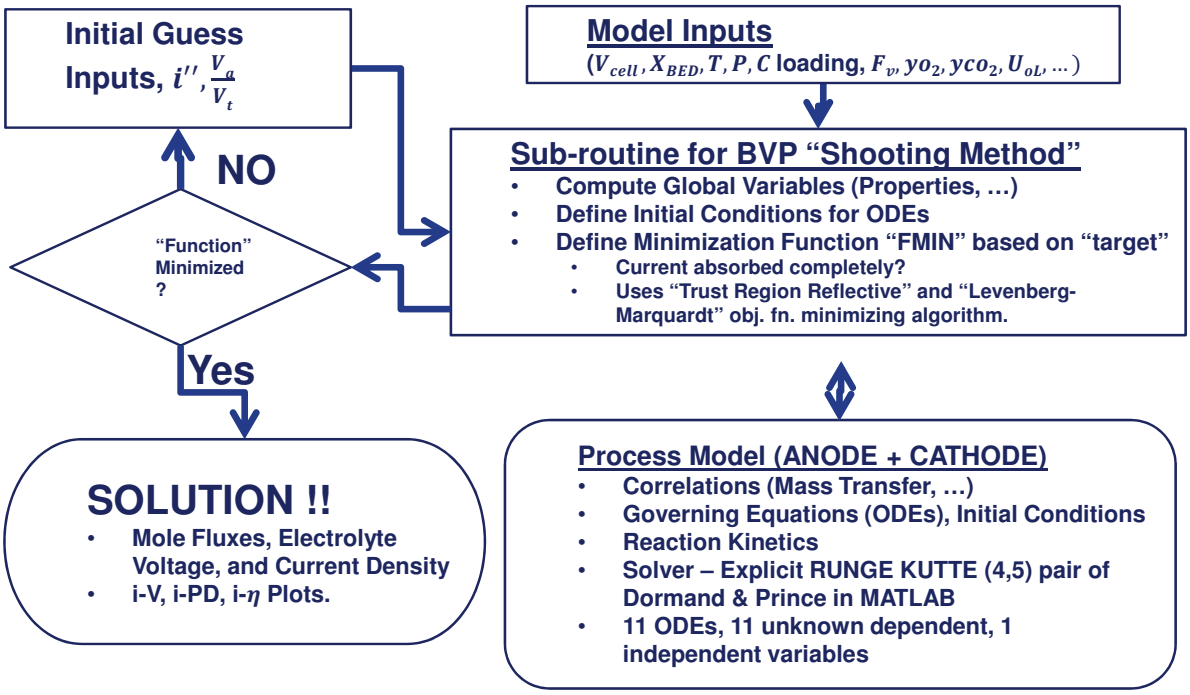

Figure 3.12: Flowchart showing solution methodology for the overall fuel cell model.

The two initial value problem are described by equations 3.79 - 3.84 in the cathode and equations 3.101 - 3.111 in the anode. The initial value problem solution techniques for cathode and anode are summarized in figures 3.13 and 3.14.

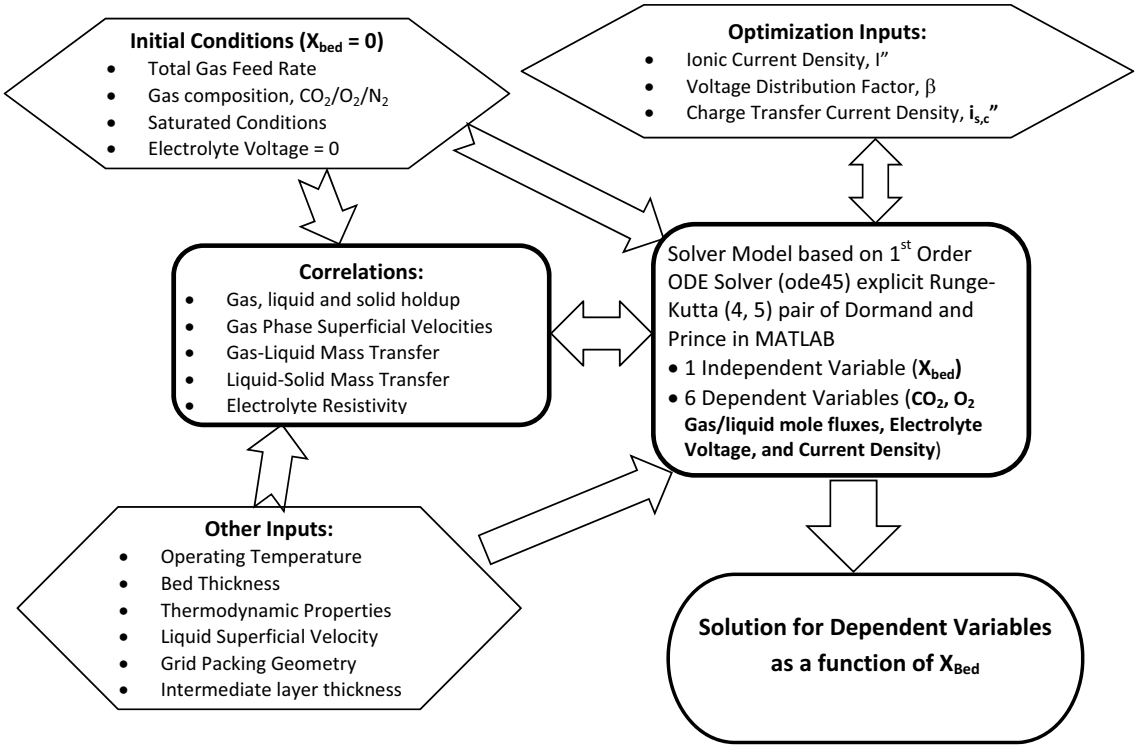

Figure 3.13: Mathematical solution technique used to solve 6 ordinary differential equations describing electrochemical processes in the cathode bed.

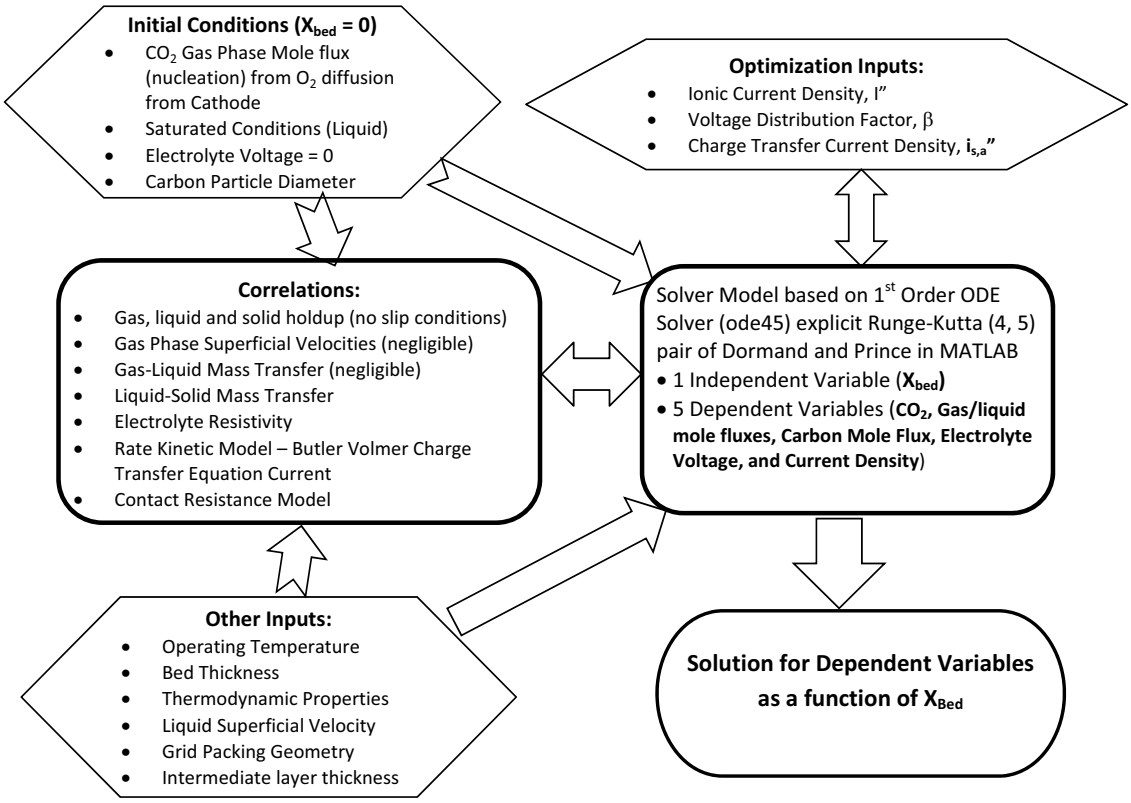

Figure 3.14: Mathematical solution technique used to solve 5 ordinary differential equations describing electrochemical processes in the anode bed.

Chapter 4

Results and Discussion

The 5 ordinary differential equations (ODE's) in the anode bed and 6 ODE's in the cathode bed are solved using MATLAB ODE45 solver as in MATLAB [2014]. Initial conditions were initial overpotential (based on cell output voltage and open circuit voltage), current density at the interface between the two electrodes, and mole fluxes of various constituents. The initial overpotential was divided between the anode and cathode. The differential equations were stepped forward in space until either

1. one of the reactants was exhausted,
2. the overpotential dropped to zero, or
3. the current was absorbed completely by the electrode.

In cases (1) and (2) the initial conditions did not represent a possible operating point and either current density or output cell voltage had to be decreased, or reactant feed had to be increased. In case (3), the bed depth at which the current was absorbed completely was the design bed depth for that operating condition

and the corresponding overpotential provided the cell voltage for the same operating condition. This methodology also provided basis for an optimization code that implemented the above three cases in such a way as to solve for the current - voltage relationship.

4.1 Base Case Results

The base case results are produced by solving the ordinary differential equations as described in previous sections. The equations involved solving for electrolyte current density, potential, and mole flux concentrations of the involved species (CO_2 and O_2 in cathode and C and CO_2 in the anode). The reaction kinetics and exponents for reaction steps for the Butler Volmer equations (charge-transfer current density equation) were derived from the work of Wilemski [1983] for the cathode and from the work of Weaver et al. [1979] for the anode. The differences between various reaction mechanisms in the cathode have been explained in earlier sections. Reaction kinetics in cathode developed by Wilemski [1983] uses peroxide mechanism in a eutectic ternary melt of alkali molten carbonates. A ternary mixture of molten carbonate salts (Li-Na-K::43.5:31.5:25) is used for the cathode. For the anode, a preliminary kinetic model is developed using Butler Volmer equations in a manner similar to what was used by Wilemski [1983]. The kinetic parameters for the anode have been empirically developed from the work of Ateya in Weaver et al. [1979][Appendix B]. Fortunately, work of Ateya in Weaver et al. [1979] also involved the use of ternary mixture of alkali molten carbonate salts consistent with the electrolyte use in the cathode work.

Table 4.1 shows input parameters used in solving the 11 ordinary differential equations in anode and cathode beds.

Table 4.1: Input Anode and Cathode Parameters for Base Case Conditions

Parameter	Value in Anode	Value in Cathode
Wire-mesh size	24 mesh	30 mesh
Wire-mesh Opening, [mm]	0.70	0.54
Grid Area per unit Volume, A''' $[m^2/m^3]$	1186	1848
Void Fraction, ε	0.89	0.86
Volume Fraction Electrode, ζ	0.11	0.14
Cell Temperature, T [K]	973	973
Cell Pressure, P [atm]	1	1
Kinetic Rate Parameters	Empirical data used from work by Ateya in Weaver et al. [1979]	Directly used from Wilemski [1983]
Reaction Kinetics Model/Butler Volmer Equations	Developed here based on work by Wilemski [1983]	Model developed by Wilemski [1983]
Open Circuit Voltage (@ Standard Conditions), V_{oc} [Volt]	1.026	1.026
Liquid Superficial Velocity, U_{oL} [m/sec]	0.1	0.1
Feed Gas Flow Rate (per cm^2) , F_v $[m^3/hr]$	-	0.1
CO_2 mole fraction at feed inlet, $y_{co_2,i}$ [frac]	-	0.20
O_2 mole fraction at feed inlet, $y_{o_2,i}$ [frac]	-	0.168
N_2 mole fraction at feed inlet, $y_{N_2,i}$ [frac]	-	0.632
Carbon Hold-up, h_c [frac]	0.19	-

It was not possible to solve the complete set of differential equations analytically owing to complex nature of the solution arising from the use of full Butler Volmer equation and the ensuing interdependence between charge transfer (surface) current density and gas species concentration in bulk liquid and at the reacting surface. It maybe possible to get an analytical solution if the Butler Volmer equations are used in the Tafel form. However, Tafel form is relevant for higher over-potentials

(perhaps higher than 0.3 or 0.4 V). In the present work, both anode and cathode involve chemical over-potentials that remain mostly below 0.4 V for most of the cases and therefore Tafel form is not used. The reason is primarily because in the present work, there is distribution of polarization in both anode and cathode beds leading to lower chemical over-potentials available for each separate bed.

The base case results have been evaluated using bed depth of 10cm in both anode and cathode. The thermo-physical properties for the base-case conditions are estimated from various sources and produced in the table 4.2. The proper-

Table 4.2: Thermo-Physical Properties for Electrolyte and Gas Species for the Base Conditions.

Parameter	Value	Source
Cell Temperature, T [K]	973	-
Cell Pressure, P [atm]	1	-
Electrolyte	$(Li-Na-K)_2CO_3$ Eutectic	-
Electrolyte Composition	Li-Na-K :: 43.5-31.5-25	-
Electrolyte Viscosity, μ_L $[Pa-sec]$	1.15×10^{-3}	Janz et al. [1979]
Electrolyte Density, ρ_L $[kg/m^3]$	1983.4	Janz et al. [1979]
Electrolyte Kinematic Viscosity, ν_L $[m^2/sec]$	5.8×10^{-7}	Janz et al. [1979]
Electrolyte Conductivity, κ_L $[Ohm^{-1}-m^{-1}]$	183.9	Janz et al. [1979]
Electrolyte Surface Tension, σ_L $[N-m^{-1}]$	0.2195	Janz et al. [1979]
Electrolyte Molecular Wt, M_L $[kg-kmol^{-1}]$	100.06	-
CO_2 Henry's Law Constant (@ 973 K), k_{H,CO_2} $[kmol/m3-kPa]$	1.18×10^{-4}	Wilemski [1983]
O_2 Henry's Law Constant (@ 973 K), k_{H,O_2} $[kmol/m3-kPa]$	5.93×10^{-6}	Wilemski [1983]
CO_2 Henry's Law Constant (@ 923 K), $k_{H,CO_2,e}$ $[kmol/m3-kPa]$	1.15×10^{-4}	Wilemski [1983]
O_2 Henry's Law Constant (@ 923 K), $k_{H,O_2,e}$ $[kmol/m3-kPa]$	3.88×10^{-6}	Wilemski [1983]
CO_2 Molecular Diffusivity in the Electrolyte (@ 973 K), D_{CO_2} $[m^2-s^{-1}]$	1.27×10^{-9}	Wilemski [1983]
O_2 Molecular Diffusivity in the Electrolyte (@ 973 K), D_{O_2} $[m^2-s^{-1}]$	1.51×10^{-9}	Wilemski [1983]
CO_2 Kinematic Viscosity (@ 973 K), ν_{CO_2} $[m^2-s^{-1}]$	7.07×10^{-7}	Kays and Crawford [1980]
O_2 Kinematic Viscosity (@ 973 K), ν_{O_2} $[m^2-s^{-1}]$	1.19×10^{-4}	Kays and Crawford [1980]
CO_2 Density (@ 973 K), ρ_{CO_2} $[kg-m^{-3}]$	0.55	Kays and Crawford [1980]
O_2 Density (@ 973 K), ρ_{O_2} $[kg-m^{-3}]$	0.40	Kays and Crawford [1980]

ties of electrolyte and gases used in the anode will be slightly different than what's shown in the table 4.2. Anode contains a slurry mixture of carbon (or coal) and the selected electrolyte of alkali based molten carbonates. The slurry properties are evaluated as described earlier in section on modeling. The evaluation of properties require the knowledge of mass fraction of carbon present in the electrolyte. It should be noted that the although the true density of coal particles (pyrolitic graphite in the current work) is roughly 2200 kg/m^3 but due to void fractions, bulk density of graphite particles is in the range of 560 kg/m^3 [Valves, 2014]. High porosity could signify lower bulk density but possibly higher reactivity (owing to more reaction sites available) and vice-versa, however this is not considered due to unavailability of sufficient data on contact resistance.

4.1.1 Cell Performance Results

The fuel cell performance is measured through various indicators as elaborated further:

Current Density - Cell Voltage plot:

This plot shows the activation over-potential drop from the open-circuit potential at very low current densities (Region 1). Subsequently, the plot shows a linear-region indicating ohmic polarization (Region 2). Eventually, at limiting current densities (high overpotential-low cell voltage, mass-transfer limitations might be indicated by non-linearity (Region 3). These characteristics are shown in figure 4.1, which shows current density - cell voltage characteristics for the base case conditions.

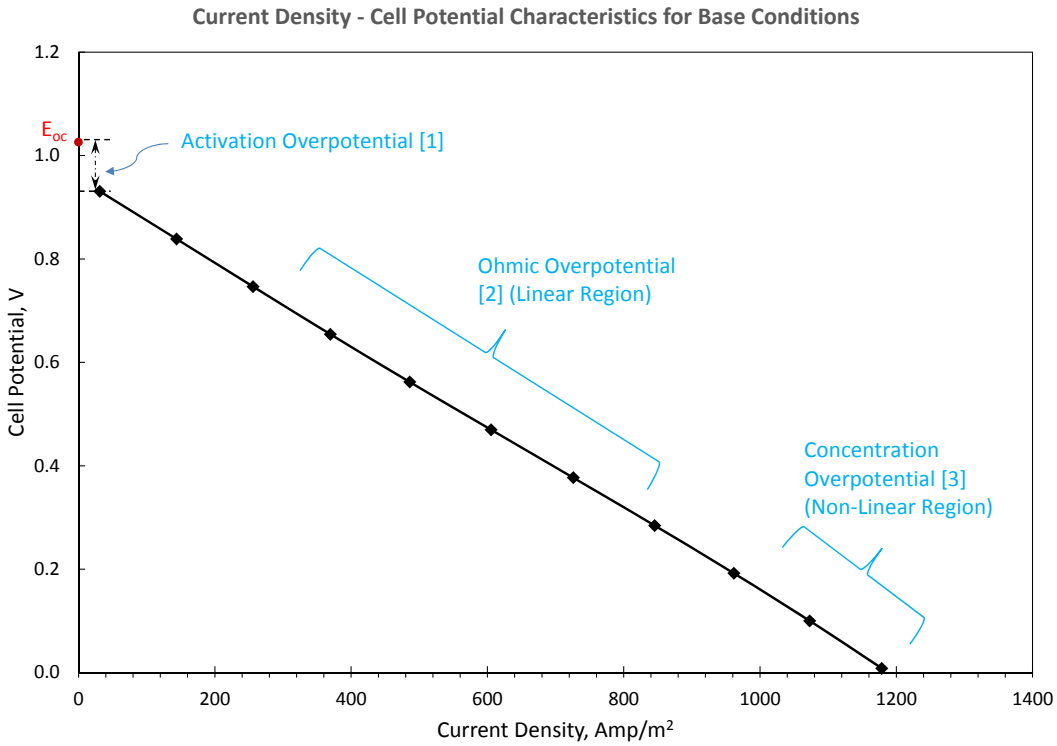

Figure 4.1: Current Density - Cell Voltage Plot showing various regions of polarization for the base case conditions.

Current Density - Power Density plot:

This performance indicator shows parabolic nature of the power density curve with the maximum happening near the current density that is roughly half the limiting current density. Cell doesn't necessarily have to operate at maximum power density, and can depend upon other factors like cell operating efficiency or dictated by the requirements of the operating voltage. The power density is calculated from the product of cell voltage and the current density,

$$P = V_{cell} \times i'' \tag{4.1}$$

Units of Power are in W/m^2, if V_{cell} is in Volts and i'' is in A/m^2.

The plot in figure 4.2 below shows the combined plot of i-V and i-P.D under base conditions. The base case condition relates to bed depths of 10cm for both anode and cathode.

Current Density - Cell efficiency Plot:

The net cell efficiency is calculated as a product of various efficiencies (as given by Cooper, 2012):

$$\eta_{total} = \eta_{util}\,\eta_{coul}\,\eta_{vi}\,\eta_{nernst}\,\eta_{theor} \tag{4.2}$$

As per Cooper, the total net cell efficiency is a product of utilization efficiency (η_{util}), coulombic efficiency (η_{coul}), voltage efficiency (η_{vi}), Nernst efficiency (η_{nernst}), and the theoretical efficiency (η_{theor}).

Utilization efficiency (η_{util}) represents the fuel efficiency and the for the present work it's assumed that all carbon is consumed eventually. Therefore, just like in the work of [Cooper, 2012] the utilization efficiency for the present work is assumed

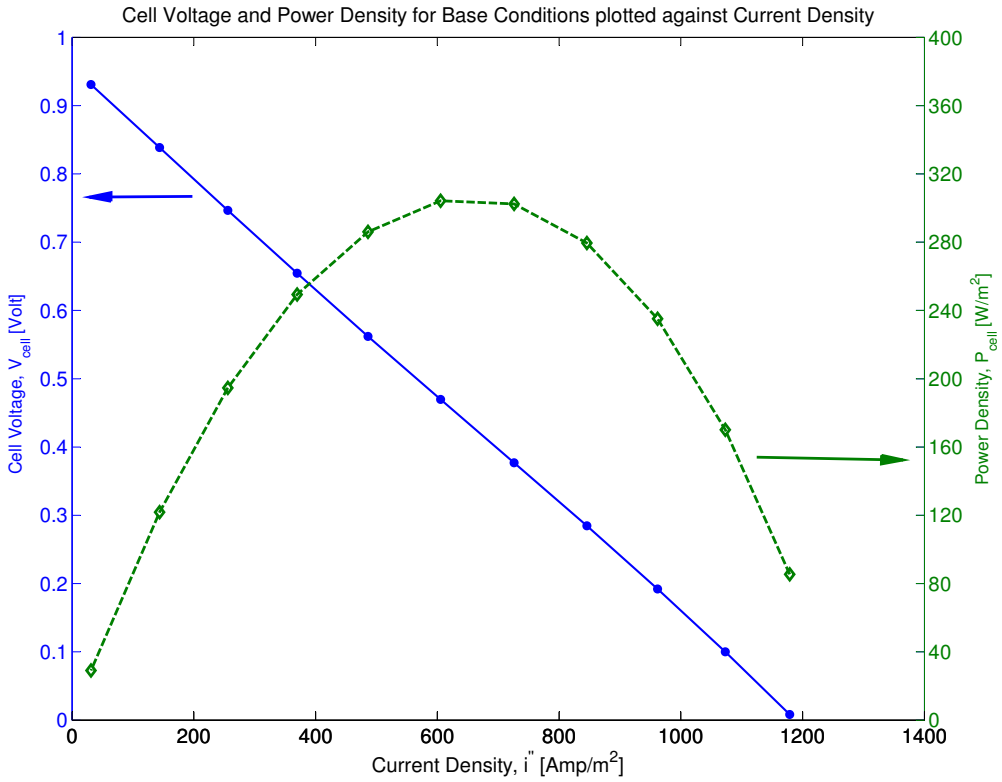

Figure 4.2: Current Density - Voltage and Current Density - Power Density variations for base case conditions.

to be 1.0 as well. Generation of slag/ash in the cell and removed through a side-stream operation is not accounted for in these calculations. It should be noted here that the carbon feed into the cell is maintained as an overfeed factor (γ_c) times the net consumption of carbon throughout the anode bed. For the purpose of modeling, an initial average diameter of carbon particle is assumed. The diameter of carbon particle reduces through the packed bed as the carbon is consumed in the reaction producing CO_2. The effect of carbon particle diameter on the cell performance is studied in the parametric variation section.

Coulombic efficiency (η_{coul}) can indicate the reaction path taken by the cell. There is significant gap in the understanding of actual reaction mechanism taking place for both cathode and anode. Cooper, 2012 shows this efficiency to be only slightly lower than 1.0 and for the purpose of the present work, this factor is assumed to be 1.0.

The Voltage efficiency and the Nernst efficiency have been combined and written as the ratio of cell voltage and the open circuit voltage at reference conditions of 0.67/0.33 atm CO_2/O_2.

$$\eta_{vi}\,\eta_{nernst} = \frac{V_{cell}}{V_{oc,ref}} \tag{4.3}$$

The theoretical efficiency (η_{theor}) indicates the theoretical conversion efficiency of carbon to carbon-dioxide through the oxidation reaction

$$\mathrm{C} + \mathrm{O_2} \longrightarrow \mathrm{CO_2} \tag{4.4}$$

and is given by

$$\eta_{theor} = \frac{\Delta \bar{G}}{\Delta \bar{H}_{reaction}} \tag{4.5}$$

where the heat of reaction ($\Delta \bar{H}_{reaction}$) in the above equation is -393 kJ/mol or -94.05 kcal/mol. For the Base conditions, the change in Gibbs Energy of the above carbon

oxidation reaction is calculated to be -395.92 kJ/mol. The theoretical efficiency is therefore calculated to be 1.0062 or 100.62%. The plot in figure 4.3 below shows the efficiency and power density of the direct carbon molten carbonate fuel cell under base case conditions. The maximum power density occurs at cell efficiency which is slightly higher than 40%.

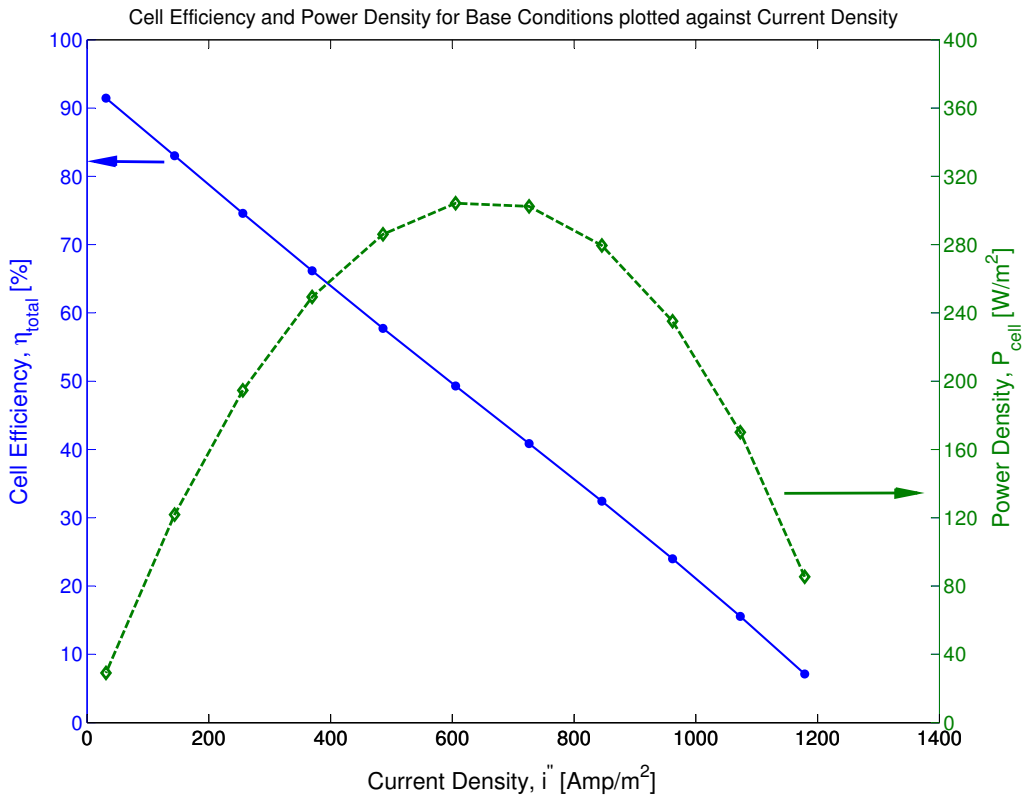

Figure 4.3: Current Density - Efficiency and Current Density - Power Density variations for base case conditions.

4.1.2 Voltage Gradient with Bed Thickness

By making an assumption of a reference voltage being zero at the interface of electrolyte between anode and the cathode beds, open circuit potential, cell potential and chemical over-potential for both beds is shown in figure 4.4. Also shown is the intermediate channel between the anode and the cathode bed which is associated with the transport of carbonate ions from cathode to anode. The thickness of this layer for the base case is 1 cm compared to 10 cm bed thickness for each of anode and cathode. For the base case, and at operating cell voltage of 0.47 V, current density of 605 A/m^2 is achieved. This voltage also includes the voltage drop of roughly $0.03V$ in the intermediate thickness layer. The reason for such low voltage drop is because of the assumption of no grid in the intermediate layer and therefore 100% electrolyte solution to conduct ions.

As can be seen, chemical over-potential is the largest at the beginning of the bed for both anode and cathode. For the cathode, beginning of the bed signifies the inlet of gaseous CO_2 and O_2 and also establishes highest current density in the electrolyte phase due to the high-overpotential. The electrolyte current density drops to zero at the end of the bed due to over-potential getting smaller and smaller. For the anode bed, beginning of the bed also signifies the input of the carbon and molten carbonate slurry.

Voltage drop due to Contact resistance is not evident in the above shown plot of voltage gradient. The reason for this is because the settled particle resistivity for the base case is assumed to be 0.0004 $\Omega - m$ considering work of Kusakabe et al. [1981], Morooka et al. [1981] on measuring particle resistivity of copper particles with stainless steel grid. However, it's possible that the settled particle resistivity is

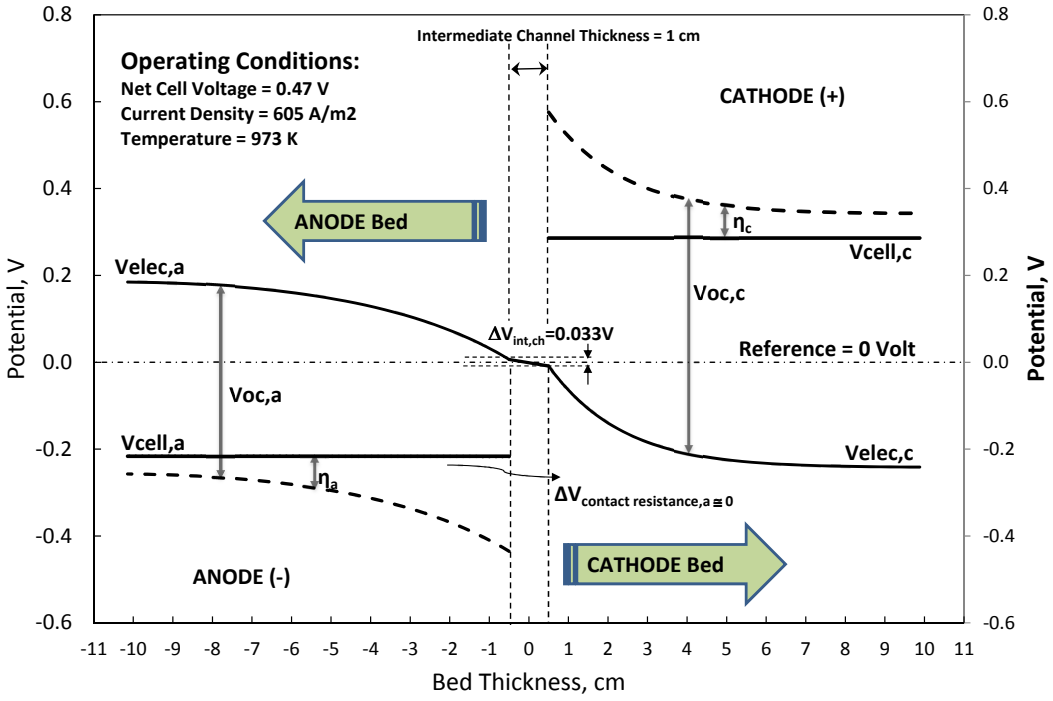

Figure 4.4: Potential Gradients in Cathode and Anode Beds varying with bed thickness for the base case conditions. Electrolyte Used as Base Case - Li/Na/K ternary eutectic - 43.5/31.5/25 mole%; Settled Particle Resistivity in Anode Bed, $\rho_{ct,0} = 0.0004\,\Omega - m$**; Liquid Electrolyte Superficial Velocity (anode/cathode) =** $0.1\,m/s$**, Bed depth (anode/cathode) =** $10\,cm/10\,cm$**; Cathode gas composition - CO_2 =** $0.2\,atm$**, O_2 =** $0.168\,atm$ **and N_2 = remaining; Feed Gas Flow Rate in Cathode;** $F_V = 0.1\,m^3/hr$ **per** $1cm^2$ **cell area;** $T = 973\,K$**; Carbon particle initial diameter,** $D_{c,ini} = 175\,\mu m$**; Grid Packing:: Wire-Mesh # 24 (anode), # 30 (cathode); Solid hold-up (carbon) at anode inlet =** 0.21**.**

two order of magnitude higher than what has been assumed because conductivity of graphite is at least two orders of magnitude lower than that of copper. Due to lack of experimental data in this regard, this assumption had to be considered. The sensitivity to settled particle resistivity is also later on covered in the parametric variation to show it's effect on the cell performance.

Presently, assuming settled particle resistivity to be 0.04 $\Omega - m$, contact resistance in anode suddenly becomes significant. This effect is observed in figure 4.5 below. It can be seen that the voltage drop due to contact resistance is much higher at the beginning of the bed and diminishes to a negligible value at the end of the bed. This is due to it's dependence on the volume based charge-transfer current density (reaction rate). Due to additional voltage drop due to contact resistance, cell performance has dropped down to 556 A/m^2 from the earlier value of 605 A/m^2.

4.1.3 Anode Kinetics and Mass Transfer

The anode kinetics have been described through the use of kinetic data from experiments conducted by Ateya for the SRI coal research reported by Weaver et al. [1979][Appendix B] and the Butler Volmer type charge-transfer current density equations developed in this thesis. The data from Ateya have not indicated dependence of the kinetics on the CO_2 concentration at the reaction site or in the bulk liquid. It is indicated that the open circuit potential are measured relative to the reference electrode 0.67/0.33 CO_2/O_2 and also based on the CO_2 partial pressure being 1.0. It's not very clear if the CO_2 was used along with the purge gas helium during the experiment since no dependence on mole fractions of CO_2 is

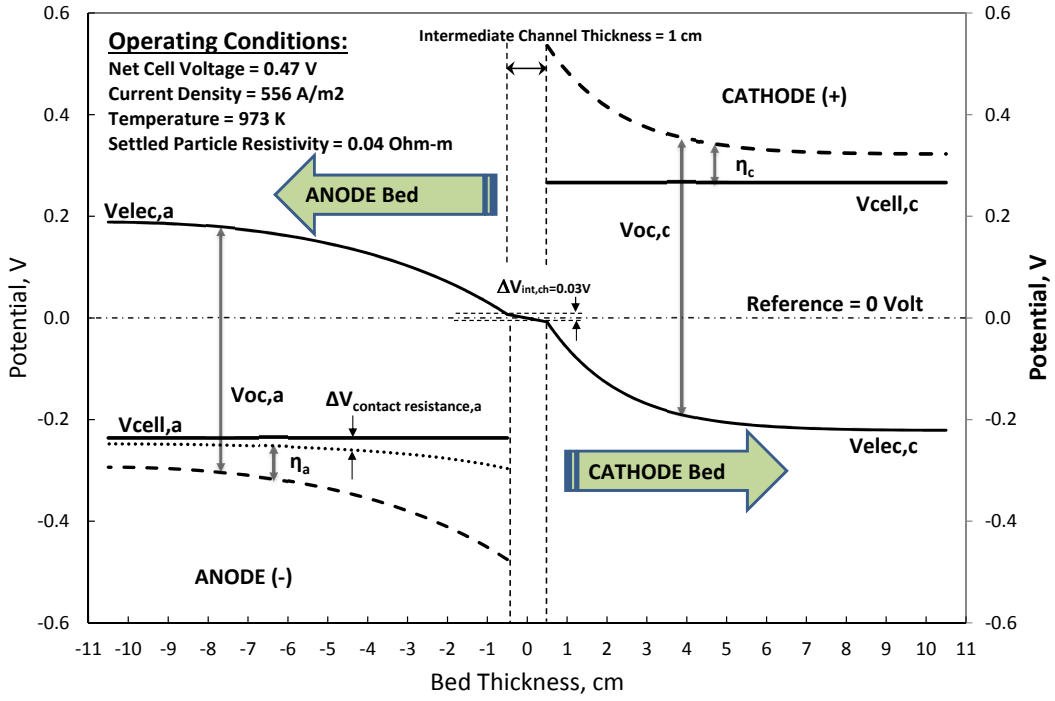

Figure 4.5: Potential Gradients in Cathode and Anode Beds varying with bed thickness showing voltage drop due to contact resistance. Electrolyte Used as Base Case - Li/Na/K ternary eutectic - 43.5/31.5/25 mole%; Settled Particle Resistivity in Anode Bed, $\rho_{ct,0} = 0.04\,\Omega - m$**; Liquid Electrolyte Superficial Velocity (anode/cathode) =** $0.1\,m/s$**, Bed depth (anode/cathode) =** $10\,cm/10\,cm$**; Cathode gas composition - CO_2 =** $0.2\,atm$**, O_2 =** $0.168\,atm$ **and N_2 = remaining; Feed Gas Flow Rate in Cathode;** $F_V = 0.1\,m^3/hr$ **per** $1cm^2$ **cell area;** $T = 973\,K$**; Carbon particle initial diameter,** $D_{c,ini} = 175\,\mu m$**; Grid Packing:: Wire-Mesh # 24 (anode), # 30 (cathode); Solid hold-up (carbon) at anode inlet =** 0.21**.**

shown. Vutetakis [1985] experiments used coal slurry and similar set-up using 3% and 100% CO_2 in the purge gases. However, it seems from the experimental data that there is no significant effect on the current density for the two different cases of 3% and 100% CO_2 as shown in figure 4.6.

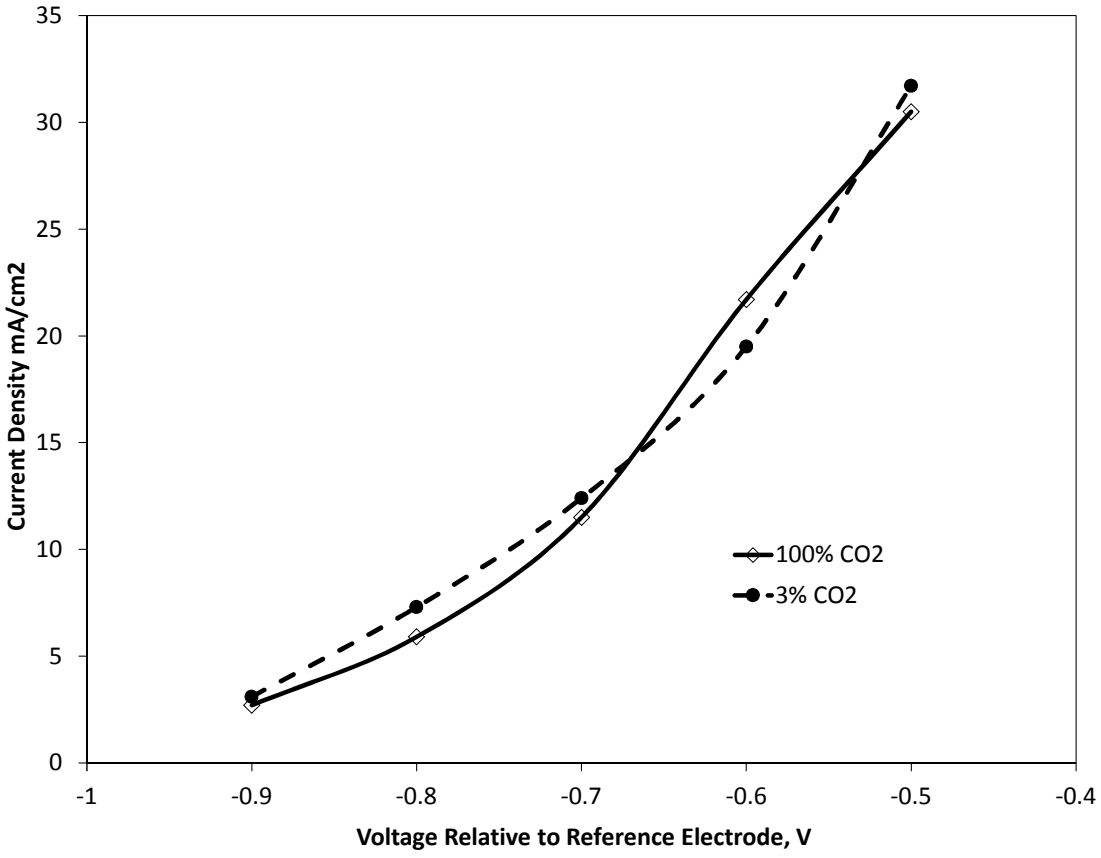

Figure 4.6: Experimental results extracted from the work of Vutetakis [1985] indicating no influence of inert purge gas on the current density.

This situation is clarified by the work of Yasuda done as part of SRI coal research reported by Weaver et al. [1979][Appendix A]. As per this work, it is sufficiently clear that the data at open circuit conditions is normally determined with

the electrolyte melt saturated with dissolved CO_2 that is in equilibrium with the CO_2 at 1 atm pressure (evaluated through Henry's Law solubility relationship). It is therefore posited that at non-zero currents, CO_2 is in a super-saturated state at the carbon particle surface reaction sites and also in the bulk liquid and that there is a net driving force (concentration difference) from the surface of the carbon particle (reaction site) and into the gas bubbles. The driving force is met with the mass transfer resistance that is a combination of resistance from solid-to-bulk liquid and from bulk liquid-to-gas bubble.

Figure 4.7 shows molar concentration of CO_2 at the carbon particle surface (reaction site) for base case conditions. Three different operating conditions are shown in the plot indicating that the higher driving force for the anodic reaction indicates higher current densities. It should be noted that for current densities approaching zero (approaching open circuit conditions), the concentration approaches the reference concentration of CO_2 which is also same as the concentration in the gas bubble. The difference in concentrations at the carbon surface and in the bulk liquid phase provides the driving force required to facilitate the reaction at the anode. At bed depth, $x_a = 0$, the driving force is the maximum and the concentration of CO_2 in the bulk liquid phase is roughly in equilibrium with the CO_2 in the gas bubble phase. But as the distance into the bed increases, more CO_2 is evolved at the surface causing the electrolyte liquid melt to become super-saturated with CO_2. This effect is shown for both high and low current density situations in figure 4.8.

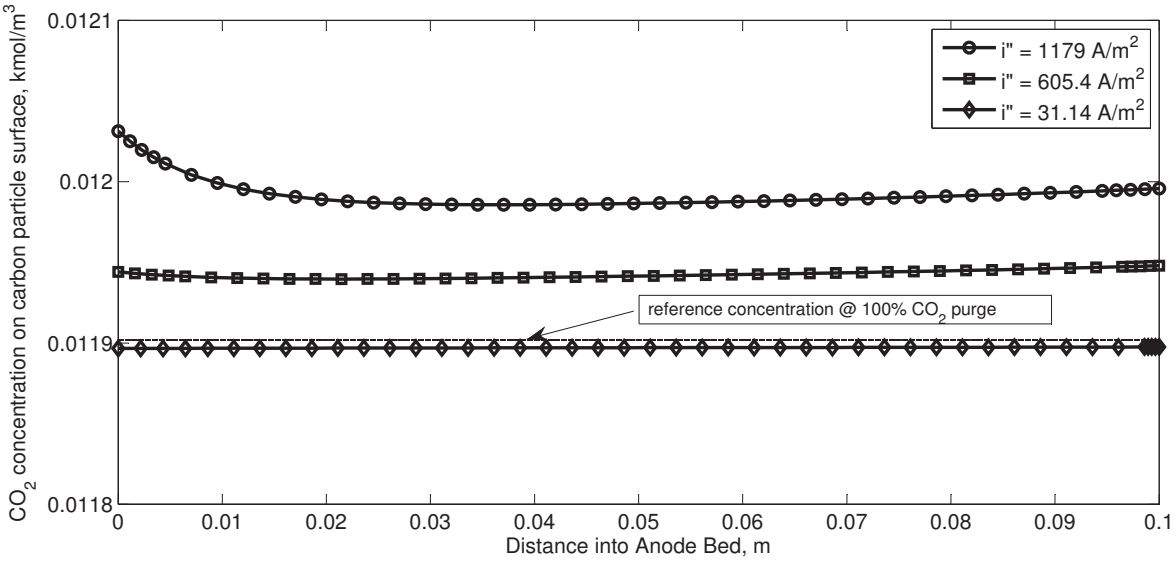

Figure 4.7: Molar Concentration of CO_2 at the carbon particle surface (reaction site) for base case conditions.

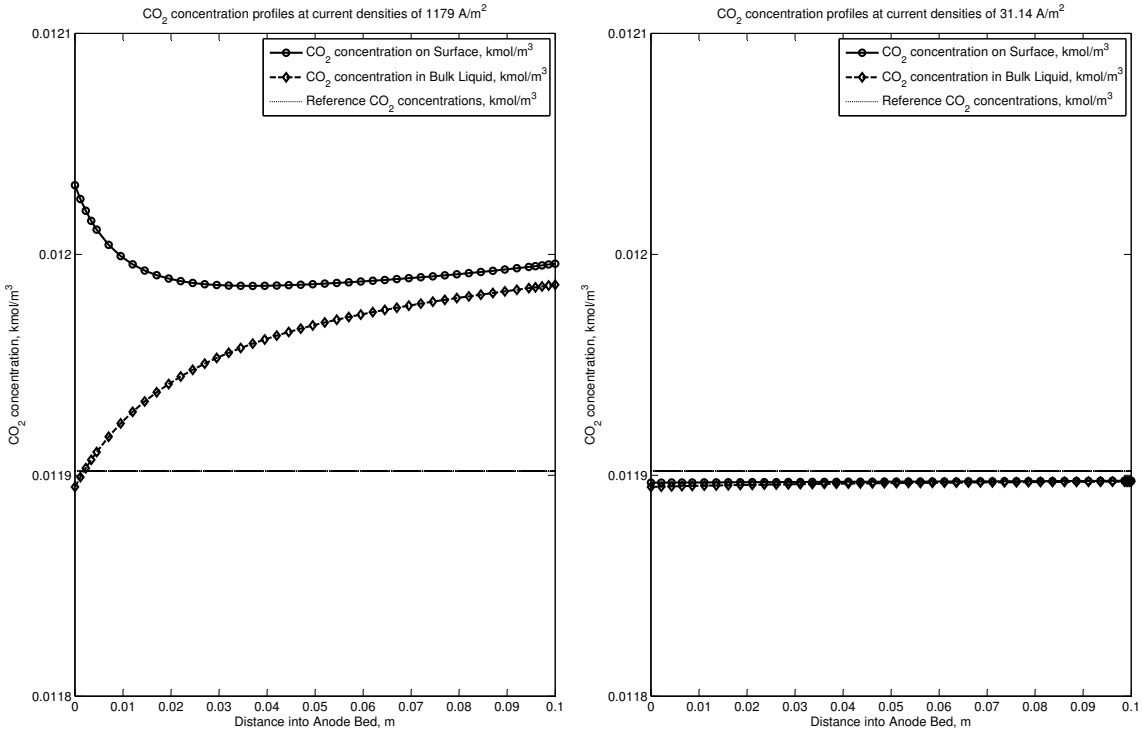

(a) (b)

Figure 4.8: CO_2 Concentration Profiles at the surface, bulk liquid, and at equilibrium for base case conditions. (a) High Current Density (=1179 A/m^2) region (b) Low Current density (=34 A/m^2) region. Base Conditions described by:: Electrolyte - Li/Na/K ternary eutectic - 43.5/31.5/25 mole%; Settled Particle Resistivity in Anode Bed, $\rho_{ct,0} = 0.0004\,\Omega - m$; Superficial Liquid Velocity (Anode/Cathode) = $0.1\,m/s$, Bed thickness (Anode/Cathode) = $10\,cm/10\,cm$; Cathode gas composition - CO_2 = $0.2\,atm$, O_2 = $0.168\,atm$ and N_2 = remaining; Feed Gas Flow Rate in Cathode; $F_V = 0.1\,m^3/hr$ per $1cm^2$ cell area; $T = 973\,K$; Carbon particle initial diameter, $D_{c,ini} = 175\,\mu m$; Grid Packing:: Wire-Mesh # 24 (anode), # 30 (cathode); Solid hold-up (carbon) at anode inlet = 0.21.

4.1.4 Cathode Kinetics and Mass Transfer

The base case results presented here use the cathodic reaction kinetics model developed by Wilemski [1983] guided by the peroxide mechanism as has been explained in previous sections. The kinetic model demonstrates dependence of exchange current density on the partial pressures of the gas species, CO_2 and O_2. The model incorporates the rate kinetic factors developed from experimentally validated data in the form of a charge-transfer current density equation in the form of a Butler Volmer equation for a multi-step reaction mechanism. The charge-transfer current density equation is dependent upon the concentrations of species CO_2 and O_2 at the reaction sites (packing grid surface), the over-potential that is the difference between the open circuit potential and the cell voltage, the exchange current density that is experimentally determined, and the temperature of the cell.

Higher concentrations of species CO_2 and O_2 at the reaction sites (packing grid surface) can enable better cell performance by providing better charge-transfer kinetics at higher current densities (or higher over-potential). At lower current densities (higher cell voltage and lower over-potential), the effect will be significantly smaller. This is also very clearly demonstrated using the base case results from cathode bed analysis.

Concentration Profiles

For higher current densities, figure 4.9 [left] presents the CO_2 concentration gradients responsible for driving the forward reactions in cathode. It's clear from the plots that at high current densities, significant driving force is available from liquid to surface mass transport of CO_2 compared with the difference in concentrations

at bulk liquid and the equilibrium. The reason for this big driving force is because the concentration of CO_2 at the grid surface is depleted rapidly under conditions of oxidation (reaction with O_2) to form carbonate ions. At start of the bed (cathode inlet, $x = 0$), it is assumed that the molten carbonate salt electrolyte is saturated with CO_2 which is also evident from the graph. However, further into the bed, concentration of CO_2 in the bulk liquid goes below the equilibrium conditions due to mass transport to the grid surface where the cathode reaction takes place.

For low current density condition (low over-potential or high cell-voltage) figure 4.9 [right] presents the CO_2 concentration profiles in the bed at the grid surface, in bulk liquid and in equilibrium. Due to very low reaction rates, the mass transport of CO_2 from gas-bubble phase to bulk-liquid and to grid surface is quite slow as can be seen from the lack of any significant variation in the concentration profiles.

The less the CO_2 and O_2 reach the grid surface to react, less will be the reaction rate. Alternatively, for lower current densities, the driving forces (concentration gradients) are not very large when compared with the higher current density case and therefore quite insignificant.

The concentration profiles for O_2 are shown in the figure 4.10. There's at least one order of magnitude difference in the concentrations in the gas phase, liquid phase, and at grid surface. However, the gas-liquid mass transfer still offers significant resistance to the cathode kinetics.

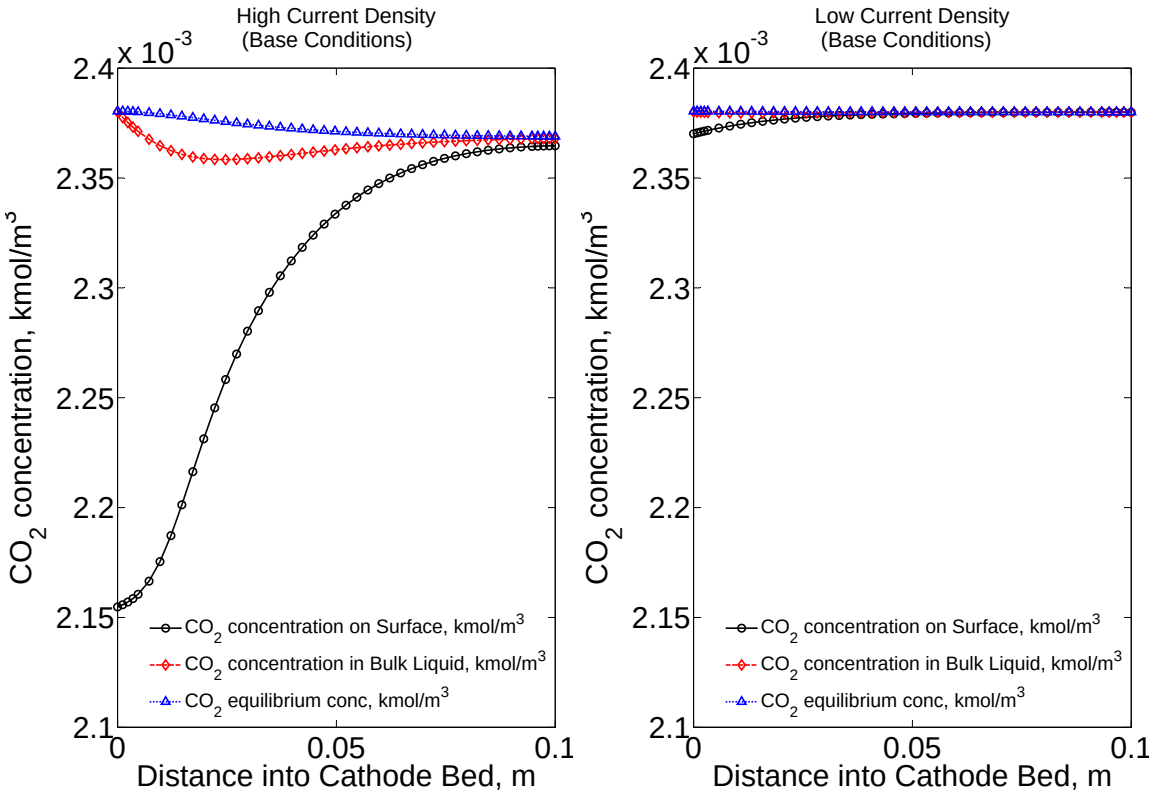

(a) (b)

Figure 4.9: CO_2 Concentration Profiles at the surface, bulk liquid, and at equilibrium for base case conditions. (a) High Current Density (=1179 A/m^2) region (b) Low Current density (=34 A/m^2) region. Base Conditions described by:: Electrolyte - Li/Na/K ternary eutectic - 43.5/31.5/25 mole%; Settled Particle Resistivity in Anode Bed, $\rho_{ct,0} = 0.0004\,\Omega - m$; Superficial Liquid Velocity (Anode/Cathode) = $0.1\,m/s$, Bed thickness (Anode/Cathode) = $10\,cm/10\,cm$; Cathode gas composition - CO_2 = $0.2\,atm$, O_2 = $0.168\,atm$ and N_2 = remaining; Feed Gas Flow Rate in Cathode; $F_V = 0.1\,m^3/hr$ per $1cm^2$ cell area; $T = 973\,K$; Carbon particle initial diameter, $D_{c,ini} = 175\,\mu m$; Grid Packing:: Wire-Mesh # 24 (anode), # 30 (cathode); Solid hold-up (carbon) at anode inlet = 0.21.

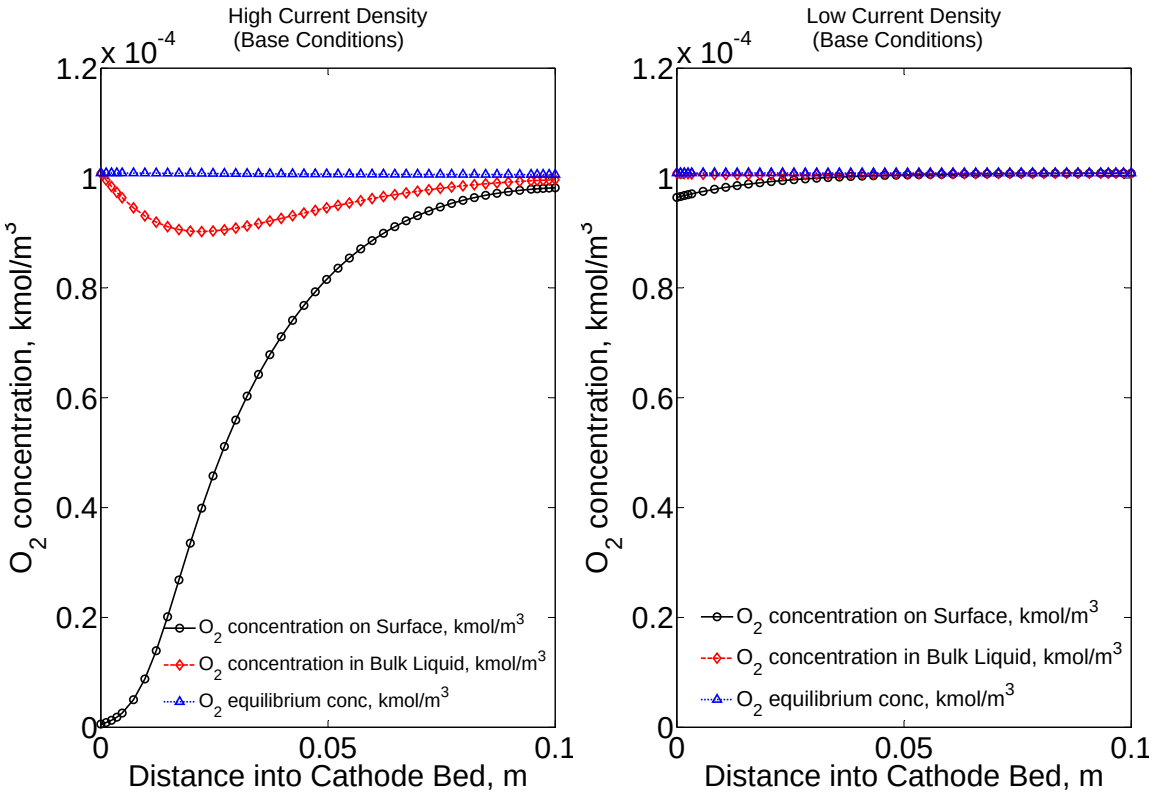

(a) (b)

Figure 4.10: O_2 Concentration Profiles at the surface, bulk liquid, and at equilibrium for base case conditions. (a) High Current Density (=1179 A/m^2) region (b) Low Current density (=34 A/m^2) region. Base Conditions described by:: Electrolyte - Li/Na/K ternary eutectic - 43.5/31.5/25 mole%; Settled Particle Resistivity in Anode Bed, $\rho_{ct,0} = 0.0004\,\Omega - m$; Superficial Liquid Velocity (Anode/Cathode) = $0.1\,m/s$, Bed thickness (Anode/Cathode) = $10\,cm/10\,cm$; Cathode gas composition - CO_2 = $0.2\,atm$, O_2 = $0.168\,atm$ and N_2 = remaining; Feed Gas Flow Rate in Cathode; $F_V = 0.1\,m^3/hr$ per $1cm^2$ cell area; $T = 973\,K$; Carbon particle initial diameter, $D_{c,ini} = 175\,\mu m$; Grid Packing:: Wire-Mesh # 24 (anode), # 30 (cathode); Solid hold-up (carbon) at anode inlet = 0.21.

Mass Transfer

Tha mass transfer of species CO_2 and O_2 from gas phase to bulk liquid phase and from bulk liquid phase to the grid surface has been estimated using various correlations from the literature as shown in previous section on process modeling. It must be noted that these correlations provide approximate orders of magnitude and has not been validated with any experimental data. The actual mass transfer rates could be better or worse than that provided by the empirical correlations. One way to demonstrate sensitivity of mass transfer effects would be to conduct parametric variations for mass transfer coefficients and observe the effect on the performance of the cell. This analysis is presented in later results section.

4.2 Parametric Analysis with Respect to Design Parameters

This section presents results from the sensitivity analysis conducted on some important parameters that can cause significant change in overall fuel cell performance. The basic fuel cell performance indicators such as: current density-voltage relationship plots, fuel cell efficiency and power density for different current densities. The following independent variables are selected for this analysis:

1. Feed Gas Flow Rate in the Cathode
2. Cathode Bed Depth
3. Anode Bed Depth
4. Rate Kinetics - Cathode
    - Cathode Feed Gas Composition - Variation in CO_2 partial pressure
    - Cathode Feed Gas composition - Variation in O_2 partial pressure
5. Cell Temperature
6. Liquid Electrolyte Velocity (Cathode and Anode)
7. Effect of the intermediate electrolyte layer between cathode and anode responsible for the transport of carbonate ions from cathode to anode.
8. Packing Characteristics - Wire-mesh of different sizes or perforated plates with different hole sizes and transverse inter-spacing - Change in area per

unit volume that affects the hold-up, mass transfer and area current density in cathode.

9. Carbon particle diameter - The average carbon particle diameter is used to evaluate area current density in the anode bed. Higher the carbon particle diameter, lower is the area per unit volume and therefore lower will be the area current density. Also from the liquid-solid holdup correlations in the anode, reduction in carbon particle diameter also reduces solid-holdup that tends to increase contact resistance slightly which can reduce the current density. There will be be an optimized size of carbon particle that is a result from this analysis.

4.2.1 Feed Gas Flow Rate in the Cathode:

The default feed gas flow rate selected for base case operating condition is 0.1 m^3/hr. Values of 0.01 and 1.0 are selected to show the effect that a change in feed gas flow will have on the cell performance.

Lower feed gas flow rate of 0.01 m^3/hr will mean availability of less gas flux within the cathode bed signifying lower gas holdup in the liquid electrolyte and possibly causing lower ohmic resistance offered by the bed against the current flow and may mean lower polarization and better cell performance. Now, the model operates in a steady state mode and assumes the liquid electrolyte in cathode to be saturated with the feed gas. Therefore lowering the feed gas flow rate would imply that during the transient phase of cell operation it might take additional residence time for the liquid electrolyte to reach the state of saturation. However, for the purpose of evaluating cell performance, lower gas flow should not negatively affect

the cell performance but in fact improve it owing to less ionic resistance from the bubbles in the electrolyte. Alternatively, higher gas flow would signify higher gas hold-up and therefore higher ionic resistance from more bubbles in the electrolyte. This parametric variation is shown in figure 4.11 and results are as expected.

What has been observed is that the gas holding capacity of the molten carbonate salt is quite large and therefore maintaining low gas flow rates would not be able to bring the molten carbonate saturated with CO_2 and O_2 eventually and affect cell performance. Higher gas flow rates will encounter higher ohmic resistance and reduced cell performance. There is probably an optimum gas flow rate that maintains higher cell performance, however this effect has not been studied in greater detail and maybe considered for future work.

4.2.2 Variation in Cathode Bed Depth

This analysis has been performed for higher and lower feed gas flow rates. From 4.12, it is observed that there are some accountable differences in the performance of fuel cell at different cathode feed gas flow rates of 0.01 and 1 m^3/hr when compared to variations at different cathode bed depth. It is observed that at lower cathode feed gas flow rates and smaller bed depth, volumetric current density (based on Butler Volmer kinetics) is left unused at the end of the cathode bed and is much greater than the expected value of zero. This possibly signifies mixed kinetic and mass transfer control and that the limitation is reduced by having larger bed depth. At higher bed depths ohmic polarization is more in control as can be seen from the linearity of the V-I curve near higher over-potential region because overall effect of kinetics and mass transfer is not limiting the reaction. It is therefore

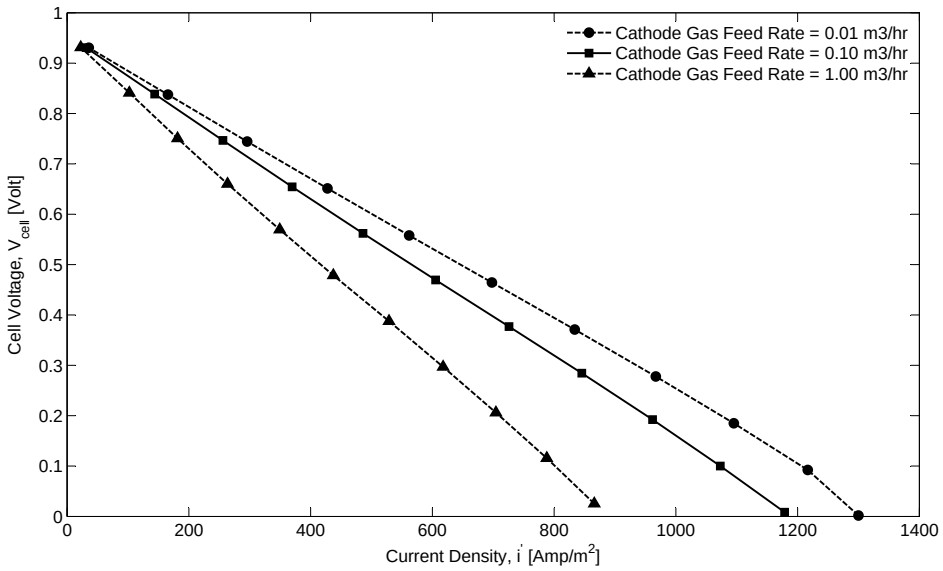

Figure 4.11: Current Density - Cell Voltage Variation with cathode feed gas flow rate. Electrolyte - Li/Na/K ternary eutectic - 43.5/31.5/25 mole%; Settled Particle Resistivity in Anode Bed, $\rho_{ct,0} = 0.0004\,\Omega - m$**; Liquid Electrolyte Superficial Velocity (anode/cathode) =** $0.1\,m/s$**, Bed depth (anode/cathode) =** $10\,cm/6\,cm$**; Cathode gas composition - CO_2 =** $0.2\,atm$**, O_2 =** $0.168\,atm$ **and N_2 = remaining; Feed Gas Flow Rate in Cathode;** $F_V = 0.01, 0.1 and 1.0\,m^3/hr$ **per** $1cm^2$ **cell area;** $T = 973\,K$**; Carbon particle initial diameter,** $D_{c,ini} = 175\,\mu m$**; Grid Packing:: Wire-Mesh # 24 (anode), # 30 (cathode); Solid hold-up (carbon) at anode inlet =** 0.21**.**

favorable to have the maximum possible bed depth that can be achieved in any cell design. However, having maximum depth of bed beyond a feasible limit can tend to increase cost of bed materials, increased residence time of electrolyte within the bed, and a dead volume that does not contribute to the fuel cell performance. It seems from the results that an optimum cathode bed depth between 8-10 cm is quite reasonable considering versatile operating conditions.

4.2.3 Variation in Anode Bed Depth

The variation in anode bed depth produces similar results as in the cathode. As shown in figure 4.13, at lower bed depths, the fuel cell operation remains under mixed kinetic and mass transfer control. This limitation is not discernible as soon as the bed depth remains higher than 10 cm. At 5 cm bed depth, the volumetric current density in anode has not reduced to zero but is of significant value causing kinetic/mass transfer limitation.

4.2.4 Charge-Transfer Current Density in Cathode

The charge transfer volumetric current density is the rate kinetic Butler Volmer equation to predict variation in current density with respect to over-potential at the reaction site (grid surface). The area current density is calculated from the product of volumetric current density and area per unit bed volume of the grid surface. The equation for charge transfer volumetric current density is derived from the work of Wilemski et al. [1979], Wilemski [1983] which itself utilizes data from experiments conducted on molten carbonate fuel cells using Li/Na/K ternary eutectic and Na/K

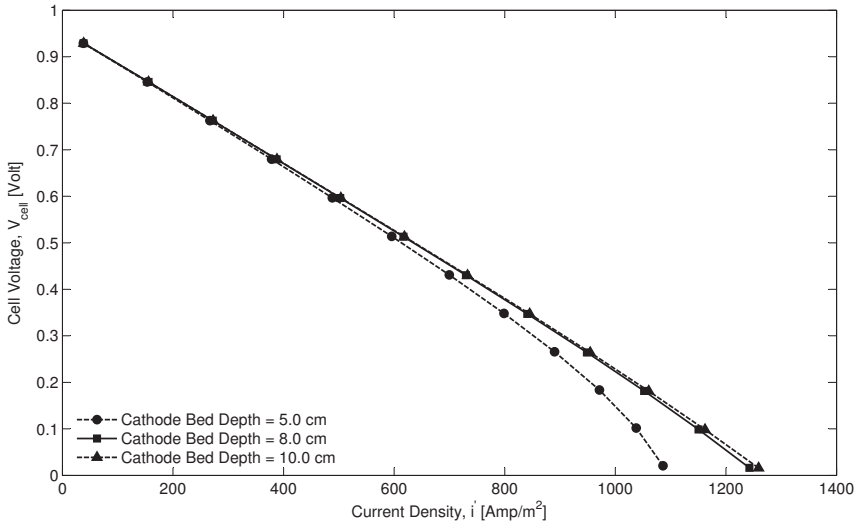

(a)

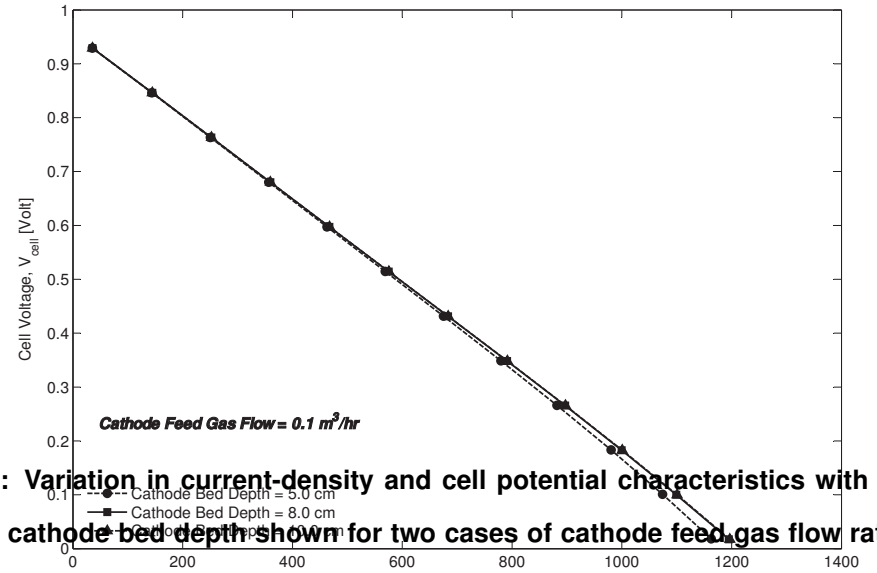

(b)

Figure 4.12: Variation in current-density and cell potential characteristics with respect to variation in cathode bed depth shown for two cases of cathode feed gas flow rates, F_V. (a) 0.01 m3/hr (b) 0.1 m3/hr. Electrolyte - Li-Na-K ternary eutectic - 43.5/31.5/25 mole%; Settled Particle Resistivity in Anode Bed, $\rho_{ct,0} = 0.0004\,\Omega - m$; Liquid Electrolyte Superficial Velocity (anode/cathode) = $0.1\,m/s$, Bed depth (anode/cathode) = $10cm/6cm$; Cathode gas composition - CO_2 = $0.1/0.2/0.3\,atm$, O_2 = $0.168\,atm$ and N_2 = remaining; Feed Gas Flow Rate in Cathode; $F_V = 0.1\,m^3/hr$ per $1cm^2$ cell area; $T = 973\,K$; Carbon particle initial diameter, $D_{c,ini} = 175\,\mu m$; Grid Packing:: Wire-Mesh # 24 (anode), # 30 (cathode); Solid hold-up (carbon) at anode inlet = 0.21.

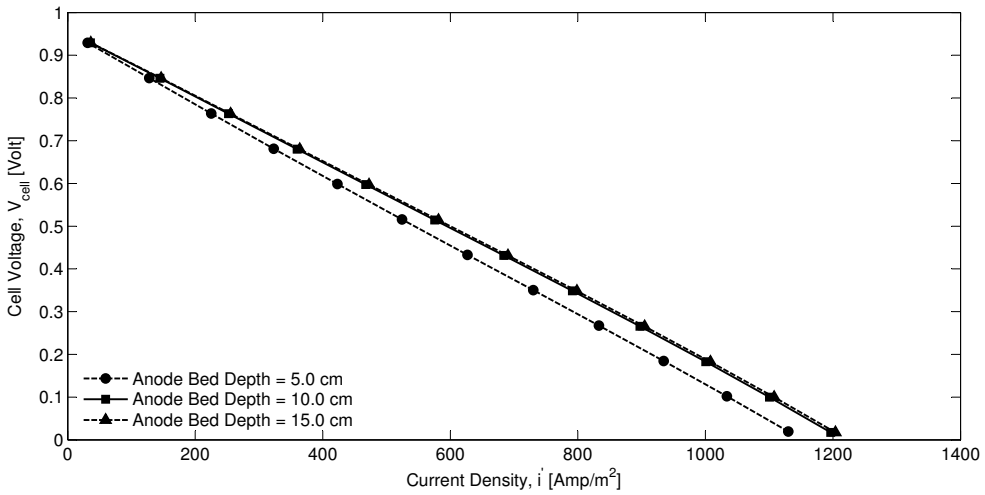

Figure 4.13: Current Density - Cell Voltage Variation with varying anode bed depth. Electrolyte - Li/Na/K ternary eutectic - 43.5/31.5/25 mole%; Settled Particle Resistivity in Anode Bed, $\rho_{ct,0} = 0.0004\,\Omega - m$**; Liquid Electrolyte Superficial Velocity (anode/cathode) =** $0.1\,m/s$**, Bed depth (anode/cathode) =** $10\,cm/6\,cm$**; Cathode gas composition -** CO_2 **=** $0.1/0.2/0.3\,atm$**,** O_2 **=** $0.168\,atm$ **and** N_2 **= remaining; Feed Gas Flow Rate in Cathode;** $F_V = 0.1\,m^3/hr$ **per** $1cm^2$ **cell area;** $T = 973\,K$**; Carbon particle initial diameter,** $D_{c,ini} = 175\,\mu m$**; Grid Packing:: Wire-Mesh # 24 (anode), # 30 (cathode); Solid hold-up (carbon) at anode inlet =** 0.21**.**

binary mixtures of molten carbonate salts at the Institute of Gas Technology (IGT). Wilemski put efforts to validate/fit either peroxide or super-oxide mechanism with the experimental data and came up with the:

1. Exponents on CO_2 and O_2 concentrations in the forward and reverse current conditions;

2. Coefficients vital to the rate kinetics - charge transfer coefficient, α and exchange current density, i_o''; and

3. Exponents that are responsible for the variation in exchange current density as a function of CO_2 and O_2 concentrations.

Typically, points number 1 and 3 maybe combined to simply yield a necessity for exponents on CO_2 and O_2 concentrations in the forward and reverse current conditions and the kinetic constants - α and i_o''. However, this kind of separation between bullet points 1 and 3 is also preserved by many other researchers Winnick and Ross Jr. [1981], Kunz et al. [1984], Uchida et al. [1986], Yuh and Selman [1991], Lu and Selman [1992] and preserved in the current work as well.

According to Wilemski et al. [1979], and as shown in section on Electrode Kinetics, two possible mechanisms for reduction of oxygen in alkali molten carbonate salts are considered, i.e. first wave (peroxide) and second wave (super-oxide). From this work, it's clear that expressions for i'' and i_o'' should depict increased electrode performance with increased partial pressures of oxygen plus carbon dioxide but the opposite is predicted from the models developed for both waves. And therefore, work from Wilemski et al. [1979], Wilemski [1983] indicate a development of a general charge transfer volumetric current density equation with exponents and

charge transfer coefficient that best fits the overall experimental data.

In this section, we must look at the observed effect on fuel cell performance with variation in partial pressures of CO_2 and O_2.

O_2 inlet partial pressure in cathode

The independent variation in O_2 inlet partial pressure in cathode without varying CO_2 partial pressure is practically only possible if oxygen supply is used instead of air mixed with CO_2. However, it would be pertinent to see the individual effect on the cell performance when O_2 inlet partial pressure is varied in the range of 0.08 - 0.25 atm. Practically, when air is being used then the O_2 and CO_2 inlet partial pressures are tied together by the remaining component N_2. Any changes in CO_2 inlet partial pressure produces variation in O_2 inlet partial pressure and vice-versa.

The effect on current density - cell voltage relationship with variation in O_2 inlet partial pressure is shown in figure 4.14: The charge-transfer current density expression for cathode is a function of exchange current density and the net forward reaction rate that depends upon the charge transfer coefficient, over-potential and the concentrations of gaseous species on the grid surface (reaction sites). The exchange current density itself is a function of partial pressure of O_2 and CO_2. However in the base case expression the partial pressure of CO_2 and O_2 are raised to the power 0 and 0.4 respectively as per recommendation from Wilemski [1983]. The effect of O_2 partial pressure on exchange current density probably overwhelms any negative effect due to the reverse reaction (at lower over-potential or higher cell voltages). However, this is not the case when inlet partial pressure of CO_2 is varied because it's exponent, $\tau = 0$.

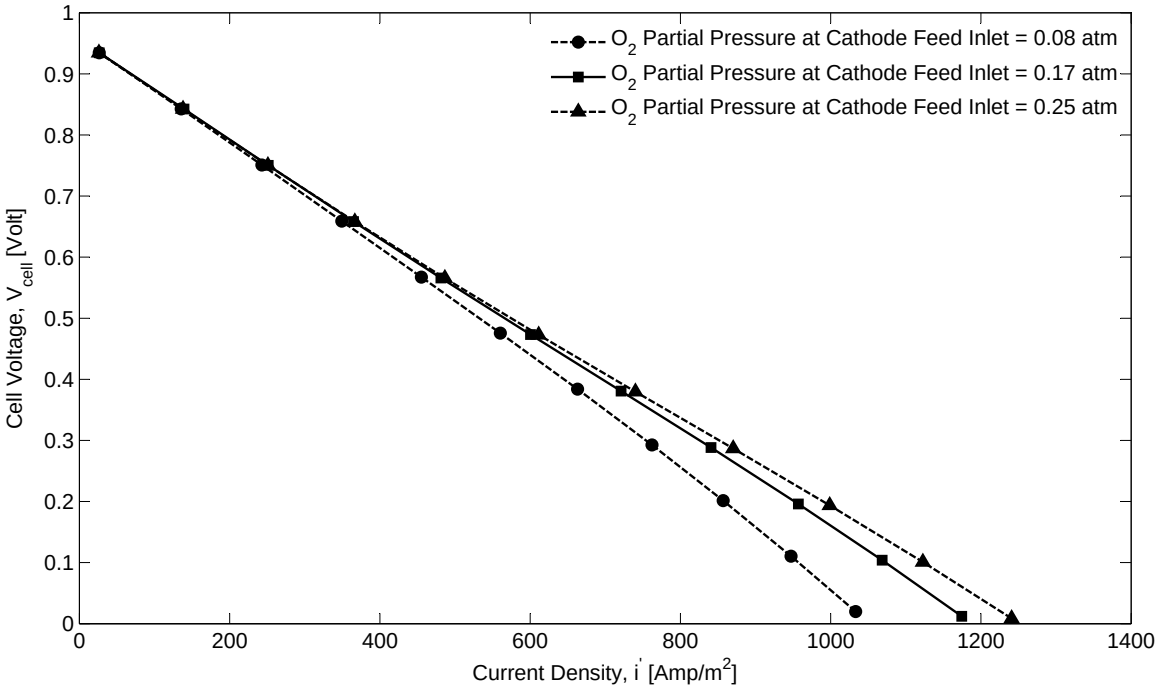

Figure 4.14: Current Density - Cell Voltage Variation with varying O_2 inlet partial pressure. Electrolyte - Li/Na/K ternary eutectic - 43.5/31.5/25 mole%; Settled Particle Resistivity in Anode Bed, $\rho_{ct,0} = 0.0004\,\Omega - m$; Liquid Electrolyte Superficial Velocity (anode/cathode) = $0.1\,m/s$**, Bed depth (anode/cathode) =** $10\,cm/6\,cm$**; Cathode gas composition - CO_2 =** $0.2\,atm$**, O_2 =** $0.17\,atm$ **and N_2 =** $0.63\,atm$**; Feed Gas Flow Rate in Cathode;** $F_V = 0.1\,m^3/hr$ **per** $1cm^2$ **cell area;** $T = 973\,K$**; Carbon particle initial diameter,** $D_{c,ini} = 175\,\mu m$**; Grid Packing:: Wire-Mesh # 24 (anode), # 30 (cathode); Solid hold-up (carbon) at anode inlet =** 0.21**.**

CO_2 inlet partial pressure in cathode

Figure 4.15 shows current-density and cell voltage performance characteristics with the change in the inlet partial pressure of CO_2 in the feed gas in cathode. The results are shown for 0.1, 0.2, and 0.3 atm. The O_2 partial pressure is kept constant at 0.168 atm while remaining is the N_2. The air composition with respect to O_2 and N_2 is not maintained for this analysis so as to avoid the effects of variability in O_2 partial pressure. Results show higher activation losses for low values of CO_2 partial pressure (0.1 atm) when compared to performance at higher CO_2 partial pressure (0.3 atm). The limiting current density is not affected much by the change in CO_2 partial pressure which probably signifies kinetic control. The limiting current density is only affected by change in partial pressure of O_2 and not CO_2 simply because of strong dependence of exchange current density upon O_2 partial pressure and not at all on the partial pressure of CO_2.

4.2.5 Cell Temperature

The variation in cell current-density - potential with respect to variation in cell temperature is shown in figure 4.16. As seen from the figure, temperature variation seems to have a very significant effect on the cell performance. The most plausible reason for such variation can be explained by the fact that reaction kinetics depend significantly upon the temperature and typically lower temperature indicates slower kinetics whereas high temperature can make it possible for the rate-determining reaction step to proceed faster than that at lower temperature. This is clearly seen from the kinetic factors like exchange current density and charge transfer coefficient being functions of temperature. Works of Wilemski [1983] and Weaver

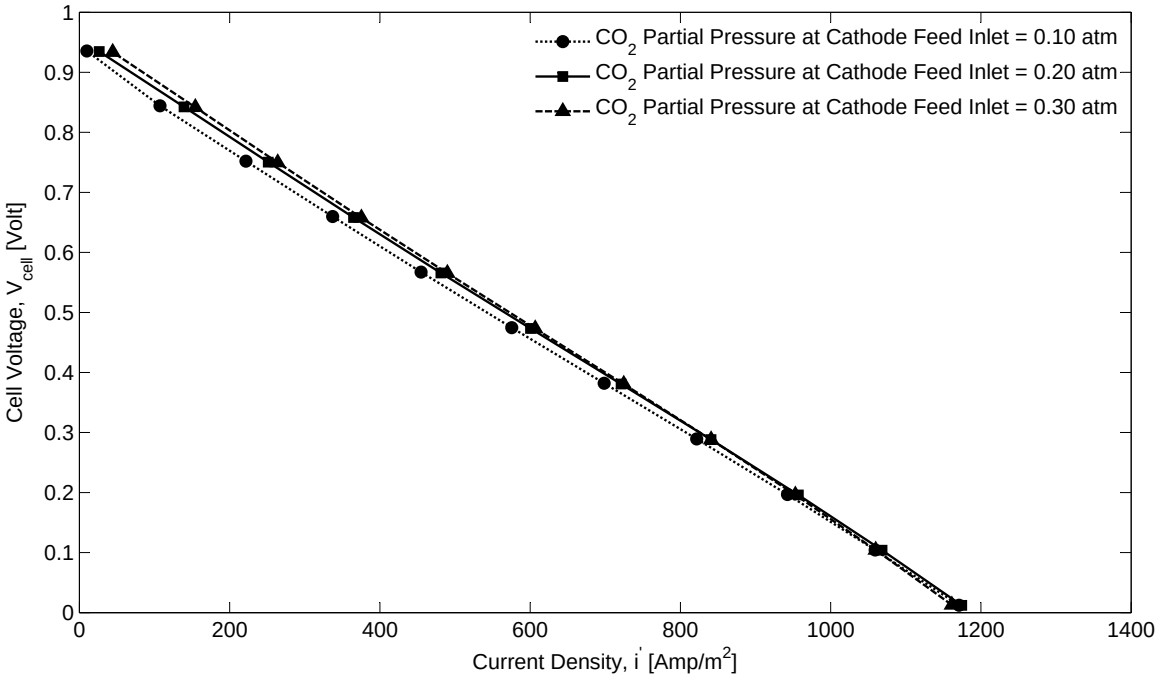

Figure 4.15: Current Density - Cell Voltage Variation with varying CO_2 inlet partial pressure. Electrolyte - Li/Na/K ternary eutectic - 43.5/31.5/25 mole%; Settled Particle Resistivity in Anode Bed, $\rho_{ct,0} = 0.0004\,\Omega - m$; Liquid Electrolyte Superficial Velocity (anode/cathode) = $0.1\,m/s$**, Bed depth (anode/cathode) =** $10\,cm/6\,cm$**; Cathode gas composition - CO_2 =** $0.1/0.2/0.3\,atm$**, O_2 =** $0.168\,atm$ **and N_2 = remaining; Feed Gas Flow Rate in Cathode;** $F_V = 0.1\,m^3/hr$ **per** $1cm^2$ **cell area;** $T = 973\,K$**; Carbon particle initial diameter,** $D_{c,ini} = 175\,\mu m$**; Grid Packing:: Wire-Mesh # 24 (anode), # 30 (cathode); Solid hold-up (carbon) at anode inlet =** 0.21**.**

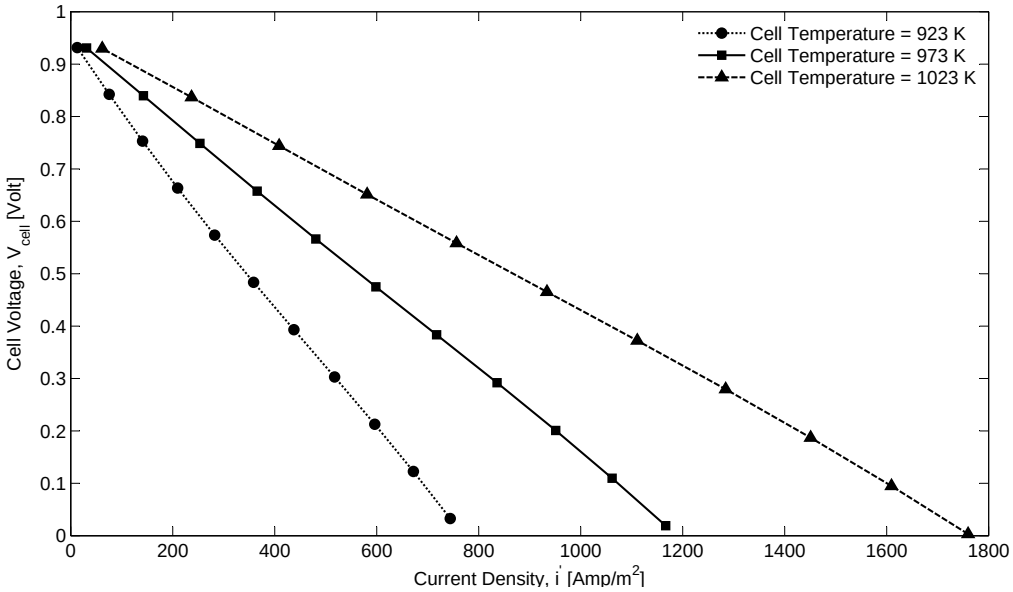

Figure 4.16: Current Density - Cell Voltage Variation with varying fuel cell temperature, $T = 923, 973 and 1023\,K$**. Electrolyte Used as Base Case - Li/Na/K ternary eutectic - 43.5/31.5/25 mole%; Settled Particle Resistivity in Anode Bed,** $\rho_{ct,0} = 0.0004\,\Omega - m$**; Liquid Electrolyte Superficial Velocity (anode/cathode) =** $0.1\,m/s$**, Bed depth (anode/cathode) =** $10\,cm/6\,cm$**; Cathode gas composition -** CO_2 **=** $0.1/0.2/0.3\,atm$**,** O_2 **=** $0.168\,atm$ **and** N_2 **= remaining; Feed Gas Flow Rate in Cathode;** $F_v = 0.1\,m^3/hr$ **per** $1cm^2$ **cell area; Carbon particle initial diameter,** $D_{c,ini} = 175\,\mu m$**; Grid Packing:: Wire-Mesh # 24 (anode), # 30 (cathode); Solid hold-up (carbon) at anode inlet =** 0.21**.**

et al. [1979][Appendix B] for the cathode and anode respectively indicates lower exchange current densities for lower temperature and vice versa. Charge transfer coefficient (α_z for the anode is observed to be stable around 0.5 at temperatures of higher than 700 $^\circ$ C.

It would seem advantageous to use higher temperatures to achieve higher reaction rates however there are two factors that can work against the performance of direct carbon fuel cell described in the current work. Firstly, operating temperature of 800 $^\circ C$ signify equilibrium (Boudouard) of the reaction $CO_2 + C \longrightarrow 2\,CO$ shifting towards right and pointing towards higher production of CO which eventually would have to be electrochemically or chemically re-converted to CO_2. This could hurt the cell performance as has been shown by past researchers Weaver et al. [1979], Vutetakis [1985], Cherepy et al. [2005]. Although, Hauser Jr. [1964] has demonstrated that the production of CO at temperatures of 800 $^\circ C$ might only 1-2%, it could be higher still according to later researchers Weaver et al. [1979], Vutetakis [1985]. But all three Hauser Jr. [1964], Weaver et al. [1979], Vutetakis [1985] report quite low mole fraction of CO (of the order of $< 1\%$) at temperatures 700 $^\circ C$ and lower. The base case condition is therefore limited to 700 $^\circ C$ for this exact reason. Secondly, higher temperatures are also accompanied by possible corrosion effects which being a vast subject in itself has not been studies under the present work but nevertheless is quite important in the design of DCFCs.

Power density curve for cell Temperature variation is also shown here in 4.17. As can be seen maximum power densities in the range of $> 400 W/m^2$ may be achieved.

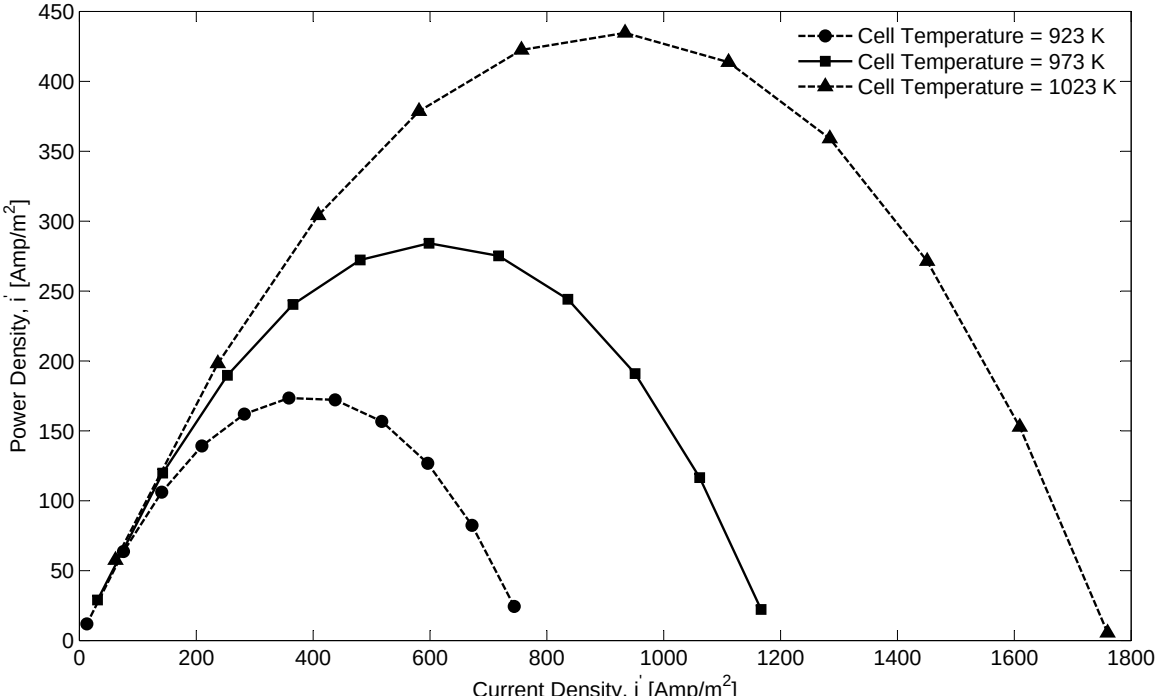

Figure 4.17: Current Density - Power Density Variation with varying cell temperature: 923, 973, and 1023 K. Electrolyte Used as Base Case - Li/Na/K ternary eutectic - 43.5/31.5/25 mole%; Settled Particle Resistivity in Anode Bed, $\rho_{ct,0} = 0.0004\,\Omega - m$**; Liquid Electrolyte Superficial Velocity (anode/cathode) =** $0.1\,m/s$**, Bed depth (anode/cathode) =** $10\,cm/10\,cm$**; Cathode gas composition -** CO_2 **=** $0.2\,atm$**,** O_2 **=** $0.168\,atm$ **and** N_2 **= remaining; Feed Gas Flow Rate in Cathode;** $F_V = 0.1\,m^3/hr$ **per** $1cm^2$ **cell area; Carbon particle initial diameter,** $D_{c,ini} = 175\,\mu m$**; Grid Packing:: Wire-Mesh # 24 (anode), # 30 (cathode); Solid hold-up (carbon) at anode inlet =** 0.21**.**

4.2.6 Charge-Transfer Current Density in Anode

The charge transfer volumetric current density is the rate kinetic Butler Volmer equation to predict variation in current density with respect to over-potential at the reaction site (porous sites on the surface of carbon particles). The area current density is calculated from the product of volumetric current density and area per unit bed volume of the carbon particle surface. Experiments were conducted on spectrographic carbon (Weaver et al. [1979][Appendix A]) and pyrolitic graphite Weaver et al. [1979][Appendix A,B] to estimate kinetic factors like charge transfer coefficient (α_a) and exchange current density ($i''_{o,a}$). Most reliable to use is the data evaluated by Ateya given in Weaver et al. [1979][Appendix B] for the pyrolitic graphite.

4.2.7 Liquid Electrolyte Superficial Velocity

Cathode Bed

The variation of cell performance with liquid superficial velocity within the cathode bed is shown in figure 4.18. At higher velocities, the mass transfer from bulk liquid to reaction surface is better and therefore implies improved performance. Lower velocities can perpetuate lower mass transfer and therefore affect limiting current densities at higher over-potential.

Anode Bed

Even though the liquid velocities in the anode are at par with that in the cathode, the physics of flow is quite different in the anode. The primary difference is that in

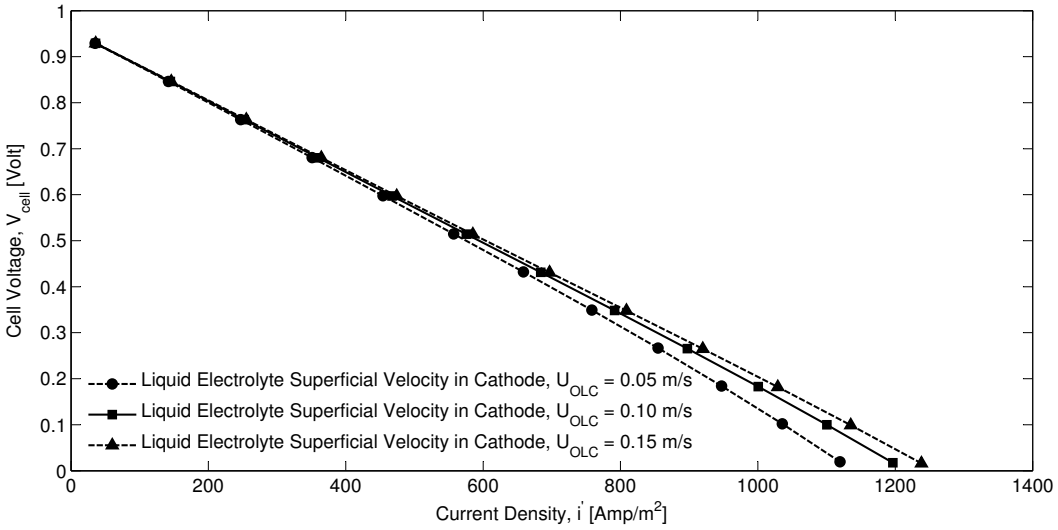

Figure 4.18: Current Density - Cell Voltage Variation with varying liquid electrolyte superficial velocities at the cathode inlet. Electrolyte Used as Base Case - Li/Na/K ternary eutectic - 43.5/31.5/25 mole%; Settled Particle Resistivity in Anode Bed, $\rho_{ct,0} = 0.0004\,\Omega - m$**; Liquid Electrolyte Superficial Velocity (anode) =** $0.1\,m/s$**, Bed depth (anode/cathode) =** $10\,cm/10\,cm$**; Cathode gas composition - CO_2 =** $0.2\,atm$**, O_2 =** $0.168\,atm$ **and N_2 = remaining; Feed Gas Flow Rate in Cathode;** $F_v = 0.1\,m^3/hr$ **per** $1cm^2$ **cell area;** $T = 973\,K$**; Carbon particle initial diameter,** $D_{c,ini} = 175\,\mu m$**; Grid Packing:: Wire-Mesh # 24 (anode), # 30 (cathode); Solid hold-up (carbon) at anode inlet =** 0.21**.**

the cathode the gas feed is entrained within the electrolyte and can be regulated to a high or low flow depending upon the overall material balance around the fuel cell operation. In the anode, the CO_2 is produced on the carbon particle surface and transports via diffusion into the bulk liquid. Depending on the saturation level of CO_2 in the molten salt electrolyte and the solubility coefficient at the operating temperatures, gaseous CO_2 can either dissolve into the bulk liquid or get entrained in the form of bubbles. From preliminary calculations, it's clear that a certain initial gaseous mole flux of CO_2 has to be assumed. However, this assumed value has to be significantly lower than the total amount of CO_2 produced within the anode bed.

There is no significant variation in fuel cell performance with variation in liquid electrolyte superficial velocity in the anode bed as shown in figure 4.19. The reason for this is attributed to relatively improved liquid-solid mass transfer and not so good gas-liquid mass transfer. Better liquid-solid mass transfer is due to enhancement provided by the agitation from slurry flow through wire-mesh packing. Due to better liquid-solid mass transfer cell performance is not limited by the mass transfer but by kinetics and ohmic polarization. A marginal increase or reduction in superficial liquid velocity ($U_{oLa} \Rightarrow 0.05 \leftrightarrow 0.1 \leftrightarrow 0.15 m/s$) thus has negligible effect.

The effect of liquid superficial velocity on gas-liquid mass transfer also has no effect on fuel cell performance. The reason for that is because in the anode, the effect of gas bubbles is considered small owing to significantly lower initial conditions for CO_2 mole flux in the gas phase (nucleation effect). This aspect is covered in more detail in section dedicated to CO_2 gas bubble evolution in anode (CITE section). Being quite insignificant, the gas mole flux of CO_2 in the anode doesn't

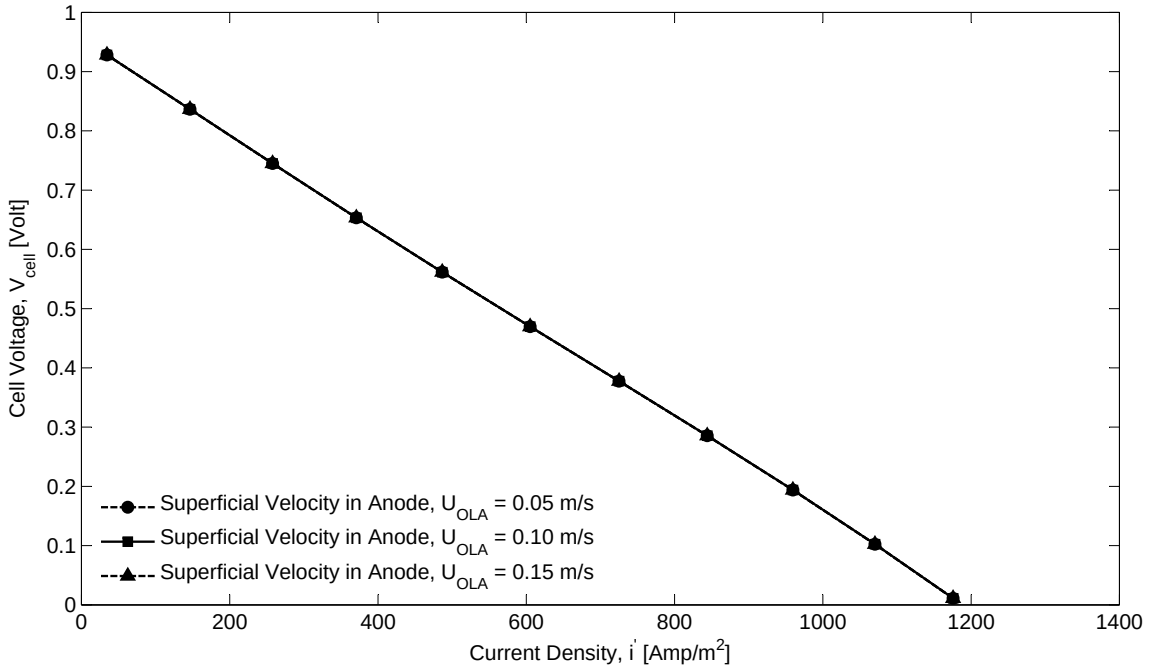

Figure 4.19: Current Density - Cell Voltage Variation with varying liquid electrolyte superficial velocities at the anode inlet. Electrolyte Used as Base Case - Li/Na/K ternary eutectic - 43.5/31.5/25 mole%; Settled Particle Resistivity in Anode Bed, $\rho_{ct,0} = 0.0004\,\Omega - m$**; Liquid Electrolyte Superficial Velocity (cathode) =** $0.1\,m/s$**, Bed depth (anode/cathode) =** $10\,cm$**; Cathode gas composition - CO_2 =** $0.2\,atm$**, O_2 =** $0.17\,atm$ **and N_2 =** $0.63\,atm$**; Feed Gas Flow Rate in Cathode;** $F_V = 0.1\,m^3/hr$**;** $T = 973\,K$**;** $D_{c,ini} = 175\,\mu m$**; Anode Grid Packing:: #24; Cathode Grid Packing:: Wire-Mesh # 30; Solid hold-up (carbon) at anode inlet =** 0.21**.**

introduce any significant gas bubble hold-up that might affect ohmic polarization. And therefore again, marginal variation in superficial liquid velocity produces no changes in fuel cell performance.

4.2.8 Effect of intermediate electrolyte layer

The purpose of the intermediate layer is to keep the connectivity of the ionic solution between cathode and anode beds so as to permit transport of carbonate ions from cathode into the anode. The conceptual design calls for this layer to act as a separate electrolyte loop and under a slightly higher pressure than the pressure in cathode and anode beds. A slight positive pressure in the intermediate layer will prevent any crossover of carbon particles from anode towards cathode or the cross-over of the gaseous species CO_2 and O_2 from cathode into the anode. However, diffusion of gases that are already dissolved into the liquid phase can be transported. It's of the opinion of author that the possible cross-over of O_2 (from cathode) maybe of small concentrations and therefore does not affect the overall kinetics in the anode bed although may act as a catalyst for the formation of CO_2 at the beginning of anode bed.

The variation with the change in intermediate layer thickness is shown in figure 4.20.

4.2.9 Grid Packing Variations

The following table shows various mesh sizes with respective area per unit volume and void fraction left in the bed. These wire-mesh are commercially available and

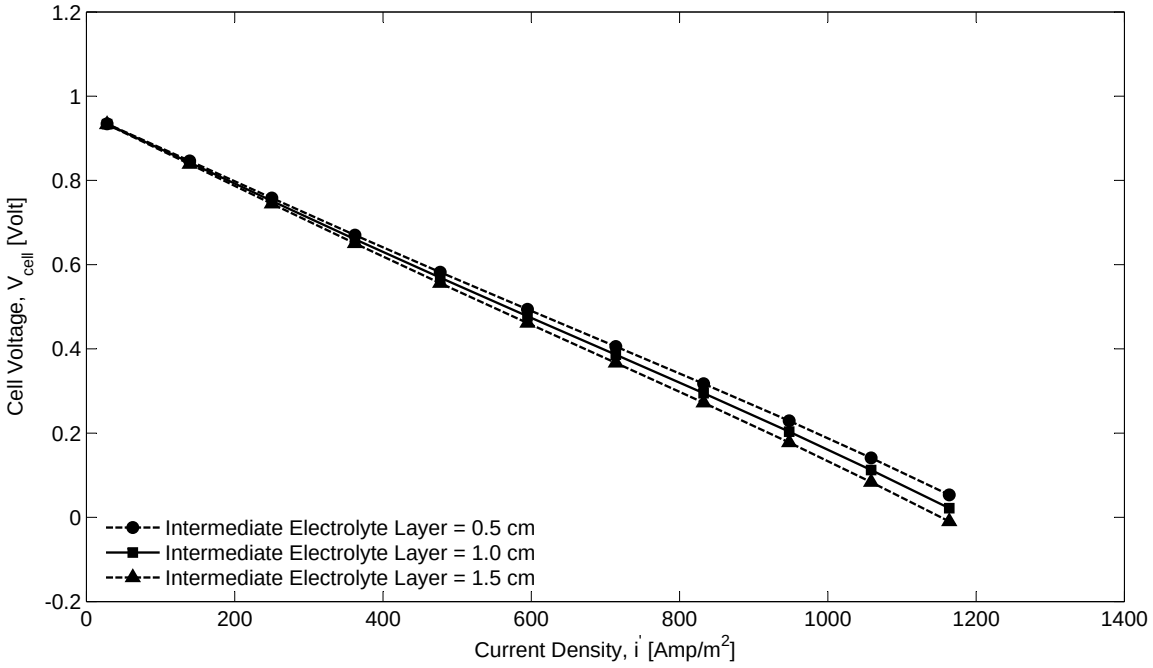

Figure 4.20: Current Density - Cell Voltage Variation with varying intermediate layer (between cathode and anode). Electrolyte - Li/Na/K ternary eutectic - 43.5/31.5/25 mole%; Anode grid packing Wire-Mesh #24; Settled Particle Resistivity in Anode Bed, $\rho_{ct,0} = 0.0004\,\Omega - m$**; Liquid Electrolyte Superficial Velocity (anode/cathode) =** $0.1\,m/s$**, Bed depth (anode/cathode) =** $10\,cm$**; Cathode gas composition -** CO_2 **=** $0.2\,atm$**,** O_2 **=** $0.17\,atm$ **and** N_2 **=** $0.63\,atm$**; Feed Gas Flow Rate in Cathode;** $F_V = 0.1\,m^3/hr$**;** $T = 973\,K$**;** $D_{c,ini} = 175\,\mu m$**; Cathode Grid Packing:: Wire-Mesh # 30; Solid hold-up (carbon) at anode inlet =** 0.21**.**

the parametric studies based on them are investigated in this section.

Table 4.3: Wire-mesh packing characteristics chart

S. No.	Mesh Size	Mesh Width	Wire Diameter	Wire-mesh inter-spacing	Area per Unit Volume	Void Fraction
		mm	mm	mm	m^2/m^3	fraction
1	#20	1.27	0.41	1.626	1237	0.874
2	#20	1.27	0.58	2.337	1237	0.819
3	#24	1.06	0.36	1.422	1484	0.868
4	#30	0.85	0.30	1.219	1855	0.859
5	#40	0.64	0.25	1.016	2474	0.843
6	#50	0.51	0.23	0.914	3092	0.823
7	#80	0.32	0.14	0.559	4947	0.827
8	#100	0.25	0.11	0.457	6184	0.823

Grid Packing Variation in Cathode:

The grid packing made out of SS-304, or SS-316, serves not only as the current collector in cathode but also active site for cathodic reactions to take place. It has been proposed that the cathodic reactions involve reduction of oxygen in the alkali molten carbonate salt consuming 2 moles of CO_2 and 2 electrons to produce 1 mole of carbonate ions. The ionic (area based) current density therefore is a function of how much grid surface is available for reaction. The grid volume affects the void fraction in the bed and thereby affecting the fraction of volume available for transport of carbonate ions through the molten carbonate electrolyte which is responsible for variation in the overall bed resistance (ohmic polarization). The grid surface area per unit bed volume also influences concentration polarization by affecting mass transfer from bulk liquid phase to the solid (grid surface) phase

for the gaseous species CO_2 and O_2. These effects are combined when variation in grid packing is done to compare fuel cell performance. The higher grid surface area per unit volume is expected to improve fuel cell performance however, the design may be limited when the improvement becomes only marginal. If the wire-mesh grid is placed perpendicular to the flow direction then finer grid may affect transport of gas bubbles that may negatively influence cell performance. However, this aspect has not been covered because of the need to model gas bubble phase characteristics accurately through the bed packing and is considered out of scope for the current work. The wire-mesh grid may be placed in parallel with the flow direction and therefore cause no impediment to the movement of gas bubbles. Again, looking at the transverse or longitudinal placement of wire-mesh grid is not in the scope of the current work and has not been pursued further.

The cell performance variation with change in grid packing is shown in figure 4.21.

Grid Packing Variation in Anode

The grid packing in anode is made out of SS-304, or SS-316, and serves only as the current collector. The anodic reactions takes place on the surface of carbon but charge is transferred via collision of carbon particles with the grid. This mechanism is shown in figure 3.10 in an earlier section in anode modeling. The drop in voltage attributed to the contact resistance is inversely proportional to the square of grid surface area per unit volume ($A'''_{g,a}$). Finer wire-mesh produces higher grid surface area per unit volume and therefore lower drop in voltage. However, the grid size opening should be sufficiently larger to allow carbon particles to pass through.

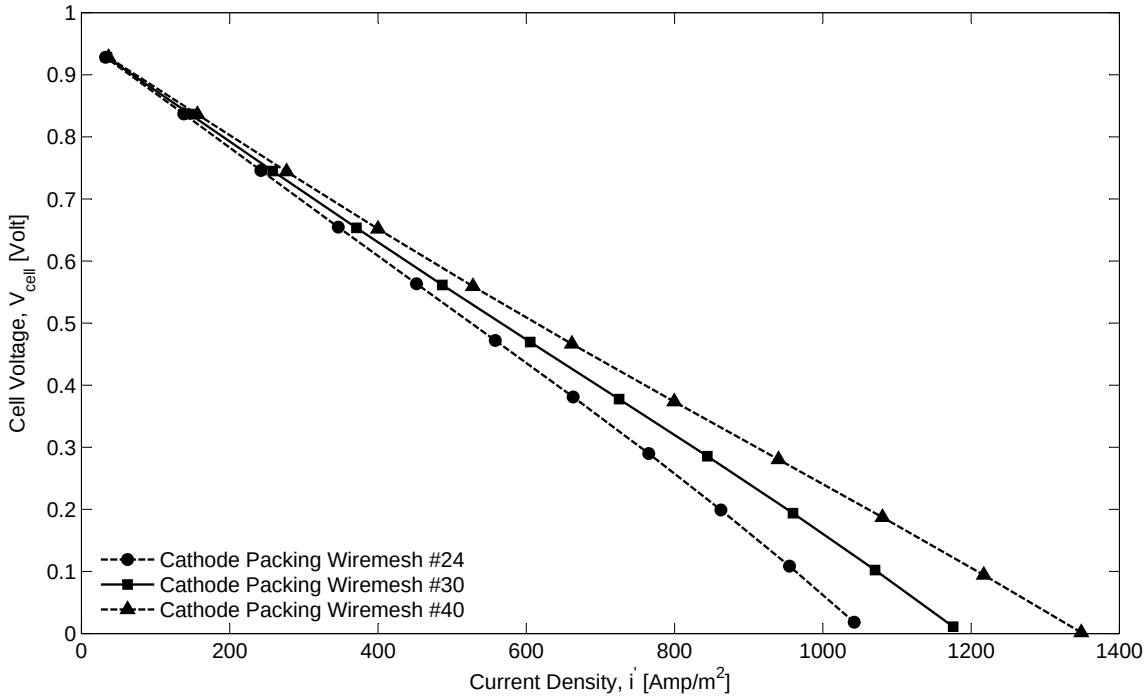

Figure 4.21: Current Density - Cell Voltage Variation with varying Cathode grid packing (Wire-Mesh #24, #30, and #40). Electrolyte Used as Base Case - Li/Na/K ternary eutectic - 43.5/31.5/25 mole%; Settled Particle Resistivity in Anode Bed, $\rho_{ct,0} = 0.0004\,\Omega - m$**; Liquid Electrolyte Superficial Velocity (anode/cathode) =** $0.1\,m/s$**, Bed depth (anode/cathode) =** $10\,cm$**; Cathode gas composition - CO_2 =** $0.2\,atm$**, O_2 =** $0.17\,atm$ **and N_2 =** $0.63\,atm$**; Feed Gas Flow Rate in Cathode;** $F_V = 0.1\,m^3/hr$**;** $T = 973\,K$**;** $D_{c,ini} = 175\,\mu m$**; Anode Grid Packing:: #24; Solid hold-up (carbon) at anode inlet =** 0.21**.**

The effect of grid packing can be found more pronounced if the cell performance is severely limited by contact resistance. However, if the particle resistivity is estimated to be quite low ($\rho_{ct,0} -> 0.0004\,\Omega - m$) then the grid packing variation will not have significant effect. This effect is shown in figure 4.22 The effect of grid pack-

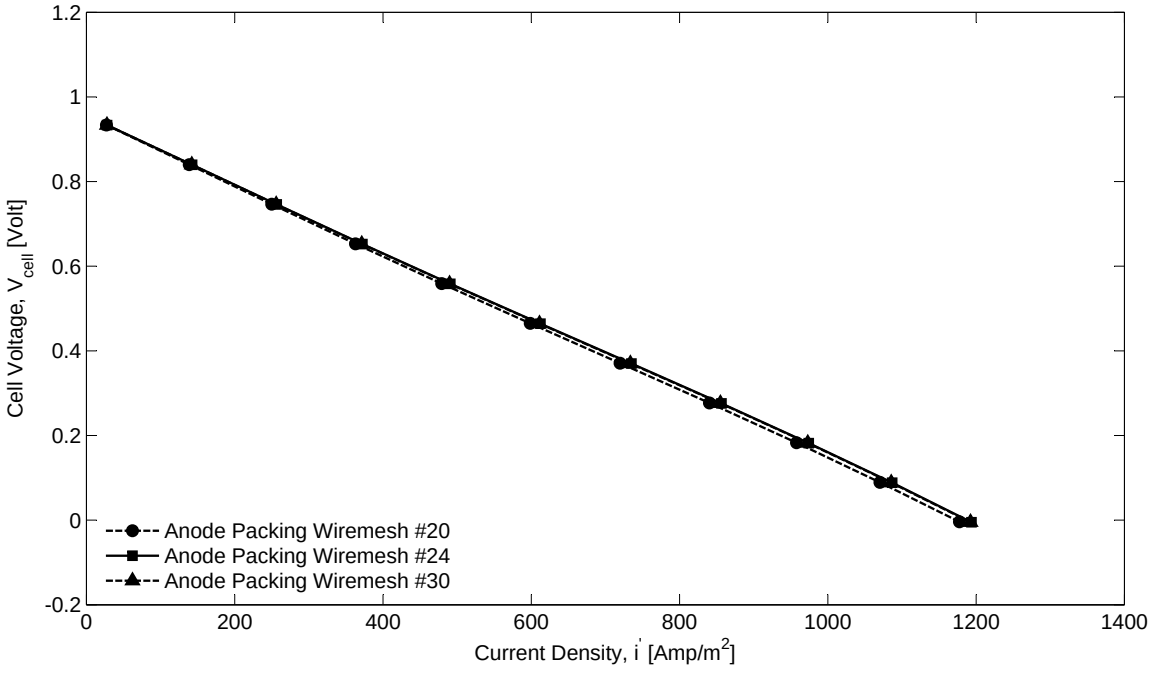

Figure 4.22: Current Density - Cell Voltage Variation with varying Anode grid packing (Wire-Mesh #20, #24, and #30). Electrolyte Used as Base Case - Li/Na/K ternary eutectic - 43.5/31.5/25 mole%; Settled Particle Resistivity in Anode Bed, $\rho_{ct,0} = 0.0004\,\Omega - m$**; Liquid Electrolyte Superficial Velocity (anode/cathode) =** $0.1\,m/s$**, Bed depth (anode/cathode) =** $10\,cm$**; Cathode gas composition - CO_2 =** $0.2\,atm$**, O_2 =** $0.17\,atm$ **and N_2 =** $0.63\,atm$**; Feed Gas Flow Rate in Cathode;** $F_V = 0.1\,m^3/hr$**;** $T = 973\,K$**;** $D_{c,ini} = 175\,\mu m$**; Cathode Grid Packing:: Wire-Mesh # 30; Solid hold-up (carbon) at anode inlet =** 0.21**.**

ing (more pronounced) on the current density - cell voltage relationship for settled

particle resistivity ($\rho_{ct,0} \rightarrow 0.04\,\Omega - m$) is shown in figure 4.23.

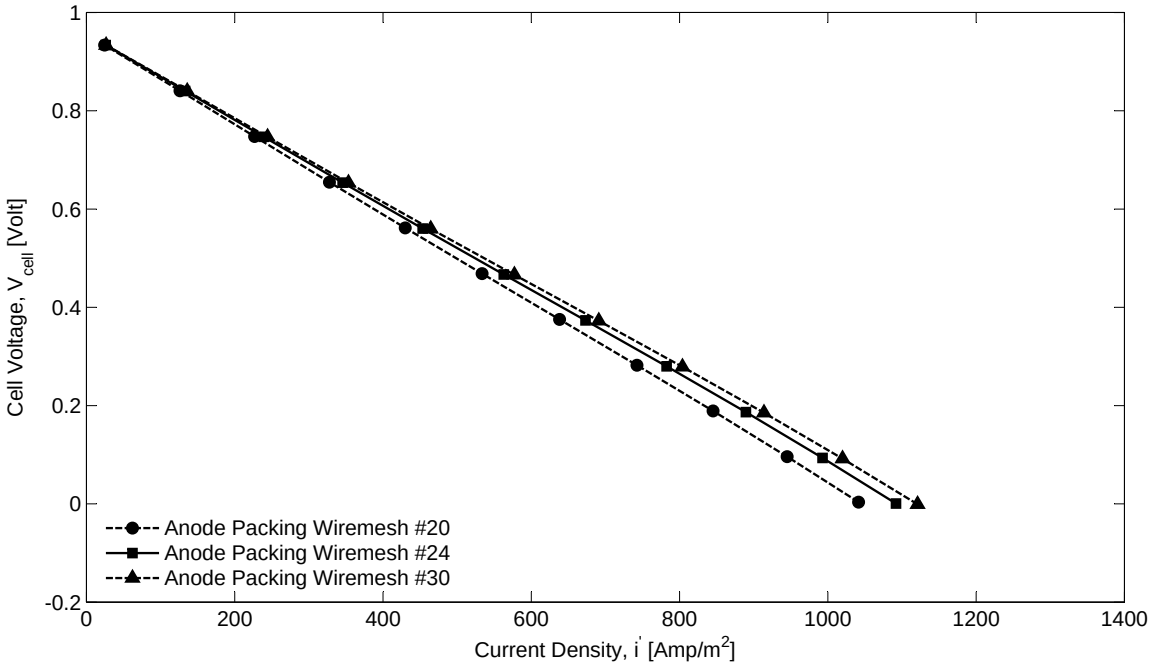

Figure 4.23: Current Density - Cell Voltage Variation with varying Anode grid packing (Wire-Mesh #20, #24, and #30). Electrolyte Used as Base Case - Li/Na/K ternary eutectic - 43.5/31.5/25 mole%; Settled Particle Resistivity in Anode Bed, $\rho_{ct,0} = 0.04\,\Omega - m$**; Liquid Electrolyte Superficial Velocity (anode/cathode) =** $0.1\,m/s$**, Bed depth (anode/cathode) =** $10\,cm$**; Cathode gas composition - CO_2 =** $0.2\,atm$**, O_2 =** $0.17\,atm$ **and N_2 =** $0.63\,atm$**; Feed Gas Flow Rate in Cathode;** $F_v = 0.1\,m^3/hr$**;** $T = 973\,K$**;** $D_{c,ini} = 175\,\mu m$**; Cathode Grid Packing:: Wire-Mesh # 30; Solid hold-up (carbon) at anode inlet =** 0.21**.**

4.2.10 Carbon Particle Diameter

It has already been indicated in previous sections that the anodic reaction of the fuel cell presented here happens on the surface of the carbon particle. The carbon particles are assumed to be quite small - of the order of roughly 100-250 mesh. This automatically means that the wire-mesh size provided as the anode packing should be significantly higher than the mesh size selected for the carbon particle diameter. As a base case, the anode wire-mesh packing as an opening of 0.7 mm which is quite higher than 0.17 mm of carbon particle diameter. As far as anode kinetics is concerned, data from the work of Weaver et al. [1979][Appendix B] suggests the use of pyrolitic graphite as the anode material. The properties for carbon has been selected based on pyrolitic graphite. Also, procurement of graphite powder can be easily justified in the range of 100-250 mesh for the purpose of parametric results (cite some pictures of commercially available graphite powder).

Fuel cell performance variation with carbon particle diameter is shown in figure 4.24.

This kind of effect has also been shown by Li et al. [2008] for the direct carbon fuel cells using carbon particles. Now, it would seem from these results that finer the size of carbon particles, better is the cell performance. However, the particle resistivity equations used in the simulation refer to the empirical equations developed using work of Kusakabe et al. [1981], Morooka et al. [1981] where typical particle sizes used were roughly 500 microns. Even then, as per the reference work, there doesn't seem to be a reliable dependence of particle resistivity presented as a function of particle diameter. Now as per another research work by Reed and Goldberger [1966], authors present clear evidence that particle resistivity goes up

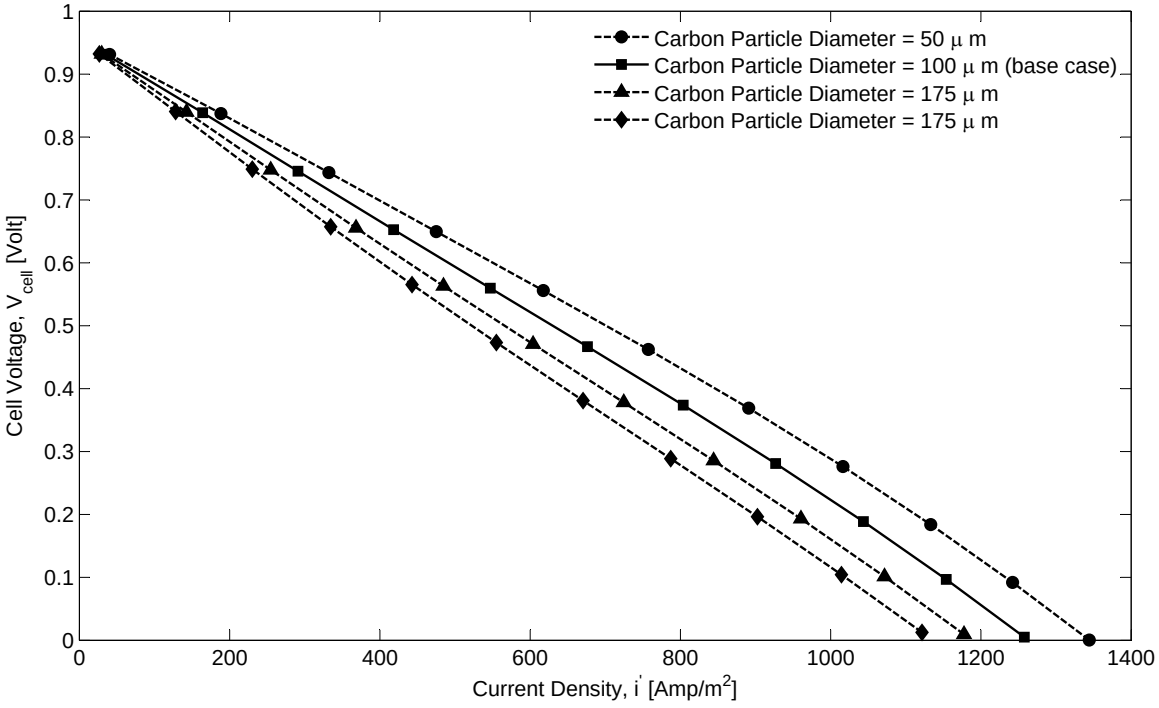

Figure 4.24: Current Density - Cell Voltage Variation with varying carbon particle diameter at the anode inlet (Carbon particle initial diameter, $D_{c,ini} = 50, 100, 175,$ and $250\,\mu m$). Electrolyte - Li/Na/K ternary eutectic - 43.5/31.5/25 mole%; Settled Particle Resistivity in Anode Bed, $\rho_{ct,0} = 0.0004\,\Omega - m$; Liquid Electrolyte Superficial Velocity (anode/cathode) = $0.1\,m/s$, Bed depth (anode/cathode) = $10\,cm/10\,cm$; Cathode gas composition - CO_2 = $0.1/0.2/0.3\,atm$, O_2 = $0.168\,atm$ and N_2 = remaining; Feed Gas Flow Rate in Cathode; $F_v = 0.1\,m^3/hr$ per $1cm^2$ cell area; $T = 973\,K$; Grid Packing:: Wire-Mesh # 24 (anode), # 30 (cathode); Solid hold-up (carbon) at anode inlet = 0.21.

as the particle diameter goes down. Although this work was clearly done for the gas (nitrogen) fluidized bed for graphite particles coming into contact with copper mesh screens, it seems likely that this applies to the present work. However, there is absence of any dependable empirical correlations for particle resistivity as a function of particle diameter that may be reliably used for modeling interaction of graphite particles with stainless steel (and/or nickel coated) wire-mesh screen packing in the presence of molten carbonate salt. Not to mention the fact that superficial gas velocities in the anode bed are quite low and therefore experimental data on particle resistivity as a function of particle diameter and attributed to fluidized beds might not apply.

4.3 Parametric Analysis with Respect to Uncertainties in Correlations Used

This section presents results from the sensitivity analysis conducted on variance in parameters arising from uncertainties in correlations or from literature data used that can cause significant change in overall fuel cell performance. The basic fuel cell performance indicators such as: current density-voltage relationship plots, fuel cell efficiency and power density for different current densities are considered. The following independent variables are selected for this analysis:

1. Rate Kinetics - Cathode
    - Oxygen reduction mechanism in Cathode - Variation in exponents for different mechanisms
    - Cathode Exchange Current Density ($i''_{o,c}$) Variation
2. Rate Kinetics - Anode
    - Exchange Current Density ($i''_{o,a}$) Variation
    - Mole flux of CO_2 in the gas phase in anode at the beginning of bed.
3. Contact Resistance in Anode - Understanding effect of variation in Contact Resistance is important because a crude model has been developed in this work based on experimental data for particle resistivity of copper particles in an ionic solution. In addition to the uncertainties in the developed correlation equation for the resistivity of carbon particles in the current work, there is a lack of credible experimental data for the carbon/graphite particles interaction

with a packed bed grid made out of stainless steel that can be put to use in the present work.

4. Mass Transfer in Anode and Cathode

    - Liquid-Solid Mass Transfer in Anode and cathode
    - Gas-Liquid Mass Transfer variation in Cathode
    - Gas-Liquid Mass Transfer variation in Anode. This will probably have significant effect only at non-negligible gas holdup. Should be performed at substantial mole flux of CO_2 in the gas phase in anode at the beginning of bed.

5. Solubility of O_2 and CO_2 - Various literature references suggest a significant variance in the reported data in some cases having variation as far as 2 orders of magnitude for the CO_2 while a good reliable data exists for the O_2. The variances may also reflect changes in performance as a result of utilizing different mixture of alkali carbonates.

6. Molecular Diffusivity of CO_2 and O_2 in mixtures of alkali molten carbonates. The variances may also reflect changes in performance as a result of utilizing different mixture of alkali carbonates.

7. Electrolyte Composition - Effect on bed resistance due to change in electrolyte conductivity.

4.3.1 Charge-Transfer Current Density in Cathode

The charge transfer volumetric current density is the rate kinetic Butler Volmer equation to predict variation in current density with respect to over-potential at the reaction site (grid surface). The area current density is calculated from the product of volumetric current density and area per unit bed volume of the grid surface. The equation for charge transfer volumetric current density is derived from the work of Wilemski et al. [1979], Wilemski [1983] which itself utilizes data from experiments conducted on molten carbonate fuel cells using Li/Na/K ternary eutectic and Na/K binary mixtures of molten carbonate salts at the Institute of Gas Technology (IGT). Wilemski put efforts to validate/fit either peroxide or super-oxide mechanism with the experimental data and came up with the:

1. Exponents on CO_2 and O_2 concentrations in the forward and reverse current conditions;

2. Coefficients vital to the rate kinetics - charge transfer coefficient, α and exchange current density, $i_o^{''}$; and

3. Exponents that are responsible for the variation in exchange current density as a function of CO_2 and O_2 concentrations.

Typically, points number 1 and 3 maybe combined to simply yield a necessity for exponents on CO_2 and O_2 concentrations in the forward and reverse current conditions and the kinetic constants - α and $i_o^{''}$. However, this kind of separation between bullet points 1 and 3 is also preserved by many other researchers Winnick and Ross Jr. [1981], Kunz et al. [1984], Uchida et al. [1986], Yuh and Selman [1991], Lu and Selman [1992] and preserved in the current work as well.

According to Wilemski et al. [1979], and as shown in section on Electrode Kinetics, two possible mechanisms for reduction of oxygen in alkali molten carbonate salts are considered, i.e. first wave (peroxide) and second wave (super-oxide). From this work, it's clear that expressions for i'' and i''_o should depict increased electrode performance with increased partial pressures of oxygen plus carbon dioxide but the opposite is predicted from the models developed for both waves. And therefore, work from Wilemski et al. [1979], Wilemski [1983] indicate a development of a general charge transfer volumetric current density equation with exponents and charge transfer coefficient that best fits the overall experimental data.

In this section, we must look at the observed effects of exponents, kinetic coefficients and model equation used for both waves, and also look at the effect on fuel cell performance with variation in partial pressures of CO_2 and O_2.

Cathode Mechanism

The variation in exponents for the concentration of CO_2 and O_2 is done in accordance with the models proposed in Wilemski et al. [1979] as per dominance of first wave (peroxide) or second wave (super-oxide) mechanism. The reason for this investigation in the present work is to show sensitivity in cell performance considering the cathode kinetics as suggested by other authors Winnick and Ross Jr. [1981], Kunz et al. [1984], Uchida et al. [1986], Yuh and Selman [1991], Lu and Selman [1992]. Since it was difficult to obtain any reasonable experimental data in the literature for the determination of cathodic kinetic exponents, exponents from the work of Wilemski et al. [1979] were selected. The present analysis is definitely not limited by the exponents used and neither it is the intention of the present work

to prefer one model over another. The original base case model is selected by utilizing kinetic data and also exponents from the work of Wilemski [1983].

The different exponents selection is presented in the table 4.4 that apply to the Butler Volmer Charge Transfer Volumetric Current Density equation for cathode (reproduced from earlier section on Electrode Kinetics):

$$i''_{\mathrm{s,c}} = i''^{0}_{\mathrm{s,c}} \left(f_{\mathrm{o_2}}{}^{s} \; f_{\mathrm{co_2}}{}^{t} \exp\left[\frac{\alpha_{\mathrm{c}}\mathbf{F}}{\bar{R}T}\eta_{\mathrm{c}}\right] - f_{\mathrm{o_2}}{}^{u} \; f_{\mathrm{co_2}}{}^{v} \exp\left[\frac{(\alpha_{\mathrm{c}}-n)\mathbf{F}}{\bar{R}T}\eta_{\mathrm{c}}\right] \right)$$

where

$$i''^{0}_{\mathrm{s,c}} = i''^{0}_{c} \; (p_{\mathrm{o_2}}/P)^{\sigma} \; (p_{\mathrm{co_2}}/P)^{\tau}$$

Table 4.4: Cathode Mechanism for oxygen reduction in Ternary Eutectic mixture of $(\mathbf{Li{-}Na{-}K})_{\mathbf{2}}\mathbf{CO_3}$ from the work of Wilemski et al. [1979], Wilemski [1983]

Exponent Description	First Wave (Peroxide)	Second Wave (Superoxide)	Base Case Model Wilemski [1983]
Forward rate exponent on O_2 concentration, s	0.5	0.75	0.5875
Forward rate exponent on CO_2 concentration, t	-1	-0.5	0.375
Reverse rate exponent on O_2 concentration, u	0	0	0.0875
Reverse rate exponent on CO_2 concentration, v	-2	-2	-0.625
O_2 partial pressure in i''_o, σ	0.3125	0.5625	0.4
CO_2 partial pressure in i''_o, τ	-1.375	-0.875	0.0

The variation in current density - cell voltage relationship for various exponents presented in table 4.4 has been applied on the fuel cell model in the current work and results plotted and shown in figure 4.25.

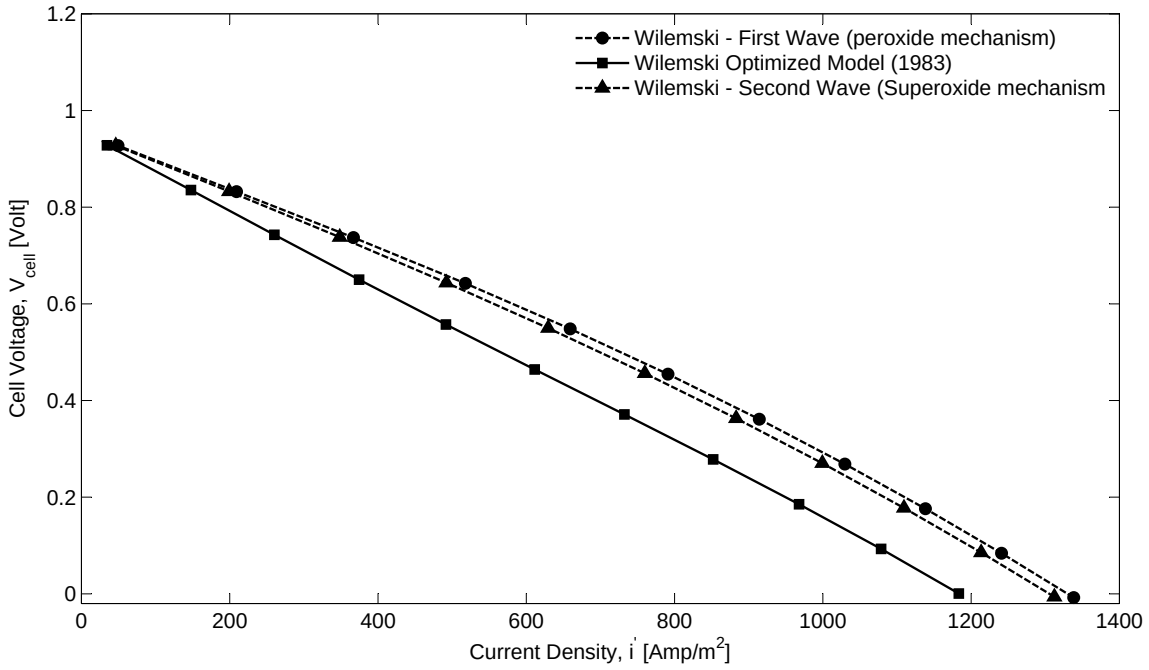

Figure 4.25: Current Density - Cell Voltage Variation with varying exponents in the kinetic rate expression for cathode. Electrolyte - Li/Na/K ternary eutectic - 43.5/31.5/25 mole%; Anode grid packing Wire-Mesh #24; Settled Particle Resistivity in Anode Bed, $\rho_{ct,0} = 0.0004\,\Omega - m$**; Liquid Electrolyte Superficial Velocity (anode/cathode) =** $0.1\,m/s$**, Bed depth (anode/cathode) =** $10\,cm$**; Cathode gas composition - CO_2 =** $0.2\,atm$**, O_2 =** $0.17\,atm$ **and N_2 =** $0.63\,atm$**; Feed Gas Flow Rate in Cathode;** $F_v = 0.1\,m^3/hr$**;** $T = 973\,K$**;** $D_{c,ini} = 175\,\mu m$**; Cathode Grid Packing:: Wire-Mesh # 30; Solid hold-up (carbon) at anode inlet =** 0.21**.**

Exchange Current Density Variation

Recent studies Uchida et al. [1986], Yuh and Selman [1991], Lu and Selman [1992] indicate that the exchange current densities from the experimental data of Appleby and Nicholson [1972, 1974, 1977] that support dominance of peroxide mechanism in the reduction of oxygen for molten carbonate fuel cell cathode and also used in Wilemski [1983] might be lower by one order of magnitude compared to experimental data for the cases where super-oxide mechanism is dominating. Janowitz et al. [1999] has gone to the extent of confirming some of these earlier studies by Lu and Selman [1992] and others in terms of kinetic data for oxygen reduction in MCFC cathode using binary mixtures of alkali molten carbonates indicating exchange current densities of the order of $10^2\ A/m^2$. This provides motivation to look at how the overall cell performance varies with variation in exchange current data in cathode. The exchange current density as used from the work of Wilemski [1983] is used as the base case and two higher values (maximum of one order of magnitude) are simulated for observing cell performance variation. The maximum value considered in the sensitivity analysis is still lower than predicted by some of the researchers mentioned above.

Considering that the charge transfer current density approaches zero only 6 cm into the cathode bed depth for the non-base cases (due to higher reaction rate), comparison simulations are conducted for a cathode bed thickness of 6cm instead of 10cm bed thickness typical of the base case simulations. The results are presented in figure below:

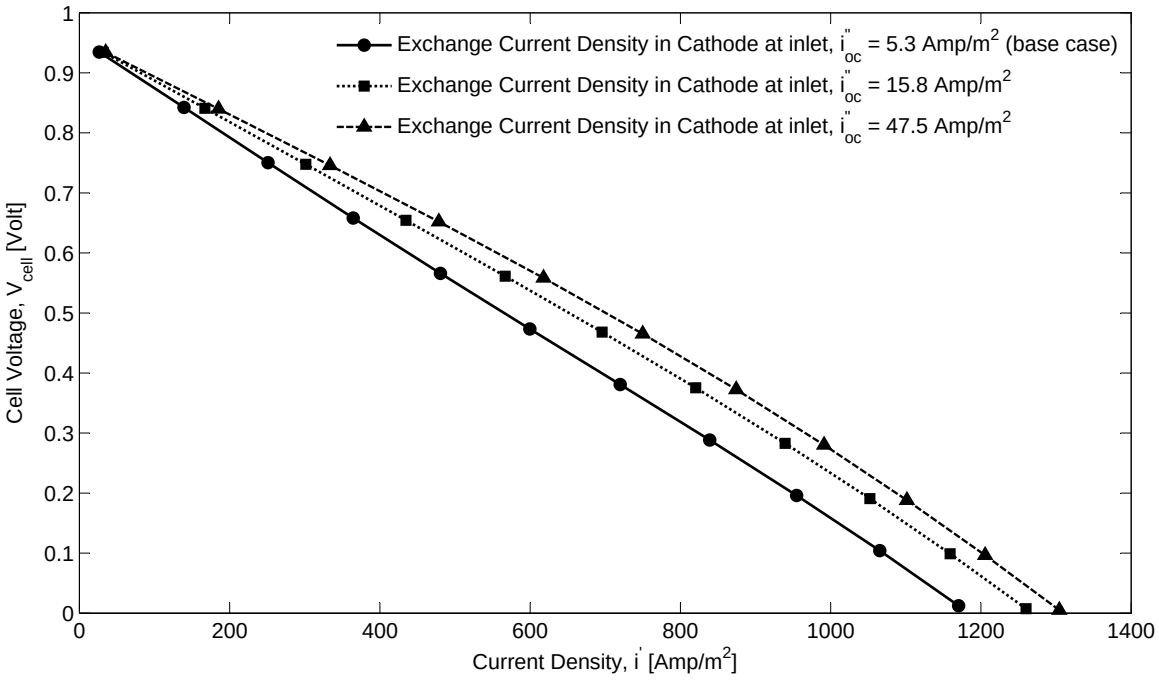

Figure 4.26: Current Density - Cell Voltage Variation with varying exchange current density in the kinetic rate expression for cathode. Electrolyte - Li/Na/K ternary eutectic - 43.5/31.5/25 mole%; Settled Particle Resistivity in Anode Bed, $\rho_{ct,0} = 0.0004\,\Omega - m$**; Liquid Electrolyte Superficial Velocity (anode/cathode) =** $0.1\,m/s$**, Bed depth (anode/cathode) =** $10\,cm/6\,cm$**; Cathode gas composition -** CO_2 **=** $0.2\,atm$**,** O_2 **=** $0.17\,atm$ **and** N_2 **=** $0.63\,atm$**; Feed Gas Flow Rate in Cathode;** $F_V = 0.1\,m^3/hr$ **per** $1cm^2$ **cell area;** $T = 973\,K$**; Carbon particle initial diameter,** $D_{c,ini} = 175\,\mu m$**; Grid Packing:: Wire-Mesh # 24 (anode), # 30 (cathode); Solid hold-up (carbon) at anode inlet =** 0.21**.**

4.3.2 Charge-Transfer Current Density in Anode

The charge transfer volumetric current density is the rate kinetic Butler Volmer equation to predict variation in current density with respect to over-potential at the reaction site (porous sites on the surface of carbon particles). The area current density is calculated from the product of volumetric current density and area per unit bed volume of the carbon particle surface. Experiments were conducted on spectrographic carbon (Weaver et al. [1979][Appendix A]) and pyrolitic graphite Weaver et al. [1979][Appendix A,B] to estimate kinetic factors like charge transfer coefficient (α_a) and exchange current density ($i''_{o,a}$). Most reliable to use is the data evaluated by Ateya given in Weaver et al. [1979][Appendix B] for the pyrolitic graphite.

Exchange Current Density Variation

The exchange current density for the base case results uses empirical correlation developed from experimental data presented in Weaver et al. [1979][Appendix B] for the pyrolitic graphite. As per another literature reference Vutetakis [1985], exchange current density estimated by Weaver et al. [1979][Appendix B] seems low to the extent of one order of magnitude. In fact Vutetakis [1985] himself ran experiments with slurry of darco-activated carbon and alkali molten carbonate salts. But kinetic data presented by Vutetakis [1985] is not very reliable as per the author himself; perhaps because of availability of only 3 data points.

In light of this evidence, the purpose in this section was to do a sensitivity analysis on the exchange current density and also cover lousy kinetic data that may be estimated from much lower quality coal. The results from the simulation of

these cases is presented in figure 4.27:

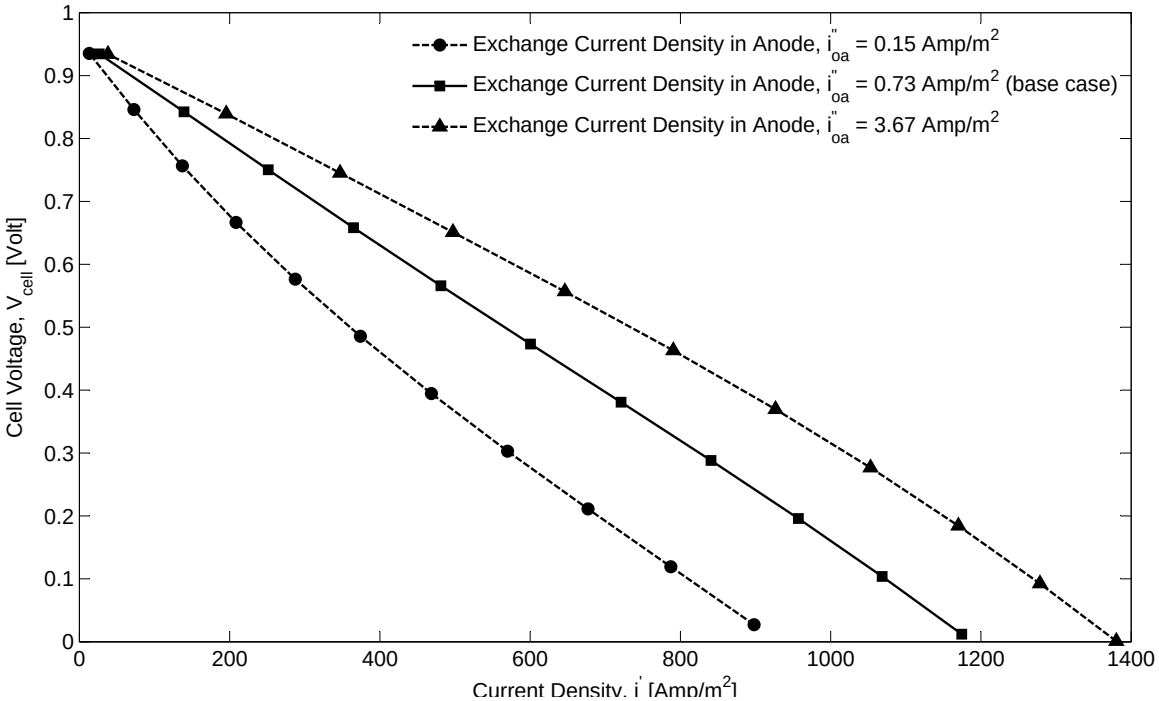

Figure 4.27: Current Density - Cell Voltage Variation with varying exchange current density in anode bed. Electrolyte - Li/Na/K ternary eutectic - 43.5/31.5/25 mole%; Settled Particle Resistivity in Anode Bed, $\rho_{ct,0} = 0.0004\,\Omega - m$**; Liquid Electrolyte Superficial Velocity (anode/cathode) =** $0.1\,m/s$**, Bed depth (anode/cathode) =** $10\,cm/6\,cm$**; Cathode gas composition - CO_2 =** $0.2\,atm$**, O_2 =** $0.168\,atm$ **and N_2 = remaining; Feed Gas Flow Rate in Cathode;** $F_V = 0.1\,m^3/hr$ **per** $1cm^2$ **cell area;** $T = 973\,K$**; Carbon particle initial diameter,** $D_{c,ini} = 175\,\mu m$**; Grid Packing:: Wire-Mesh # 24 (anode), # 30 (cathode); Solid hold-up (carbon) at anode inlet =** 0.21**.**

4.3.3 Contact Resistance Variation in Anode

The correlation for contact resistance used in this work is developed on the presumption that the charge transfer current density varies linearly with the overpotential. In reality, that might not be the case and therefore it seems prudent to show some sensitivity in overall cell performance based on variation in some aspects of how contact resistance has been evaluated.

The contact resistance in the anode can affect performance of the fuel cell by influencing anodic polarization through following effects:

1. Carbon solid hold-up variation.

2. Uncertainties in using resistivity correlation

The variation with respect to carbon solid hold-up is shown in figure 4.28

The variation is also shown with respect to the particle resistivity at settled conditions. As per the literature Kusakabe et al. [1981], from where the correlation for particle resistivity has been developed, the settled conditions refer to zero bed expansion or the value of expansion coefficient, E to be 1. The resistivity based on the settled condition from the correlation is $0.0004\,\Omega - m$. Now, the resistivity of copper material is much lower $(10^{-8}\,\Omega - m)$ than this resistivity value at settled conditions. The lower resistivity in copper material simply means the hindrance to the movement of electrons within the material is lower than that seen in packed beds where the mode of charge transfer is through both conduction and collision and even for the conduction mechanism, the point of contact between aggregated particles might allow, comparatively, limited charge transfer.

For graphite particles, the particle resistivity is somewhat higher than copper

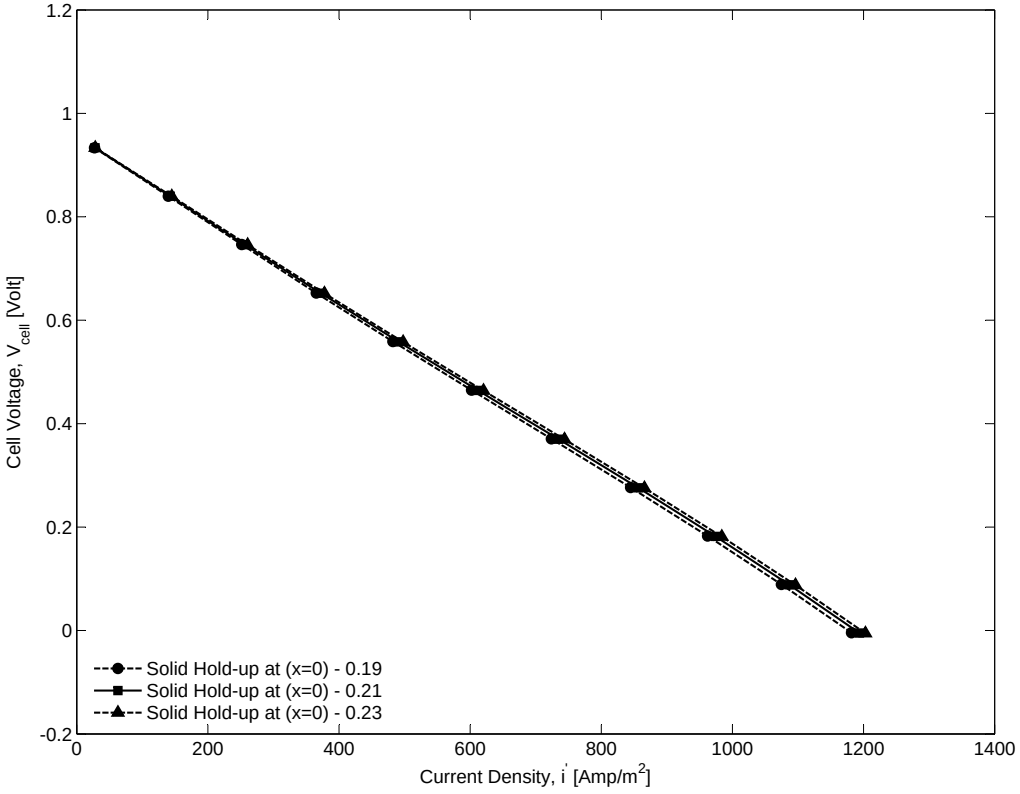

Figure 4.28: Current Density - Cell Voltage Variation with varying carbon solid holdup at the anode inlet. Electrolyte - Li/Na/K ternary eutectic - 43.5/31.5/25 mole%; Settled Particle Resistivity in Anode Bed, $\rho_{ct,0} = 0.0004\,\Omega - m$**; Liquid Electrolyte Superficial Velocity (anode/cathode) =** $0.1\,m/s$**, Bed depth (anode/cathode) =** $10\,cm/6\,cm$**; Cathode gas composition - CO_2 =** $0.2\,atm$**, O_2 =** $0.168\,atm$ **and N_2 = remaining; Feed Gas Flow Rate in Cathode;** $F_V = 0.1\,m^3/hr$ **per** $1cm^2$ **cell area;** $T = 973\,K$**; Carbon particle initial diameter,** $D_{c,ini} = 175\,\mu m$**; Grid Packing:: Wire-Mesh # 24 (anode), # 30 (cathode); Solid hold-up (carbon) at anode inlet =** 0.21**.**

and therefore, it's possible that the particle resistivity for settled conditions ($\rho_{ct,0}$) might be higher. Figure 4.29 shows the current density - voltage curves with respect to variation in $\rho_{ct,0}$. As can be seen from the figure, the lower resistivity (developed from the correlation and $\rho_{ct,0} = 0.0004\,\Omega - m$) does show better cell performance but in the case that the particle resistivity is higher for the present work, the fuel cell performance is not adversely affected for one order of magnitude higher resistivity. However, cell performance is marginally lower if the settled particle resistivity were two orders of magnitude higher ($\rho_{ct,0} = 0.04\,\Omega - m$).

4.3.4 Mass Transfer

This section presents variation in cell performance with respect to parametric changes performed on the mass transfer coefficients in both anode and cathode beds. There are two different mass transfer coefficients involved for the gaseous species transport from solid surface to the gas bubble phase (anode) or from gas bubble phase to the solid surface (cathode), i.e. liquid-solid mass transfer coefficient (K_{LS}) and gas-liquid mass transfer coefficient ((K_{GL}). In anode, only the CO_2 species mass transport is important (assuming no CO production) whereas in cathode, mass transport of both CO_2 and O_2 is important.

Now, as evaluated in earlier sections, the gas-holdup is significantly small in the anode bed and even if it were significant would affect mostly the ohmic polarization in the bed. The expected effect of gas-liquid mass transfer in the anode bed is insignificant because the kinetic equation involves driving force between concentration in bulk liquid phase and at the carbon particle surface. Therefore, cell performance attributed to mass transfer effects in anode maybe limited more by

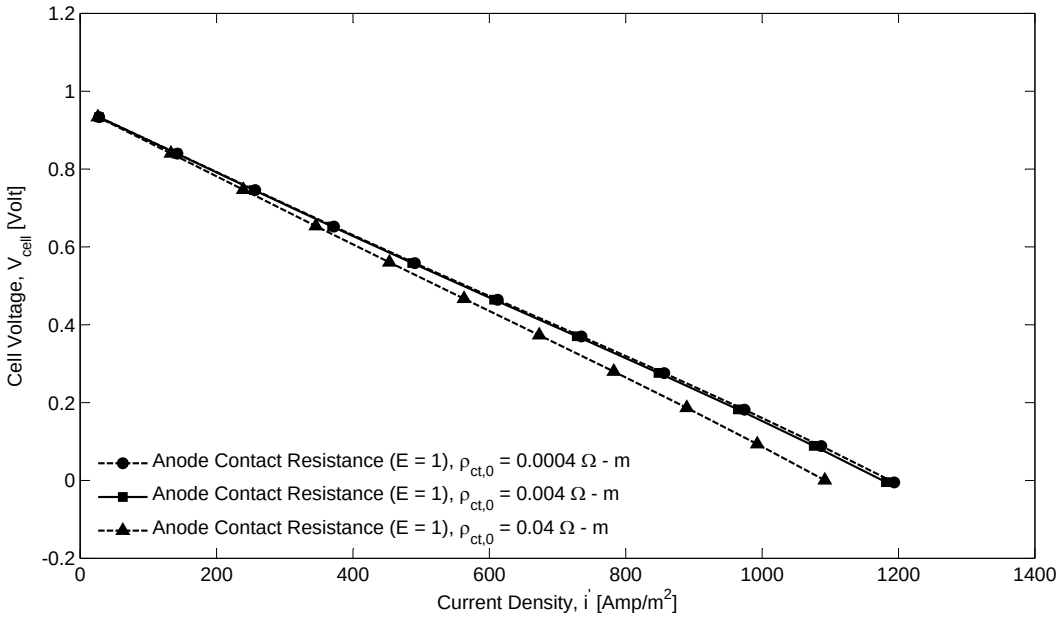

Figure 4.29: Current Density - Cell Voltage Variation with varying particle resistivity at settled conditions ($\rho_{ct,0}$). Electrolyte - Li/Na/K ternary eutectic - 43.5/31.5/25 mole%; Settled Particle Resistivity in Anode Bed, $\rho_{ct,0} = 0.0004/0.004/0.04\,\Omega - m$; Liquid Electrolyte Superficial Velocity (anode/cathode) = $0.1\,m/s$**, Bed depth (anode/cathode) =** $10\,cm/6\,cm$**; Cathode gas composition - CO_2 =** $0.2\,atm$**, O_2 =** $0.168\,atm$ **and N_2 = remaining; Feed Gas Flow Rate in Cathode;** $F_V = 0.1\,m^3/hr$ **per** $1cm^2$ **cell area;** $T = 973\,K$**; Carbon particle initial diameter,** $D_{c,ini} = 175\,\mu m$**; Grid Packing:: Wire-Mesh # 24 (anode), # 30 (cathode); Solid hold-up (carbon) at anode inlet =** 0.21**.**

the liquid-solid mass transfer coefficient or the rate-kinetics itself and not by the gas-liquid mass transfer coefficient.

The above argument also applies to the cathode however, the biggest difference is the presence of significant gas hold-up in the cathode which can account for significant ohmic polarization losses in addition to contributing some current density limitation due to gas-liquid mass transfer. Again, as explained above for anode, in cathode too, the bulk-liquid - solid surface mass transfer coefficient is the main driving force behind reaction rate in cathode and can limit the cell performance.

The results are presented and discussed below.

Liquid-Solid Mass Transfer in Cathode

The mass transfer coefficient betwen the liquid and the packing correlation is a result of empirical equation developed by Kirillov and Nasamanyan [1976] through experiments conducted on benzoic acid spheres (8 mm and 30 mm size) and Raschig rings ($12 \times 12 \times 2$ size) in a three-phase fixed bed reactor. True velocities (based on free-cross section) in the range of 0-0.5 m/s for gas and 0.01-0.02 m/s for liquid were used by the author.

The liquid velocities in the current work are one order of magnitude higher and the use of the correlation may be questionable for such higher liquid velocities. However, it is anticipated that the sensitivity of mass transfer coefficient by a factor of two in both directions (lower and higher) can cover the extent of uncertainty introduced by the use of such correlation. This sensitivity effect is produced in the figure 4.30 below and as expected, cell performance viewed through current density - cell voltage relationship is quite sensitive to the liquid-solid mass transfer

coefficient.

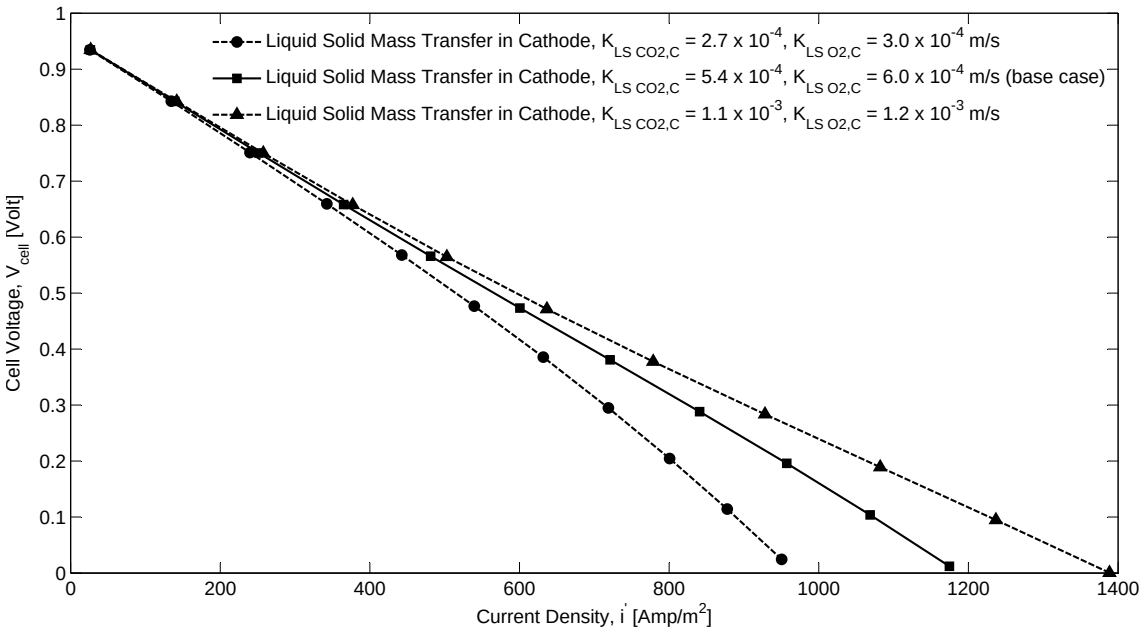

Figure 4.30: Current Density - Cell Voltage Variation with varying liquid-solid mass transfer coefficients for both CO_2 and CO_2 in the cathode bed. Electrolyte - Li/Na/K ternary eutectic - 43.5/31.5/25 mole%; Settled Particle Resistivity in Anode Bed, $\rho_{ct,0} = 0.0004\,\Omega - m$; Liquid Electrolyte Superficial Velocity (anode/cathode) = $0.1\,m/s$, Bed depth (anode/cathode) = $10\,cm/6\,cm$; Cathode gas composition - CO_2 = $0.1/0.2/0.3\,atm$, O_2 = $0.168\,atm$ and N_2 = remaining; Feed Gas Flow Rate in Cathode; $F_V = 0.1\,m^3/hr$ per $1cm^2$ cell area; $T = 973\,K$; Carbon particle initial diameter, $D_{c,ini} = 175\,\mu m$; Grid Packing:: Wire-Mesh # 24 (anode), # 30 (cathode); Solid hold-up (carbon) at anode inlet = 0.21.

Liquid-Solid Mass Transfer in Anode

As expected, fuel cell performance viewed through the current density - cell voltage relationship is not limited by the liquid-solid mass transfer coefficient for CO_2 in the

anode as shown in figure 4.31. It's clear that the driving force between concentration of CO_2 at the carbon particle surface and the concentration in the bulk-liquid is quite small and any increase in mass transfer coefficient tends to reduce this driving force further. In addition, the kinetic rate equation (butler volmer charge transfer current density equation) dependance on the concentration of CO_2 at the carbon particle surface is not significant for the forward reaction as has been indicated before owing to work of Vutetakis [1985]. This has been explained in earlier sections in Electrode Kinetics.

Gas-Liquid Mass Transfer in Cathode

The basis for doing sensitivity in the fuel cell performance with respect to gas-liquid mass transfer in cathode is because the empirical correlations used for the work cannot be fully relied on considering these correlations were not developed for electrochemical reactors involving molten carbonate salts but for simple reactors involving three-phase flow. In addition, the range of gas and liquid velocities that are used in the correlations may not be commiserate with the velocities used in the present work. In light of such uncertainties, sensitivity analysis involving mass transfer coefficients varying by 2 to 4 orders of magnitude might be quite relevant to the present work to show extent of variation in fuel cell performance based on wide variations in mass transfer coefficients.

The gas-liquid mass transfer coefficient for both CO_2 and O_2 were varied simultaneously and variances are recorded in the figure 4.32.

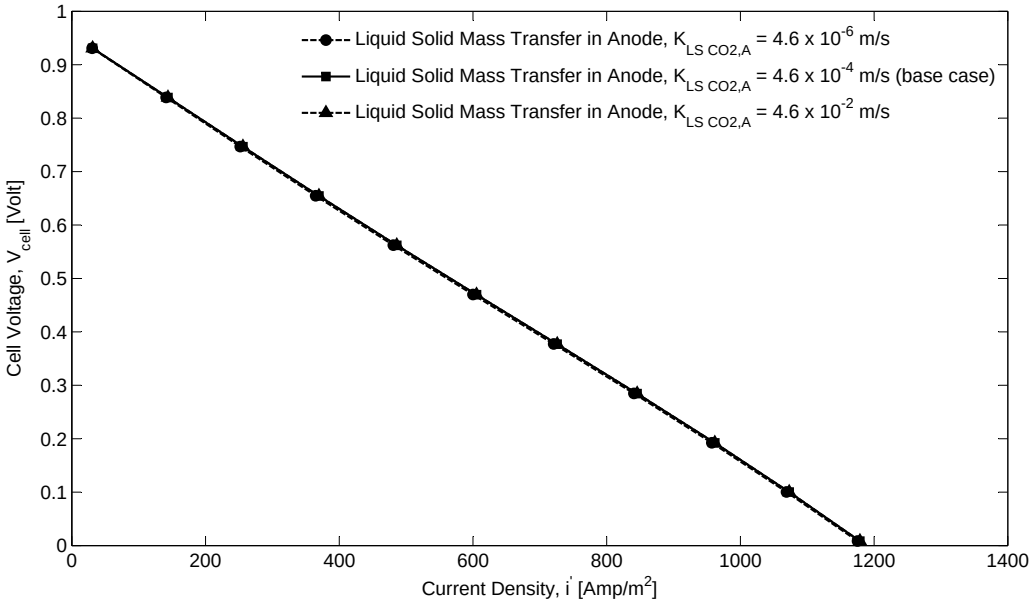

Figure 4.31: Current Density - Cell Voltage Variation with varying liquid-solid mass transfer coefficients for CO_2 in the anode bed. Electrolyte - Li/Na/K ternary eutectic - 43.5/31.5/25 mole%; Settled Particle Resistivity in Anode Bed, $\rho_{ct,0} = 0.0004\,\Omega - m$; Liquid Electrolyte Superficial Velocity (anode/cathode) = $0.1\,m/s$**, Bed depth (anode/cathode) =** $10\,cm/6\,cm$**; Cathode gas composition - CO_2 =** $0.1/0.2/0.3\,atm$**, O_2 =** $0.168\,atm$ **and N_2 = remaining; Feed Gas Flow Rate in Cathode;** $F_v = 0.1\,m^3/hr$ **per** $1cm^2$ **cell area;** $T = 973\,K$**; Carbon particle initial diameter,** $D_{c,ini} = 175\,\mu m$**; Grid Packing:: Wire-Mesh # 24 (anode), # 30 (cathode); Solid hold-up (carbon) at anode inlet =** 0.21**.**

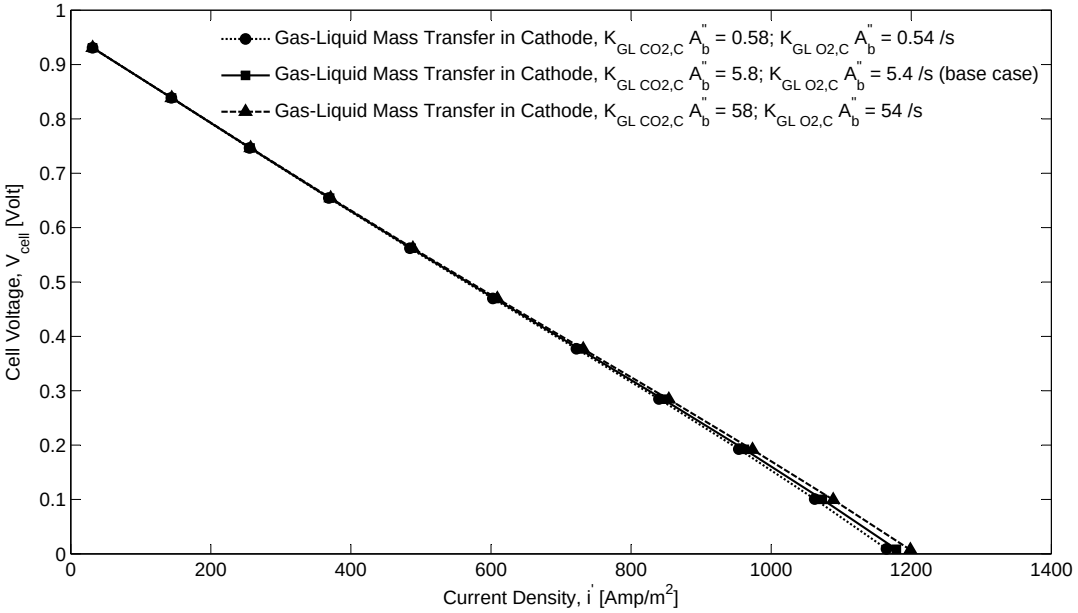

Figure 4.32: Current Density - Cell Voltage Variation with varying gas-liquid mass transfer coefficients for CO_2 and O_2 in the cathode bed. Electrolyte - Li/Na/K ternary eutectic - 43.5/31.5/25 mole%; Settled Particle Resistivity in Anode Bed, $\rho_{ct,0} = 0.0004\,\Omega - m$; Liquid Electrolyte Superficial Velocity (anode/cathode) = $0.1\,m/s$, Bed depth (anode/cathode) = $10\,cm/6\,cm$; Cathode gas composition - CO_2 = $0.1/0.2/0.3\,atm$, O_2 = $0.168\,atm$ and N_2 = remaining; Feed Gas Flow Rate in Cathode; $F_V = 0.1\,m^3/hr$ per $1cm^2$ cell area; $T = 973\,K$; Carbon particle initial diameter, $D_{c,ini} = 175\,\mu m$; Grid Packing:: Wire-Mesh # 24 (anode), # 30 (cathode); Solid hold-up (carbon) at anode inlet = 0.21.

Gas-Liquid Mass Transfer in Anode

The gas-liquid mass transfer in a multi-phase flow through packed beds depends largely upon superficial liquid and gas velocities. In the anode, the superficial gas velocities are quite negligible. In fact, the amount of gas present in the anode bed is largely negligible as has been shown before. It would be pertinent to mention that in such a situation, there is no easy way to reliably estimate gas-liquid mass transfer coefficient that will help in the growth of nucleating bubbles that generate on the surface of carbon particles. Although, preliminary estimations suggest the coefficient to be quite negligible.

In any case, given the fact that gas content in anode is negligible relative to the liquid phase present in the bed, the anode kinetics are largely dependent upon the driving forces arising from differences in concentration of CO_2 on the surface of carbon particle and in the bulk liquid phase.

Simulations conducted to look at the effect of arbitrary increase in gas-liquid mass transfer coefficient by 3-4 orders of magnitude did not produce any significant variation in the fuel cell performance. The reason for that is because of effect of gas phase hold-up mainly on increasing the bed resistivity rather than limiting the current density.

4.3.5 Solubility in Molten Carbonate Salts

There is a certain degree of uncertainties that have been recorded for solubility of gaseous CO_2 and CO_2 in binary and ternary mixtures of alkali molten carbonate salts. For CO_2, there are uncertainties in magnitudes of solubility as reported by various researchers Dubois [1965], Appleby and Van Drunen [1980], Wilemski

[1983], Claes et al. [1999], Kanai et al. [2013]. For O_2, there has been lot of uncertainty regarding actual mechanism involved in the reduction of O_2 due to which solubility data present in the literature may have significant uncertainty Appleby and Nicholson [1972, 1974, 1977, 1980], Appleby and Van Drunen [1980], Moyaux et al. [1993], Uchida et al. [1986], Nishina et al. [1994], Lu [1985], Selman [1992]. For this purpose, solubility of both CO_2 and O_2 have been varied to evaluate sensitivity in the resulting fuel cell performance.

Variation in Solubility of CO_2

The solubility of CO_2 in various alkali mixtures of molten carbonate salts has been the focus of many researchers in the past. Most notable work is from Dubois [1965], Appleby and Van Drunen [1980], Wilemski [1983], Claes et al. [1999], Kanai et al. [2013] involving experiments conducted to record solubility of CO_2 in ternary eutectic mixture of Lithium-Sodium-Potassium (Li/Na/K - 43.5/25/31.5 mol%) molten carbonate salt. The experiments have been conducted for various temperatures in the range of 833K - 973K. The parametric analysis will uncover any possible sensitivity of the solubility of CO_2 on fuel cell performance. Sensitivity analysis for only 973 K is considered here.

The solubility data that is used for the variance study is provided in table 4.5. There is slight to negligible variance in performance as seen from figure 4.33.

The lack of any variation in cell performance due to change in solubility of CO_2 could be due to the fact that the electrolyte is mostly in a CO_2 saturated condition in the cathode at the beginning of the bed and starts getting below saturation condition as the electrolyte flows through the bed because of depletion of CO_2 due to the

Table 4.5: Solubility data for CO_2 in Ternary Eutectic mixture of $(Li-Na-K)_2CO_3$ from different sources in literature at 973 K.

Solubility, H_{CO_2} $\left[\frac{kmol}{m^3 - kPa}\right]$	Source
3.6×10^{-5}	Appleby and Van Drunen [1980]
1.17×10^{-4}	Wilemski [1983]
9.4×10^{-4}	Claes et al. [1999]
2.0×10^{-3}	Kanai et al. [2013]

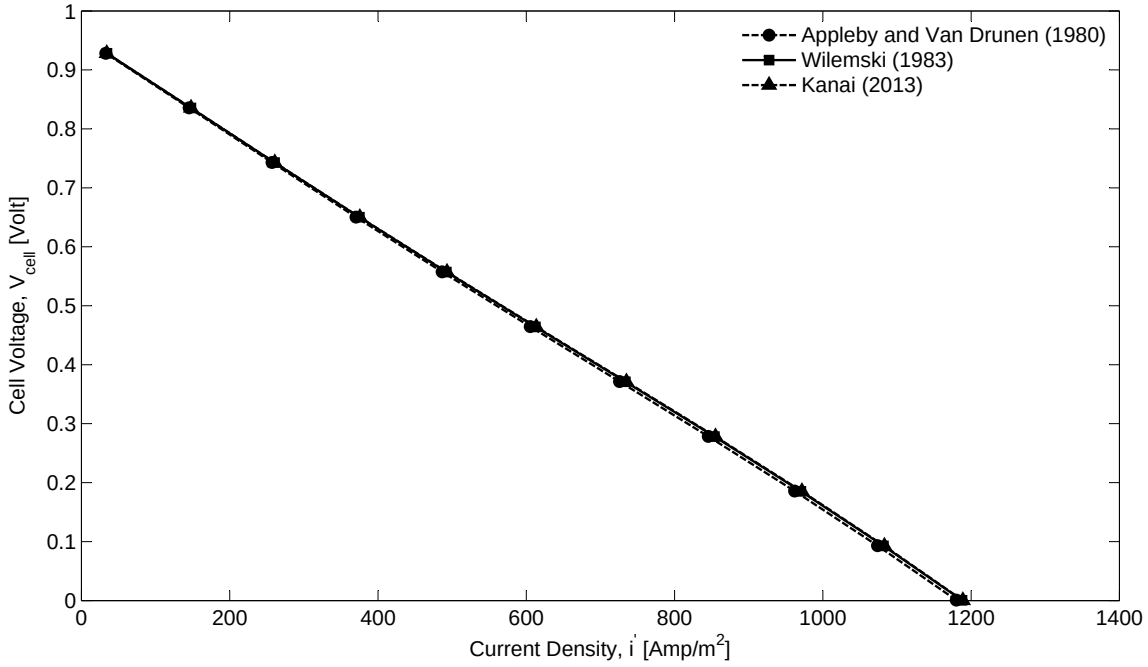

Figure 4.33: Current Density - Cell Voltage Variation with varying solubility of CO_2 in the molten carbonate salt. Electrolyte - Li/Na/K ternary eutectic - 43.5/31.5/25 mole%; Anode grid packing Wire-Mesh #24; Settled Particle Resistivity in Anode Bed, $\rho_{ct,0} = 0.0004\,\Omega - m$**; Liquid Electrolyte Superficial Velocity (anode/cathode) =** $0.1\,m/s$**, Bed depth (anode/cathode) =** $10\,cm$**; Cathode gas composition - CO_2 =** $0.2\,atm$**, O_2 =** $0.17\,atm$ **and N_2 =** $0.63\,atm$**; Feed Gas Flow Rate in Cathode;** $F_V = 0.1\,m^3/hr$**;** $T = 973\,K$**;** $D_{c,ini} = 175\,\mu m$**; Cathode Grid Packing:: Wire-Mesh # 30; Solid hold-up (carbon) at anode inlet =** 0.21**.**

electrochemical reactions. Same situation exists in the anode bed also where the electrolyte is saturated with CO_2 to begin with and ends up being super-saturated at the end of the bed.

The possible reason is that reaction rate is not limited by the concentration of CO_2 in the electrolyte melt and therefore there is no appreciable change in cell performance.

Variation in Solubility of O_2

The solubility data for CO_2 although more readily available than that of CO_2. However, reduction of O_2 in alkali molten carbonate melts is a very complex subject as has been elaborated by various researchers (CITE). For that reason, the actual species responsible for reduction of O_2 in alkali molten carbonate melts has not been clearly established. The cathode kinetic model on which the current work is based on has been developed by Wilemski [1983] using experimental data (Broers) for ternary eutectic mixture of Li/Na/K carbonate. This particular model utilizes peroxide mechanism for the rate kinetics. This particular model can be used for a wide variety of temperatures. Another work by Lu and Selman [1992] utilizes super-oxide mechanism but the limited experimental data is based on binary eutectic mixture of Li/K carbonate at 923K.

The henry's solubility coefficient for O_2 was varied from $3 \times 10^{-6} - 1.2 \times 10^{-5}$ and the variation in cell performance is quite strong as shown in figure 4.34. This clearly means that the rate kinetics as suggested by Wilemski [1983] using peroxide mechanism is severely limited by O_2 concentration in the salt electrolyte.

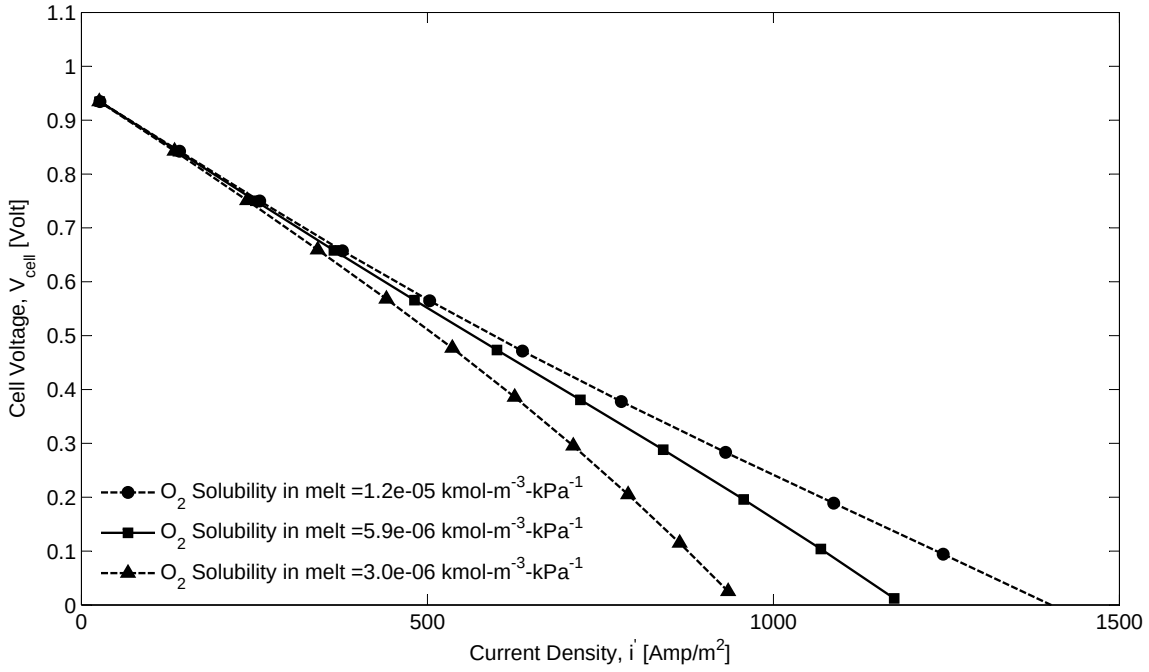

Figure 4.34: Current Density - Cell Voltage Variation with varying solubility of O_2 in the molten carbonate salt. Electrolyte - Li/Na/K ternary eutectic - 43.5/31.5/25 mole%; Anode grid packing Wire-Mesh #24; Settled Particle Resistivity in Anode Bed, $\rho_{ct,0} = 0.0004\,\Omega - m$**; Liquid Electrolyte Superficial Velocity (anode/cathode) =** $0.1\,m/s$**, Bed depth (anode/cathode) =** $10\,cm$**; Cathode gas composition - CO_2 =** $0.2\,atm$**, O_2 =** $0.17\,atm$ **and N_2 =** $0.63\,atm$**; Feed Gas Flow Rate in Cathode;** $F_V = 0.1\,m^3/hr$**;** $T = 973\,K$**;** $D_{c,ini} = 175\,\mu m$**; Cathode Grid Packing:: Wire-Mesh # 30; Solid hold-up (carbon) at anode inlet =** 0.21**.**

4.3.6 Molecular Diffusivity of Gaseous species

Simulations run on varying diffusivity of CO_2 in the melt produced no significant variation in cell performance (and therefore results not reported). This could be attributed to the fact that the rate kinetic model developed by Wilemski [1983] is more sensitive to the oxygen reduction rather than the concentration of CO_2 in the melt. The peroxide mechanism used in developing the rate kinetic equation is limited more by the concentration of O_2 and can be validated by varying diffusivity of O_2 only slightly. The purpose of the parametric variation reported here is to present sensitivity in the cell performance with respect to any change in properties of electrolyte or the participating gaseous species.

Diffusivity of CO_2

No significant variation was observed.

Diffusivity of O_2

Variation in the diffusivity of O_2 by a factor of two can be justified from the work of Nishina et al. [1994] where the authors show the O_2^- ion to be more participating in the reduction of oxygen at cathode. The diffusivity of O_2^- in binary eutectic mixture of Li/K carbonates later in the work is shown to be of the order of 10^{-10} to $10^{-9}\, m^2/s$. The variation in current density - cell voltage relationship with respect to variation in diffusion coefficient of O_2 in molten carbonate salts is presented in figure 4.35.

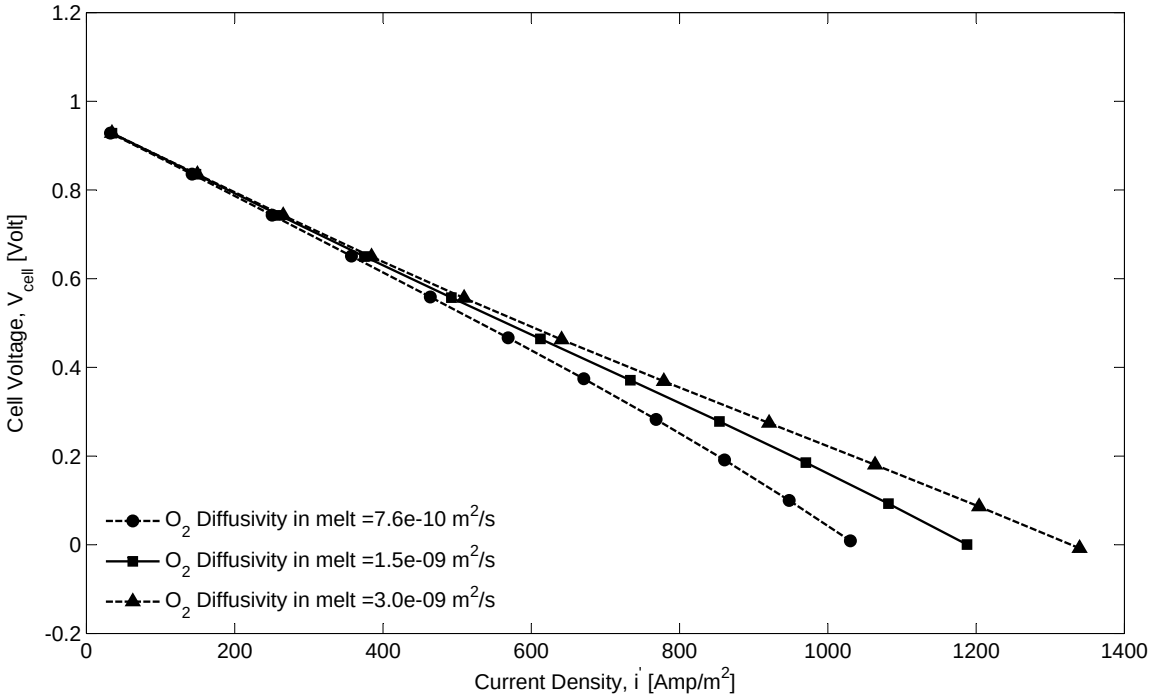

Figure 4.35: Current Density - Cell Voltage Variation with varying diffusion coefficient of O_2 in the molten carbonate salt. Electrolyte - Li/Na/K ternary eutectic - 43.5/31.5/25 mole%; Anode grid packing Wire-Mesh #24; Settled Particle Resistivity in Anode Bed, $\rho_{ct,0} = 0.0004\,\Omega - m$; Liquid Electrolyte Superficial Velocity (anode/cathode) = $0.1\,m/s$, Bed depth (anode/cathode) = $10\,cm$; Cathode gas composition - CO_2 = $0.2\,atm$, O_2 = $0.17\,atm$ and N_2 = $0.63\,atm$; Feed Gas Flow Rate in Cathode; $F_v = 0.1\,m^3/hr$; $T = 973\,K$; $D_{c,ini} = 175\,\mu m$; Cathode Grid Packing:: Wire-Mesh # 30; Solid hold-up (carbon) at anode inlet = 0.21.

4.3.7 Electrolyte Composition Variation

The parametric study conducted here has a potential to cover a much bigger span of variations that range from varying molecular diffusivity and solubility of gas species CO_2 and O_2 in various mixtures of molten carbonate salts in addition to molten salt properties variations in density, viscosity, conductivity, and surface tension.

The sensitivity in the performance of fuel cell model to variations in solubility and diffusivity parameters has already been covered above. The viscosity or surface tension effects have not been investigated.

As for the kinetics which are also dependent on the change in physical properties of electrolyte and participating species, the kinetic data for only cathode is available for an alkali molten carbonate mixture of Lithium and Potassium (Li/K - 62/38 mol% binary mixture) compared to the base case involving ternary mixture of Lithium, Sodium and Potassium (Li/Na/K - 43.5/25/31.5 mol% ternary eutectic mixture). Separate sensitivity investigation with respect to variation in kinetic data for both anode and cathode has already been performed in previous subsections here. The purpose in this section is to look at the effect of varying electrical conductance of various alkali molten carbonate mixtures on the fuel cell model.

It is clear from Janz et al. [1979] that the alkali molten carbonate salts in pure form have very high melting points with pure Li_2CO_3 having the least value, i.e. 996 K which is still higher than the preferred operating temperature for the fuel cell model presented in this work. Using pure Li_2CO_3 as the electrolyte can potentially yield an electrical conductivity of $409 Ohm^{-1} - m^{-1}$ (at 1010 K) which is roughly twice the value that is supplied by a ternary eutectic mixture of Li-Na-K ($204 Ohm^{-1} -$

m^{-1} at 1000 K) but also may need a slightly higher operating temperature (¿1000 K due to higher melting point). Higher temperature although better for kinetics also favor production of more carbon-monoxide (CO). If the advantages resulting from better kinetics and better electrical conductivity outweighs the disadvantages arising from increased CO production then an optimization of operating conditions may be possible. This optimization, however, is not within the scope of the current work and a task for future work.

Alternatively, mixtures of various alkali carbonates can reduce the melting point significantly making it favorable for the operating conditions anticipated for the present work. For example, mixture of Li and Na can yield between roughly $250 - 290\, Ohm^{-1} - m^{-1}$ (for mole% Na_2CO_3 ranging from 50% - 30%) at base case operating temperatures of 973 K in the present work. Similar results yield for binary mixtures of Li-K carbonates in various percentages. On the lower side, specific conductance of $147\, Ohm^{-1} - m^{-1}$ at the base operating temperatures (973K) has been reported for equal ternary mixture of Li-Na-K.

Although, the upside for having a lower specific conductance is not clear, it might still be pertinent to put a perspective on the sensitivity in fuel cell performance based on variation in specific conductance of the molten salt electrolyte in case there are possible benefits from kinetics.

The parametric variation in fuel cell performance with respect to variation in the specific conductance of molten carbonate electrolyte is shown in figure 4.36.

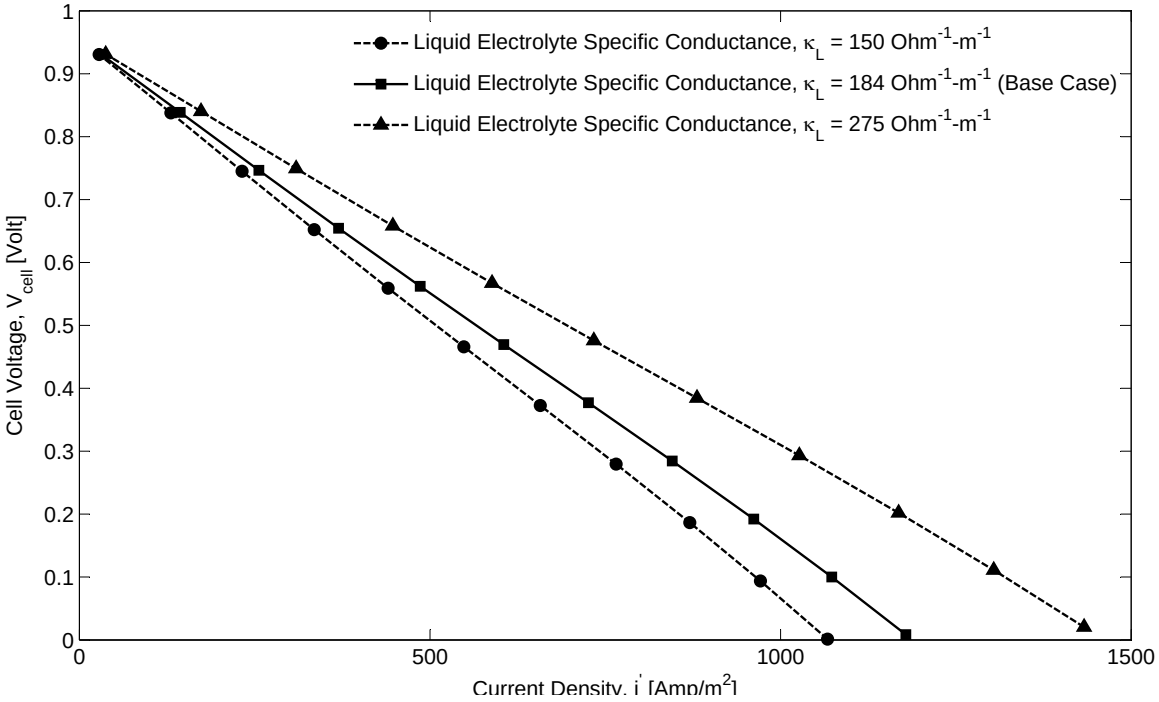

Figure 4.36: Current Density - Cell Voltage Variation with varying specific conductance of molten carbonate electrolyte. Electrolyte Used as Base Case - Li/Na/K ternary eutectic - 43.5/31.5/25 mole%; Settled Particle Resistivity in Anode Bed, $\rho_{ct,0} = 0.0004\,\Omega - m$**; Liquid Electrolyte Superficial Velocity (anode/cathode) =** $0.1\,m/s$**, Bed depth (anode/cathode) =** $10\,cm/6\,cm$**; Cathode gas composition - CO_2 =** $0.2\,atm$**, O_2 =** $0.168\,atm$ **and N_2 = remaining; Feed Gas Flow Rate in Cathode;** $F_v = 0.1\,m^3/hr$ **per** $1cm^2$ **cell area;** $T = 973\,K$**; Carbon particle initial diameter,** $D_{c,ini} = 175\,\mu m$**; Grid Packing:: Wire-Mesh # 24 (anode), # 30 (cathode); Solid hold-up (carbon) at anode inlet =** 0.21**.**

4.4 Discussion Of Results

The model presented in the thesis has not been independently validated with experimental data conducted for same conditions as the model. However, in this section an operating envelope using the parametric study as the basis is established and compared with some experimental data from other literature sources. One of the purpose of the current study was to demonstrate the feasibility of building process simulation models for direct carbon type of fuel cells with sufficient details. This can enhance our ability to conceptualize novel design configurations and design/conduct experiments based on optimum operating conditions.

As discussed in literature review before, researchers at Lawrence Livermore National Laboratory [Cooper et al., 2002, 2003, Cooper, 2004a, Cherepy et al., 2005] have developed a cell in which a paste of carbon particles suspended in $(Li/K)_2CO_3$ binary eutectic electrolyte is fed to a porous membrane current collector made of nickel foam. The LLNL workers have attained 1.0 kW/m^2 membrane at 80% efficiency and 4.5 kW/m^2 membrane at maximum power, using a variety of coal- and biomass-derived carbon fuels. Some experiments (3 data-sets extracted) conducted on the carbon black sample 5 (called the Arosperse 3, from furnace oil) at 700 $^\circ C$ is compared with model results at the same temperature. One data-set is extracted from the experiment using needle petroleum coke (sample 8) at 800 $^\circ C$ from the LLNL work in Cherepy et al. [2005] and compared with the model results at same temperature and same average carbon particle size. The experiments by LLNL researchers used air and CO_2 in the composition which is very close to what has been used in the model. The model is run using properties of ternary eutectic mixture (43.5/31.5/25 mol%) of Li/Na/K carbonates due to lack of property

information for the binary mixture of Li/K (38/62 mol%) carbonates. Two more data-sets were extracted from the experimental work on the direct carbon fuel cell using molten carbonate electrolyte [Predtechenskii et al., 2009a, Kouchachvili and Ikura, 2011]. More details are furnished in table 4.6. The data-set from Predtechenskii et al. [2009a] is compared with the model simulation that is run using pyrolitic graphite particles of 1 mm and at temperature of 750$^{\circ}C$ for a justified comparison. For comparison with data-set from Kouchachvili and Ikura [2011], model was again set for conditions similar to the experiment, however in this particular case there is no information on the carbon particle size from the experiment of Kouchachvili and Ikura [2011].

To be able to simulate the experimental conditions exactly in the model is not the purpose of this comparison work, rather to demonstrate the practical viability of the investigated fuel cell model in light of literature data available for similar experimental conditions.

4.4.1 Experimental data comparison with model at 700 $^{\circ}C$

As detailed above in table 4.6, two sets of experimental data have been used to compare process simulation model at operating temperatures of 700 $^{\circ}C$. The results of comparison are shown in terms of current density - cell voltage and current density - power density relationships in figures 4.37 and 4.38. The model performance bounds are used from the parametric results variations and shown through the range of values for various input parameters in the figure caption.

Peak power of $\approx$450 W/m^2 at a current density of $\approx$1100 A/m^2 is observed at the operating anode/cathode potential difference of 0.45 V. The comparable data

Table 4.6: Data-set information from LLNL [Cherepy et al., 2005], Kouchachvili and Ikura [2011], and Predtechenskii et al. [2009a] with experimental details, used for comparison with the model

Data-set for comparison	Temperature	Sample information	Carbon particle size	Electrolyte
Cherepy et al. [2005] data-set # 1	700$^{\circ}C$	Arosperse 3, sample 5, furnace black fuel	0.03 μm	Li/K 38/62 mol%
Cherepy et al. [2005] data-set # 2	800$^{\circ}C$	Arosperse 3, sample 5, furnace black fuel (day 1)	0.03 μm	Li/K 38/62 mol%
Cherepy et al. [2005] data-set # 3	800$^{\circ}C$	Arosperse 3, sample 5, furnace black fuel (day 3)	0.03 μm	Li/K 38/62 mol%
Cherepy et al. [2005] data-set # 4	800$^{\circ}C$	Needle petroleum coke, sample 8	3-100 μm	Li/K 38/62 mol%
Predtechenskii et al. [2009a] data-set	750$^{\circ}C$	Dispersed graphite particles	1 mm	Li/K 38/62 mol%
Kouchachvili and Ikura [2011] data-set	700$^{\circ}C$	Needle petroleum coke	-	Li/Na/K 43.5/31.5/25 mol%

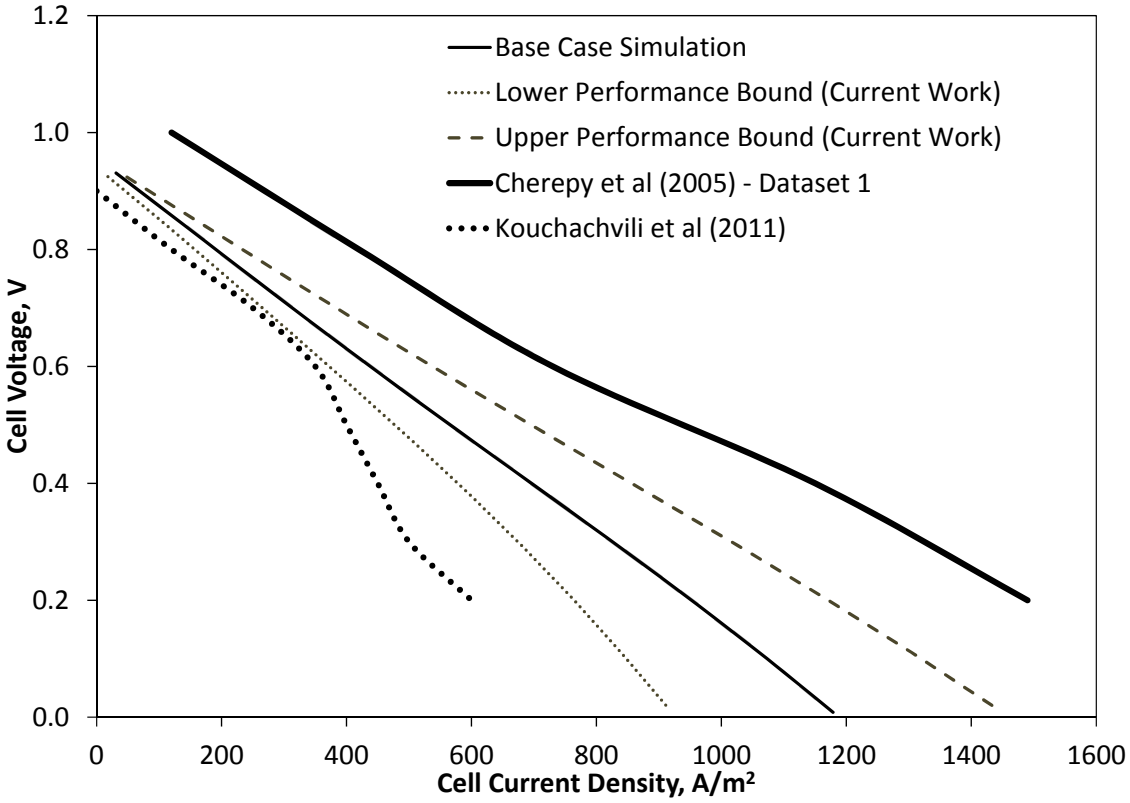

Figure 4.37: Current Density - Cell Voltage process simulation results comparison with experimental data from LLNL and others. Model Simulation Parameters: Settled Particle Resistivity in Anode Bed, $\rho_{ct,0} = 0.0004 - 0.04\,\Omega - m$**; Liquid Electrolyte Superficial Velocity (anode/cathode) =** $0.05 - 0.15\,m/s$**, Bed depth (anode/cathode) =** $5 - 15\,cm/5 - 15\,cm$**; Cathode gas composition -** CO_2 **=** $0.1 - 0.3\,atm$**,** O_2 **=** $0.15 - 0.19\,atm$ **and remaining** N_2**; Feed Gas Flow Rate in Cathode;** $F_V = 0.01 - 1\,m^3/hr$ **per** $1cm^2$ **cell area;** $T = 973\,K$**/700** $^{\circ}C$**; Carbon particle initial diameter,** $D_{c,ini} = 50 - 250\,\mu m$**; Grid Packing:: Wire-Mesh # 20,24,30 (anode), # 24,30,40 (cathode); Solid hold-up (carbon) at anode inlet =** $0.19 - 0.23$**, specific conductance of molten carbonate electrolyte = 150-275** $Ohm^{-1} - m^{-1}$

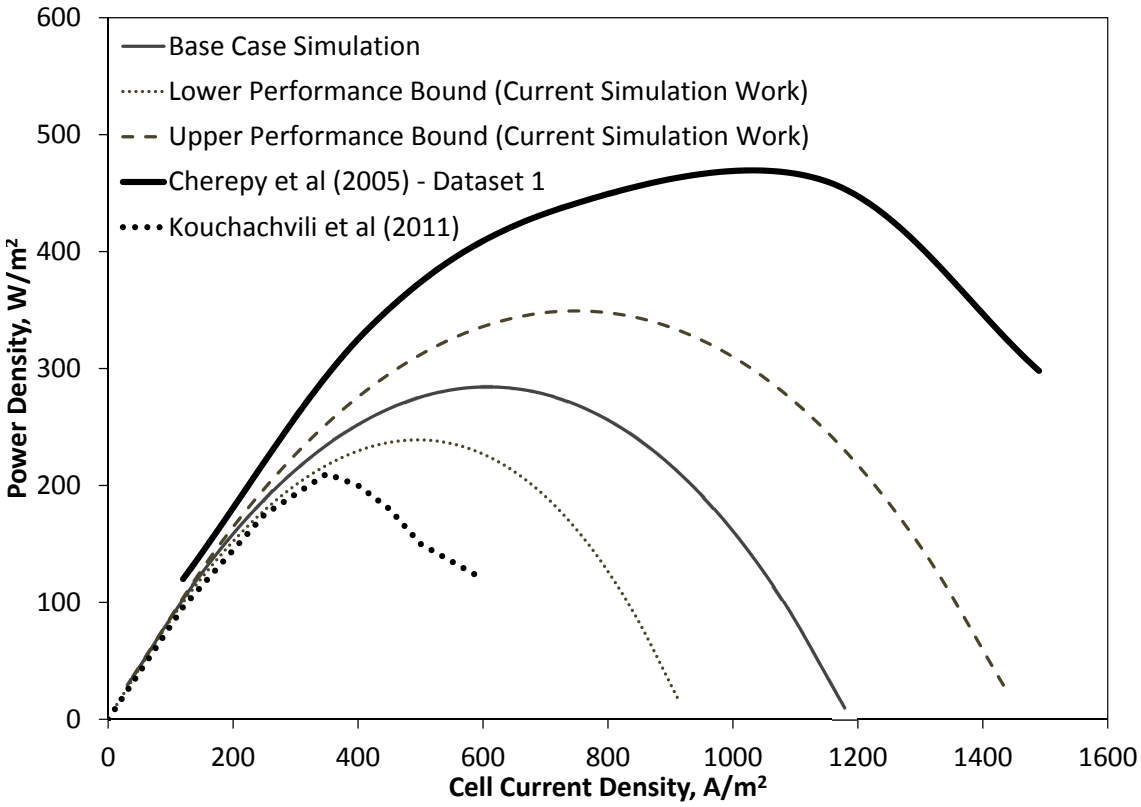

Figure 4.38: Current Density - Power Density process simulation results comparison with experimental data from LLNL and others. Settled Particle Resistivity in Anode Bed, $\rho_{ct,0} = 0.0004 - 0.04\,\Omega - m$**; Liquid Electrolyte Superficial Velocity (anode/cathode) =** $0.05 - 0.15\,m/s$**, Bed depth (anode/cathode) =** $5 - 15\,cm/5 - 15\,cm$**; Cathode gas composition - CO_2 =** $0.1 - 0.3\,atm$**, O_2 =** $0.15 - 0.19\,atm$ **and remaining N_2; Feed Gas Flow Rate in Cathode;** $F_V = 0.01 - 1\,m^3/hr$ **per** $1cm^2$ **cell area;** $T = 973\,K$**/700** $^\circ C$**; Carbon particle initial diameter,** $D_{c,ini} = 50 - 250\,\mu m$**; Grid Packing:: Wire-Mesh # 20,24,30 (anode), # 24,30,40 (cathode); Solid hold-up (carbon) at anode inlet =** $0.19 - 0.23$**, specific conductance of molten carbonate electrolyte = 150-275** $Ohm^{-1} - m^{-1}$

Table 4.7: Process simulation results comparison with experimental data from LLNL [Cherepy et al., 2005] and Kouchachvili and Ikura [2011] including current density, cell voltage, and power density at 700 $^{\circ}C$ temperature.

Parameters	Process simulation Model	Cherepy et al. [2005] data-set 1	Kouchachvili and Ikura [2011] data-set
Carbon Particle Type	Pyrolitic Graphite	Arosperse 3 furnace black fuel (sample 5)	Needle Petroleum Coke
Carbon Particle Size	50-250 μm	3 nm	n/a
Limiting Current Density, $[A/m^2]$	911-1433	> 1600	-
Current Density at 0.6 V, $[A/m^2]$	360-520	730	-
Max. Power Density, $[W/m^2]$	240-350	460	-

for model vs experimental results is tabulated in table 4.7.

The purpose of published work by Kouchachvili and Ikura [2011] was to show improvement in performance of a direct carbon fuel cell by using additives, i.e. 20 wt% Cs_2CO_3 in a ternary eutectic mixture of $(Li/Na/K)_2CO_3$ in mol% 43.5/31.5/25.0. The base case for comparison in this experiment was without additives which is what has been used to compare model simulation results in the present work. For clarity purposes, it should be mentioned that in their experiment, Kouchachvili and Ikura [2011] found significant improvement in the cell performance with the addition of 20 wt% Cs_2CO_3 by achieving limiting current densities of more than 800 A/m^2.

4.4.2 Experimental data comparison with model at 750 $^{\circ}C$

The simulation model has been run at 750 $^{\circ}C$ and compared with experimental data extracted from the work of Predtechenskii et al. [2009a]. This particular experimental work used binary electrolyte mixture of Li/K 38/62 mol% with 1 mm dispersed graphite particles suspended in the melt. Cathode consisted of a NiO coated SS wire netting and was kept under slightly pressurized conditions of 150-700 mm water column above standard pressure. The composition of gas input to the cathode was in the ratio of CO_2/O_2 = 0.1. The cathode composition, temperature, and carbon particle size were matched in the simulation model. The current density - cell voltage and current density - power density plots are shown in figure 4.39.

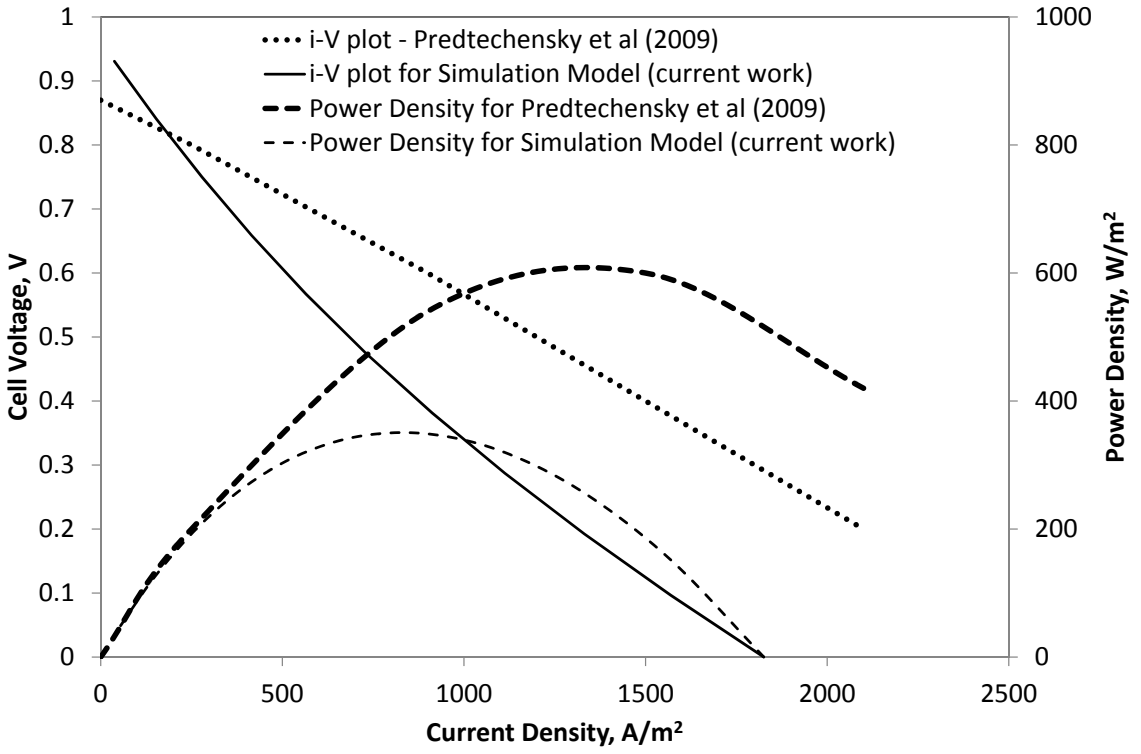

Figure 4.39: .

] Current Density - Cell Voltage process simulation results comparison with experimental data from LLNL [Cherepy et al., 2005][Figure 8, top]. Settled Particle Resistivity in Anode Bed, $\rho_{ct,0} = 0.0004\,\Omega - m$; Liquid Electrolyte Superficial Velocity (anode/cathode) = $0.1\,m/s$, Bed depth (anode/cathode) = $10\,cm/10\,cm$; Cathode gas composition - CO_2 = $0.1\,atm$, O_2 = $0.9\,atm$; Feed Gas Flow Rate in Cathode; $F_v = 0.1\,m^3/hr$ per $1cm^2$ cell area; $T = 1023\,K$/750 $^\circ C$; Carbon particle initial diameter, $D_{c,ini} = 1\,mm$; Grid Packing:: Wire-Mesh #24 (anode), # 30 (cathode); Solid hold-up (carbon) at anode inlet = 0.21, specific conductance of molten carbonate electrolyte = 184 $Ohm^{-1} - m^{-1}$

4.4.3 Experimental data comparison with model at 800 $^{\circ}C$

As detailed above in table 4.6, three experimental data-sets have been used to compare process simulation model at operating temperatures of 800 $^{\circ}C$. All three data-sets are extracted from the work of Cherepy et al. [2005]. The results of comparison are shown in terms of current density - cell voltage and current density - power density relationships in figures 4.40.

The simulation model was also run at another operating condition where, T = 800 $^{\circ}C$, 60 μm diameter graphite particles other parameters remaining the same as in the base case conditions. The temperature was selected to match the operating data of the experimental conditions from LLNL given by [Cherepy et al., 2005] for the petroleum needle coke whose size was given as 3 - 100 μm. Due to higher temperature, reaction rate is higher and therefore lower bed depths can be used for running the process simulation model. The comparison of key data between the results from the simulation model and from the experimental data by [Cherepy et al., 2005] is given in table 4.8. The current-density and cell-voltage plots comparing the model and experimental data is shown in figure 4.40. The comparison seems to be of good quality considering the design by [Cherepy et al., 2005] to be conceptually similar to the design presented in this work. The power density plot comparison between the results from process simulation model and the experimental data from [Cherepy et al., 2005] is shown in figure 4.41. The comparison seem to depict quite a good match.

The process simulation run at T = 800 $^{\circ}C$ is considered under certain assumptions. The most important one being that at such higher temperature, there may be some amount of CO generation at the anode as has been indicated by Weaver

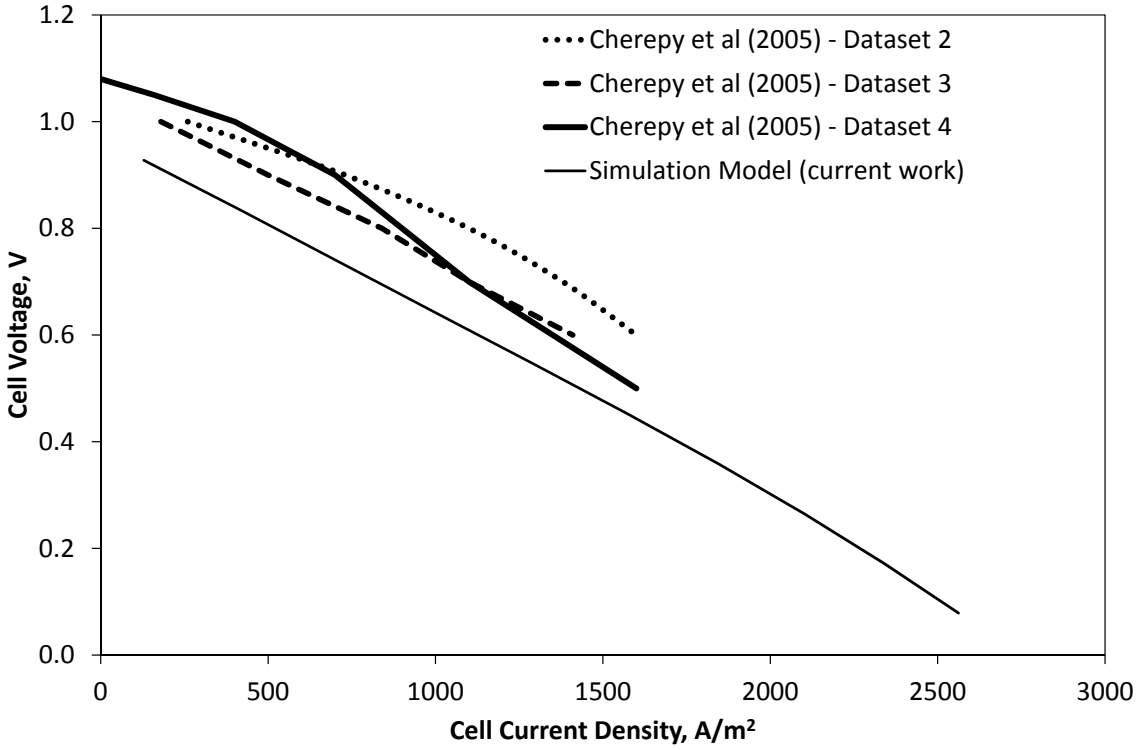

Figure 4.40: .

] Current Density - Cell Voltage process simulation results comparison with experimental data from LLNL [Cherepy et al., 2005][Figure 8, top]. Settled Particle Resistivity in Anode Bed, $\rho_{ct,0} = 0.0004\,\Omega - m$; Liquid Electrolyte Superficial Velocity (anode/cathode) = $0.1\,m/s$, Bed depth (anode/cathode) = $6\,cm/8\,cm$; Cathode gas composition - CO_2 = $0.2\,atm$, O_2 = $0.17\,atm$ and remaining N_2; Feed Gas Flow Rate in Cathode; $F_v = 0.1\,m^3/hr$ per $1cm^2$ cell area; $T = 1073\,K$/800 $^\circ C$; Carbon particle initial diameter, $D_{c,ini} = 60\,\mu m$; Grid Packing:: Wire-Mesh #24 (anode), # 30 (cathode); Solid hold-up (carbon) at anode inlet = 0.21, specific conductance of molten carbonate electrolyte = 184 $Ohm^{-1} - m^{-1}$

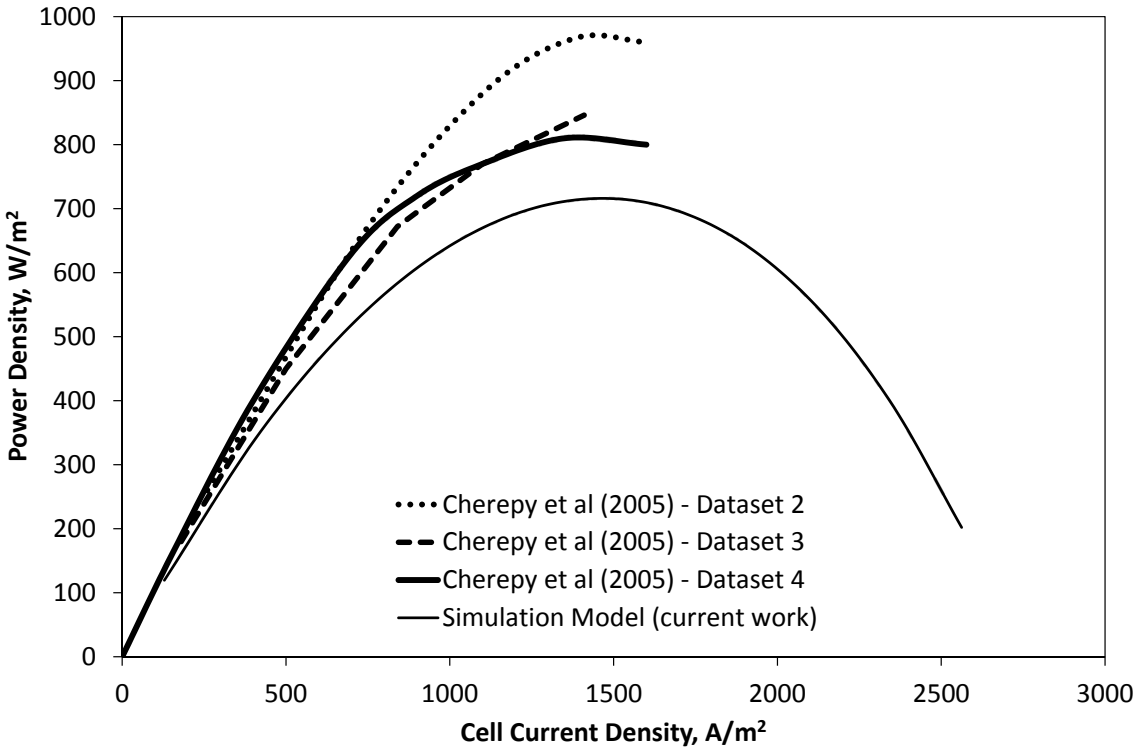

Figure 4.41: Current Density - Power Density process simulation results comparison with experimental data from LLNL [Cherepy et al., 2005]. Settled Particle Resistivity in Anode Bed, $\rho_{ct,0} = 0.0004\,\Omega - m$**; Liquid Electrolyte Superficial Velocity (anode/cathode) =** $0.1\,m/s$**, Bed depth (anode/cathode) =** $6\,cm/8\,cm$**; Cathode gas composition - CO_2 =** $0.2\,atm$**, O_2 =** $0.17\,atm$ **and remaining N_2; Feed Gas Flow Rate in Cathode;** $F_V = 0.1\,m^3/hr$ **per** $1cm^2$ **cell area;** $T = 1073\,K$**/800** $^\circ C$**; Carbon particle initial diameter,** $D_{c,ini} = 60\,\mu m$**; Grid Packing:: Wire-Mesh #24 (anode), # 30 (cathode); Solid hold-up (carbon) at anode inlet =** 0.21**, specific conductance of molten carbonate electrolyte = 184** $Ohm^{-1} - m^{-1}$

Table 4.8: Process simulation results comparison with experimental data from LLNL [Cherepy et al., 2005] including current density, cell voltage, and power density at 800 $^{\circ}C$ temperature.

Parameters	Process simulation Model	Cherepy et al. [2005] data-set 2	Cherepy et al. [2005] data-set 3	Cherepy et al. [2005] data-set 4
Carbon Particle Type	Pyrolitic Graphite	Arosperse 3 furnace black fuel (sample 5)	Arosperse 3 furnace black fuel (sample 5)	Needle Petroleum Coke (sample 8)
Carbon Particle Size	60 μm	0.003 μm	0.003 μm	3-100 μm
Limiting Current Density, [A/m^2]	2600	> 1600	> 1600	> 1600
Current Density at 0.6 V, [A/m^2]	$\approx$950	1600	1410	1350
Max. Power Density, [W/m^2]	710	960	850	810

et al. [1979], Vutetakis [1985] among others. However, considering a very earlier work by [Hauser Jr., 1964][Tables XIX, XX and XXI] on graphite anodes, it's clear that at T = 700 $^{\circ}C$, amount of CO generated is $< 1\%$, for T = 800 $^{\circ}C$, the amount of CO in the anode off-gas could be 1-2%, and the mole fraction of CO approaches 10% when the temperature approaches 870 $^{\circ}C$.

The model has been developed considering no generation of CO at the anode, however still considering such low amounts of CO present in the off-gases at 800 800 $^{\circ}C$, the comparison seems quite fair. Apart from the past work by Cherepy et al. [2005] and more recent work by Kouchachvili and Ikura [2011] to ascertain current-density, cell-voltage and power density relationships for direct carbon fuel cells, there has been other experimental efforts by Zhang et al. [2011] and Li et al. [2010] where different feedstocks have been used in various configurations to investigate half-cell performance.

Considering all the work that has been done in the current work to model electrode kinetics in anode and cathode, various hold-up and mass transfer correlations, and the governing equations with initial conditions, this is a very positive step in the direction of being able to model complex electrochemical processes involving direct carbon fuel cells.

4.5 Results Summary

1. An appropriate design of the packed bed anode and cathode is conceptualized for the Entrained Fuel and Oxidizer (EFO) fuel cell. The cathode involves perforated plates or wire-mesh made of nickel coated stainless steel working both as an electrode and current collector. In the anode, carbon particles themselves act as anode and the perforated plates or wire-mesh made of nickel coated stainless steel act as the current collector.

2. A preliminary energy balance of the fuel cell and the balance-of-plant was done during the initial phase of the project. During the later phase, a one-dimensional model for the fuel cell was developed. Using an optimization routine this model is able to establish cell voltage vs current density relationships or the polarization curve given certain load conditions.

3. The results from the energy balance reveals that the efficiency is determined predominantly by CO/CO_2 ratio leaving the anode. Experiments by others have shown that CO_2 concentrations exceed those predicted by Boudouard equilibrium. Therefore, a useful alternate model is clearly necessary for good cell design and accurate prediction of cell performance.

4. The effect of temperature is investigated both during the energy balance of the cell and the balance-of-plant and also while analyzing the one-dimensional fuel cell model. If decoupled from the CO/CO_2 ratio, temperature has a relatively small effect on first law efficiency. Increasing cell temperature generally increases work output slightly and also increases the value of the waste heat. However, the most important effects of temperature is on the reaction rates.

This is witnessed from the increase in cell performance with the increase in cell temperature. However, high temperature also leads to low CO_2 yield which in turn tends to reduce the first law efficiency. Therefore, an optimum cell temperature will lead to optimum cell performance along with the first law efficiency. This is only possible if an alternate model to describe the CO/CO_2 ratio leaving the anode is built. It may be, for cells of the type described here, that there is considerable temperature difference between the anode and the cathode. Determining this difference will require information on the thermodynamic properties of $CO_3^=$ in molten salts. Therefore, the energy balance analysis was done assuming an isothermal cell.

5. One of the major achievements in the modeling of processes was to understand that the packed bed geometry is capable of producing large area per unit volume available for reaction. Large surface area when used for the chemical reaction produces high mass transfer rates and good economies of scale. Moreover, the mass transfer processes in the direct carbon molten carbonate (DCMC) fuel cell are surely effective but still need more investigation before reaching an optimum design.

6. Base Case results were generated at temperatures of 700 $^{\circ}C$. These included generation of current density - cell voltage relationships that shows activation losses at high cell voltage (low current density) and also demonstrates the ohmic resistance and possible mass transfer limitations on the cell performance. The cell performance was mainly under ohmic and kinetic control for the base case condition.

7. Parametric variations using design considerations involved changing feed gas flow rate to the cathode, bed thickness of anode and cathode, varying feed gas composition (i.e. CO_2 and O_2) into cathode, operating cell temperatures, liquid electrolyte velocities in both anode and cathode beds, effect of intermediate layer between anode and cathode, change in packing characteristics (i.e. surface area per unit volume, bed voidage, etc), and varying diameter of carbon particles.

8. Reduction in feed gas flow rate to cathode amounted to reducing gas hold-up which tend to increase cell performance because of reduction in ohmic losses as given by Bruggeman's relationship. It's not clear if there will be a trade-off in this regard due to cell performance being more sensitive to changes in O_2 gas concentration in the liquid melt which could be because of low solubility of O_2 (2 order of magnitude lower as compared to CO_2) limiting the rate kinetics. Many researchers have already indicated the complexity of oxygen reduction mechanism in molten carbonate salts [Appleby and Nicholson, 1972, 1974, 1977, Yuh and Selman, 1991, Uchida et al., 1986, Lu, 1985, Nishina et al., 1994, Moyaux et al., 1993, Kunz et al., 1984, Winnick and Ross Jr., 1981, McHardy, 1979, Lu and Selman, 1992, Selman, 1992]. Further investigation into this could be a part of future work.

9. Increase in bed thickness causes increase in cell performance but after a certain optimum thickness, the benefits start diminishing. Opposite trend is observed when the bed thickness is reduced. The reason for this is anticipated to be a balance between kinetic and ohmic control. At lower bed depths, kinetics are mainly controlling the cell performance and at higher bed

depths, ohmic resistance is substantial.

10. CO_2 variation in cathode feed gas composition has insignificant effect on the cell performance compared to the O_2 variation. This is due to low solubility of O_2 (2 order of magnitude lower as compared to CO_2) in molten carbonate salts limiting the rate kinetics.

11. Variation in cell temperature probably has the biggest effect amongst all design considerations. This is mainly because of cell performance controlled by rate kinetics. Improved kinetics at higher temperature and vice-versa is the observed effect as expected. However, higher temperature rate kinetics may also be mired by higher CO production due to Boudouard equilibrium and possible corrosion with stainless steel grid which is being used as electrode/current collector.

12. Variation in liquid electrolyte velocities tend to influence mass transfer and therefore has a significant effect as seen from the results.

13. The purpose of the intermediate layer between the cathode and anode is to facilitate transport of carbonate ions from the electrolyte in the cathode distributor into the anode bed. It maybe expected to have a quiescent layer of electrolyte present within intermediate layer so as keep cathode/anode electrolyte loops segregated electrically but allow ions to transport. More thickness means more ohmic polarization and therefore thinner the better. No preliminary designs have been made for the distributor section or how this will physically be done. This would be a consideration while designing the cell internals, feed/distributor manifolds, and the section of the main reactor.

14. Higher surface area per unit volume in the cathode packing tend to provide better cell performance as expected owing to more reactive sites for reactions to proceed. However, in anode the reaction takes place on the surface of the carbon particles and therefore insignificant effect of packing in anode is observed.

15. Carbon particle diameter is used to evaluate area current density in the anode bed. Higher the carbon particle diameter, lower is the area per unit volume and therefore lower will be the area current density. Also from the liquid-solid holdup correlations in the anode, reduction in carbon particle diameter also reduces solid-holdup that tends to increase contact resistance slightly which can reduce the current density. Although, a trade-off must be observed here but currently not because of non-availability of a proper correlation that can link contact resistance to the diameter of particles.

Chapter 5

Conclusions

1. Design Concept

The co-current flow concept has been developed for the direct carbon fuel cell based on molten carbonate recirculating electrolyte. Cathode and anode beds are separated by a quiescent layer of electrolyte in the intermediate layer that allows for the transport of carbonate ions from cathode to anode.

In the cathode, co-current flow of electrolyte with entrained CO_2 and O_2 is sent in the upward direction. The gas entrainment in the electrolyte is done at the entry of the cathode bed.

In the anode, co-current flow of a slurry of electrolyte entrained with carbon particles of pre-defined size is sent in the downward direction. The nucleation of gaseous CO_2 is assumed to take place at the beginning of anode bed where some dissolved O_2 diffuses from the cathode bed through the intermediate layer. The velocity of the electrolyte is such that it keeps the carbon particles and the evolved CO_2 gas bubbles entrained within the liquid while flowing downward.

Based on preliminary work with the process model, a design was developed

that had reasonable, though not yet optimized, performance. The parameters for this design are shown in table 5.1. These parameters were used the as the base case for model studies.

2. Process Model Development

A model of the processes within the co-current molten carbonate DCFC has been developed.

- In the cathode bed, transport equations for the mass transfer of CO_2 and O_2 from the gas phase (bubbles) to the liquid phase and from liquid phase to the solid phase (grid surface) have been developed.

  In the anode bed, transport equations for the mass transfer of CO_2 from the solid phase (carbon particle surface) to the liquid phase and from the liquid phase to the gas phase (bubbles) have been developed.

  It was found that for both anode and cathode, the transport of CO_2 and O_2 was dominated by gases dissolved in the liquid phase. The axial transport of CO_2 and O_2 in the gas phase was relatively small.

- The thermo-physical properties in gas, liquid and solid phase for pure components and mixtures have been estimated from data in the literature. A complete set of properties, e.g. density, solubility, and molecular diffusivity were available for the case where electrolyte was a ternary eutectic mixture of lithium, potassium and sodium carbonates. Limited data was available for the cases where the electrolyte was a binary mixture using combinations of lithium, potassium and sodium carbonates.

Slurry properties in the anode were evaluated from the properties of solid carbon and the liquid electrolyte using literature correlations.

- The literature on electrochemical kinetics for oxygen reduction in the cathode of molten carbonate fuel cells was reviewed and two different models were developed for the reaction rate. The models utilized Butler-Volmer type reaction rate equations and were developed based on the ”peroxide” mechanism and ”superoxide” mechanism for oxygen reduction reactions.

  The model based on peroxide mechanism was developed for the electrolytes that are a ternary eutectic mixture of lithium, potassium and sodium carbonates. The model based on superoxide mechanism was developed for the binary eutectic mixture of lithium, and potassium carbonates.

  This combination of mechanisms and electrolytes was dictated by the availability of data in the literature.

  Owing to the availability of limited data for the thermo-physical properties for a binary eutectic mixture of lithium, and potassium carbonates, the super-oxide reaction rate model has not been used.

- An electrochemical kinetic rate equation for pyrolitic graphite carbon oxidation in the anode has been developed from experimental data available in the literature. Empirical models for the kinetic rate coefficients, i.e. charge transfer coefficient and exchange current density, have been developed as a function of temperature. The resulting Butler-Volmer type kinetic rate equation has been developed as a function of surface over-potential, CO_2 concentration and the kinetic coefficients. Adequate data for modeling was available only

for pyrolitic graphite.

- Models for predicting ionic resistance in the electrolyte due to the presence of gas bubbles, solid particles and metallic grid have been developed using literature correlations for effective conductivity in dispersions.

- Base case design and input parameters have been developed based on the preliminary evaluation of the model. They are shown in table 5.1.

3. Evaluation of Model and of Cell Design

- Cell performance is strongly penalized by ohmic polarization. This is due to large ionic conduction distances relative to a membrane type fuel cell. In the anode, insignificant losses from diffusion and contact resistance were observed. Most losses were from ionic conduction resistance and chemical kinetics.

  Ionic conduction loss was large because of distance. It can be minimized by:

  - Minimizing interference from solid bed and bubbles
  - Selecting salt with good conduction

  Anode kinetic losses were affected by temperature and availability of reacting sites on carbon surface. It can be minimized by:

  - Operating the cell at maximum temperature compatible with materials and low CO production

Table 5.1: Fuel cell modeling parameters investigated in the current work.

Parameters	Base Case Value	Possible Range	Criteria
Molten salt electrolyte blend	Li/Na/K ternary eutectic	Li/Na/K ternary eutectic, Li/K and Na/K binary eutectic	Most data available
Liquid electrolyte flow	0.10 m/s	0.05 - 0.15 m/s	Typical velocities of saturated solutions flowing through packing
Gas flow	0.1 m^3/hr	0.01 - 1.0 m^3/hr	Give better fuel cell performance
Cathode gas composition	CO_2 = 0.2, O_2 = 0.17, N_2=0.63	CO_2 = 0.1 - 0.3, remaining O_2/N_2 ratio as in air	Better cathode kinetics
Anode packing screen size	#24 mesh	#20 -#30 mesh	Allow carbon particles to flow through
Anode bed thickness	10 cm	5-15 cm	Adequate cell current densities, physical construction limit
Cathode packing screen size	#30 mesh	#24 -#40 mesh	High surface area per unit volume
Cathode bed thickness	10 cm	5-15 cm	Adequate cell current densities, physical construction limit
Temperature	973 K	923-1023 K	Trade-off between low CO production and better anode kinetics
Carbon loading	21%	19%-23%	Limited by settled (no flow) conditions and contact resistance correlation
Carbon particle diameter	175 μm	50-250 μm	Smaller is better, limited by contact resistance correlation
Intermediate layer thickness	1.0 cm	0.5-1.5 cm	Physical construction limit

- Coking or otherwise pretreat coal or biomass to maximize reacting site density
- Changing salt compositions to include other than Li/Na/K carbonates.

Cathode kinetic losses were affected by varying O_2/CO_2 molar ratio in the gas feed, temperature, salt composition and wire mesh grid. It can be minimized by:

- Setting O_2/CO_2 mole ratio in the gas feed that gives best performance
- Operating the cell at maximum temperature compatible with materials
- Using finer grid to increase reacting sites availability
- Changing salt compositions to include other than Li/Na/K carbonates.

♦ Base case model results were evaluated by comparison with the experimental results from other researchers working with similar similar molten carbonate electrolyte-based DCFC designs. The performance of this cell was competitive with that of the other designs. The quantitative and qualitative similarity with experimental results gave a rough assurance that modeling was done correctly.

♦ Parametric studies based on variations in operating design conditions were performed on 12 different parameters. Two parameters that produced no significant variation were liquid superficial velocity and the grid packing in anode. The strongest variation was observed with respect to changes in operating temperature due to effect on chemical kinetics.

- Parametric studies based on estimated uncertainties in correlations from the literature were performed on thirteen parameters. Four parameters were found to have no significant effect on the cell performance. These were gas-liquid and liquid-solid mass transfer coefficients in anode and solubility and diffusivity of CO_2 in molten carbonate salts. Strongest effect was seen as the result of varying exchange current density in anode and cathode and varying electrolyte conductivity.

Chapter 6

Future Work

1. Model Validation is an important aspect of any process development in the industry due to its ability to save unnecessary capital cost in a nascent technology, especially the kind of direct carbon fuel cell technology using porous bed electrodes that has been presented in the current work. Many design changes can be simulated and only the ones that have a significant effect need to be addressed.

2. Carbon fed slurry concept has recently gained popularity amongst researchers from being used in the molten carbonate salts to being used along-with high performance SOFC cathodes with extended anodes. Current experimental work on this new direction is lacking efforts that show scaling up of these designs suited for an industrial/commercial plant. Many explored designs utilize stagnant carbon entrained molten salts that would require a concept similar to the one presented in the current work for the scaling up process.

3. Comprehensive anode kinetics for DCFC that can either reliably confirm or negate the hypothesis of no-effect of CO_2 concentration in the purge gas (3% or 100% when used in conjunction with an inert gas) on the rate kinetics

at both higher and lower over-potentials. Construction of a half-cell anode to validate the model presented is a possible suggestion. A secondary expected result will be an improved basic understanding of the chemical and electrochemical processes occurring at carbon anodes in molten carbonate salts. Of particular importance is an understanding of the role of carbon porosity and reacting site density, since this understanding could lead to improved methods of fuel preparation for direct carbon molten carbonate cells.

4. To increase the basic understanding of the chemical and electrochemical processes at a carbon anode in a molten carbonate electrolyte. This would entail development of anode kinetic models/experiments for possible higher temperature by accommodating CO production due to the equilibrium $CO_2 + C \longrightarrow 2\,CO$ (Boudouard) at the anode surface and to develop steps for validating the model with experimental data. Measurements can be made over a range of temperatures and gas concentrations and for various electrolyte blends and carbon types. This complete experiment-model study should provide information on current vs. voltage as well as on relative carbon monoxide and carbon dioxide production.

5. To develop comprehensive cathode kinetics for the development of a reliable Butler-Volmer type of equation that can show dependence on CO_2/O_2 concentrations in the high or low over-potential regions suited to porous bed electrodes. This is required because of a lack of understanding of mechanisms responsible for the reduction of oxygen in the cathode region. Improved models for predicting variation in kinetic data (exchange current density and charge transfer coefficients) with temperature, type of electrolyte,

and type of reacting surface (cathode current-collector grid) will eventually help in building and improving the models for overall plant design for direct carbon fuel cells.

6. Variation in cell performance with carbon particle diameter is an important area to understand to be able to develop reliable model for the anode. This can have two different effects which are explained below:

    - Contact resistance is a very important part of anode kinetics and although significant efforts were made to model this resistance as a part of anode bed design. However, a crude model for voltage drop due to contact resistance was developed in this work. This was in addition to insignificant variation in voltage drop due to contact resistance for changing carbon particle size diameter. Some literature work show that contact resistance should become significant as the particle size is reduced owing to reduced charge-transfer via conduction due to increased probability of breakdown of aggregated particle linkages. However, utilization of this piece of information in terms of a model that can be incorporated into the anode model is a work recommended for future.
    - In the model presented, carbon particle size is considered to be non-varying in axial direction (perpendicular to the flow). In addition, a very high carbon loading has been used (like a slurry/paste of carbon+molten carbonate salt) while the consumption due to electrochemical oxidation is relatively much smaller. Due to this, the variation in carbon particle size is relatively unchanged even in the direction of the flow. However, electrochemical oxidation is affected significantly by the size of carbon

particle used in the model. Smaller the diameter, larger is the reacting surface area and therefore larger can be the area current density and vice-versa. However, as mentioned above smaller particle size can entail larger polarization due to contact resistance.

Therefore, there must be a trade-off which has not been observed in the model owing to inadequacy of the contact resistance model. It would be vital for a future improved model to predict anode performance based on an aggregated model for carbon particles of various sizes.

7. Design and construction of distributor systems for electrolyte and entrained gases and solid carbon for the cathode and anode beds is vital to the technology advancement. Current work only tries to show conceptually how the cell should configured but does not show any practical design that may work without difficulties.

8. Understanding the physics of bubble evolution (CO_2 in anode) to be able to model ohmic resistance in anode more accurately.

9. There has been reports of enhancing catalytic activity through the use of additives to the molten salts or to use some chemicals to improve reactivity of carbon particles. No work has been attempted in the present thesis but might be of interest if this work needs to be taken to the next step of experimental validation.

10. Design and construction of packed bed DCFC or possibly using molten salts other than carbonates or possibly low temperature alkaline cells to demonstrate the concept presented in this work.

Appendices

Appendix A

Contact Resistance Model

The contact resistance is defined as the ionic resistance that exists when charge from the carbon particle is transferred to the porous-bed grid. The purpose is to evaluate the voltage loss due to contact resistance between carbon particle and the grid. This voltage loss is then subtracted from the difference of open-circuit potential and the cell potential to produce the net overpotential available for chemical reaction. The voltage loss due to contact resistance can be evaluated if particle phase resistivity is known. Particle phase resistivity is evaluated using literature correlation from Kusakabe et al. [1981].

The resistivity correlation from Kusakabe et al. [1981] is:

$$\rho_{\mathrm{m}} \ (\text{in } \Omega \text{ m}) = 0.0004\, E^2 \tag{A.1}$$

where the expansion E is defined in terms of particle hold-up at settled condition and in fluidized condition

$$E = \left[\frac{h_{so}}{h_s} - 1\right] \times 100 \tag{A.2}$$

The resulting equation for particle phase resistivity is then:

$$\rho_{\mathrm{m}} \ (\text{in } \Omega \text{ m}) = 0.0004 \left[\left(\frac{h_{so}}{h_s} - 1\right) \times 100\right]^2 \tag{A.3}$$

The above correlation was estimated for copper particles in contact with copper feeder plates.

Assumption is made that the correlation applies to the collision of carbon particles with stainless steel or nickel current collector plates or wiremesh.

An analogical model from heat transfer is used to develop a crude model for voltage drop due to contact resistance in the porous-bed anode. Solid with internal generation is analogous to solid with ”current sources” (ionic current $\leftrightarrow$ electronic current). This mapping is shown in figure A.1.

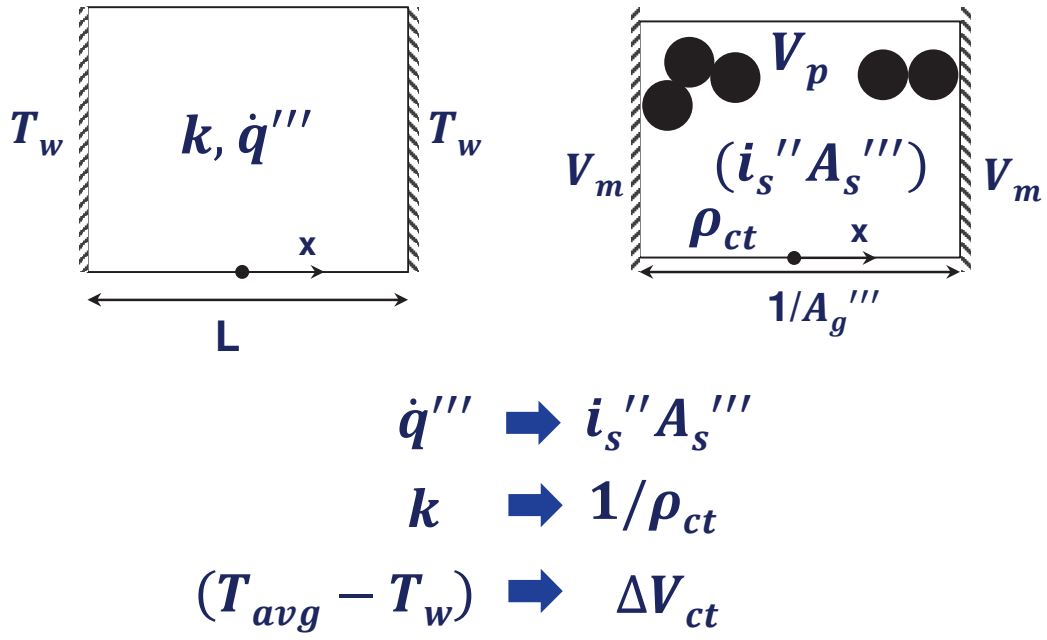

Figure A.1: Model development for contact resistance voltage loss using analogical concepts from heat transfer.

For a flat plate with walls at T_{w}, half-thickness L, and conductivity k, the temperature difference relationship is given from Carslaw and Jaeger [1986] as,

$$T - T_{\mathrm{w}} = \frac{\dot{q}'''\ \left(L^2 - x^2\right)}{2k} \tag{A.4}$$

The average relationship can then be computed to be,

$$T_{\mathrm{avg}} - T_{\mathrm{w}} = \frac{\dot{q}'''}{2k} \frac{\int_0^L \left(L^2 - x^2\right) dx}{L} = \frac{\dot{q}'''\ L^2}{3k} \tag{A.5}$$

Converting to i instead of q, $\dot{q}'''$ becomes $(i_{\mathrm{s}}'' A_{\mathrm{s}}''')$, k becomes $(1/\rho_{\mathrm{m}})$, and $\left(T_{\mathrm{avg}} - T_{\mathrm{w}}\right)$ becomes (ΔV_{CR}). So we have,

$$\Delta V_{\mathrm{CR}} = \frac{\rho_{\mathrm{m}}\ i_{\mathrm{s}}''\ A_{\mathrm{s}}'''\ L^2}{3} \tag{A.6}$$

where A_{s}''' is the carbon particle surface area per unit volume. Now, this model is crude because i_{s}'' is not constant and is higher when ΔV is lower.

For 3-D geometry, (1/L) is equivalent to the area per unit volume (A'''). In the case of anode packed bed it's the grid area per unit volume of the bed (A_{g}'''). So, for the drop in the voltage due to contact resistance, we have the following equation

$$\Delta V_{\mathrm{CR}} = \frac{\rho_{\mathrm{m}}\ i_{\mathrm{s}}''\ A_{\mathrm{s}}'''}{3\left(A_{\mathrm{g}}'''\right)^2} \tag{A.7}$$

where A_{s}''' is same as $A_{C,\mathrm{a}}'''$ given in equation C.24.

Appendix B

Open Circuit Potential

Open-Circuit Voltage for Fuel Cells

Equilibrium open circuit voltage for a fuel cell can be ideally defined in terms of difference of Gibb's energy, and the amount of transferred charge in the proceeding reactions.

$$E^{o}_{oc} = -\frac{\Delta G^{\circ}}{nF} = \frac{\Sigma G^{\circ}_{R} - \Sigma G^{\circ}_{P}}{nF} \tag{B.1}$$

The open circuit voltage (based on actual concentration of reactants and products) for a typical reaction $\nu\mathrm{R} \rightleftharpoons \nu\mathrm{P} + \mathrm{ne}^{-}$ is given by:

$$E_{oc} = -\frac{\Delta G}{nF} \tag{B.2}$$

For an ideal gas, the open circuit voltage can be expanded as below:

$$E_{oc} = -\frac{\Delta G}{nF} = \frac{\Sigma\left(G^{\circ}_{R} + RT\ln\left[\frac{P_R}{P^{\circ}}\right]^{\nu R}\right) - \left(G^{\circ}_{P} + RT\ln\left[\frac{P_P}{P^{\circ}}\right]^{\nu P}\right)}{nF} \tag{B.3}$$

which can be re-written as:

$$E_{oc} = E^{o}_{oc} + \frac{RT}{nF}\left(\Sigma\ln\left[\frac{P_R}{P^{\circ}}\right]^{\nu R} - \ln\left[\frac{P_P}{P^{\circ}}\right]^{\nu P}\right) \tag{B.4}$$

and further simplified into the following equation

$$E_{oc} = E^{o}_{oc} + \frac{RT}{nF} \ln \frac{\prod \left[\frac{P_R}{P^\circ}\right]^{\nu R}}{\prod \left[\frac{P_P}{P^\circ}\right]^{\nu P}} \tag{B.5}$$

The final equation for the open circuit voltage for ideal gases is then written as:

$$E_{oc} = E^{o}_{oc} + \frac{RT}{nF} \left(\ln \frac{\prod P_R^{\nu R}}{\prod P_P^{\nu P}} (P^\circ)^{\nu P - \nu R} \right) \tag{B.6}$$

The P_R, P_P and P° represents the partial pressure of the reactants, products and the pressure at reference conditions respectively and ν_R, and ν_P are the stoichiometric exponents for reactants and products respectively.

When $P_R < P^\circ$ or $P_P > P^\circ$, the logarithmic term is negative and can be referred to as the diffusion voltage loss relative to the reference conditions.

Open-Circuit Voltage for Current Work

For a situation as described in the current work involving reactants and products in liquid and gas phase, and applying Henry's law $\rho = H\,P$ for considering concentration of component in the liquid phase which is in equilibrium with the gas phase, we can get:

$$E_{oc} = E^{o}_{oc} + \frac{RT}{nF} \left(\ln \frac{\prod \left[\frac{\rho_R}{H_R}\right]^{\nu R}}{\prod \left[\frac{\rho_P}{H_P}\right]^{\nu P}} (P^\circ)^{\nu P - \nu R} \right) \tag{B.7}$$

Now, for the electrochemical oxidation of carbon involves the following reaction: $C + O_2 \longrightarrow CO_2$. And since carbon is in solid phase and assuming activity of 1, we can write the open circuit potential as:

$$E_{oc} = E^{\circ}_{oc} + \frac{RT}{4F} \ln \left[\frac{\rho_{O_2} H_{CO_2}}{\rho_{CO_2} H_{O_2}} \right] \tag{B.8}$$

where E°_{oc} is the standard chemical potential of the cell reaction $C + O_2 \longrightarrow CO_2$ calculated at standard conditions equivalent to the reference potential at the hydrogen electrode and calculated from the enthalpy (ΔH) and entropy (ΔS) data from thermodynamic tables Gurvich et al. [1989] and calculated as:

$$E^{\circ}_{oc} = \frac{\Delta G^{\circ}_{O_2} + \Delta G^{\circ}_{C} - \Delta G^{\circ}_{CO_2}}{4F} \tag{B.9}$$

where the change in Gibbs Energy for various species is calculated using the thermodynamic relationship:

$$\Delta G = H^{298} - T(S(T) - R \ln P/P^{\circ}) \tag{B.10}$$

The subscript "298" in the enthalpy H^{298} equation signifies that the enthalpy is based off on reference temperature of 298.15 K and P° is the standard atmospheric pressure of 1 atm. The second term in the entropy equation vanishes if the cell operation is at atmospheric pressure.

For the present work, it is assumed that the open-circuit voltage at reference condition (E^{o}_{oc}) is divided in the fraction ratio of β and $1-\beta$ between anode and cathode half-cells. Anode and cathode voltage relative to electrolyte depends on electrode used to measure electrolyte voltage.

The kinetic model for cathode is developed by Wilemski [1983] based on experimental data from IGT (Institute of Gas Technology) reports. This work uses conditions of 0.67/0.33 atm CO_2/O_2 for the reference (gold) electrode. The kinetic model for anode was developed using the kinetic data presented by Ateya [Weaver et al., 1979][Appendix B] and the reference conditions for measuring anode potential were also 0.67/0.33 atm CO_2/O_2 for the reference (gold) electrode. These conditions are retained for the current modeling work too.

The cell voltage, which is a measurable quantity in an experiment, is an input to the model. The electrolyte voltage is assumed to be zero at the center of interface between cathode and anode but varies with the bed thickness. This representation is shown in other sections describing potential-current density variations for porous beds.

The voltage distribution factor, β is estimated along-with the cell current density for a given input of cell voltage. The estimation assumes that the area current density is highest at the starting of the bed and goes down to zero at the end of the bed. This is discussed further in the solution technique described in later sections.

In addition, work on half-cell investigation using carbon anodes for direct carbon fuel cells by [Hauser Jr., 1964, Weaver et al., 1979, Vutetakis, 1985] shows negative open-circuit potential. In the model, positive values are assumed since it's the magnitude of potential difference that is important.

Appendix C

Estimation of Packed Bed Parameters

Perforated Plates as Packing Material

Calculation of Area per Unit Volume of the Packed Bed

Here we will consider a packed bed of rectangular cross-section with packing sheet plates stacked in a staggered configuration to enhance mass transfer. We get for the surface area of one such packing sheet as,

$$S_{\text{plate}} = N_{\text{hole}}\,\pi\,D_{\text{h}}\,t + 2\,L_{\text{b}}\,W_{\text{b}}\,(1 - OA) \tag{C.1}$$

where N_{hole} is the number of holes in one packing sheet, D_{h} is the diameter of the hole, t the thickness of the packing sheet, L_{b} and W_{b} are the length and breadth of the packing sheet, OA is the open area of one packing sheet.

The number of holes in one packing sheet, N_{hole} can be found out from,

$$N_{\text{hole}} = \frac{L_{\text{b}}\,W_{\text{b}}\,(OA)}{(\pi\,D_{\text{h}}^2/4)} \tag{C.2}$$

The equation for the surface are of one packing sheet then simplifies into

$$S_{\text{plate}} = L_{\text{b}}\, W_{\text{b}} \left[\frac{4\,(OA)\,t}{D_{\text{h}}} + 2\,(1-OA) \right] \tag{C.3}$$

If h is the plate spacing, and H_{b} is the total height of the bed, then total plate surface area within the packed bed is given as

$$S_{\text{p}} = \frac{H_{\text{b}}}{h}\, L_{\text{b}}\, W_{\text{b}} \left[\frac{4\,(OA)\,t}{D_{\text{h}}} + 2\,(1-OA) \right] \tag{C.4}$$

Since the volume of the bed is $L_{\text{b}}W_{\text{b}}H_{\text{b}}$, surface area per unit volume of the packed bed is given by

$$A'''_{\text{bed}} = \frac{S_{\text{p}}}{L_{\text{b}}W_{\text{b}}H_{\text{b}}} = \frac{4\,(OA)\,t}{h\,D_{\text{h}}} + \frac{2\,(1-OA)}{h} \tag{C.5}$$

Calculation of Volume fraction of Electrode

Volume of (H_{b}/h) number of packing sheet plates is given by,

$$V_{\text{electrode}} = L_{\text{b}}\, W_{\text{b}}\, t\, (1-OA)\, \frac{H_{\text{b}}}{h} \tag{C.6}$$

Volume fraction of Electrode is then given by

$$\zeta = \frac{V_{\text{electrode}}}{L_{\text{b}}W_{\text{b}}H_{\text{b}}} = \frac{t}{h}\,(1-OA) \tag{C.7}$$

Calculation of Packed Bed Void Fraction

The total void volume within the bed is given by

$$V_{\text{void}} = \left[H_{\text{b}} - \left(\frac{H_{\text{b}}}{h}\, t \right) \right] W_{\text{b}}L_{\text{b}} + \left(\frac{H_{\text{b}}}{h} \right) \left[\frac{W_{\text{b}}\, L_{\text{b}}\, (OA)}{\pi D_{\text{h}}^2/4} \right] (\pi D_{\text{h}}^2\, t/4) \tag{C.8}$$

The packed bed void fraction, ε can then be calculated as

$$\varepsilon = \frac{V_{\text{void}}}{L_{\text{b}}W_{\text{b}}H_{\text{b}}} = 1 - \frac{t}{h}\,[1-(OA)] \tag{C.9}$$

Geometrical parameters using Wire-mesh as the Packing

A schematic with a unit size of two wire-meshes in a cubic configuration is shown in figure C.1. The mesh size which is same for the wire-mesh in both directions is

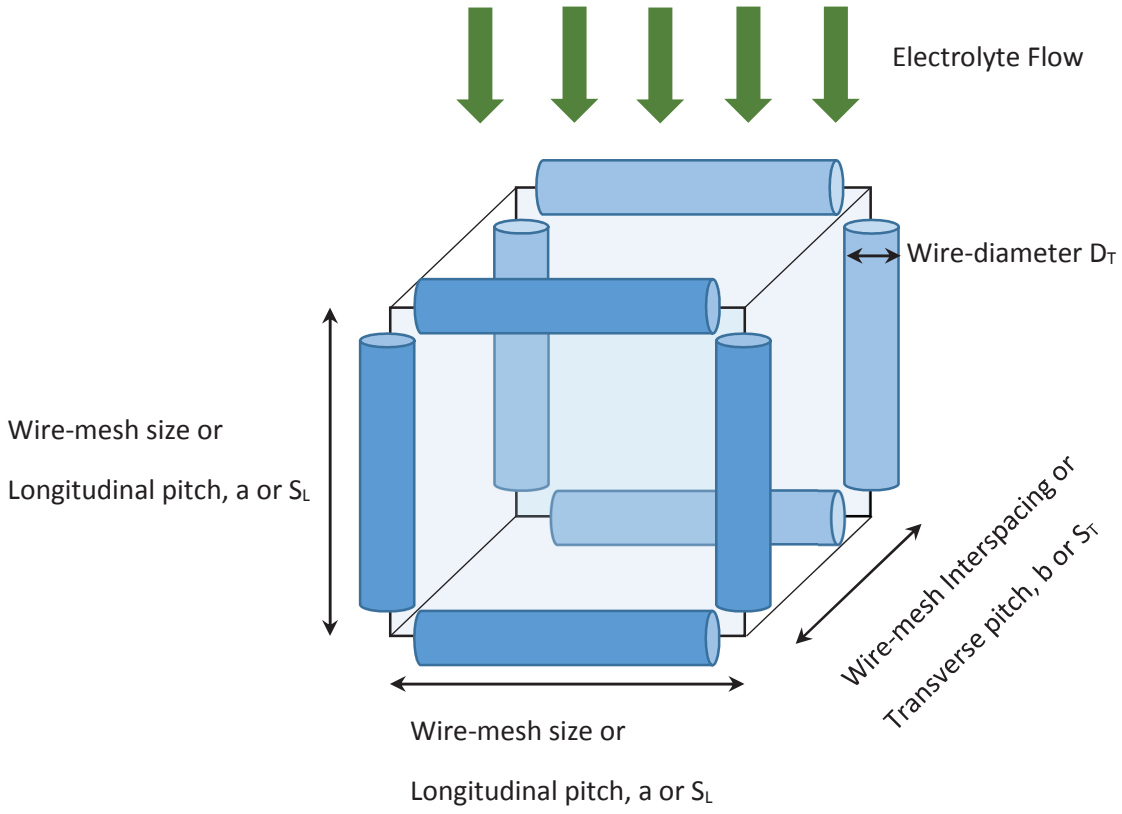

Figure C.1: Schematic with a unit size of two wire-meshes.

a or S_L, the horizontal inter-spacing between the two wire-meshes is b or S_T, and the wire diameter is D_T. The total surface area of the wire-mesh for the unit cube

size can be given as:

$$S = \frac{\pi D_T}{4} 8a = 2\pi\, a\, D_T \tag{C.10}$$

The volume of the unit cube is $V = a^2 b$, therefore surface area available for reaction per unit volume of the bed (unit cube) shown is going to be:

$$A_b''' = \frac{S}{V_{tot}} = \frac{2\pi\, D_T}{a\, b} = \frac{2\pi\, D_T}{S_L\, S_T} \tag{C.11}$$

The total volume of the metal component in the wire-mesh stored in the unit size cube is given as:

$$V_m = \frac{1}{4}\,\frac{\pi D_T^2}{4} 8a = \frac{\pi\, D_T^2\, a}{2} = \frac{\pi\, D_T^2\, S_L}{2} \tag{C.12}$$

Then the nominal packing diameter (D_p) can be given as:

$$D_p = 6\left(\frac{V_m}{S}\right) = \frac{3}{2} D_T \tag{C.13}$$

and Volume fraction of the packing is then given as:

$$\zeta = \frac{V_m}{V_{tot}} = \frac{\pi\, D_T^2}{2\, a\, b} = \frac{\pi\, D_T^2}{2\, S_L\, S_T} \tag{C.14}$$

Carbon surface area per unit volume model

We first assume that the molten salt is entrained with spherical carbon particles. We also assume that the carbon particle flux, $\dot{N}''$ (number of carbon particles flowing through the bed per unit area per unit time) will be constant. Now, molar flux of carbon in the salt can be written as

$$\dot{n}_C'' = U_C\, h_C\, \bar{\rho}_C \tag{C.15}$$

where U_C is the downward velocity of the carbon particle, h_C is the carbon holdup within the anode packed bed, and $\bar{\rho}_C$ is the molar density of carbon. The carbon particle flux is given by

$$\dot{N}'' = \frac{\dot{n}_C''}{n_{\text{part}}} \tag{C.16}$$

where n_{part} is the carbon moles per particle.

At any bed position, x , particle flux is given by,

$$\dot{N}'' = \frac{\dot{n}_C''(x)}{\bar{\rho}\left(\frac{\pi D_C(x)^3}{6}\right)} \tag{C.17}$$

which is also equal to the particle flux at the bed start position

$$\dot{N}'' = \frac{\dot{n}_{C,\text{init}}''}{\bar{\rho}\left(\frac{\pi D_{C,\text{init}}^3}{6}\right)} \tag{C.18}$$

Simplifying equation C.17 and C.18 we get,

$$D_C(x) = D_{C,\text{init}}\left(\frac{\dot{n}_C''(x)}{\dot{n}_{C,\text{init}}''}\right)^{1/3} \tag{C.19}$$

If the initial size of the carbon particle and the initial molar flux of carbon is specified and the molar flux of carbon at any bed location x is known from the solution of the differential equations for the anode bed, then the size of the carbon particle at any x location within the bed would be easily determined. The initial size of the carbon particle is chosen to be 74 micron found out from the 200 mesh screen sizes provided in Bab [1975] on page 9-5.

Now, carbon holdup in general is given by volume of carbon particles per unit volume of the bed.

$$h_C = V_C''' = \frac{\text{Volume of Carbon Particles}}{\text{Volume of the Bed}} \tag{C.20}$$

The instantaneous carbon holdup with bed position x can then be written as

$$h_C(x) = \frac{\text{(Number of Carbon Particles at any x) } (V_{\text{part}}(x))}{\text{Volume of the Bed}} = N'''_{\text{part}}(x)\, V_{\text{part}}(x) \quad \text{(C.21)}$$

The reaction surface area of carbon per unit volume of the bed can then be computed from

$$A'''_{\text{part}}(x) = N'''_{\text{part}}(x)\ (\pi D^2_{\text{part}}(x)) = \frac{h_C(x)}{V_{\text{part}}(x)}\ \pi D^2_{\text{part}}(x) \quad \text{(C.22)}$$

Simplifying the above equation, the carbon particle area per unit volume of the bed, $A'''_{\text{s,a}}$ is given by

$$A'''_{C,\text{a}}(x) = \frac{6h_C(x)}{D_{\text{c}}(x)} \quad \text{(C.23)}$$

It should be noted that this equation doesn't take into account the volume fraction of the anode packing material within the bed. So, taking into account the volume fraction of the anode, we get

$$A'''_{C,\text{a}}(x) = \frac{6h_C(x)}{D_{\text{c}}(x)}(1-\zeta_{\text{a}}) \quad \text{(C.24)}$$

where ζ_{a} can be computed as in section C given appropriate specifications of the packing material in the anode.

Liquid Velocities through Packed Beds

The velocity of the vertical flow of liquid electrolyte in both anode and cathode half-cell beds can be estimated by balancing the frictional forces against the gravitational forces. The eutectic mixture of alkali carbonates, i.e. sodium carbonate, calcium carbonate and lithium carbonate is gravity-fed through the packed bed arrangement of perforated plates or wire-mesh. The velocity of the salt is a function of

friction factor, and physical properties of the salt. In case of anode, the electrolyte is entrained with the coal/biomass particles which changes the thermo-physical properties of the resulting mixture to be slightly different than the molten carbonate electrolyte used in the cathode. The friction factor for the wire-mesh packing can be determined from graphs or empirical equations presented in the literature and can be a function of wire diameter, mesh width, longitudinal pitch of wires in the wire-mesh, and the transverse pitch of multiple wire-mesh placed perpendicular to the flow. The friction term is balanced by gravity flow wherein, most of the potential energy of the fluid is converted to kinetic energy and remaining is dissipated as heat through viscous and frictional losses. As per Leva [1949], the modified friction factor in packed bed of granular solids can be estimated using figures 1 and 1a (in the original paper [Leva, 1949]) and equations C.25.

$$f_m = \frac{D_p \rho \phi_s^{3-n} \varepsilon^3}{2G^2(1-\varepsilon)^{3-n}} \frac{|\Delta p|}{L} \tag{C.25a}$$

$$Re' = \frac{D_p G}{\mu} \tag{C.25b}$$

To balance frictional forces with the gravitational forces, the term $\frac{|\Delta p|}{L}$ is equal to ρg. Equation C.25 then simplifies to,

$$V_{avg} = \left[\frac{D_p \phi_s^{3-n} \varepsilon^3}{2 f_m (1-\varepsilon)^{3-n}} \right]^{1/2} \tag{C.26}$$

For an assumed average velocity, modified Reynolds number can be calculated from equation C.25. Using this calculated value of modified Reynolds number, friction factor and shape factor can be estimated from Leva [1949][Fig 1,1a]. If the average packing diameter D_p, and void fraction of the packing are known, velocity of the liquid flow through the packed bed can be estimated.

Alternatively, the electrolyte flow over the packed bed of wire-mesh can be assumed to be analogous to a flow of liquid over the tube banks. The friction factor for dynamics of flow over tube banks have been studied exhaustively in the literature by Gram et al. [1958], Grimison [1937], and Zukauskas [1972]. However, correlations from Grimison [1937] indicate absolutely no data for laminar flow with Reynolds number much lower than 2000. Gram et al. [1958] does manage to produce significant amount of data for Re = 600 (Reynolds number based on tube diameter, and in the present work wire diameter). Work of Zukauskas [1972] can be used in a different approach where drag force (dominant portion of friction factor) can be correlated for various grid spacing. However, lot of uncertainties in this work again forces one to consider only the work of Gram et al. [1958] for estimating friction factor for electrolyte flow over a grid made up of wire-mesh stacked perpendicular to the flow. The spectrum of empirical data from various sources will help put limits on the possible electrolyte velocities in the fuel cell design presented in the thesis and to establish the operating envelope of the fuel cell. The figure from Perry's Handbook is reproduced here that demonstrates staggered and in-line tube-bank configurations.

From various experimental data correlated by Gram et al. [1958] and Grimison [1937], it's clear that the higher the longitudinal pitch of the wire-mesh, higher will be the friction factor and lower will be the liquid velocity and vice-versa. Higher transverse pitch has the potential to reduce the friction resistance by increasing the distance between multiple wire-meshes but also tends to reduce the area per unit volume available for mass transfer and the reaction rate that are required for modeling the electrochemical reactions in anode and cathode. Data from literature

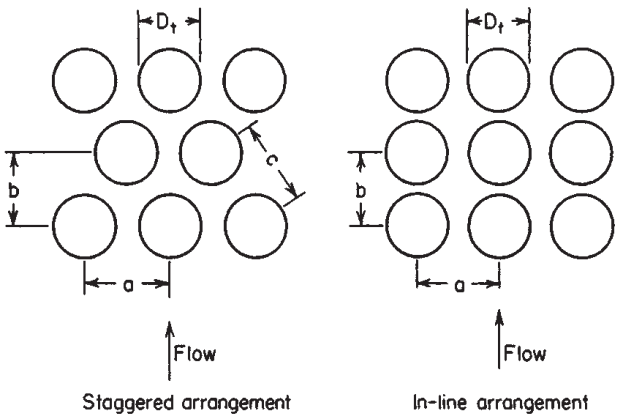

Figure C.2: Possible configurations of electrolyte flow over wire-mesh packed bed.

[Gram et al., 1958][figure 8 and 9] have proved quite useful in the determination of an appropriate friction factor for the current work.

Table C.1 shows possible commercially available wire-mesh that can be utilized for building the packed bed in anode and cathode. Transverse pitch is dependent upon the placement of multiple-wire mesh perpendicular to the electrolyte flow. As an example, friction factor in data no. 4 has been estimated (f = 0.038) using one of the correlations provided by Gram et al. [1958] but is limited to a value of 600 for the Reynolds number. But the calculated Reynolds number is much lower, say 140. For this specification, the friction factor is estimated to be even lower to justify such lower values of Reynolds number and liquid velocities can be even higher. For this specification, Friction factor can be estimated in the range of 0.02-0.03 leading to average velocities of 0.4-0.5 m/s or maximum velocities of 0.49-0.59 m/s.

The other parameters for the wire-mesh selection are given in table C.2

[1] Based on ternary Li-Na-K eutectic mixture conductivity @ T = 1000 K

Table C.1: Wire-mesh selection and calculated parameters

No.	Mesh Size	Mesh Wire Dia	Longitudinal Pitch	Longitudinal Ratio	Transverse Pitch	Transverse Ratio	Area per Unit Volume	Friction Factor	Average Velocity	Source
	W	D_t	S_L	S_L/D_t	S_T	S_T/D_t	A'''	f	V_{avg}	
	mm	mm	mm		mm		m^2/m^3		m/s	
1	0.63	0.32	0.95	3.0	1.92	6.0	1123	0.04	0.57	Gram et al. [1958]
2	0.63	0.32	0.95	3.0	1.28	4.0	1675	0.10	0.32	Gram et al. [1958]
3	0.50	0.30	0.8	2.7	1.20	4.0	1987	0.029	0.55	Gram et al. [1958]
4	0.20	0.16	0.36	2.3	0.96	6.0	2937	0.02-0.03	0.4-0.5	[Gram et al., 1958, pg 34, fig9]
5	0.70	0.36	1.06	2.9	0.96	6.0	1095	0.06	0.49	[Gram et al., 1958, pg-34,fig-9]
6	0.98	0.44	1.42	3.2	2.29	5.2	948	0.064	0.53	Gram et al. [1958]
7	0.82	0.45	1.27	2.8	2.34	5.2	1063	0.054	0.55	Gram et al. [1958]

Table C.2: Wire-mesh packing parameters calculation required for governing equations

No.	Mesh Wire Dia	Longitud'l Pitch	Transv. Pitch	Area per Unit Volume	Packing Dia.	Packed Bed Fraction	Void Fraction	Bed Resistance[1]
	D_t	S_L	S_T	$A''' = 2\pi D_T/(S_L S_T)$	$d_p = 6/A'''$	$\zeta = \pi D_T^2/(2 S_L S_T)$	$\varepsilon = 1-\zeta$	R
	mm	mm	mm	m^2/m^3	m	fraction	fraction	Ohm-m
1	0.32	0.95	1.92	1123	0.0053	0.088	0.912	0.0056
2	0.32	0.95	1.28	1675	0.0036	0.132	0.868	0.0061
3	0.30	0.80	1.20	1987	0.0030	0.147	0.853	0.0062
4	0.16	0.36	0.96	2937	0.0020	0.116	0.884	0.0059
5	0.36	1.06	0.96	1095	0.0055	0.089	0.911	0.0056
6	0.44	1.42	2.29	948	0.0063	0.094	0.906	0.0057
7	0.45	1.27	2.34	1063	0.0056	0.107	0.893	0.0058

The eutectic mixture of alkali carbonates used in the cathode is also used in anode but mixed with carbon particles that can range anywhere from 50 microns to 300 microns in size. Average particle size maybe be assumed 100 microns for all practical purposes. The properties of the dispersed phase, i.e. density, viscosity, etc can be determined from material balance and some correlations presented in the literature. The physical properties of the carbon entrained molten carbonate slurry can then be calculated. The friction factor and corresponding average velocity for the flowing slurry can then be evaluated in a manner similar to that for the cathode. For the purposes of finding velocities in anode, it will be assumed that slurry does move at a consistent homogenous velocity.

Appendix D

Thermo-Physical Properties

Properties in molten salt electrolyte

The properties of eutectic mixture of the carbonate of alkali metals, Li-Na-K has been studied in much detail by Janz et al. [1979]. For the present work, various thermophysical properties like density, viscosity, conductivity, etc are required to analyze the fuel cell model. The diffusion coefficients for transport of solute gases like CO_2, and O_2 through the molten salt electrolyte would be required to solve differential equations through the packed bed of electrolyte for different solute gases, i.e. CO_2, and O_2. In the anode bed, the molten salt electrolyte is entrained with coal/biomass particles. The correlations and differential equations in anode can be solved in a manner similar to that for cathode, provided the slurry properties of entrained mixture of molten electrolyte and coal is evaluated. Effective Density comes from conservation of mass. The slurry can be considered to be moving at roughly the same velocity although carbon particles being lighter than molten carbonate might not move as fast as the electrolyte.

Properties of gases

Properties of CO_2, and O_2 in the gas phase mixture: CO_2, O_2, in air/N_2 in the cathode and CO_2, in H_2O or N_2 in the anode.

Diffusion Coefficient

The diffusion coefficient for binary gas systems at low pressures is predicted from theory by Poling et al. [2001] as:

$$D_{AB} = \frac{0.00266T^{3/2}}{PM_{AB}^{1/2}\sigma_{AB}^2\Omega_D} \tag{D.1}$$

where D_{AB} is the diffusion coefficient in cm^2/s, T is the temperature in Kelvin, P is the pressure in bar, σ_{AB} is the characteristic length in Å, and Ω_D is the diffusion collision integral and is dimensionless. The molecular weight of the binary mixture, M_{AB}, is defined as:

$$M_{AB} = 2\left[(1/M_A) + (1/M_B)\right]^{-1} \tag{D.2}$$

where M_A, M_B are the molecular weights of A and B.

The key to the use of eq. D.1 is the selection of an intermolecular force law to evaluate σ_{AB} and Ω_D. The theory and equations to evaluate σ_{AB} and Ω_D is provided by Poling et al. [2001] through the use of Lenard-Jones Potential concept. The individual values of characteristic length and energy for the participating species is represented by σ and ε. The σ_{AB} and ε_{AB} are therefore simply the interaction values that can be determined from the individual values through the use of simple

rules given as:

$$\sigma_{AB} = \frac{\sigma_A + \sigma_B}{2} \tag{D.3}$$

$$\varepsilon_{AB} = (\varepsilon_A \varepsilon_B)^{1/2} \tag{D.4}$$

The individual values of σ and ε for various compounds are given in the Appendix B of Poling et al. [2001]. Ω_D can be estimated from the following equation:

$$\Omega_D = \frac{A}{(T^*)^B} + \frac{C}{\exp(DT^*)} + \frac{E}{\exp(FT^*)} + \frac{G}{\exp(HT^*)} \tag{D.5}$$

where $T^* = kT/\varepsilon_{AB}$, k is the Boltzmann's constant, T is the absolute Temperature, $A = 1.06036$, $B = 0.15610$, $C = 0.19300$, $D = 0.47635$, $E = 1.03587$, $F = 1.52996$, $G = 1.76474$, and $H = 3.89411$ The properties data for various compounds, namely σ, and ε/k, are presented in table D.1. Also tabulated are the calculated characteristics for binary mixtures anticipated in both anode and cathode half-cells. Eventually, the diffusion coefficient of CO_2 and O_2 in various binary gas mixtures has been calculated and appended to the table. These coefficients will be shown later on to be used in the estimation of gas-side mass transfer coefficient.

Density and Viscosity

The density and viscosity of CO_2 and O_2 is estimated from regressed equation using empirical data from Kays and Crawford [1980]. The range of data is from 220 - 1400 Kelvin for the independent variable temperature. The range of data for the dependent variables density and viscosity is 0.3831 - 2.4728 kg/m^3 and 4.525 -129.7 $\times 10^{-6}$ m^2/sec respectively. All empirical data is measured at atmospheric pressure of 101.325 kPa. The empirical equations for density and viscosity are:

$$\rho_{co_2} = 555.23\, T^{-1.005} \tag{D.6}$$

Table D.1: Characteristics required to estimate diffusion coefficients of binary gas mixtures (Data used under fair use, 2014. from Appendix B of the reference B.E. Poling, J.M. Prausnitz, and J.P. O'Connell. *The Properties of Gases and Liquids.* McGraw Hill, 2001).

Property	Units	A = CO_2 B = Air	A = CO_2 B = H_2O	A = O_2 B = N_2
σ_A	Å	3.941	3.941	3.467
σ_B	Å	3.711	2.641	3.798
ε_A/k	K	195.2	195.2	106.7
ε_B/k	K	78.6	809.1	71.4
σ_{AB}	Å	3.826	3.291	3.6325
ε_{AB}/k	K	123.9	397.4	87.3
$T^* = kT/\varepsilon_{AB}$	dimensionless	8.07	2.52	11.46
Ω_D		0.769	0.998	0.725
M_A	$gm/gm-mol$	44	44	15.998
M_B	$gm/gm-mol$	28.97	18.01528	28
M_{AB}	$gm/gm-mol$	34.9	25.5	20.4
D_{AB}	cm^2/sec	1.263	1.539	1.947

$$\nu_{CO_2} = (4.485 \times 10^{-5}\, T^2 + 0.03471\, T - 6.114) \times 10^{-6} \tag{D.7}$$

Molar Densities and Concentrations

Molar Density of molten salt (in kmol/m^3) is given by,

$$\bar{\rho}_{\text{salt}} = \frac{\rho_L}{M_L}$$

where ρ_L is the density of the molten salt (in kg/m^3) and M_L is the molecular weight of the molten salt (in kmol/kg).

Molar flux of molten salt (in kmol/m^2-s) is given by,

$$\dot{n}_L'' = \frac{U_{0L}}{\bar{\rho}_{\text{salt}}}$$

Mole fractions of molten salt used in the study and the variations in density (ρ), surface tension (γ), viscosity (μ), and electrical conductance (κ) of the molten salt with temperature for different compositions is as given in Janz et al. [1979]. The gas properties variation with temperature is referenced from Kays and Crawford [1980].

Appendix E

Transport Processes for Gravity Flow Concept

The velocity of gas flowing through the gas chamber and past the electrolyte falling through the packed bed is a parameter that maybe operationally controlled. Variation in gas velocity affects the mass transfer rate that is required to characterize the convective boundary condition at liquid-gas interface. In both the electrodes, the mass transfer resistance from the gas side dominates the liquid side resistance [Johnstone and Pigford, 1942]. The convective boundary condition is applied in a manner similar to that seen in heat transfer. The driving force being the difference between the concentration of gas species in the liquid phase that is in equilibrium with that in vapor and the concentration of gas species in the bulk liquid at the liquid-gas boundary. This driving force applied with the mass transfer resistance should be equal the diffusive flux that goes through the packed bed.

The mass transport in the packed bed section of both anode and cathode is dictated by transverse diffusion. It's postulated that transverse diffusion is equivalent to turbulent diffusivity of gas species through the electrolyte flowing through

the packed bed of wire mesh or perforated sheet. Relationship between the transverse diffusivity and the molecular diffusivity of flow in packed bed of spheres can be evaluated using work of Delgado [2006]. The Peclet number based on transverse diffusivity approaches a value of 12 for high values of Peclet number based on molecular diffusivity which makes it simpler to evaluate transverse diffusion coefficients based on the knowledge of molecular diffusion coefficients.

Chemical reaction in the anode bed takes place on the surface of carbon particle. Mass transport coefficient from bulk liquid to the carbon particle surface will be required to establish relationship between reaction rate and bulk liquid concentrations. Mass transport correlations based on dissipation energy can be estimated as a function of superficial gas and liquid velocities and other physical properties.

Gas Velocities

The gas velocities in the gas chambers of cathode and anode half cells is a function of gas flow rate. For the purposes of fuel cell modeling the gas velocities in each gas chamber maybe assumed some plausible value for baseline case. However, to demonstrate dependence of fuel cell performance on the gas velocity, it can be varied within some reasonable range. Since, gas chamber geometry would be needed to estimate mass transfer coefficient in the gas phase, table E.1 demonstrates typical square cross-section sizing that can be applied for both anode and cathode gas chambers. For annular cross-section, the gas chamber sizing is shown in table E.2. The packed bed thickness is a dependent variable as far as fuel cell modeling is concerned. The thickness will vary with varying fuel cell voltage on load and has to

Table E.1: Gas Chamber Specifications for Square Cross-section.

Parameter	Symbol	Units	Value	Source
Chamber Length	L_g	m	0.02	Input
Chamber Width	W_g	m	0.02	Input
Flow X-sectional Area	A_g	m^2	4×10^{-4}	$A_g = L_g \times W_g$
Flow X-sectional Perimeter	P_g	m	0.08	$P_g = 2\,(L_g + W_g)$
Hydraulic Radius	r_h	m	0.005	$r_h = A_g / P_g$
Equivalent Diameter	d_{eq}	m	0.02	$d_{eq} = 4 \times r_h$

be fixed in terms of design condition. This might lead to mathematical iterations to evaluate optimized fuel cell performance and to provide an optimized packed bed thickness which will then make the mass transfer coefficient independent of bed thickness. Until then, it's reasonable to have a range of bed thickness to work with.

Table E.2: Gas Chamber Specifications for Annular Cross-section.

Parameter	Symbol	Units	Value	Source
Chamber Length	L_g	m	0.02	Input
Pkd bed thickness perp to flow	L_b	m	0.02	Fuel Cell Model
Flow X-sectional Area	A_g	m^2	3.77×10^{-3}	$A_g = \pi\left[(L_g + L_b)^2 - L_b^2\right]$
Flow X-sectional Perimeter	P_g	m	0.08	$P_g = 2\pi(L_g + L_b)$
Hydraulic Radius	r_h	m	0.005	$r_h = A_g / P_g$
Equivalent Diameter	d_{eq}	m	0.02	$d_{eq} = 4 \times r_h$

Flow in Cathode

The dependent and independent variables in the cathode model are shown schematically in figure E.1. The dependent variables are:

- molar CO_2 concentration in the liquid phase,
- molar O_2 concentration in the liquid phase,
- ionic current density in the liquid phase,
- electrolyte voltage

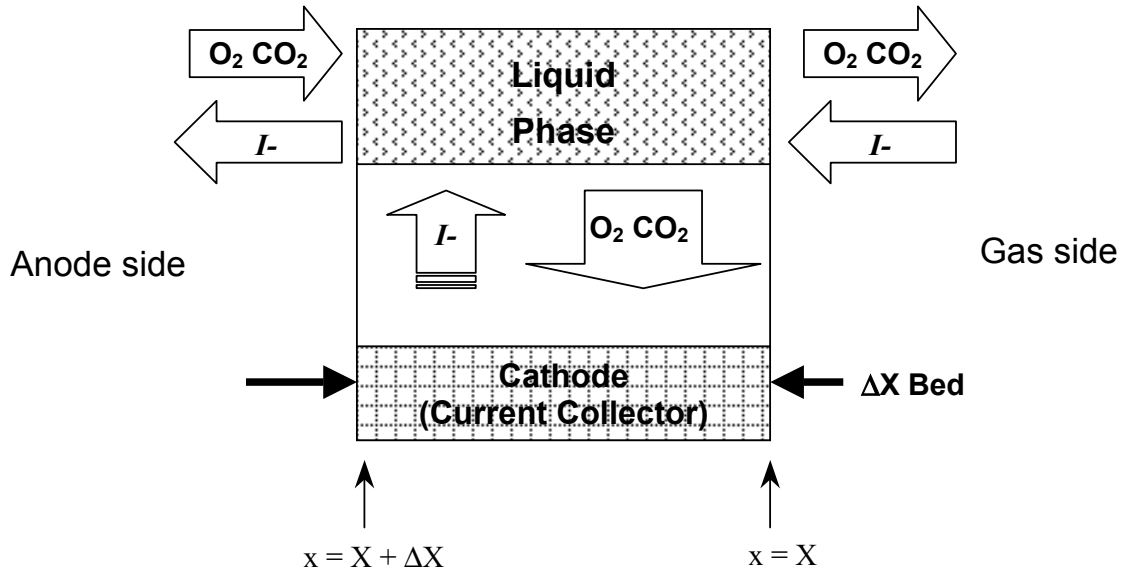

Figure E.1: Differential Element of a Cathode Model showing the Dependent and Independent Variables.

Unlike the concurrent flow concept, there is no molar concentrations for the gaseous phase for CO_2 and O_2 because below saturation conditions has been considered

and so no bubble formation is attained. Axial diffusion has been neglected. The independent variable is the location within the cathode bed.

Flow in Anode

As in the cathode, the packed bed anode consists of an electrically-connected porous bed. The openings in the bed allow passage of molten salt with carbon particles and generated gases entrained. The concept for anode design is also a stack of screens or perforated plates, spaced and supported by horizontal rods that double as electron conductors. With the help of insert type distributor arrangement, carbon entrained in the molten salt flows downward on the inside of the anode tube as a falling film through the stack of screens and perforated plates that serve as a packed bed similar to cathode and also shown in figure 2.2. The carbonate

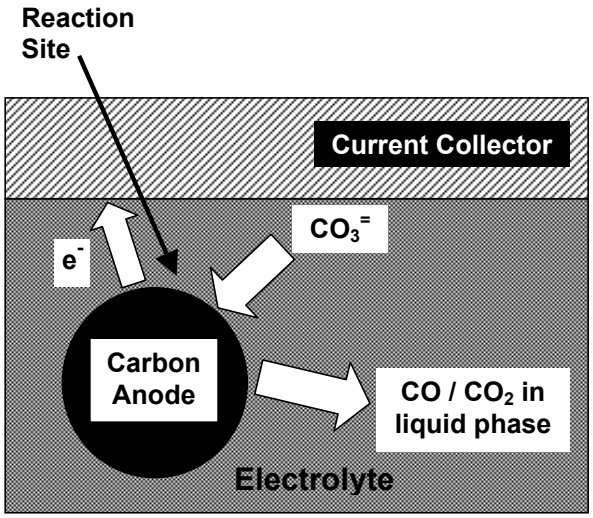

Figure E.2: Mass Transfer in Porous Bed Anode in a gas-bubble free electrolyte.

ions, $CO_3^=$, migrating by ionic conduction to the anode, diffuses through the molten

salt electrolyte and reacts at the surface of carbon to form CO/CO_2, depending upon equilibrium. The CO_2 that remains undissolved in the molten salt can escape through the remaining section of the inside tube. The molten salt could easily be separated from the dissolved CO_2 in a gas-liquid separator and recirculated. Unlike the cathode bed, which acted as an electrode, the anode bed acts only as a current collector. As seen in Figure E.2, the carbon particles themselves act as the anode, exchanging electronic current with each other and with the bed through collisions. There is a net mass transfer of CO_2 from carbon anode to the bulk electrolyte. The

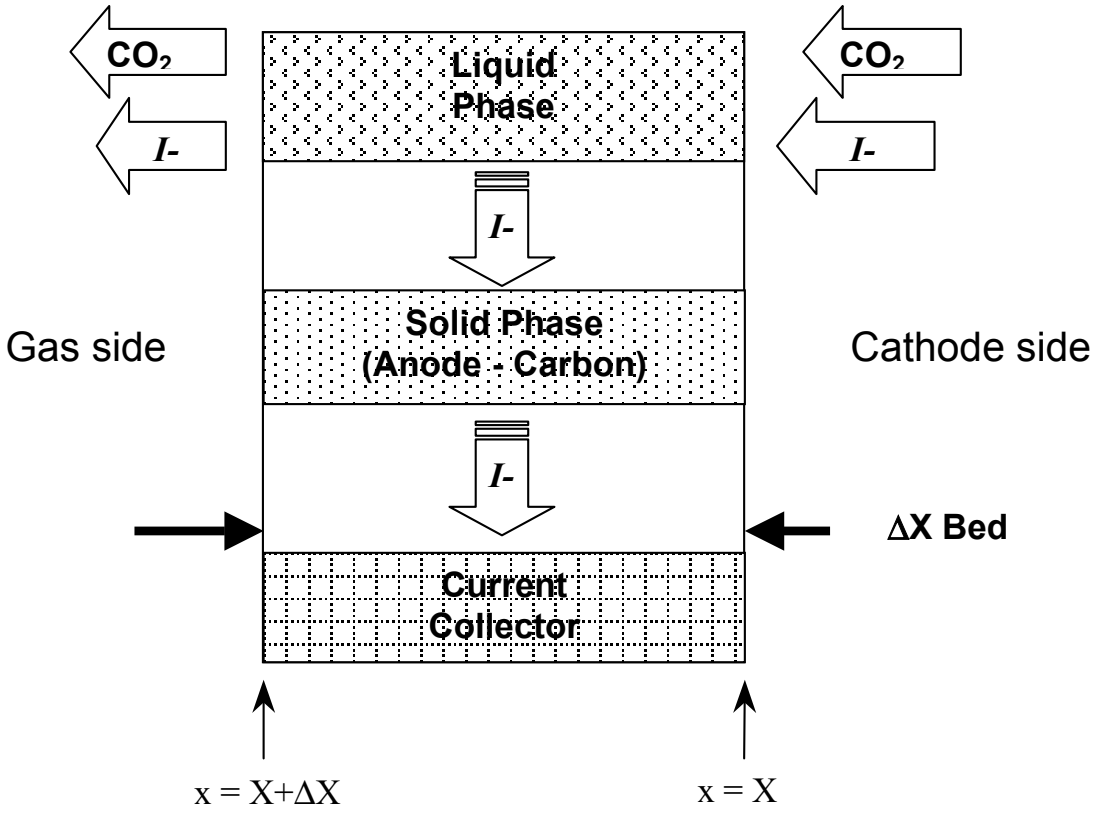

Figure E.3: Differential Element of Anode Model showing the Dependent and Independent Variables.

dependent and independent variables in the anode model are shown schematically in figure E.3. The dependent variables are:

- molar CO_2 concentration in the liquid phase,
- ionic current density in the liquid phase,
- electrolyte voltage

Unlike the earlier model, there is no molar concentrations for the CO_2 in gaseous phase and for O_2 in gas as well as liquid phase. It is assumed that whatever O_2 migrates from cathode to anode reacts with the carbon particle right away to form CO_2 which either gets dissolved into the molten salt or escapes through the open section of the tube. Also since below saturation conditions has been considered therefore no bubble formation is attained and therefore no CO_2 in gas phase. Carbon monoxide production and axial diffusion have been neglected. The independent variable is the location within the anode bed.

Governing Equations

The overall cell modeling has been kept simple and straightforward. The variation of various parameters in cathode and anode is considered with the changing location within the bed. Currently, an axisymmetric one-dimensional model is built, but can be easily extended to radial or rectangular geometries. The variation of various parameters like gas concentration and carbon utilization is not considered because a snapshot in the vertical direction is considered for now that can be extended to two-dimensional variation after a favorable one-dimensional modeling is

accomplished. The four partial differential equations in cathode and three equations in anode have to be written within one code unlike the earlier model where there were two separate cathode and anode models. The reason being that the boundary conditions in cathode and anode are connected to each other. The following sections present the differential equation set within the cathode and anode bed, the boundary conditions required to solve them, and the mass transfer and diffusion correlations/ equations required for various parameters. The partial differential equations presented here are based on the fact that diffusion is the dominating factor in the mass transfer and the amount of mass transfer due to diffusion is in some proportion to the amount of coloumbic charge generated and this proportionality is duly represented in the differential equations. Unlike the earlier model, there are no differential equations in the gas phase but the equations in the liquid phase are written this time in terms of molar gas concentration rather than molar gas flux. The differential equations for ionic current density and for electrolyte voltage remains unchanged. Unlike the earlier model, the diffusion coefficient used in the differential equations and the boundary conditions is the transverse (and not molecular) diffusion coefficient. The reason for this is explained in the later sections.

Cathode Bed

CO_2 in liquid phase:

$$\alpha_c D_{\mathrm{co}_2} \frac{d^2}{dx^2}\left[\bar{\rho}_{\mathrm{co}_2,\ell}(x)\right] - \frac{A'''_{s,c}(x) i''_{s,c}(x)}{2F} = 0 \tag{E.1}$$

O_2 in liquid phase:

$$\alpha_c D_{o_2} \frac{d^2}{dx^2} \left[\bar{\rho}_{o_2,\ell}(x)\right] - \frac{A'''_{s,c}(x) i''_{s,c}(x)}{4F} = 0 \tag{E.2}$$

ΔV in molten salt:

$$\frac{dV}{dx} = i''(x) R_c(x) \tag{E.3}$$

Ionic current flux perpendicular to falling film flow direction:

$$\frac{di''}{dx} = i''_{s,c}(x) A'''_{s,c}(x) \tag{E.4}$$

Anode Bed

CO_2 in liquid phase:

$$\alpha_a D_{co_2} \frac{d^2}{dx^2} \left[\bar{\rho}_{co_2,\ell}(x)\right] + \frac{A'''_{s,a}(x) i''_{s,a}(x)}{2F} = 0 \tag{E.5}$$

ΔV in molten salt:

$$\frac{dV}{dx} = i''(x) R_a(x) \tag{E.6}$$

Ionic current flux perpendicular to falling film flow direction:

$$\frac{di''}{dx} = i''_{s,a}(x) A'''_{s,a}(x) \tag{E.7}$$

Boundary Conditions

The boundary conditions for the gas concentrations are written from direct analogy of heat transfer to mass transfer. The correlations for the mass transfer coefficients for CO_2 and O_2 used in cathode as well as anode will be discussed in further sections. The thickness of ceramic cloth separator will be assumed to be negligible

and located at x = 0. The co-ordinate system is considered to be positive towards the anode and therefore $x = L_a$ at the end of the anode film. The co-ordinate system is considered to be in the negative direction towards the cathode where, $x = -L_c$ at the end of the the cathode film.

Whatever O_2 migrates from cathode to anode is considered to be consumed right away at $x = 0^+$ by reacting with carbon. Since, carbon loading is not considered for now, therefore, a matching condition for this reaction described above is also included at $x = 0$. The current is depleted at the gas-liquid boundary and therefore ionic current density is zero at both cathode and anode gas-liquid boundaries. A net cell output voltage of V_{cell} is desired from this fuel cell model and therefore there is a discontinuity in the electrolyte potential at $x = 0$ equal in amount to V_{cell}. The ionic current density, however, is continuous at $x = 0$ and is equal to the current density fed into the porous beds. The boundary conditions are tabulated in Table E.3.

Mass Transfer Correlations

Mass Transport at Gas-Liquid Boundary

The CO_2 and O_2 required for the cathode reaction is transported to the cathode bed via the gas chamber (rectangular or tubular/annulus geometry as discussed in cell geometry section). The gases could be transported in a particular molar ratio of 2:1 for CO_2 and O_2 which can be kept same as the molar ratio of CO_2 and O_2 during the reaction at cathode. The molar ratio could also be different than 2:1 if different overfeed rates are required of the two gases. The gases could also

Table E.3: Boundary Conditions for the Partial Differential Equations

Variable	Boundary	BC Equation	Remarks
CO_2 conc., $\bar{\rho}_{co_2}$	$x = -L_c$	$\alpha_c D_{co_2} \frac{d\bar{\rho}_{co_2}(-L_c)}{dx} = K_{g,co_2,c}\left(\frac{P_{co_2,c}}{H_{co_2}} - \frac{\bar{\rho}_{co_2}(-L_c)}{\bar{\rho}_{salt}}\right)$	convective equation at cathode-gas boundary
O_2 conc., $\bar{\rho}_{o_2}$	$x = -L_c$	$\alpha_c D_{o_2} \frac{d\bar{\rho}_{o_2}(-L_c)}{dx} = K_{g,o_2,c}\left(\frac{P_{o_2,c}}{H_{o_2}} - \frac{\bar{\rho}_{o_2}(-L_c)}{\bar{\rho}_{salt}}\right)$	convective equation at cathode-gas boundary
Electrolyte Potential, V	$x = -L_c$	$\frac{dV}{dx} = 0$	zero voltage gradient
Ionic Current Density, i''	$x = -L_c$	$i'' = 0$	zero current density at the gas-liquid interface
CO_2, O_2 conc.,$\bar{\rho}_{co_2}$,$\bar{\rho}_{o_2}$	$x = 0$	$\alpha_c D_{co_2} \frac{d\bar{\rho}_{co_2}(0^-)}{dx} + \alpha_c D_{o_2} \frac{d\bar{\rho}_{o_2}(0^-)}{dx} = \alpha_a D_{co_2} \frac{d\bar{\rho}_{co_2}(0^+)}{dx}$	matching condition and the O_2-CO_2 reaction
Electrolyte Potential, V	$x = 0$	$V(0^+) = V(0^-) + V_{cell}$	discontinuity due to cell voltage
Ionic Current Density, i''	$x = 0$	$i''(0^+) = i''(0^-) = i''_{cell}$	continuity in the current density
CO_2 conc., $\bar{\rho}_{co_2}$	$x = L_a$	$\alpha_a D_{co_2} \frac{d\bar{\rho}_{co_2}(L_a)}{dx} = K_{g,co_2,a}\left(\frac{\bar{\rho}_{co_2}(L_a)}{\bar{\rho}_{salt}} - \frac{P_{co_2,a}}{H_{co_2}}\right)$	convective equation at anode-gas boundary
Potential, V	$x = L_a$	$\frac{dV}{dx} = 0$	zero voltage gradient at gas-liquid interface
Current Density, i''	$x = L_a$	$i'' = 0$	zero current density at the gas-liquid interface

possibly be fed as CO_2 + Air which would entail presence of N_2 in the gas mixture as well and can affect the reaction kinetics due to reduced mole fractions of CO_2 and O_2. The effects of mole fractions on rate of reaction are covered in detail in the subsection ”Reaction Kinetics”.

The mass transport of CO_2 and O_2 from the gas chamber into the cathode bed takes place at the gas-liquid interface via equations E.8 and E.9 and is found to be a function of gas-side mass transfer coefficient only since the mass transfer resistance offered by the liquid film is negligible (Bravo et al. [1985])

$$\delta_c D_{\mathrm{co_2}} \left[\frac{d\bar{\rho}_{\mathrm{co_2}}}{dx}\right]_{x=L_c} = K_{\mathrm{g,co_2},c} \left[P_{\mathrm{co_2},c} H_{\mathrm{co_2}} - (\bar{\rho}_{\mathrm{co_2}})_{x=L_c}\right] \tag{E.8}$$

$$\delta_c D_{\mathrm{o_2}} \left[\frac{d\bar{\rho}_{\mathrm{o_2}}}{dx}\right]_{x=L_c} = K_{\mathrm{g,o_2},c} \left[P_{\mathrm{o_2},c} H_{\mathrm{o_2}} - (\bar{\rho}_{\mathrm{o_2}})_{x=L_c}\right] \tag{E.9}$$

where δ_c is the void fraction of the cathode packed bed, D_{CO_2} is the molecular diffusivity of gaseous carbon-dioxide in air, D_{O_2} is the molecular diffusivity of gaseous oxygen in nitrogen, K_g is the mass transfer coefficient in the gas phase, $P_{CO_2,C}$ and $P_{O_2,C}$ are respectively the partial pressures of carbon dioxide and oxygen in the cathode gas chamber, H_{CO_2} and H_{O_2} are respectively the Henry's Law solubility coefficients for carbon dioxide and oxygen in the molten salt electrolyte, $\bar{\rho}_{\mathrm{co_2}}$ and $\bar{\rho}_{\mathrm{o_2}}$ are respectively the molar concentrations of CO_2 and O_2 in the liquid phase at the gas-liquid interface, and L_c is the cathode bed thickness.

The equations E.8 and E.9 representing boundary conditions at the cathode gas-liquid interface are quite analogous to equation one might encounter in a heat

transfer problem where diffusion coefficient is like the conductivity, molar concentration is like the temperature and mass transfer coefficient is like the heat transfer coefficient. The idea is to bring molar concentrations in gas and liquid phase to equilibrium while incorporating the possible resistance that is offered. Similar approach is followed in the anode bed as well and the boundary equation can be defined similarly:

$$\delta_a D_{\mathrm{co}_2} \left[\frac{d\bar{\rho}_{\mathrm{co}_2}}{dx}\right]_{x=L_a} = K_{\mathrm{g,co}_2,a} \left[(\bar{\rho}_{\mathrm{co}_2})_{x=L_a} - P_{\mathrm{co}_2,a} H_{\mathrm{co}_2}\right] \tag{E.10}$$

As per Johnstone and Pigford [1942], not more than 10% of the total resistance to mass transfer in a wetted-wall column lies in the liquid phase. The estimation of the gas-side mass transfer coefficient for the packed bed is based on extensive investigations done on wetted-wall columns by Johnstone and Pigford [1942], Sherwood, Gilliland, etc. Bravo et al. [1985] investigated various correlations for the mass transfer in packed bed columns and arrived at an equation similar to that proposed by Johnstone and Pigford [1942] but having a slightly different coefficient. However, the mass transfer coefficient was shown to depend on Reynolds number raised to exponent 0.8 and on Schmidt number raised to exponent 0.333. The equation proposed by Bravo et al. [1985] for mass transfer in gauze packings is used in the present work. The equation proposed by Bravo et al. [1985] uses the original correlation proposed by Johnstone and Pigford [1942] and experimental data from the work of Billet at BASF in West Germany and Fractionation Research Inc.

$$Sh_G = 0.0338\, Re^{0.8}\, Sc^{0.333} \tag{E.11}$$

where Sh_G ($= k_G d_{eq} / D_G$) is the Sherwood number for gas, k_G is the mass transfer coefficient, d_{eq} is the equivalent diameter of the packing and D_G is the molecular diffusivity of the gas species. In the current work, k_G is the unknown variable that is to be estimated from the correlation equation as above.

The molecular diffusivity of gas species, namely CO_2 and O_2 in various possible gas mixtures need to be known to determine the mass transfer coefficient. It's anticipated that the gas chamber in cathode would mainly contain CO_2, O_2, and N_2 therefore molecular diffusion of CO_2 and O_2 in air with a possibly skewed ratio of O_2 and N_2 in the air needs to be determined. In anode, it's anticipated that CO_2 will be generated within anode bed and will evolve through the anode gas chamber in the presence of water-vapor. The air or water-vapor will help in controlling the vapor pressure of CO_2 so as to facilitate optimum fuel cell operation. Therefore, in anode, molecular diffusion of CO_2 in air or water-vapor needs to be determined. Chapter 11 in Poling et al. [2001] is used to estimate the molecular diffusion coefficients for each of these set of cases. As shown by many authors, the gas side mass transfer coefficient is dominant in the wetted-wall falling liquid scenarios in the absorption or distillation columns. The equation E.11 can be used to estimate the gas side mass transfer coefficient assuming turbulent vapor/gas flow (Perry 5-61). The gas mixture of CO_2, O_2, and N_2 is sent through the gas chamber in the cathode side. The ratio of O_2, and N_2 will be different than that in the air due to the reaction of CO_2 and O_2 to form carbonate ions within cathode. The diffusion coefficients of CO_2 and O_2 are then estimated using equations as above and presented in table D.1.

Other physical properties of CO_2, O_2, and N_2 etc from NP Bansal.

Table E.4: Gas-side mass transfer at cathode gas-liquid interface for square bed cross-section.

Parameter	Symbol	Units	Value	Source	Remarks
Gas Velocity	$U_{g,c}$	m/s	0.2	Input	
Superficial Liquid Velocity	$U_{o,c}$	m/s	0.4-0.5	Table C.1, Mesh no. 4	
Bed Void Fraction	δ_c	fraction	0.884	Table C.2	
True Liquid Velocity	$U_{l,c,eff}$	m/s	0.59	$U_{true} = U_{supf}/\delta_c$	
Equivalent Dia	$d_{eq,sq}$	m	0.02	Table E.1	
CO_2 Kinematic viscosity	ν_{CO_2}	m^2/s	7.4×10^{-5}	eqn. D.7	@ 1000 K
O_2 Kinematic viscosity	ν_{O_2}	m^2/s	1.24×10^{-4}		@ 1000 K
Diffusivity of CO_2 in air	$D_{\mathrm{CO}_2,air}$	m^2/s	1.26×10^{-4}	Table D.1	
Diffusivity of O_2 in N_2	$D_{\mathrm{CO}_2,\mathrm{N}_2}$	m^2/s	1.95×10^{-4}	Table D.1	
Gas-side mass transfer coefficient, CO_2	$K_{G,\mathrm{CO}_2,c}$	m/s	0.0168	Bravo et al. [1985]	
Gas-side mass transfer coefficient, O_2	$K_{G,\mathrm{O}_2,c}$	m/s	0.0176	Bravo et al. [1985]	

Mass Transport at Electrode Surface

This is required to establish relationship between reaction rates on the surface of electrode as a function of bulk liquid concentration. The calculation of concentration of gas species present within the film surrounding the electrode surface will be needed to establish that relationship and requires estimation of the rate of mass transport.

The packed bed cathode has a structure that allows flow of gases and electrolyte while the cathode structure remains electrically connected. The concept for cathode design is a stack of wire-mesh screens or perforated plates, spaced and supported by horizontal rods that double as electron conductors. The anode and cathode tubes are separated by an electrically insulating annulus through which flows the molten salt. With the help of insert type distributor arrangement, the molten salt electrolyte is allowed to fall on the outside of the cathode tube as a falling film through the stack of screens and perforated plates that serve as a packed bed as shown in figure 2.2.

Liquid to Electrode Surface mass transport in Cathode:

The CO_2 and the air is pumped upward through the gas chamber adjacent to the gravity-fed flow of electrolyte passing through packed bed of wire-mesh or perforated stainless steel sheets. CO_2 and O_2 are transported into the liquid electrolyte at the liquid-gas boundary through convective mass transfer where most of the resistance is offered by the gas side. The CO_2 and O_2 then diffuses from the liquid-gas convective boundary into the bulk liquid phase. The dissolved gases CO_2 and O_2 diffuse through the molten salt to reach the electrode reaction sites

where the reaction takes place as shown in figure E.4. This mass transport of CO_2 and O_2 from the bulk liquid phase onto the wire-mesh grid (electrode) surface is subjected to a liquid-to-solid mass transfer resistance which needs to be evaluated to be able to determine reaction rates necessary for predicting fuel cell performance. CO_2 and O_2 reacts on the electrode surface to produce carbonate ion CO_3^{2-} which migrates by ionic conduction towards the anode.

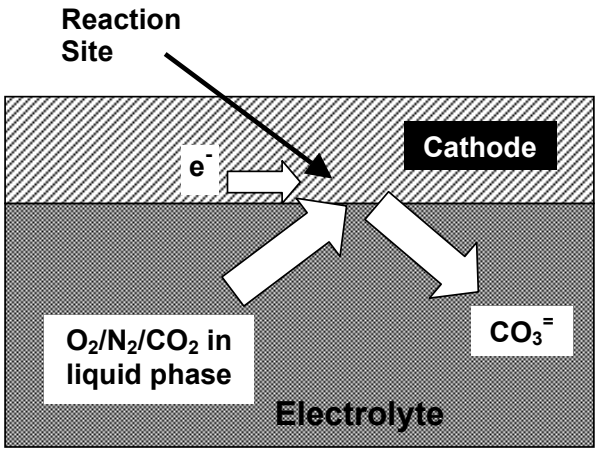

Figure E.4: Mass Transport in Porous Bed Cathode in a gas-bubble free electrolyte.

The correlations for mass transfer coefficient, diffusion coefficient, bed resistivity and related parameters are described in this section and tabulated in Tables E.6 and E.7.

Cathode Bed

One of the changes in the packed bed correlations for cathode from the earlier model is that gas bubbles are not present. Due to this the mass transfer from the

Table E.5: Liquid-solid mass transfer in the cathode bed.

Parameter	Symbol	Units	Value	Source	Remarks
Liquid Electrolyte Kinematic Viscosity	ν_L	m^2/s	5.04×10^{-7}	Janz et al. [1979]	Ternary Li-Na-K carbonate eutectic melt 1000 K
Superficial Liquid Velocity	$U_{o,c}$	m/s	$0.4 - 0.5$	Table C.1, Mesh no. 4	
Bed Void Fraction	δ_c	fraction	0.884	Table C.2	
True Liquid Velocity	$U_{l,c,eff}$	m/s	0.59	$U_{true} = U_{supf}/\delta_c$	
Molecular diffusivity of CO_2 in molten salt	$D_{m,\mathrm{CO_2}}$	m^2/s	1.48×10^{-9}	Wilemski [1983]	data for Na-K binary melt
Molecular diffusivity of O_2 in molten salt	$D_{m,\mathrm{O_2}}$	m^2/s	1.76×10^{-9}	Wilemski [1983]	data for Na-K binary melt
Wire diameter	d_t	m	0.00016	Table C.1, Mesh no. 4	
Equivalent packing diameter	$d_e = d_t(\varepsilon/1-\varepsilon)$	m	0.00122	Hughmark [1972]	
Reynolds number	$Re_c^{''}$		1096	$Re = U_{l,c,eff} d_e/\nu_L$	
Schmidt Number	Sc		$Sc_{\mathrm{CO_2}} = 341$, $Sc_{\mathrm{O_2}} = 286$	$= \nu_L/D_m$	
Sherwood Number	Sh		$Sh_{\mathrm{CO_2}} = 418$, $Sc_{\mathrm{O_2}} = 394$	Ranz [1952]	
Liquid-solid mass transfer coefficient, CO_2	$K_{LS,\mathrm{CO_2},c}$	m/s	5.1×10^{-4}	$k = ShD_m/d_e$	
Liquid-solid mass transfer coefficient, O_2	$K_{LS,\mathrm{O_2},c}$	m/s	5.7×10^{-4}	$k = ShD_m/d_e$	

gas film to the surface of the bulk electrolyte (in the falling film) has to be reconsidered . Although there are various correlations in the literature for a gas film resistance in a wetted wall column, the correlation of Bravo et al. [1985] describes the gas film resistance for a packed bed which is the closest correlation that could be found. The gas side mass transfer resistance is then evaluated from the correlation for $K_{g,c}$.

The mass transfer from the bulk electrolyte to the cathode electrode surface also changes in the same respect; the absence of gas bubbles. The correlation given by Azbel [1981] basically covers lot of empirical and semiempirical data from the literature and is the closest possible for the present work. Another justification is that according to Azbel the correlation is correct for calculating mass-transfer coefficients for fixed solid particles in a flowing liquid or settling particles in a still liquid, and former seems to be the exact case at hand in the present work. The fixed solid particles are analogous to the packed bed and flowing liquid to the electrolyte.

Resistivity correlation is defined from the Bruggeman's equation De La Rue and Tobias [1959] in a similar way as defined in the earlier model except that the bed voidage, ζ_c, is only due to the packed bed media and not the gas bubbles.

The transverse dispersion is considered over molecular dispersion in the present work. The reason is that the, unlike the earlier model where there was was no free surface and no possibility of waves, the present work does have a free gas surface and therefore waves might develop in the falling film giving rise to diffusion in transverse direction. This phenomena is shown schematically in Figure E.5. The concentration of gases might be different on the boundary due to this aspect and

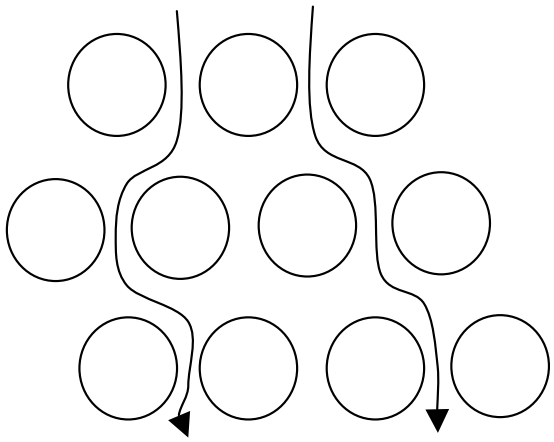

Figure E.5: Transverse dispersion in packed bed falling films.

therefore transverse dispersion rather than molecular diffusion is considered. Delgado [2006] work appropriately correlates transverse dispersion in packed beds as a function of molecular dispersion for various conditions of the Schmidt number and the Peclet number based on the molecular dispersion.

Anode Bed

The Sherwood number describing gas phase resistance is same as that in the cathode, except that combined average properties should be considered for entrained carbon in the electrolyte instead of just electrolyte.

The correlation for mass transfer from the bulk electrolyte to the carbon particle is taken from Rahman and Streat [1981]. Although this correlation is suggested for Reynolds numbers between 2 and 25, Rahman and Streat suggests that the extrapolation upto $Re_s \approx 2000$ provides a satisfactory fit of mass transfer data in

Table E.6: Correlations Used for the Cathode Packed Bed Falling Film

Parameter	Description	Correlation	Remarks	References
Pe_T	Peclet number	$\frac{1}{Pe_T} = \frac{1}{\tau Pe_m} + \frac{1}{12} - \left(\frac{Sc}{1500}\right)^{4.8} \times (\tau Pe_m)^{3.83-1.3log_{10}(Sc)}$	$Sc \leq 550$, $Pe_m \leq 1600$	Delgado [2006]
		$Pe_T = (0.058Sc+14) - (0.058Sc+2)\exp\left(-\frac{352Sc^{0.5}}{Pe_m}\right)$	$Sc \leq 550$, $Pe_m > 1600$	
		$\frac{1}{Pe_T} = \frac{1}{\tau Pe_m} + \frac{1}{12} - 8.1 \times 10^{-3}(\tau Pe_m)^{0.268}$	$Sc > 550$, $Pe_m \leq 1600$	
		$Pe_T = 45.9 - 33.9\exp\left(-\frac{15Sc}{Pe_m}\right)$	$Sc > 550$, $Pe_m > 1600$	
		where $Pe_m = \frac{ud}{D_m}$, $Sc = \frac{\mu}{\rho D_m}$, and $\tau = \sqrt{2}$	value of τ is for unconsolidated porous media	Sherwood et al. [1975]
D_T	Transverse dispersion	$D_T = \frac{ud}{Pe_T}$		
Sh_G	Gas Phase Sherwood no.	$Sh_G = 0.0338 Re_G^{0.8} Sc^{0.333}$, where $Re_G = \frac{(U_{0G}+U_L)d_e}{\nu_G}$	$d_e = \frac{2}{3} d_p \frac{\varepsilon}{1-\varepsilon}$	Bravo et al. [1985]
$K_{g,c}$	Gas side mass transfer coefficient	$K_{g,c} = \frac{D_T P_T Sh_G}{P_{g,c} RT\, dP_{BM,G}}$		
		where $b = 0.439 + 0.1807 d_p^{1/2} + 0.234\alpha(\alpha+0.05) Re_L^{1/2}$	$\alpha \simeq 0.33$.	
$K_{l-s,c}$	Liquid-to-solid mass transfer coefficient	$K_{l-s,c} = \frac{Sh_{l-s} D_T}{\ell}$		
R_c	Resistivity	$R_c = \frac{1}{K_{salt}}(1-\zeta_c)^{-3/2}$		Tobias [1966]

fixed and fluidised beds.

Resistivity correlation is defined from Bruggeman's equation De La Rue and Tobias [1959] in a similar way as defined in the earlier model except that the bed voidage, ζ_a, is now due to the packed bed media and the carbon particles but not the gas bubbles.

The correlation for transverse dispersion is not readily available for the anode bed. However, a correlation for thermal diffusivity is available [Borodulya et al., 1983] for a case similar to that of the anode bed. For the total diffusivities in heat transfer and mass transfer, we can write, $\alpha_{tot} = \alpha + \alpha_{turb}$, and $D_{tot} = D + D_{turb}$. The Reynold's analogy from Sherwood et al. [1975] tells us that, $\alpha_{turb} = D_{turb}$. Simplifying gives us,

$$D_{tot} = D + (\alpha_{tot} - \alpha)$$

Now, if the time for diffusion to take place is large enough then $D \ll D_{tot}$ and $\alpha \ll \alpha_{tot}$ and we get,

$$D_{tot} = \alpha_{tot} \tag{E.12}$$

The equation for $D_{t,a}$ is henceforth given in the table.

Table E.7: Correlations Used for the Anode Packed Bed Falling Film

Parameter	Description	Correlation	Remarks	References
Re_{mf}	Reynolds no. for min. fluidization	$Re_{mf} = (27.2^2 + 0.0408Ar)^{1/2} - 27.2$	$Ar = \frac{\rho_f(\rho_s - \rho_f)gd_p^3}{\mu_L^2}$	Grace [1986]
U_{mf}	Min. fluidization velocity	$U_{mf} = \frac{\mu_L Re_{mf}}{\rho_f d_p}$		
D_T	Transverse diffusion coefficient	$D_T = 0.0038(\frac{U_o}{\varepsilon_p} - U_{mf})S_h Fr^{-0.09}\varepsilon_p^{-2.24}\left(\frac{S_v - d_t}{d}\right)^{0.35}$ where $Fr = \frac{\rho U_o^2}{\Delta\rho g d_p}$		Borodulya et al. [1983]
Sh_G	Gas Phase Sherwood no.	$Sh_G = 0.0338Re_G^{0.8}Sc^{0.333}$ where $Re_G = \frac{(U_{0G,eff} + U_{L,eff})d_e}{\nu_G}$	$d_e = \frac{2}{3}d_p\frac{\varepsilon}{1-\varepsilon}$	Bravo et al. [1985]
$K_{g,a}$	Gas side mass transfer coefficient	$K_{g,a} = \frac{D_T P_T Sh_G}{P_{g,a}RTdP_{BM,G}}$		
Sh_{l-s}	Liq-to-Solid Phase Sherwood no.	$Sh_{l-s} = \frac{0.86}{\varepsilon}Re_s^{1/2}Sc^{1/3}$, where $Re_s = \frac{U_s d_c}{\nu_L}$		Rahman and Streat [1981]
$K_{l-s,a}$	Liquid-to-solid mass transfer coefficient	$K_{l-s,a} = \frac{D_T Sh_{l-s,a}}{d_p}$		
R_a	Resistivity of anode bed	$R_a = \frac{1}{K_{salt}}(1 - \varepsilon_{g,a})^{-3/2}$, where $\varepsilon_{g,a} = \zeta_a + h_s(1 - \zeta_a)$		Tobias [1966]

Bibliography

H. Abernathy, R. Gemmena, K. Gerdesa, M. Koslowskeb, and T. Tao. Basic properties of a liquid tin anode solid oxide fuel cell. *Journal of Power Sources*, 196 (10):4564–4572, 2011.

S.K. Achwal and J.B. Stepanek. Holdup profiles in packed beds. *The Chemical Engineering Journal*, 12:69–75, 1976.

R. Agarwal and A.A. Kornhauser. Energy balance for a direct carbon molten carbonate fuel cell. In *ASME Heat Transfer / Fluids Engineering Summer Conference*, volume 3, Charlotte, 2004. Paper no. HT-FED2004-56887.

B.K. Andersen. *Thermodynamic Properties of Molten Alkali Carbonates*. PhD thesis, The Technical University of Denmark, 1975.

A.J. Appleby and S. Nicholson. Oxygen reduction in carbonate melts: Significance of the peroxide and superoxide ions. *J. of Electroanal. Chem. and Interf. Electrochem.*, 38:App13–App18, 1972.

A.J. Appleby and S. Nicholson. The reduction of oxygen in molten lithium carbonate. *J. of Electroanal. Chem. and Interf. Electrochem.*, 53:105–119, 1974.

A.J. Appleby and S. Nicholson. Reduction of oxygen in alkali carbonate melts. *J. of Electroanal. Chem.*, 83:309–328, 1977.

A.J. Appleby and S. Nicholson. Reduction of oxygen in lithium-potassium carbonate melt. *J. of Electroanal. Chem.*, 112:71–76, 1980.

A.J. Appleby and C. Van Drunen. Solubilities of oxygen and carbon monoxide in carbonate melts. *J. Electrochem. Soc*, 127:1655–59, 1980.

D. Azbel. *Two-phase flows in chemical engineering*. Cambridge University Press, first edition, 1981.

Steam: Its generation and use. Babcock & Wilcox, New York, N.Y. 10017, 39 edition, 1975.

E. Baur and H. Ehrenberg. New chains of combustible. *Z. Electrochem*, 18:1002, 1912.

E. Baur, A. Peterson, and G. Fullemann. Fuel chains at high temperatures. *Z. Electrochem*, 22:409, 1916.

E. Baur, W. Treadwell, and G. Trumpler. Performance of the fuel chains at high temperatures. *Z. Electrochem*, 27:199, 1921.

A.A.C.M. Beenackers, W.P.M. van Swaaij, and A. Welmers. Mechanism of charge transfer in the discontinuous metal phase of a fluidized bed electrode. *Electrochimica Acta*, 22:1277–1281, 1977.

V.A. Borodulya, Yu.S. Teplitsky, Yu.G. Epanov, and I.I. Yanovich. Lateral thermal diffusivity of a fluidized bed packed with tube bundles. *Hungarian Journal of Industrial Chemistry, Veszprem*, 11:193–205, 1983.

A. Borucka and C.M. Sugiyama. Correlation of the equilibrium potentials and micropolarization characteristics of the o2/co2 and co/co2 gas electrodes in molten carbonate. *Electrochimica Acta*, 14:871–881, 1969.

J.L. Bravo, J.A. Rocha, and J.R. Fair. Mass transfer in gauze packings. *Hydrocarbon Processing*, 64(1):91–95, 1985.

D.A.G. Bruggeman. Berechnung verschiedener physikalischer konstanten von heterogenen substanzen. i. dielektrizittskonstanten und leitfhigkeiten der mischkrper aus isotropen substanzen. *Annalen der Physik*, 416(7):636–664, 1935.

H.S Carslaw and J.C. Jaeger. *Conduction of Heat in Solids*. Oxford University Press, 1986.

M. Chen, C. Wang, X. Niu, S. Zhao, J. Tang, and B. Zhu. Carbon anode in direct carbon fuel cell. *International J. of Hydrogen Energy*, 35:2732–2736, 2010.

T.P. Chen, E. Yuan, and A.H. Pulsifer. Bed and contact resistances in an electrically conducting fluidized bed. *AIChE Symposium Series*, 73(161):51–58, 1977.

N.J. Cherepy, R. Krueger, K.J. Fiet, A.F. Jankowski, and J.F. Cooper. Direct conversion of carbon fuels in a molten carbonate electrolyte. *Journal of Electrochemical Society*, 152(1):A80–A87, 2005.

J.S. Chong, E.B. Christiansen, and A.D. Baer. Rheology of concentrated suspensions. *J of Applied Polymer Science*, 15:2007–2021, 1971.

P. Claes, D. Moyaux, and D. Peeters. Solubility and solvation of carbon dioxide in the molten li2co3/na2co3/k2co3 (43.5:31.5:25.0 mol%) eutectic mixture at 973 k i. experimental part. *Eur. J. Inorg. Chem.*, 4:583–588, 1999.

J.F. Cooper. Direct conversion of coal and coal-derived carbon in fuel cells. In *Proceedings of the* 2^{nd} *International Conference on Fuel Cell Science, Engineering, and Technolgoy*. ASME, 2004a. KH-3.

J.F. Cooper. Direct conversion of coal and coal-derived carbon in fuel cells. In *Second International Conference on Fuel Cell Science, Engineering, and Technology*, Rochester, NY, 2004b. KH-3.

J.F. Cooper, N. Cherepy, R. Upadhye, A. Pasternak, and M. Steinberg. Direct carbon conversion: Review of production and electrochemical conversion of reactive carbons, economics and potential impact on the carbon cycle. Preprint UCRL-ID-141818, Lawrence Livermore National Laboratory and Brookhaven National Laboratory, Dec 2000. Abstract and Executive Summary.

J.F. Cooper, R. Krueger, and N. Cherepy. Fuel cell apparatus and method thereof. U.S. Patent Application Publication No. US 2002/0106549 A1, 2002.

J.F. Cooper, R. Krueger, and N. Cherepy. Tilted fuel cell apparatus. U.S. Patent Application Publication No. US 2003/0017380 A1, 2003.

R.E. De La Rue and C.W. Tobias. On the conductivity of dispersions. *Journal of the Electrochemical Society*, 106:827–833, 1959.

L. Deleebeeck and K. K. Hansen. Hybrid direct carbon fuel cells and their reaction mechanisms a review. *J Solid State Electrochem*, 18:861–882, 2014.

J.M.P.Q. Delgado. A critical review of dispersion in packed beds. *Heat Mass Transfer*, 42:279–310, 2006.

P. Dubois. Carbon dioxide solubility. *Ann. Chim.*, 10:145, 1965.

G.B. Dunks and D. Stelman. Electrochemical studies of molten sodium carbonate. *Inorg. Chem.*, 22:2168–2177, 1983.

EG and G Technical Services Inc. *Fuel cell Handbook*. U.S. Department of Energy, seventh edition, 2004.

A. Einstein. Eine neue bestimmung der molekül-dimensionen. *Ann. Physik*, 19: 289–306, 1906.

M. Fleischmann and J.W. Oldfield. Fluidized bed electrodes - part ii. the effective resistivity of the discontinuous metal phase. *Journal of Electroanalytical Chemistry*, 29:231–240, 1971.

N.A. Frankel and A. Acrivos. On the viscosity of a concentrated suspension of solid spheres. *Chemical Engineering Science*, 22:847–853, 1967.

J.R. Grace. Contacting modes and behaviour classification of gas-solid and other two-phase suspensions. *The Canadian J. of Chem. Eng.*, 64(3):353–363, 1986.

A.J. Gram, C.O. Mackey, and E.S. Monroe Jr. Convection heat transfer and pressure drop of air flowing across in-line tube banks: Ii - correlation of data for ten-row-deep tube banks. *Trans. ASME*, 80:25–35, 1958.

E.D. Grimison. Correlation and utilization of new data on flow resistance and heat transfer for cross flow of gases over tube banks. *Trans. ASME*, 59:583–594, 1937.

T.M. Gür and R.A. Huggins. Direct electrochemical conversion of carbon to electrical energy in a high temperature fuel cell. *Journal of the Electrochemical Society*, 139:L95–L97, 1992.

L.V. Gurvich, I.V. Veyts, and C.B. Alcock. *Thermodynamic Properties of Individual Substances*. Hemisphere, New York, NY, 1989.

V.E. Hauser Jr. *A study of carbon anode polarization in fused carbonate fuel cells*. PhD thesis, Oregon State University, 1964.

U. Herrmann and G. Emig. Liquid phase hydrogenation of maleic anhydride to 1,4-butanediol in a packed bubble column reactor. *Ind. Eng. Chem. Res.*, 37: 759–769, 1998.

R. Holm. *Electric Contacts: Theory and Application*. Springer-Verlag, New York, 1967.

T. Horita, N. Sakai, T. Kawada, H. Yokokawa, and M. Dokiya. An investigation of anodes for direct-oxidation of carbon in solid oxide fuel cells. *Journal of the Electrochemical Society*, 142:2621–2624, 1995.

G.A. Hughmark. Momentum, heat, and mass transfer for fixed and homogeneous fluidized beds. *AIChE J.*, 18(5):1020–1024, 1972.

W.W. Jacques. Method of converting the potential energy of carbon into electricity. U.S. Patent No. 555,511, 1896.

K. Janowitz, M. Kah, and H. Wendt. Molten carbonate fuel cell research part i. comparing cathodic oxygen reduction in lithium/potassium and lithium/sodium carbonate melts. *Electrochimica Acta*, 45:1025–1037, 1999.

G.J. Janz, C.B. Allen, N.P. Bansal, R.M. Murphy, and R.P.T. Tomkins. Physical properties data compilations relevant to energy storage. - ii. molten salts: Data on single and multi-component salt systems. National Standard Reference Data System, April 1979.

H.F. Johnstone and R.L. Pigford. Distillation in a wetted-wall column. *Trans. AIChE*, 38:25, 1942.

Y. Kanai, K. Fukunaga, K. Terasaka, and S. Fujioka. Mass transfer in molten salt and suspended molten salt in bubble column. *Chem. Eng. Sci.*, 100:153–159, 2013.

W.M Kays and M.E. Crawford. *Convective Heat and Mass Transfer*. McGraw-Hill Book Company, second edition, 1980.

S.D. Kim, C.G.J. Baker, and M.A. Bergougnou. Hold-up and axial mixing characteristics of two and three phase fluidized beds. *The Canadian Journal of Chemical Engineering.*, 50:695–701, 1972.

V.A. Kirillov and M.A. Nasamanyan. Mass transfer processes between liquid and packing in a three-phase fixed bed. *International Chemical Engineering.*, 16: 538–543, 1976.

L. Kouchachvili and M. Ikura. Performance of direct carbon fuel cell. *International J. of Hydrogen Energy*, 36:10263–10268, 2011.

H.R. Kunz, L.J. Bregoli, and S.T. Szymanski. Homogeneous/agglomerate model for molten carbonate fuel cell cathodes. *J. Electrochem. Soc*, 131(12):2815–21, 1984.

K. Kusakabe, S. Morooka, and Y. Kato. Charge transfer rate in liquid-solid and gas-liquid-solid fluidized bed electrodes. *Journal of Chemical Engineering of Japan.*, 14:208–214, 1981.

P. Le Goff, F. Vergnes, F. Coeuret, and J. Bordet. Applications of fluidized beds in electrochemistry. *Industrial and Engineering Chemistry*, 61(10):8–17, 1969.

M. Leva. Fluid flow through packed beds. *Chem. Eng.*, 56(5):115–117, 1949.

X. Li, Z.H. Zhu, R.D. Marco, J. Dicks, A. Bradley, S. Liu, and G.Q. Lu. Factors that determine the performance of carbon fuels in the direct carbon fuel cell. *Ind. Eng. Chem. Res.*, 47:9670–9677, 2008.

X. Li, Z. Zhu, J. Chen, R.D. Marco, A. Dicks, J. Bradley, and G. Lua. Surface modification of carbon fuels for direct carbon fuel cells. *J. Power Sources*, 186: 1–9, 2009.

X. Li, Z. Zhu, R.D. Marco, J. Bradley, and A. Dicks. Evaluation of raw coals as fuels for direct carbon fuel cells. *J of Power Sources*, 195:4051–4058, 2010.

S.H. Lu. *O2 reduction in MCFC*. PhD thesis, Illinois Institute of Technology, Chicago, IL, 1985.

S.H. Lu and J.R. Selman. Electrode kinetics of oxygen reduction on gold in molten carbonate. *J. Electroanal. Chem.*, 333:257–271, 1992.

The Math Works MATLAB. Matlab version 8.3.0.532 release r2014a, 2014.

J. McHardy. Cathode chemistry and kinetics. In Fossil Fuel A.J. Appleby and Advanced Systems Division, editors, *Proceedings of the DOE/EPRI Workshop on Molten Carbonate Fuel Cells*, pages 1–35–1–42, November 1979. WS-78-135.

S. Morooka, K. Kusakabe, T. Watari, and Y. Kato. Effective specific resistance of a particle phase in a fluidized bed electrode. *International Chemical Engineering*, 21:465–472, 1981.

D. Moyaux, J. Glibert, and P. Claes. Dependence of the concentraiton of o(-i) on the partial pressures of oxygen and carbon dioxide in a molten li2co3 + na2co3 + k2co3 eutectic mixture at 973 k. *J. Electroanal. Chem.*, 349:415–428, 1993.

N. Nakagawa and M. Ishida. Performance of an internal direct-oxidation carbon fuel cell and its evaluation by graphic exergy analysis. *Ind. Eng. Chem. Res.*, 27: 1181–1185, 1988.

J. Newman. Transport processes in electrolytic solutions. In C.W. Tobias, editor, *Advances in Electrochemistry and Electrochemical Engineering*, volume 5, pages 87–135. Interscience, 1967.

J.S. Newman and C.W. Tobias. Theoretical analysis of current distribution in porous electrodes. *J. Electrochem. Soc.*, 109(12):1183–1191, 1962.

T. Nishina, I. Uchida, and J.R. Selman. Gas electrode reactions in molten carbonate media part v. electrochemical analysis of the oxygen reduction mechanism at a fully immersed gold electrode. *J. Electrochem. Soc*, 141(5):1191–1198, 1994.

W.H.A. Peelen, M. Olivry, S.F. Au, J.D. Fehribach, and K. Hemmes. Electrochemical oxidation of carbon in a 62/38 mol% li/k carbonate melt. *Journal of Applied Electrochemistry*, 30:1389–1395, 2000.

D.J. Pickett. *Electrochemical Reactor Design*. Elsevier, 1977.

B.E. Poling, J.M. Prausnitz, and J.P. O'Connell. *The Properties of Gases and Liquids*. McGraw Hill, 2001.

M.P. Predtechenskii, Y.D. Varlamov, O.F. Bobrenok, and S.N. Ulyankin. Solid hydrocarbon conversion in a fuel cell with molten carbonate electrolyte. *J of Engineering Thermophysics*, 18(2):93–98, 2009a.

M.P. Predtechenskii, Y.D. Varlamov, S.N. Ulyankin, and Y. D. Dubov. Direct conversion of solid hydrocarbons in a molten carbonate fuel cell. *Thermophysics and Aeromechanics*, 16(4):601–610, 2009b.

M.P. Predtechenskii, Y.D. Varlamov, and S.N. Ulyankin. Specific characteristics of molten carbonate fuel cell in realization of electrochemical coal oxidation. *Russian J of Electrochemistry*, 46(8):871–876, 2010.

K. Rahman and M. Streat. Mass transfer in liquid fluidized beds of ion exchange particles. *Chemical Engineering Science*, 36:293–300, 1981.

W.E. Ranz. Friction and transfer coefficients for single particles and packed beds. *Chem. Eng. Prog.*, 48:247–253, 1952.

A.K. Reed and W.M. Goldberger. Electrical behavior in fluidized beds of conducting solids. In J.A. Buckham and N.M. Levitz, editors, *Fluidized-bed technology*, volume 62 of *67*, pages 71–75. AIChE, 1966.

L.P. Reiss. Cocurrent gas-liquid contacting in packed beds. *Ind. Eng. Chem. Proc. Des. Dev.*, 6:486–499, 1967.

E. Sada, S. Katoh, H. Beniko, H. Yoshli, and M. Kayano. Solubility of carbon dioxide in molten salts. *J. Chem. Eng. Data*, 25:45–47, 1980.

Y. Sano, N. Yamaguchi, and T. Adachi. Mass transfer coefficients for suspended particles in agitated vessels and bubble columns. *Journal of Chemical Engineering of Japan.*, 7:255–261, 1974.

M. Schenke, G.H.J. Broers, and J.A.A. Ketelaar. The solubility of oxygen in molten carbonates. *J. Electrochem. Soc*, 113:404, 1966.

J.R. Selman. Molten carbonate fuel cell (mcfc) porous electrode and kinetic studies. Final Report TR-101070, Research Project 2278-03, Institute of Gas Technology, Chicago, Illinois, October 1992. Prepared for EPRI.

Y.T. Shah. *Gas-Liquid-Solid Reactor Design*. McGraw Hill International Book Company, Department of Chemical and Petroleum Engineering, University of Pittsburgh, Pittsburgh USA, 1979.

T.K. Sherwood, R.L. Pigford, and C.R. Wilke. *Mass Transfer*. McGraw Hill, 1975.

D.S. Smith and J. Winnick. Cesium-containing electrolyte for the molten carbonate fuel cell. *Electrochemical and Solid-State Letters*, 2(5):207–209, 1999.

S.W. Smith, W.M. Vogel, and S. Kapelner. Solubilities of oxygen in fused li2co3-k2co3. *J. Electrochem. Soc*, 129(8):1668–1670, 1982.

V. Specchia and G. Baldi. Pressure drop and liquid holdup for two phase concurrent flow in packed beds. *Chemical Engineering Science.*, 32:515–523, 1977.

M. Steinberg, J.F. Cooper, and N. Cherepy. High efficiency direct carbon and hydrogen fuel cells for fossil fuel power generation. Preprint UCRL-JC-146774, Lawrence Livermore National Laboratory and Brookhaven National Laboratory, January 2002.

T. Tao, M. Slaney, L. Bateman, and J. Bentley. Anode polarization in liquid tin anode solid oxide fuel cell. *ECS Transactions - 10th International Symposium on Solid Oxide Fuel Cells*, 7(1 part 2), 2007.

D.G. Thomas. Transport characteristics of suspensions; viii. a note on the viscosity of newtonian suspensions of uniform spherical particles. *J of Colloid Science*, 20:267–277, 1965.

Charles W. Tobias. *Advances in Electrochemistry and Electrochemical engineering*, volume 2. Interscience Publishers, 1966.

C.W. Tobias, M. Eisenberg, and C.R. Wilke. Diffusion and convection in electrolysis - a theoretical review. *J. Electrochem. Soc.*, 99(12):359C–365C, 1952.

R.P.T. Tomkins and N.P. Bansal, editors. *Gases in molten salts*. Solubility data series v. 45/46. Oxford, New York, Pergamon, 1991.

J.L. Turpin and R.L Huntington. Prediction of pressure drop for two-phase, two-component concurrent flow in packed beds. *AIChE Journal.*, 13:1196–1202, 1967.

I. Uchida, T. Nishina, Y. Mugikura, and K. Itaya. Gas electrode reactions in molten carbonate media part i. exchange current density of oxygen reduction in (li+k)co3 eutectic at 650 deg c. *J. Electroanal. Chem.*, 206:229–239, 1986.

Anval Valves. http://www.anval.net/downloads/bulk%20density%20chart.pdf, 2014.

Y.D. Varlamov, M.P. Predtechenskii, and S.N. Ulyankin. Interrelation of anode and cathode processes in electrochemical carbon oxidation in a fuel cell with molten carbonate electrolyte. *J of Engineering Thermophysics*, 21(1):16–27, 2012.

K.J. Vetter. *Electrochemical Kinetics: Theoretical and experimental aspects*. Academic Press, 1967.

W.M. Vogel, S.W. Smith, and L.J. Bregoli. Studies of the reduction of oxygen on gold in molten li2co3-k2c03 at 650 deg c. *J. Electrochem. Soc*, 130(3):574–578, 1983.

D.G. Vutetakis. *Electrochemical Oxidation of Carbonaceous Materials Dispersed in Molten Carbonate*. PhD thesis, The Ohio State University, 1985.

D.G. Vutetakis, D.R. Skidmore, and H.J. Byker. Electrochemical oxidation of molten carbonate-coal slurries. *Journal of the Electrochemical Society*, 134:3027–3034, 1987.

R.D. Weaver. Direct electrochemical generation of electricity from coal. Quarterly Progress Report No. 1 Prepared for U.S. Energy Research and Development Administration Contract no. E(04-3)-115, P.A. No. 105, SRI Project PYU 4929, SRI International, Menlo Park, California, July 1976a.

R.D. Weaver. Direct electrochemical generation of electricity from coal. Quarterly Progress Report No. 2 Prepared for U.S. Energy Research and Development Administration Contract no. E(04-3)-115, P.A. No. 105, SRI Project PYU 4929, SRI International, Menlo Park, California, October 1976b.

R.D. Weaver, L. Tietz, and D. Cubicciotti. Direct use of coal in a fuel cell: Feasibility investigation. Technical Report EPA-650/2-75-040, SRI International, Menlo Park, California, 1975.

R.D. Weaver, S.G. Leach, A.E. Bayce, and L. Nanis. Direct electrochemical generation of electricity from coal. DOE contract EY-76-C-03-0115 P.A. No. 105, May 1977-Feb 1979, SRI International, Menlo Park, California, 1979.

R.D. Weaver, S.C. Leach, and L. Nanis. Electrolyte management for the coal air fuel cell. *Proceedings of the 16 th Intersociety Energy Conversion Engineering Conference*, 1:717–721, 1981.

R.D. Weaver, S. Leach, and L. Nanis. Electrolyte management for the coal air fuel cell. In *Proceedings of the* 16^{th} *Intersociety Energy Conversion Engineering Conference*, volume 1, pages 717–721. ASME, 1982.

G. Wilemski. Simple porous electrode models for molten carbonate fuel cells. *J. Electrochem. Soc.*, 130(1):117–121, 1983.

G. Wilemski, T. Wolf, D. Bloomfield, M.L. Finson, E.R. Pugh, and K.L. Wray. Performance model for molten carbonate fuel cells. US DOE contract DE-AC-03-79ET11322, July 1978 - July 1979, Physical Sciences Inc., Woburn, Massachussetts, 1979.

J. Winnick and P.N. Ross Jr. The kinetics of the o2/co2 reaction in molten carbonate: Reaction orders for o2 and co2 on porous nio. *J. Electrochem. Soc*, 128(5): 991–995, 1981.

C.Y. Yuh and J.R. Selman. The polarization of molten carbonate fuel cell electrodes - i. analysis of steady-state polarization data. *J. Electrochem. Soc*, 138:3642–3648, 1991.

S. Zecevic, E.M. Patton, and P. Parhami. Electrochemistry of direct carbon fuel cell based on metal hydroxide electrolyte. In *NETL Direct Carbon Fuel Cell Workshop*, 2003.

S. Zecevic, E.M. Patton, and P. Parhami. Carbon-air fuel cell without a reforming process. *Carbon*, 42:1983–1993, 2004.

S. Zecevic, E.M. Patton, and P. Parhami. Direct electrochemical power generation from carbon in fuel cells with molten hydroxide electrolyte. *Chemical Engineering Communications*, 192:1655–1670, 2005.

J. Zhang, Z. Zhong, D. Shen, J. Xiao, Z. Fu, H. Zhang, J. Zhao, W. Li, and M. Yang. Characterisitics of a fluidized bed electrode for a direct carbon fuel cell anode. *J of Power Sources*, 196:3054–3059, 2011.

A. Zukauskas. Heat transfer from tubes in cross flow. In Hartnett J. P. and T. F. Irvine Jr., editors, *Advances in Heat Transfer*, volume 8, pages 93–160. Academic Press, New York, 1972.